Unsteady Hot-Wire and Hot-Film Wake Measurements of Automobile-Like Bluff Bodies

by

Christopher Mark Greiner

S.B. Aeronautics and Astronautics, M.I.T., 1983
S.M. Aeronautics and Astronautics, M.I.T., 1985

SUBMITTED IN PARTIAL FULFILLMENT OF THE
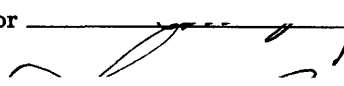REQUIREMENTS FOR THE DEGREE OF

Doctor of Philosophy
in
Aerodynamics
at the
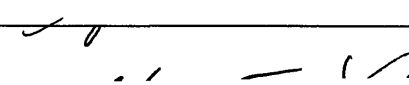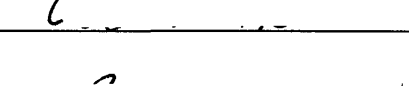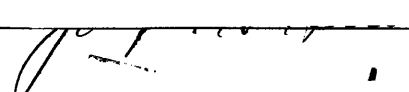Massachusetts Institute of Technology

February 1990

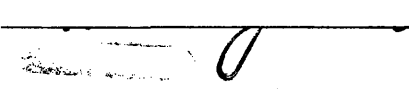©1989, Massachusetts Institute of Technology

Signature of Author _____
Department of Aeronautics and Astronautics
· 17 November 1989

Certified by _____
Professor Sheila E. Widnall
Thesis Supervisor

Certified by _____
Professor Mårten T. Landahl
Thesis Committee

Certified by _____
Dr. Joseph H. Haritonidis
Thesis Committee

Accepted by _____
Professor Harold Y. Wachman
Chairman, Department Graduate Committee

Unsteady Hot-Wire and Hot-Film Wake Measurements of Automobile-Like Bluff Bodies

by

Christopher Mark Greiner

Submitted to the Department of Aeronautics and Astronautics, November 12, 1989
in partial fulfillment of the requirements for the degree of
Doctor of Philosophy in Aerodynamics

A method of calculating vehicle drag from wake velocity measurements is presented, including an extension for finite wake traverses. The new approach varies from previous methods by including unsteady velocity effects in the surface integrals and not requiring any pressure measurements.

Wake measurements of a variable geometry, generic automobile-like fastback model were conducted with two-component hot-wire probes and three-component hot-film probes. Performance of the two-dimensional probes in the wake surveys was unacceptable due to signal contamination from the third component of velocity not being measured. Velocity corrections of the contaminated data were investigated to develop an understanding of the performance limitations of two-component probes. Three-component probe measurements were satisfactory except in regions where the angular limitation of the probe was exceeded.

Results of drag calculations from the wake surveys showed good agreement with the actual drag measured with a force balance for two intermediate backlight angles and one extreme angle. Better agreement could be expected with more complete wake surveys. Form drag was found to be between 80% and 95% of the total drag. Unsteady velocity contributions were found to be no greater than 4% of the total drag, with the remainder being the vortex drag.

Thesis Supervisor: Professor Sheila E. Widnall
Department of Aeronautics and Astronautics

For Kathleen, the one I love

Acknowledgments

Contents

List of Tables

List of Figures

List of Symbols

Roman

A_1	Cross plane upstream of body
A_2	Cross plane downstream of body, also called the Trefftz plane
a_R	Resistance overheat for hot-wires
C_d	Drag coefficient
C_l	Lift coefficient
D, D_{total}	Total drag
D_{eq}	Equivalent body diameter
D_{form}	Form drag
D_{vortex}	Vortex drag
E_1, E_2	Voltages from hot-wire anemometers
H	Total pressure
h	Yaw factor for an individual hot-film sensor
k	Pitch factor for an individual hot-film sensor
$Lift$	Total lift
$\dot{m}_1, \dot{m}_2, \dot{m}_3$	Mass flow rate
N	Transformation matrix from probe coordinates to wind tunnel coordinates
$p, \bar{p}$	Local pressure
p_∞	Freestream pressure
Q	Magnitude of the total velocity vector
q	Total velocity component lying in the X-Z plane
q_u	Component of q in the X-direction
q_w	Component of q in the Z-direction

17

r	Radial coordinate on polar look-up grid
Re_m	Reynolds number per meter
S_{body}	Cross-sectional area of model
T	Trefftz plane
U_∞, $Uinf$	Freestream velocity
U_B	Binormal component of velocity for an individual sensor
U_{eff}	Effective velocity for an individual sensor
U_N	Normal component of velocity for an individual sensor
U_T	Tangential component of velocity for an individual sensor
u, v, w	Local velocity components
$\bar{u}$, $\bar{v}$, $\bar{w}$	Local mean velocity components
$\bar{u}'$, $\bar{v}'$, $\bar{w}'$	Root-mean-square (RMS) velocity components
u', v', w'	Root-mean-square (RMS) velocity components
V_{eff}	Effective voltage for an individual sensor
X, Y, Z	Wind tunnel coordinates, and velocity components in probe coordinate axes

Greek

α	Yaw angle of single sensor and yaw angle of the velocity vector
β	Angular coordinate on polar look-up grid, and backlight angle
θ	Pitch angle of a single sensor, and angle of total velocity vector
ρ	Density
ϕ	X-wire sensor angle relative to the freestream direction

Chapter 1

Introduction

1.1 Introductory Comments

The advancement of aerodynamics in passenger vehicle design has become an increasingly important method of reducing fuel consumption by reducing the aerodynamic drag. Currently, the trend is toward a more rounded, smooth look, as compared to the flat, square-edged look of recent years. While rounding forebody corners may generally reduce drag up to a point, a complete understanding of the mechanisms of drag production will help reduce drag more effectively by allowing the designer to "tune" the flow field to a lower drag configuration. Therefore, measurement and analysis of the flow fields in the vicinity of full scale vehicles and scale model vehicle-like bluff bodies are important in understanding the mechanics of drag production.

The primary source of vehicle drag are large-scale flow separations which produce the wake. Low pressures due to vorticity and abrupt separation in the near-body wake region act on the rear of the vehicle (the base and backlight) resulting in a major fraction of the vehicle drag. Although the flow field geometry near the backlight and base appears fully three-dimensional and unsteady, much can be learned from time-averaged measurements. The majority of experimental work done on the wake regions of vehicles has consisted of time-averaged studies of velocities and pressures. The results

of these studies reveal certain global, time-average structures, such as large, counter-rotating vortices and closed, fully-separated regions in the wake. These results will be presented following the motivation for the current research.

Various acounts describing wake structures have been discussed based on the results of flow visualization methods including surface oil flow, tufts, and smoke flow. Basic-vehicle-shape wake structures and recent experimental observations of automobile-type wakes are reviewed in the following pages.

1.2 Motivation

The importance of understanding wake velocity measurements and how they re-late to vehicle drag has been a major source of motivation for vehicle aerodynamics research. To date, the primary method of data acquisition in wake surveys has been the measurement of pressures with five-, seven-, and nine-hole probes followed by a drag analysis from the data based on the work of Betz [8] and later, by Maskell [21]. Maskell's method for calculating vehicle drag is based on averaged velocity and averaged pressure measurements in the wake of the vehicle. While results using Maskell's method have generally been satisfactory, only averaged effects are included in the analysis.

A different method of extracting drag information from wake surveys has recently been proposed by Landahl [19]. This new method is based solely on velocity measure-ments in the wake and does not rely on any pressure measurements, thus allowing the techniques of hot-wire and hot-film anemometry to be utilized for the study of vehicle wakes. The primary improvement of Landahl's method over Maskell's approach is the inclusion of unsteady effects in the analysis. Since unsteady velocities cannot be mea-

sured with pressure probes, testing the validity of Landahl's method has to be done with hot-wire probes, or any other type of device capable of measuring unsteady velocities. With unsteady measurements, a more complete description of the flow field can be made, in particular, the RMS flow quantities and power spectrums to indicate the frequencies where the energy of the flow lies. Also, the effect of wake unsteadiness on vehicle drag, not included in Maskell's method, can be determined.

Since averaged pressure measurements have been the standard practice for obtaining wake velocities, attempting to make the same measurements with hot-wire and hot-film probes leads to some unanswered questions. First, are velocity measurements in vehicle wakes possible with current hot-wire probe designs, and what types of probes must be used to insure accurate velocity measurements? Can the wakes be measured with two-component or are three- component probes necessary? What are the problems, if any, with these types of probes when measuring velocities in highly three-dimensional, turbulent wakes? After these questions are answered, then application of Landahl's method to wake surveys can procede.

1.3 Basic Automobile Shape Terminology

Standard body terminology is depicted in Figure 1.1 for the three of the four basic automobile afterbody types: squareback, notchback, and fastback. The most important parameter of the fastback afterbody is the fastback, or backlight angle, β. The fourth basic automobile shape is the hatchback, which is essentially a fastback with a large backlight angle, $\beta \geq 40°$. Through various combinations of the primary parameters: backlight angle, boat-tail angle (Fig.1.2), and underbody ramp angle, a variety of flow

field characteristics can be generated. It is, therefore, necessary to limit the parameters to a reasonable number in order focus attention on some particular behavior of the flow field. Also defined in these figures are the A-pillar and the C-pillar, the corner junctions at the front and rear of the passenger compartment. After a brief discussion of the current knowledge of vehicle wakes, the logic behind the choice of model geometries used for this study will become obvious.

1.4   General Features of Vehicle Wakes

Details of vehicle wake structures were not reported until the interest in automobile aerodynamics began to increase in the early 1970's. Initial discussions were based on a variety of time-averaged measurements, a practice that still continues in the latest literature. For a general view of the gross flow field features, time-averaged measurements are useful in describing the large-scale structures and overall shape of the wake. Yet, if the wake is unsteady, a time-averaged description will lack information regarding the unsteadiness.

Some preliminary work that initially described coherent shapes in a vehicle wake was done in West Germany by Ahmed [1], [2], and [3]. Using one-quarter-scale models of the three basic afterbody shapes (fastback, notchback, and squareback), pressure surveys and surface flow visualization of the wakes were studied. To visualize the wake a vertical splitter plate was placed along the centerline of the model immediately behind the base and painted with a surface flow compound. Photographs were taken at set intervals of time to observe the wake development. The results of these tests are shown in Figures 1.3– 1.4 for fastback models with various backlight angles. Surface flow showed

a double recirculating flow pattern near the base consisting of two separate regions of counter-rotating flow. After this separation region the outer flow slowly turned towards the ground for the fastback and the notchback, but turned away from the ground for the squareback. Measurements in the far wake (after the separation bubble) showed how the gradients in the pressure field caused this to occur. Based on these observations Ahmed [4] later presents his flow field model for the flow behind a high-drag fastback, as seen in Figure 1.5.

Behind the closed separation bubble of the squareback there were seen two weak, counter-rotating, longitudinal vortices whose sense of rotation cause an upward flow along the wake centerline, which in turn causes the outer flow at the centerline to diverge from the ground. Ahmed states that these longitudinal vortices begin after the separation bubble closes. For the notchback and fastback cases, the longitudinal vortices turn in the opposite sense, resulting in flow towards the ground and away from the centerline after bubble closure. It is incorrectly stated in [2] that the vortices for the fastback and the notchback begin after the separation bubble closes. Later studies by Ahmed [1], [4] have shown that these longitudinal vortices actually begin forming at the shear layer interface between the vehicle sides and the backlight for the fastback, and at the shear layer interface between the sides, backlight, and rear deck for the notchback.

Details of the wake kinetic energy distribution calculated from the pressure measurements for the different afterbodies are presented by Ahmed [2]. Distribution of kinetic energy across the wake shows the highest peaks for the fastback configurations, as does the calculated vortex drag. Vortex drag is defined as the momentum loss due to velocities induced in a plane perpendicular to the free-stream flow direction. For the fastback, vortex drag was calculated from Maskell's method to be about 28 percent of

the total aerodynamic drag, while it was only about 8 percent for the squareback. As both the notchback and squareback have larger regions of unsteady, separated flow, and exhibit less defined trailing vortices than the fastback, this result is not surprising.

A more detailed study of time-averaged wake structures was undertaken by Davis [11] and Bearman, et al. [7] at Imperial College. Their tests consisted of pressure and force measurements of a one- tenth-scale model in a wind tunnel with a moving ground plane. Wind speed and ground plane speed were matched at 20 m/s, giving a Reynolds number, based on equivalent diameter, of $1.92 * 10^5$. Drag, calculated from wake surveys using an integral method based on Maskell's steady, averaged equations [21], is compared to the actual measured drag with good agreement. The detailed results are included in the discussion of Maskell's method in Chapter 2. Since this drag-integral method splits up the drag into two components, profile drag and vortex drag, a series of fastback angles were tested with a variety of ramp angles to vary the strength of the trailing vortices. As the fastback angle is increased from 0° (squareback) to about 30° the drag continuously increased. As the angle increased further between 30° and 40° the drag began to decrease at some angle. This is an indication of a change in the gross flow field structure and will be addressed shortly.

Bearman continues the discussion of the effects of longitudinal vortices in the far wake in [6]. Hot-wire measurements of the mean velocity taken between 2.5 and 6.5 body heights downstream show the existence of another system of vortices near the ground and outside (away from the centerline) of the main vortices. These vortices are much weaker than the main vortices and of the opposite sign. Similar secondary vortices heve been noted in the wakes of wings near the ground by Harvey and Perry [15]. Mixing interactions between the strong and weak vortices cause the main vortex

to to decay and dampen the tendency for the main vortices to move towards the ground and away from the centerline. Additional vorticity in the wake can be traced to various features on the body, including the A-pillar-windshield juncture and the windshield-roof juncture.

When the vehicle is yawed, additional vorticity may be generated from these and other body features. Side force can be calculated from wake pressure surveys for a yawed model using the work of Maskell [21].

1.4.1   Full Scale Vehicle Results

Wake studies of road vehicles are generally done with partial-scale models, although, with the recent development of a large traversing mechanism, Pininfarina [10] can now take time-averaged pressure and velocity measurements of full-scale vehicles. The measurement device consists of a non-nulling seven-hole probe that takes data "on the fly". First published results for this technique are shown in Reference [10]. Two actual cars were tested, a notchback and a fastback. Pressure contours and crossflow velocity vectors are presented for the near wake region. Both vehicles showed the usual open type of separation with two large counter-rotating vortices dominating the wake flow field. Also included in the paper are results for full-scale vehicle models with the three basic types of afterbodies: squareback, fastback, and notchback. In the notchback wake it was noted that the primary longitudinal vortices were not symmetric in size and that the vortex pattern exhibited a bistable behavior when the model was yawed less than one degree. It is believed that the bistability of the notchback wake is largely due to the interaction of the A-pillar vortices and the complicated flow patterns on the backlight. The fastback displayed a symmetric vortex pattern in the time mean. One shortcoming

of this system is its inability to measure pressures accurately at flow angles of greater than 70°.

1.4.2 Scale Model Results

Flow field tests on scale models of actual vehicles have been done at the Lockheed-Georgia Model Test Facility Wind Tunnel [14]. Reported results include the Ford Thunderbird and the experimental Ford Probe IV. The tests consisted of time-averaged wake pressure surveys at two wake plane locations measured with a traversing device carrying forty-two 7-hole pressure probes. Models were 0.154 scale with a detailed underbody and simulated radiator cooling flow on the Thunderbird. The primary concern of the researchers was to compare the drag from balance measurements to that calculated from wake measurements using an integral method by Maskell [21] with modifications by Hackett and Sugavanam [13]. Figure 1.6 shows the measured v-w velocity vectors for a wake survey 24 inches downstream from the midbody of the Thunderbird (or 0.33 body lengths from the rear of the model). A smooth belly pan was installed for this test. Note the existence of two large vortices dominating the flow field, a standard feature of notchback and fastback wakes. Comparison of force balance measurements and drag calculations from the wake surveys of the Thunderbird and a Probe IV concept vehicle gives encouraging results for the wake integral method. On the average, the integral method resulted in an 18% higher drag value than the directly measured drag for both of these vehicles. Detailed results are included in the discussion of Maskell's method in Chapter 2. Unfortunately, the wake survey also measures the velocity deficit in the wake due to the non-moving ground plane, resulting in a higher value of the drag integral. Another effect of the wake survey device is to cause a slightly larger pressure recovery

in the near wake of the model, reducing the balance-measured drag. The resulting plots of wake velocities, pressures, and energy levels presented by Hackett in [13] show some of the details of the time-averaged wake structures for actual vehicle shapes.

1.5   Effects Of Base Slant Angle

Vehicle wake structures are primarily determined by the afterbody geometry, and the predominant feature of the afterbody affecting the wake is the base slant angle. The effect of base slant angle changing both the flow geometry and drag was pointed out as early as 1974 by Janssen and Hucho [17]. They noted two completely different types of flow fields depending on the slant angle. If the angle is shallow the wake is characterized by three-dimensional open separation, i.e. two dominant, counter-rotating vortices. There is also a small closed separation bubble immediately behind the vertical base of the body. As the angle was increased, near a certain critical slant angle the flow field changed dramatically to a quasi-axisymmetric closed bubble type of separation. Up to the critical angle, drag was increasing with increasing slant angle, but after the transition at the critical angle, the drag reduced considerably. Thus, the drag was seen to have a maximum just at the point where the flow field changes modes. Increases in C_d prior to the critical angle were "due to strong edge vortices with a correspondingly large induced drag". In the current literature this "induced" drag is often referred to as "vortex" drag.

In 1978, Morel, [25],[24], and [23], investigated base slant and critical angle effects further. Utilizing two types of models, a slender, axisymmetric cylinder with a slanted base and a generic vehicle shape (Fig 1.7), he looked closely at the drag overshoot that

occurs near the critical angle. The results are shown in Figures 1.8 – 1.9. For the cylinder in a free stream, Morel noted from hot-wire measurements that the unsteadiness in the closed, bubble-type wake increases as the base angle is changed from vertical (90°) to a slant angle greater than the critical angle, and that some quasi-periodic vortex shedding is produced. Data from the vehicle-like model showed that there is only a minor change in the critical angle between the free stream and near ground tests. Near the ground, drag variation with slant angle followed the same trends as in the free stream, except that the magnitudes were reduced.

The variation of the lift on the vehicle as a function of backlight angle increased linearly up to the critical angle, at which point it dropped off suddenly, and decreased as the angle was increased. In both models the drag overshoot was accompanied by a corresponding lift peak near the critical angle. This is due, at least in part, to the suction peaks from the strong vortices acting on the backlight. Morel also noted that the angle at which the peak drag was encountered was dependent on the turbulence level.

Aspect ratio of the backlight plays an important role in determining the critical angle and the drag overshoot. Comparison of the results for both models show that the higher the aspect ratio of slant surface (defined as the surface or body width divided by the surface length), the lower the critical angle will be. The wider the backlight is, the lower the effect of the trailing vortices on the flow over the surface, resulting in a lower angle of vortex breakdown and onset of closed separation. Maull [22] reported that he was able to suppress the discontinuous jump in the drag of a 45° backlight by changing the aspect ratio of the backlight through systematically cutting cross-sections off the base of the vehicle (Figure 1.10). He also found that small changes in pitch angle of the

28

vehicle resulted in large changes in the critical angle (Figure 1.11).

Based on the above descriptions of vehicle wakes, a generic, fastback model with a series of backlight angles was chosen for the current research. Fastbacks have the most organized wake structure of the basic geometries, with two large trailing vortices and small, closed regions of separation on the base area and on the backlight for high angles. By varying the backlight angle, the strength of the trailing vortices will change, resulting in different values of the vortex drag for the different geometries. In an attempt to go past the critical backlight where the flow field changes, a large backlight angle geometry was included in the tests. Details of the models will be discussed shortly in Chapter 3. The next chapter reviews the basics of Maskell's method with some published results, then develops the new method as the starting point of this research.

BACKLIGHT

REAR DECK

BASE

NOTCHBACK VEHICLE

BASE

RAMP

RAMP ANGLE

SQUAREBACK VEHICLE

A-PILLAR

BACKLIGHT ANGLE

C-PILLAR

BACKLIGHT

BASE

FASTBACK VEHICLE
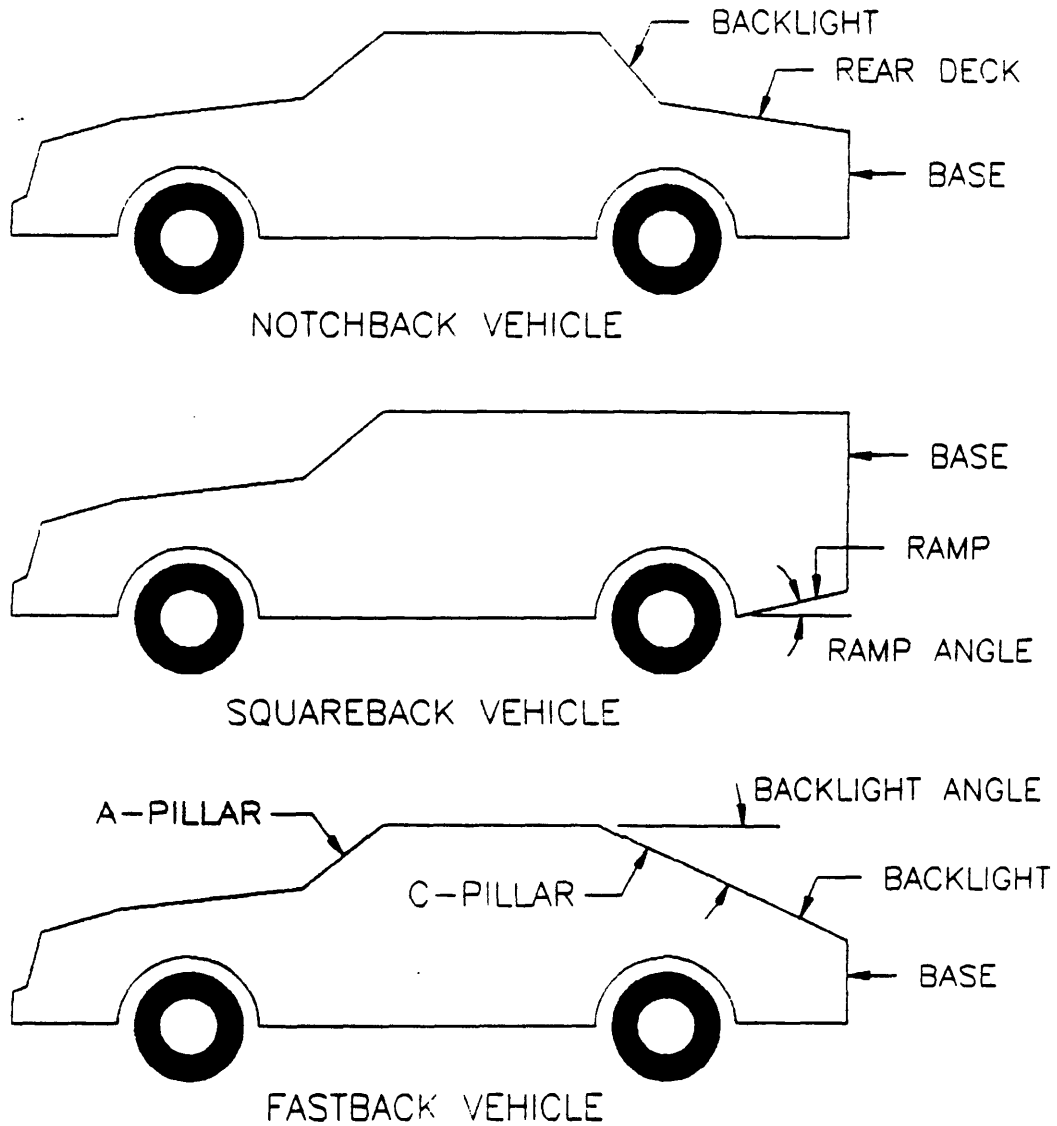
Figure 1.1: Automobile shape terminology - side view

FRONT

A—PILLAR

C—PILLAR

BOATTAIL ANGLE

REAR
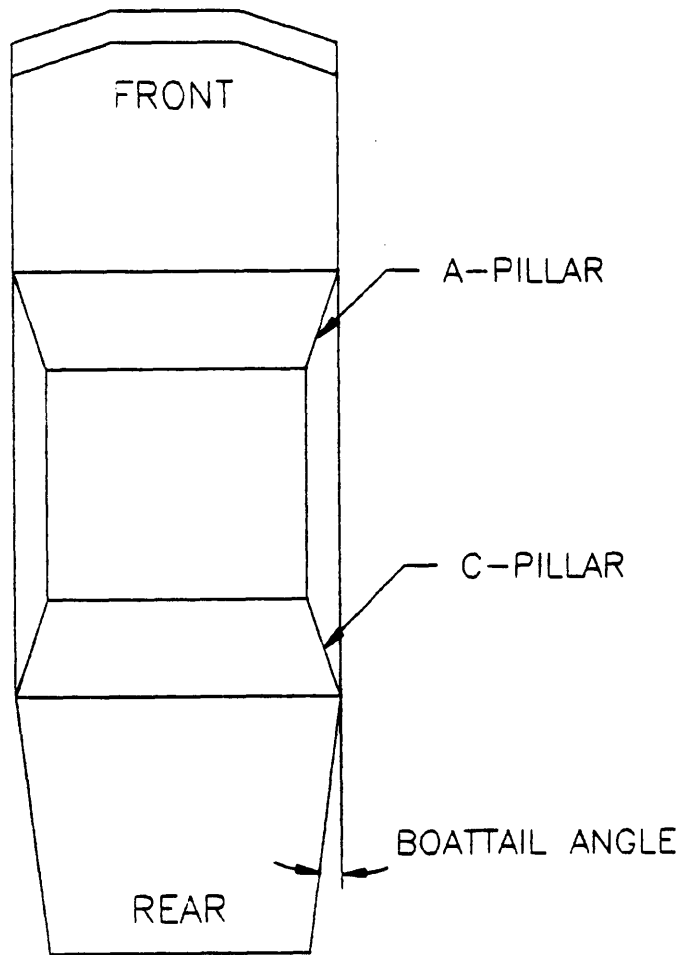
Figure 1.2: Automobile shape terminology - top view
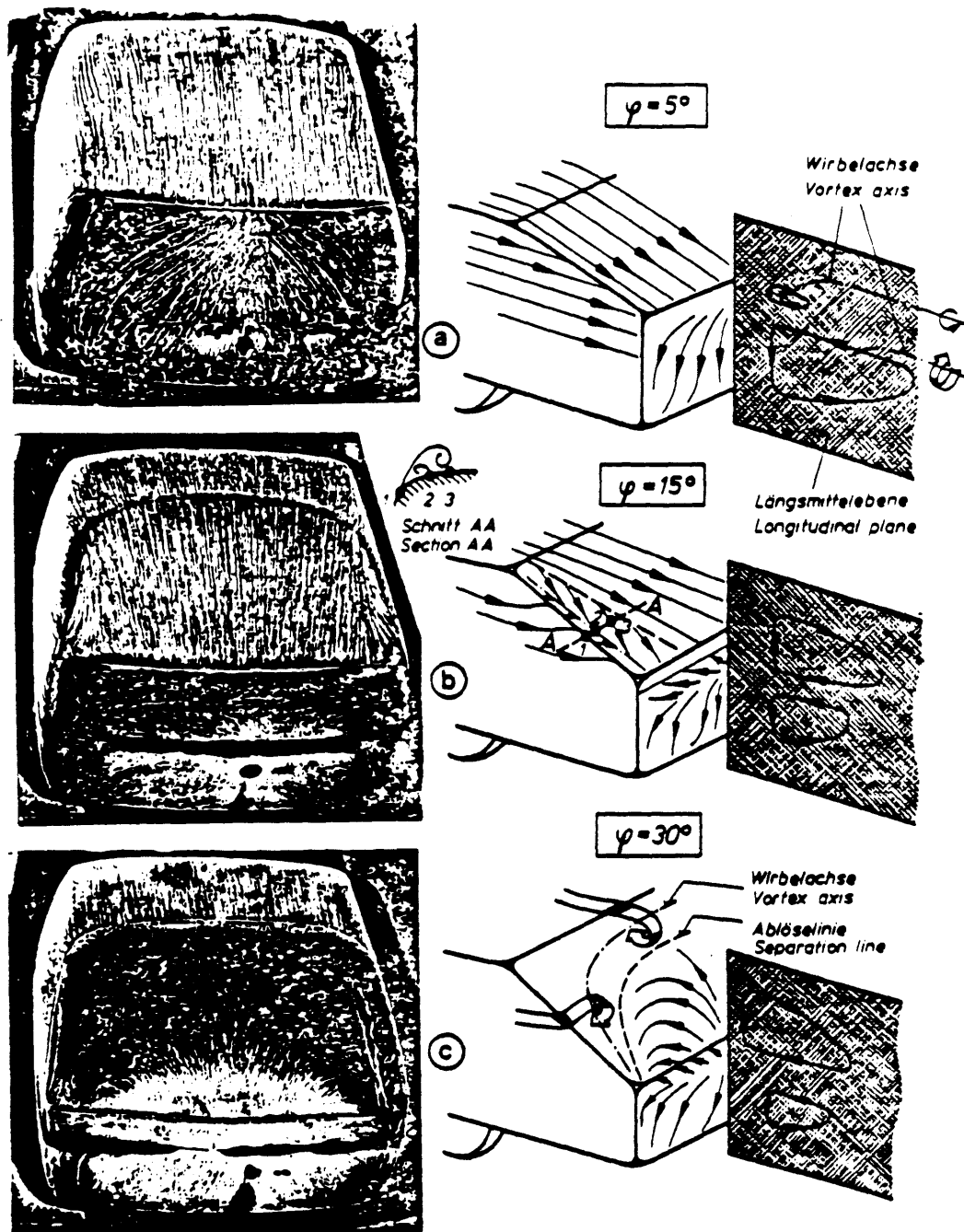
Figure 1.3: Surface oil flow visualization for various fastbacks from Ahmed [1]
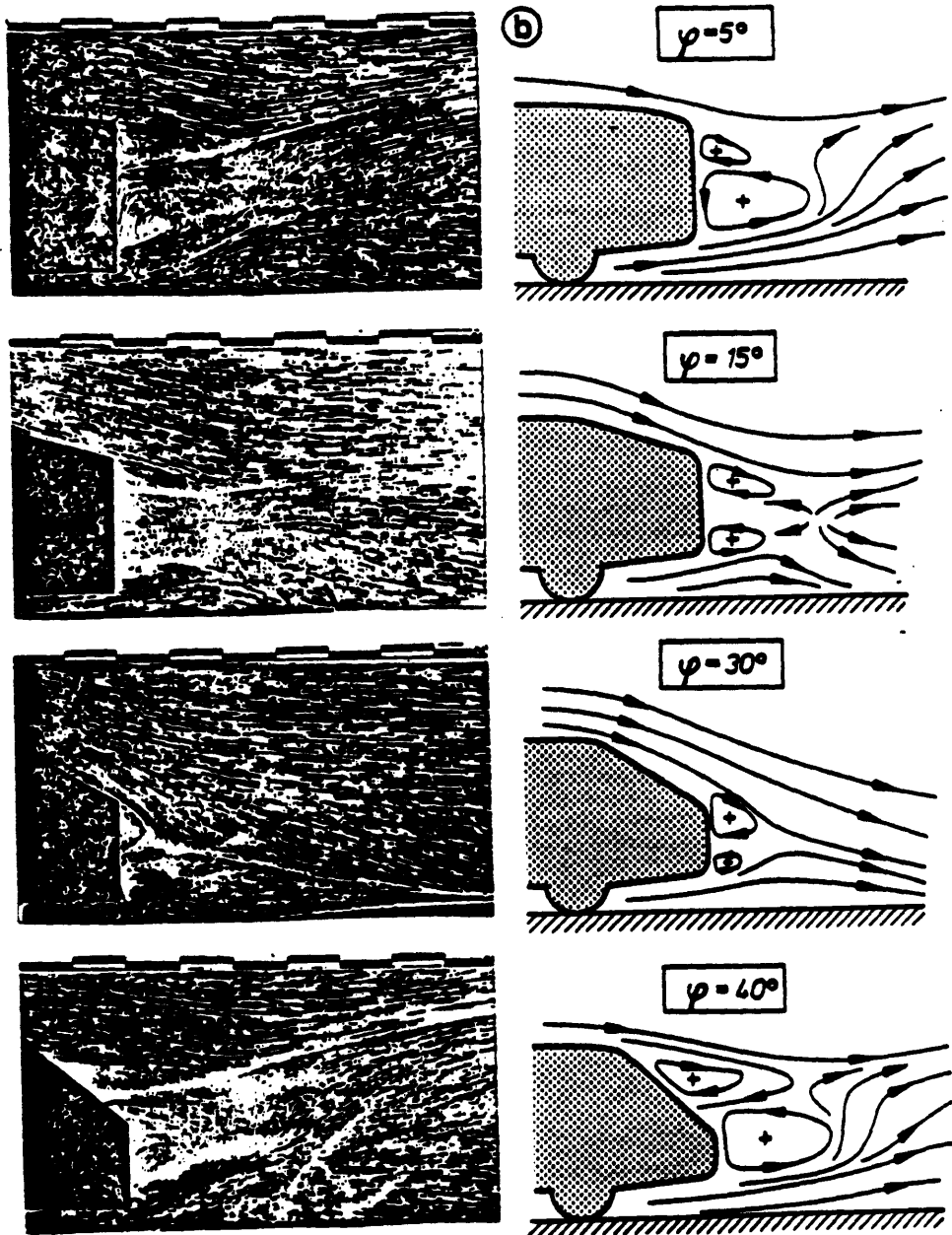
Figure 1.4: Flow field visualization from surface oil flow on a wake splitter plate from Ahmed [1]
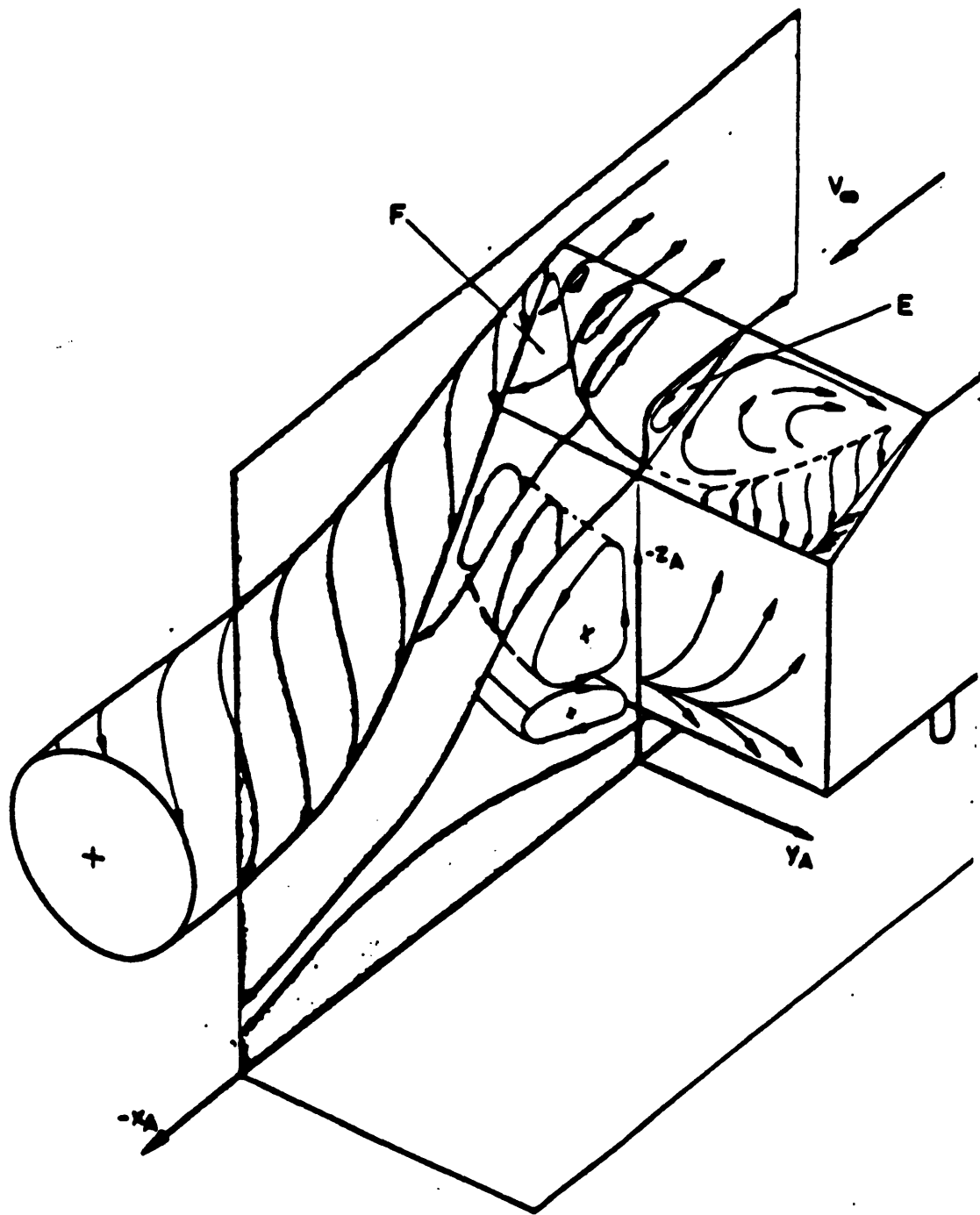
Figure 1.5: Flow field structure for a high drag 30° fastback from Ahmed [4]
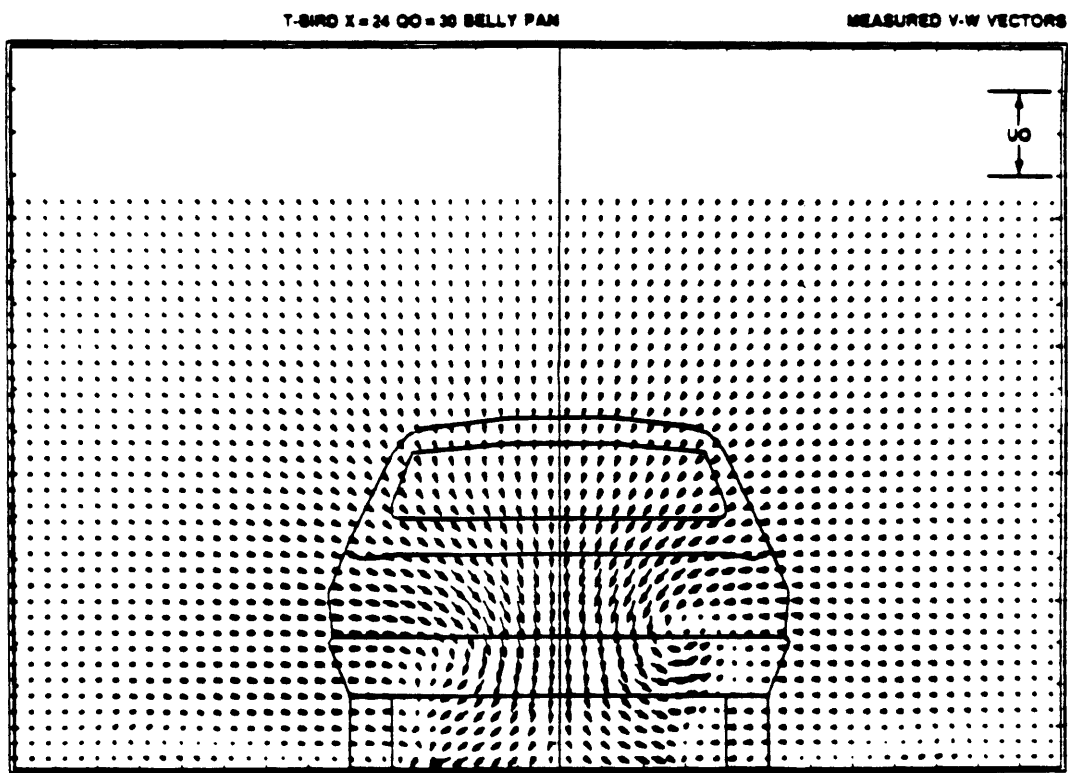
Figure 1.6: Wake v-w velocity vectors from Hackett [14]
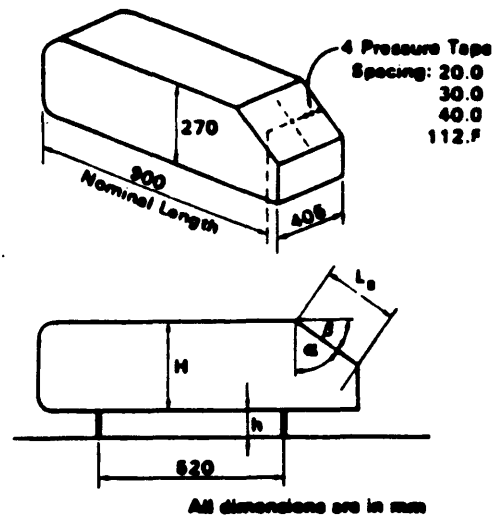
Figure 1.7: Schematic of Morel's vehicle model, from Morel [25]
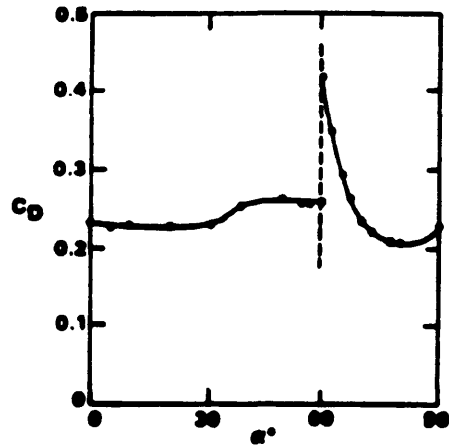
Figure 1.8: The effect of backlight angle on vehicle drag for a model in a free stream, from Morel [25]
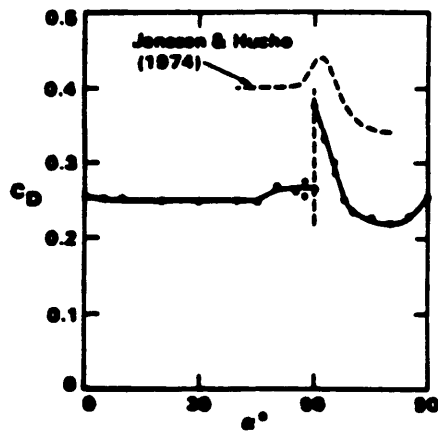
Figure 1.9: The effect of backlight angle on vehicle drag for a model near a ground plane, from Morel [25]
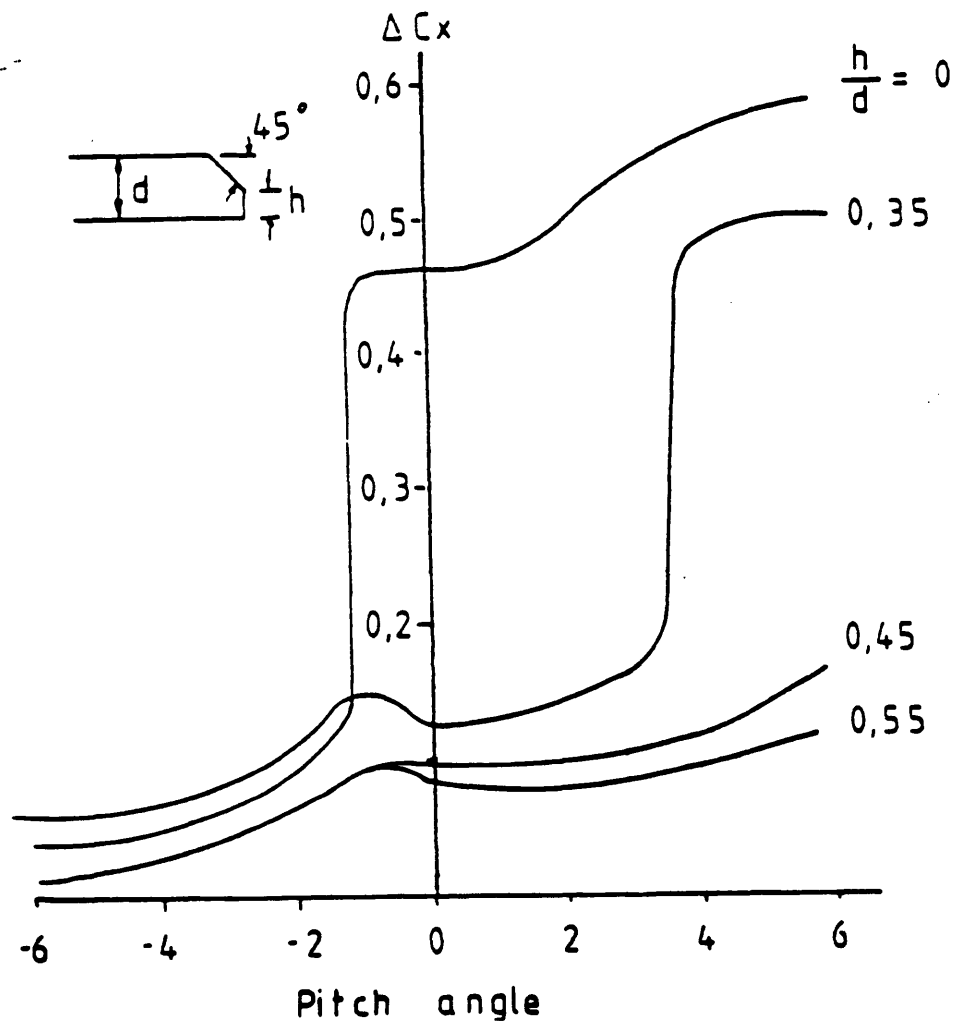
Figure 1.10: Effect of backlight length on drag, after Maull [22]
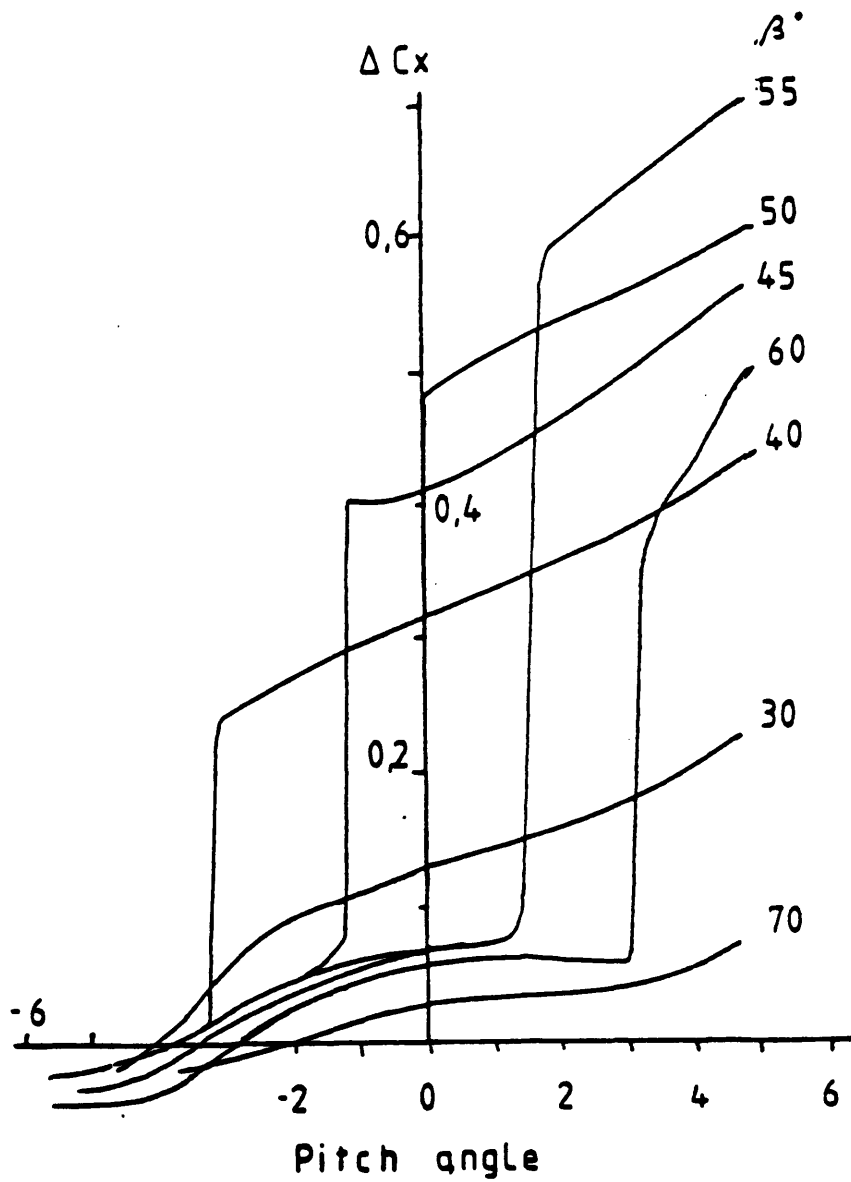
Figure 1.11: Effect of vehicle pitch on the critical backlight angle, after Maull [22]

Chapter 2

Drag Measurement Through Wake Analysis

2.1 Introductory Comments

The measurement of vehicle drag through the analysis of wake survey data serves two important purposes for the aerodynamicist. First, it permits the application of analytic methods to measured wake flow field data for the calculation of the vehicle drag, and second, it allows the drag to be divided into its form drag and vortex drag components. This natural separation of total drag brings more insight into the analysis of drag production than is available from drag measured directly with a force balance. Also, wake analysis permits drag estimations for situations where force balances cannot easily be used, as in the case of a model rolling on a moving ground plane.

During recent years, the standard technique of wake analysis has consisted of the measurement of pressures and velocities in wakes with multi-holed pressure probes and applying a steady flow momentum equation to calculate the drag that was first defined by Betz [8] and modified by Maskell [21]. Results for this method range from highly accurate to unacceptable. Maskell's method and some applications of it are briefly reviewed in the following sections.

Landahl [19] has proposed a new method for calculating drag from wake measurements. Instead of measuring pressures in the wake, only the mean square velocities are

required for the new method, measurements of which are readily obtained from hot-wires or laser anemometers. The final section of this chapter is devoted to the development of the Landahl method.

2.2   Maskell's Drag Equation

Maskell's method for calculating drag is simply a balance between the upstream and the downstream fluid momentum. It assumes a steady, laminar, inviscid flow and does not include the effects of fluctuations, thereby ignoring the transport of momentum by Reynolds stresses. First, we define a stream tube (Figure 2.1) that extends far upstream of the model such that the inlet flow is uniform and undisturbed, and the stream tube is large enough in diameter so that the pressure acting on the external surface between the ends is assumed to be constant. We then define A_1 and A_2 to be the upstream and downstream cross-sectional areas of the stream tube, and that both lie in a $y - z$ plane. The A_2 plane is called the "Trefftz plane" in aeronautical applications. Then, from a momentum balance, Maskell states that the total drag can be defined by:

$$D = \iint_{A_2} \Delta H dS + \frac{\rho}{2} \iint_{A_2} \left(U_\infty^2 - u^2 \right) dS + \frac{\rho}{2} \iint_{A_2} \left(v^2 + w^2 \right) dS \qquad (2.1)$$

where ΔH is defined as the loss of total pressure between the upstream and downstream ends of the stream tube, and is given by:

$$\Delta H = p_\infty + \frac{\rho U_\infty^2}{2} - p - \frac{\rho}{2} \left(u^2 + v^2 + w^2 \right) \qquad (2.2)$$

The first term of 2.1 need be carried out over just the wake region of A_2 as the total pressure loss behind the model is confined to this region. The second term gives the component of drag related to the loss of x-momentum and must be evaluated over

the entire area defined by A_2, where $u \neq U_\infty$. Terms one and two of Equation (2.1) combine together to give the form drag. The third term denotes the drag associated with the kinetic energy in the cross-plane of the wake and need be evaluated only over the wake region where $v \neq 0$ and $w \neq 0$. This term is call the vortex drag in classical aerodynamic texts.

It should be noted that no effects from the ground plane under the vehicle on the flow field are included in Equation (2.1), i.e. the ground plane is treated as part of the constant pressure surface bounding the stream tube. This can lead to inconsistencies between a force balance measured drag and one calculated with Equation (2.1), especially if there is a boundary layer present on the ground plane. If a survey contains data close to the ground plane, momentum losses in the boundary layer will result in a calculated drag higher than what the vehicle actually experiences. These points serve to identify some of the possible shortcomings of the Maskell momentum model, and dictates that care must be taken when applying this model to a real situation.

2.3 Experimental Results of Maskell's Method

In recent years there has been an increasing interest in experimental wake analysis, due in part to the availability of more sensitive measurement devices and computer control of many of the aspects of the experimental process. Automated wake survey methods can now produce the large amounts of data necessary for analysis of flow fields. Research of the late 1960's and 1970's brought forth the general concepts regarding the overall structures in vehicle wakes, which in turn, has lead to much of the research reported since the early 1980's involving detailed studies of wake flows and vehicle drag.

Application of Maskell's method for calculating drag from wake pressure surveys has been the topic of many researchers, with each one comparing the drag measured directly with a force balance to that which was calculated from measurements. A summary of the major works is seen in Table 2.1. The emphasis of this table lies in the column labeled "Calculated Drag," which shows the percentage difference between a direct drag measurement and the drag calculated from a wake survey by the various authors. A positive value in this column means that the calculated drag was higher than the measured value (All the data presented in Table 2.1 are the result of wake surveys done completely with various types of pressure probes, as indicated in the table). The drag error varies considerably, due to such factors as boundary layer control, extents of the traverse plane, and ground plane boundary conditions. Wake plane location as specified in the table is given in terms of the number of body lengths downstream from the rear of the model.

Davis' research [11] was based on a generic, one-tenth-scale model with a 25° fastback angle (Fig. 2.2). The results in Table 2.1 are for the specific model configuration shown in Figure 2.2 where the backlight extends to a sharp edge at the rear of the model. Two types of tests were run, one with a moving, belt-type ground plane, and the other with the ground plane stationary. The free stream velocity was limited to 19 m/s for both types of tests, corresponding to the maximum speed of the moving ground plane, and boundary layer suction was applied just ahead of the moving belt in both cases. Reynolds number, based on equivalent diameter was $1.92 * 10^5$. In the moving ground plane tests Maskell's method under-predicted the drag, while in the stationary ground plane the drag was over-predicted, and the predictions were increasingly inaccurate as the traverse plane was moved downstream.

The moving ground plane is one possible cause of the under-estimation of drag, as it feeds stream-wise momentum into the wake behind the model. The additional momentum may disturb the velocity field in the wake, which is then measured in a traverse. As for the stationary case, the existence of a developing boundary layer on the ground plane under the model and in the wake region adds to the momentum deficit measured in a wake survey, resulting in a lower than measured drag.

Hackett and Sugavanam [13] extended Maskell's method to enable the wake integrals to be made much closer to the body by incorporating a more detailed model for the source-like terms. Their approach adds an additional integral to the crossflow term and a streamwise source term that, when combined with Maskell's method, ensure that the potential flow effects result in zero drag. Using this modified approach they reported close agreement between the measured and calculated drag for a generic, notchback vehicle of approximately one-sixth-scale (Fig.2.3). Wheels were present on this model. The test section was equipped with a fixed ground plane and no boundary layer control. No indication of tunnel speed or Reynolds number was given. The results in the Drag column of Table 2.1 show two numbers that correspond to two different analytic treatments of the crossflow term. Less accurate results were also reported for the model yawed 12.5°, but uncertainty in the actual wake limits, and the inability to completely measure to the limits of the wake boundary resulted in a higher calculated value of the drag.

A one-fifth-scale notchback vehicle was the subject of a study by Onorato, et al. [26]. The afterbody was modular, allowing for the attachment of different length rear decks. Details of the model are seen in Figure 2.4. Boundary layer growth was controlled through the application of suction to a slot upstream of the model. Tests were run at

an airspeed of 40 m/sec, giving a Reynolds number of $\simeq 2 * 10^6$ based on body length. This value of Re is lower if given in terms of equivalent diameter. From Table 2.1 the accuracy of Onorato's drag calculations are clearly seen to be the best reported for both configurations he tested.

In another study headed by Hackett [14] 0.154 scale models of the Probe IV concept vehicle and a 1983 Ford Thunderbird were tested, as previously described in Chapter 1. Details of the latter model are shown in Figure 2.5. Results of drag calculations are expectedly high, on the order of 18%, as no type of boundary layer control was available.

Direct application of Maskell's momentum method to wake traverses has yielded many encouraging results. But, measuring pressures with multi-holed probes does have some drawbacks, for example, inaccuracies at large flow angles relative to the probe direction. This translates to an inability to accurately measure flow velocities very close to the vehicle, where flow angles tend to be large. This is equally true for hot-wire sensors. Another concern is using these types of probes for measuring pressures in an unsteady, turbulent flow, as it may not be clear how the averaged measurements are related to the mean flow properties, as mentioned in Hinze [16]. One possible approach to bypassing some of these problems is to use hot-wire annemometers for the wake surveys. Landahl's drag equation, developed in the following section, provides the means to analyze wakes with velocity measurements only, without the need to measure pressures.

2.4 Landahl's Drag Equation

Consider the following flow model as portrayed in Figure 2.6. A model is located near a smooth,flat ground plane, infinite in all directions. The flow is assumed to be incompressible, and, outside of the boundary layers, inviscid. Behind the model is a separated, turbulent wake which continues downstream, where possibly at some point, it attains an approximate equilibrium, i.e., the changes in the streamwise flow quantities and their derivatives change slowly in the streamwise direction. The wake itself may still have some embedded streamwise vorticity in it. We now locate a cross-flow plane, denoted T (the "Trefftz" plane) in Figure 2.6 at this downstream location and apply the momentum equation between this plane and a plane of undisturbed flow upstream of the model. The model drag from a momentum balance, ignoring the ground plane boundary layer, is given by:

$$D = -\int\int_T \left(\bar{p} - p_\infty + \rho\bar{u}^2 - \rho U_\infty^2 \right) dS \qquad (2.3)$$

The overbar denotes a time averaged term. This integral must be evaluated over the entire cross-flow plane, T. The object of the following steps is to rid Equation 2.3 of its direct dependence on the pressure. We do this by introducing the $y-$ and $z-$ components of the Euler equations,

$$\frac{1}{\rho}\frac{\partial p}{\partial y} = -\frac{\partial v}{\partial t} - \frac{\partial uv}{\partial x} - \frac{\partial v^2}{\partial y} - \frac{\partial vw}{\partial z} \qquad (2.4)$$

$$\frac{1}{\rho}\frac{\partial p}{\partial z} = -\frac{\partial w}{\partial t} - \frac{\partial uw}{\partial x} - \frac{\partial vw}{\partial y} - \frac{\partial w^2}{\partial z} \qquad (2.5)$$

and integrate them along z = constant and y = constant, respectively. By taking the time average of the resulting equations we get two alternative expressions for the pressure:

$$\bar{p} = p_\infty - \rho\bar{v}^2 - \rho \int_\infty^y [(\overline{vw})_z + (\overline{uv})_x]dy \qquad (2.6)$$

$$\bar{p} = p_\infty - \rho\overline{w^2} - \rho \int_\infty^z [(\overline{uw})_x + (\overline{vw})_y]dz \tag{2.7}$$

Equations 2.6 and 2.7 both represent the pressure at any point in the flow. With a little foresight we can see that they both contain a velocity squared term, an easy to measure flow quantity, so we take the average of 2.6 and 2.7 to obtain another equation for the pressure, as shown below.

$$\begin{aligned}\bar{p} - p_\infty &= -\frac{1}{2}\rho\overline{v^2} - \frac{1}{2}\rho\overline{w^2} - \frac{1}{2}\rho \int_\infty^y [(\overline{vw})_z + (\overline{uv})_x]dy\\ &\quad -\frac{1}{2}\rho \int_\infty^z [(\overline{uw})_x + (\overline{vw})_y]dz \end{aligned} \tag{2.8}$$

We next substitute the right hand side of 2.8 into the momentum equation 2.3 and simplify some of the terms, noting that the $y-$ and $z-$derivative terms of equation 2.8 will integrate to zero after the replacement by the following logic (shown for the $z-$derivative term:

$$\begin{aligned}\int_{-\infty}^{+\infty}\int_{-\infty}^{+\infty}\left[\int_\infty^y (\overline{vw})_z\, dy\right]dydz &= \int_\infty^y\int_{-\infty}^{+\infty}\left[\int_{-\infty}^{+\infty}(\overline{vw})_z\, dz\right]dydy\\ &= \int_\infty^y dy\int_{-\infty}^{+\infty}(\overline{vw})\, dy\\ &= 0 \end{aligned} \tag{2.9}$$

The final value of the integral is zero due the the term $\overline{vw}$ going to zero at the limits of the Trefftz plane and if we assume that $\overline{vw}$ is an odd function in z. A similar argument will show the $y-$derivative term also going to zero. The $x-$derivative terms are dealt with as follows. First, we take the $(\overline{uw})_x$ term from Equation 2.8 and reverse the order of integration, keeping track of the limits carefully,

$$\int_{-\infty}^{+\infty}\int_{z_1=A}^{z_1=z_2} f(z_1)\, dz_1 dz_2 = \int_{-\infty}^{+\infty}\int_{z_2=B}^{z_2=z_1} f(z_1)\, dz_2 dz_1 \tag{2.10}$$

where $f(z_1) = (\overline{uw})_x$, and both A and B will go to ∞ in the limit. We then calculate the z_2 integral on the left hand side of 2.10 giving,

$$\int_{-\infty}^{+\infty}\int_{z_2=B}^{z_2=z_1} f(z_1)\, dz_2 dz_1 = \int_{-\infty}^{+\infty}(z_1 - B) f(z_1)\, dz_1$$

47

$$= \int_{-\infty}^{+\infty} z_1 f(z_1)\, dz_1 - B \int_{-\infty}^{+\infty} f(z_1)\, dz_1 \qquad (2.11)$$

Physically $(\overline{uw})_x$ goes to zero for large z, and, if we assume that it is an odd function of z, then for a symmetric wake:

$$- B \int_{-\infty}^{+\infty} f(z_1)\, dz_1 = 0 \qquad (2.12)$$

A similar argument holds for the $(\overline{uv})_x$ term of Equation 2.8. Combining the results of Equations 2.8–2.12 into the momentum equation gives a new expression for drag,

$$D = \frac{\rho}{2} \int\int \left[\overline{v}^2 + \overline{w}^2 - 2\overline{u}^2 + 2U_\infty^2 - z\,(\overline{uw})_x - y\,(\overline{uv})_x \right] dS \qquad (2.13)$$

As previously stated, we will assume that the streamwise derivatives are small, and will neglect these terms from this point on.

Next, we separate the velocities into mean and fluctuating parts,

$$u = \overline{u} + u', \quad v = \overline{v} + v', \quad w = \overline{w} + w' \qquad (2.14)$$

and replace them into Equation 2.13, resulting in the final expression for the total drag of the model,

$$D = \frac{\rho}{2} \int\int \left[2U_\infty^2 - 2\overline{u}^2 + \overline{v}^2 + \overline{w}^2 - 2\overline{u'^2} + \overline{v'^2} + \overline{w'^2} \right] dS \qquad (2.15)$$

We then define the total drag as the sum of the vortex drag, D_{Vortex}, and the form drag, D_{Form}.

$$D_{Total} = D_{Vortex} + D_{Form} \qquad (2.16)$$

where

$$D_{Vortex} = \frac{\rho}{2} \int\int \left(\overline{v}^2 + \overline{w}^2 \right) dS \qquad (2.17)$$

$$D_{Form} = \rho \int\int \left[U_\infty^2 - \overline{u}^2 + \frac{1}{2} \left(-2\overline{u'^2} + \overline{v'^2} + \overline{w'^2} \right) \right] dS \qquad (2.18)$$

48

Equation 2.17 is historically called the vortex drag equation because it represents a momentum loss in the streamwise direction due to an increase in velocity (vorticity) in the cross-plane. This equation should not be interpreted as the total drag due to vortices because vortices have associated with them a deficit in the streamwise velocity, which is included in the form drag term.

If the fluctuations are approximately isotropic,

$$\overline{u'^2} \simeq \overline{v'^2} \simeq \overline{w'^2} \tag{2.19}$$

the terms in the form drag (Eqn.2.18) involving the fluctuations cancel, thus simplifying the expressions for both the form drag and the total drag.

2.5   Comparison: Landahl's Results and Maskell's Results

It is not readily apparent from the previous sections that the results of Landahl and Maskell are directly related, as Maskell's method is based on a steady, laminar flow and Landahl's is based on a turbulent flow. If we take Maskell's expression for total pressure loss (Eqn.2.2) and define a similar quantity, $\Delta \overline{H}$, the mean total pressure loss for a turbulent flow, we get:

$$\Delta \overline{H} = p_\infty + \frac{\rho}{2} U_\infty^2 - \overline{p} - \frac{\rho}{2} \left(\overline{u}^2 + \overline{v}^2 + \overline{w}^2 \right) \tag{2.20}$$

We then express the difference in pressure by averaging Equations 2.6 and 2.7 ignoring the terms involving the rate of change in the streamwise direction, as again, they are assumed small, and substitute into 2.20 giving

$$\Delta \overline{H} = \frac{\rho}{2} \left(U_\infty^2 - \overline{u}^2 \right) \tag{2.21}$$

Replacing this final expression of $\Delta \overline{H}$ into Landahl's drag equation (2.15) results in an expression identical to Maskell's which contains only mean square quantities. As Maskell's equation is based on average pressure measurements, the unsteady terms of Landahl's have not been included.

2.6   Effects of a Finite Traverse on Landahl's Equation

In order to calculate drag with Landahl's equation 2.15, one must make velocity measurements over the entire wake cross-plane area. This would be either very time consuming, or not even possible in most wind tunnel facilities. A more realistic approach to the velocity measurements would be to make measurements starting in the regions of embedded vorticity and extending out until the velocity is at the freestream conditions, or as close to freestream conditions as is experimentally feasible. Measurements of this type are concentrated in the immediate area directly behind the model, and capture all the important information in the wake. Unfortunately, the momentum balance used to determine Landahl's drag equation 2.15 is not valid in a finite wake measurement as mass is not conserved between upstream and downstream cross-planes of equal area. The following analysis incorporates the continuity equation into Landahl's discussion for drag measurement, resulting in a form of the drag equation that is valid for finite area wake velocity measurements.

Let us assume that the model is located in a real wind tunnel with a finite cross-sectional area. We then place an imaginary constant cross-section rectangular box in the flow field, which surrounds the model and extends both upstream and downstream from the model, as shown in Figure 2.7. All of the side surfaces of the box that are

parallel to the flow are assumed to be at freestream pressure and velocity conditions, with the exception of the lower surface near the ground plane. If the lower surface is placed at the ground plane level, the boundary condition for this side is that no flow passes through this surface.

For a proper force balance in the streamwise direction, we must look at the all the forces acting, pressure and momentum. Referring to Figure 2.7, the upstream surface has pressure p_∞ and momentum $U_\infty \dot{m}_1$ forces acting. The downstream cross-plane has pressure $\bar{p}$ and momentum $\bar{u}\dot{m}_2$ forces acting. Pressure forces on the sides of the box are transverse to the direction of drag and do not effect the balance. Mass flow through the sides of the box, $\dot{m}_3$, does effect the the force balance as this mass moves in the streamwise direction at the freestream conditions, speed U_∞ and pressure p_∞. Combining these forces together gives an expression for the drag,

$$D = \int\int (p_\infty - \bar{p})\, dS + U_\infty \dot{m}_1 - \bar{u}\dot{m}_2 - U_\infty \dot{m}_3 \tag{2.22}$$

where dS is the cross-sectional area of the upstream and downstream ends of the box. From mass continuity, $\dot{m}_3$ is related to the other mass flows by

$$\dot{m}_3 = \dot{m}_1 - \dot{m}_2 \tag{2.23}$$

Or, in terms of velocities, Equation 2.23 becomes

$$\dot{m}_3 = \rho \int\int (U_\infty - \bar{u})\, dS \tag{2.24}$$

Substituting 2.24 into 2.22 and replacing the other mass flow terms by their corresponding velocity equivalents gives,

$$D = \int\int \left(p_\infty - \bar{p} + \rho U_\infty^2 - \rho \bar{u}_2^2 - \rho U_\infty^2 + \rho U_\infty \bar{u}_2 \right) dS \tag{2.25}$$

The first four terms in the integral of Equation 2.25 are identical to Equation 2.3 can be replaced by the results of Landahl's unsteady analysis, Equation 2.15. Replacing

these four terms with the time-averaged Equation 2.15 and simplifying gives the final expression for the total drag,

$$D = \frac{\rho}{2} \iint \left[2U_\infty \overline{u} - 2\overline{u}^2 + \overline{v}^2 + \overline{w}^2 - 2\overline{u'^2} + \overline{v'^2} + \overline{w'^2} \right] dS \qquad (2.26)$$

Again, we divide the total drag into form drag and vortex drag terms,

$$D_{Total} = D_{Vortex} + D_{Form} \qquad (2.27)$$

where

$$D_{Vortex} = \frac{\rho}{2} \iint \left(\overline{v}^2 + \overline{w}^2 \right) dS \qquad (2.28)$$

$$D_{Form} = \rho \iint \left[U_\infty \overline{u} - \overline{u}^2 + \frac{1}{2} \left(-2\overline{u'^2} + \overline{v'^2} + \overline{w'^2} \right) \right] dS \qquad (2.29)$$

Table 2.1: Experimental Results of Maskell's Method

Author	Probe Type	Wake Plane Location Downstream	Calculated Drag (% error)	Notes
Davis (1982)	Nulling 9–Hole Nulling 9–Hole	0.85 B.L.* 1.33 B.L.	-2.5 -8.3	Moving Ground Plane
Davis (1982)	Nulling 9–Hole Nulling 9–Hole	0.85 B.L. 1.33 B.L.	+7.1 +15.4	Stationary Ground Plane
Hackett & Sugavanam (1985)	Rake of seven 5–Hole probes	0.18 B.L. 0.86 B.L.	-1.4, +1.7 -3.3, -2.8	
Hackett & Sugavanam (1985)	Rake of seven 5–Hole probes	0.18 B.L. 0.86 B.L.	+6.5, +7.7 +7.5, +7.9	Model Yawed 12.5°
Onorato, et.al. (1984)	Nulling 9–Hole	0.37 B.L.	0.0	Boundary Layer Suction
Onorato, et.al. (1984)	Nulling 9–Hole	0.36 B.L. (longer body)	-1.3	Boundary Layer Suction
Hackett, et.al. (1985)	Rake of forty-two Non-nulling 7-Hole	0.40 B.L. 0.52 B.L.	$\simeq 18$ $\simeq 18$	

* B.L.= Body Lengths
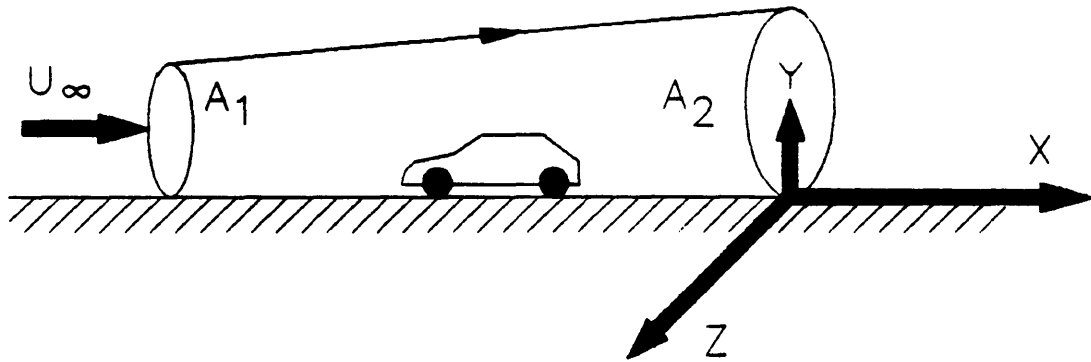
Figure 2.1: Flow field definitions for Maskell's method of drag calculation
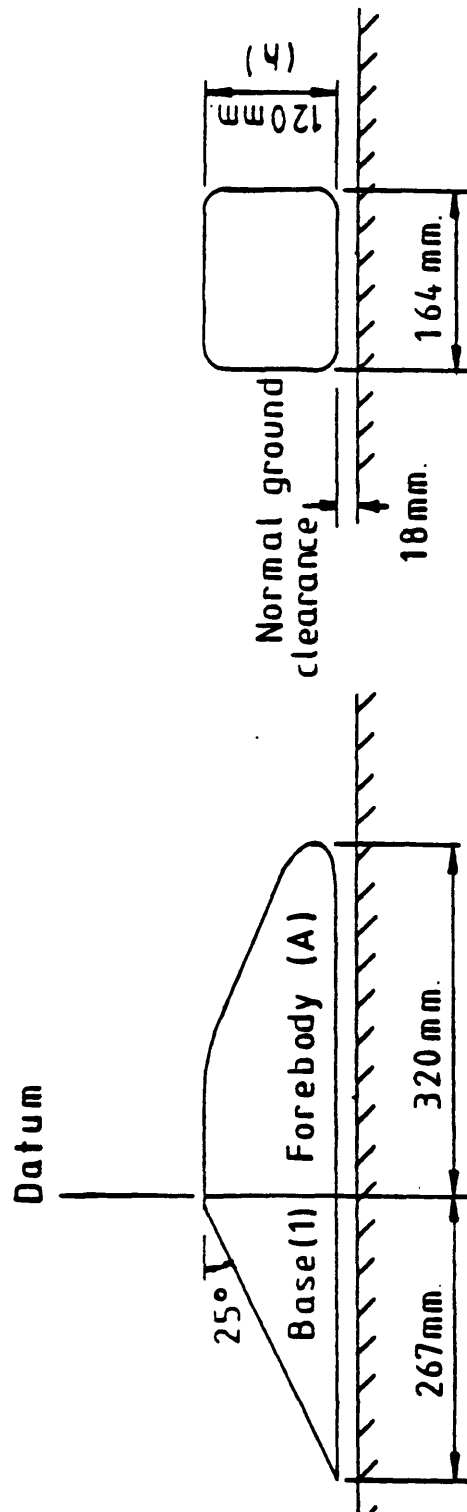
Figure 2.2: Schematic of Davis' model geometry, from Davis [11]
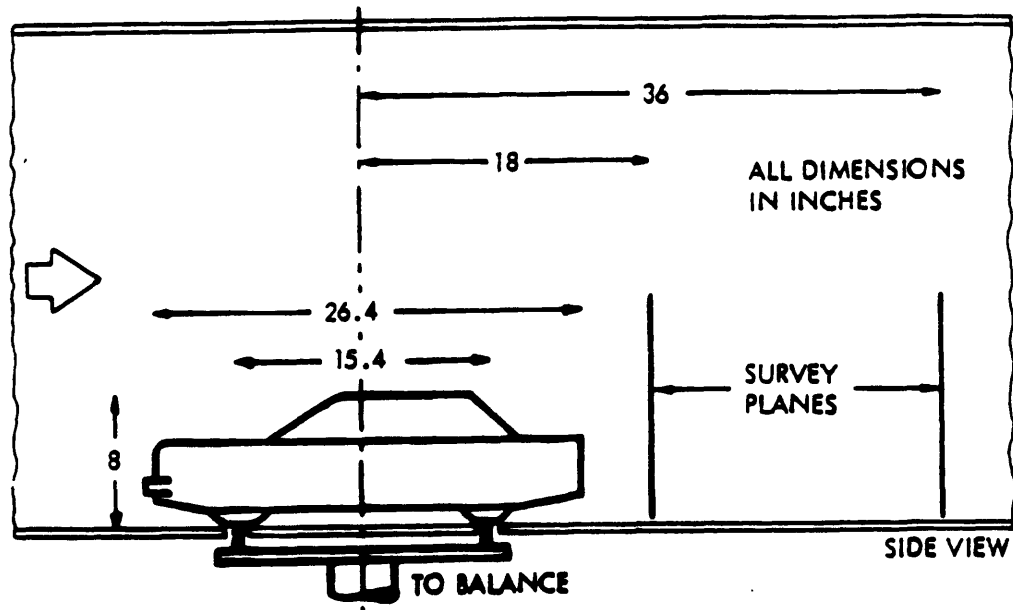
Figure 2.3: Illustration of model used by Hackett, from Hackett and Sugavanam [13]
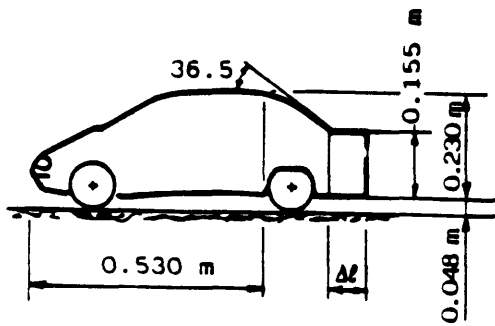
Figure 2.4: Schematic of model used by Onorato, from Onorato [26]

Figure 2.5: Ford Thunderbird model used by Hackett [14]
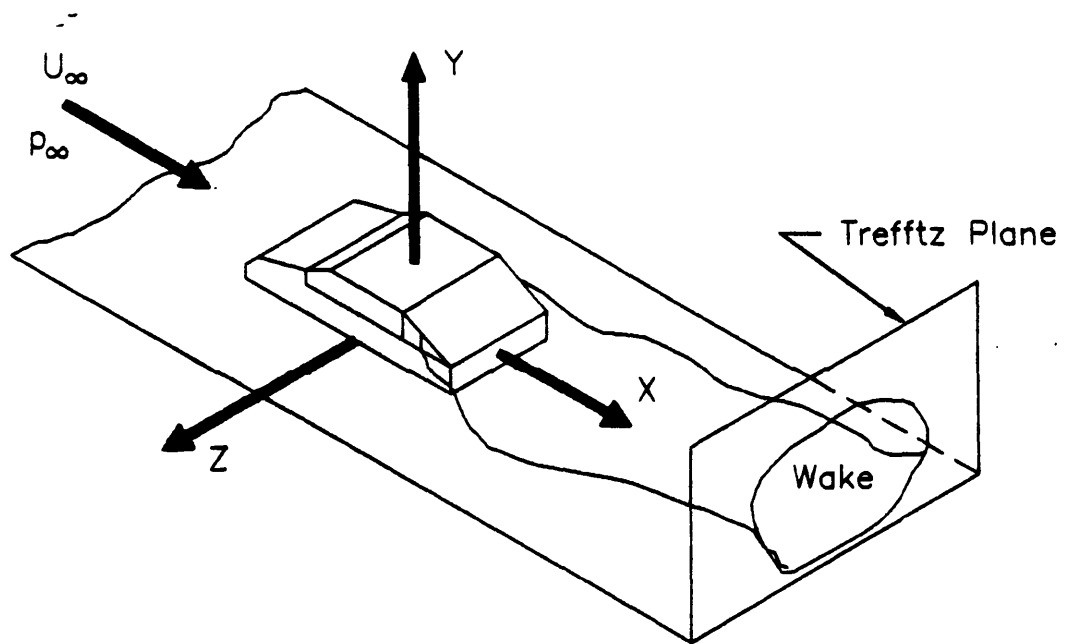
Figure 2.6: Flow field definitions for Landahl's drag calculation
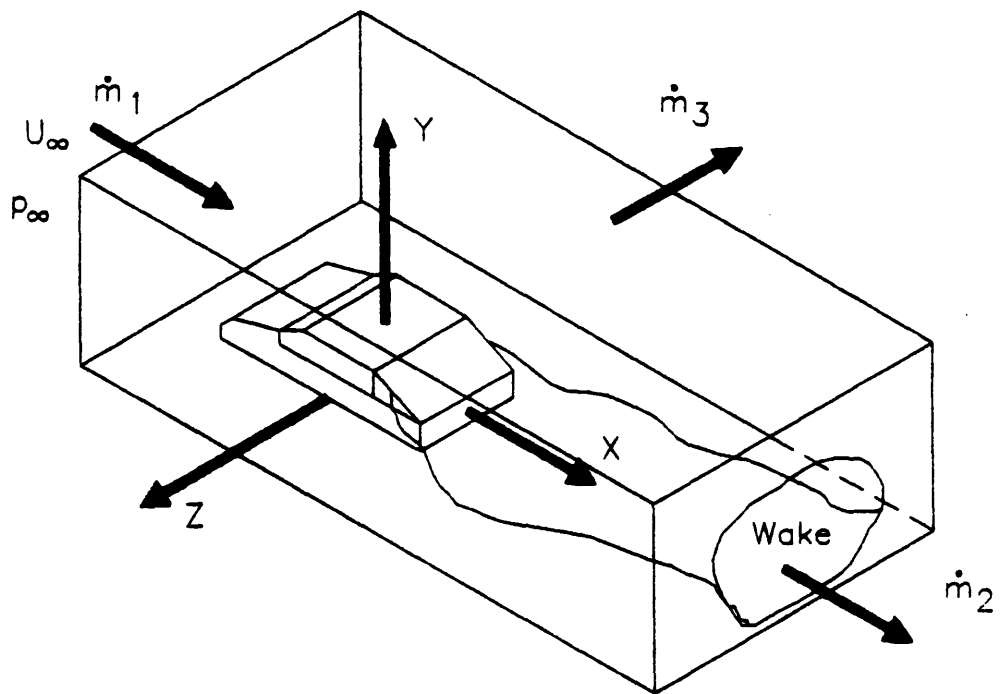
Figure 2.7: Mass flux definitions for a finite traverse.

Chapter 3

Facilities and Test Apparatus

3.1 Wind Tunnel

The site of the experiments was the MIT Low Turbulence Wind Tunnel, a closed-loop return path tunnel with two interchangeable test sections (Fig. 3.1). Test sections are 6.1 meters in length, with a rectangular cross section of 0.61 meters by 1.22 meters, the latter dimension being vertical. Flow is generated by a 50hp variable-speed DC motor driving 5-bladed fan measuring 1.52 meters in diameter. Motor speed is manually selected and constant flow velocity is maintained via a feedback loop from a tachometer mounted on the motor. Through feedback a constant load is maintained by the motor resulting in a constant flow velocity. Maximum empty test section velocity is approximately 50 meters/sec.

3.2 Test Section Modifications - Traverser

To facilitate wake surveys and flow field measurements a three-axis traversing mechanism was built and installed in one of the test sections. This required the replacement of the floor and ceiling, and all of the associated support structure. The traverser design, seen in Figures 3.2 and 3.3 is based closely on a traverser that already exists in the

second test section. Wind tunnel coordinate axes are also defined in these figures. The traverser rides on two parallel, case-hardened 25 mm diameter steel roundways aligned on the test section centerline and attached to the outside of the test section above and below the floor and ceiling. This permits motion in the x-direction down the entire length of the test section. A 25mm slot in the floor and ceiling allows the passage of the traverser. Polyurethane open cell foam strips attached to each side of the slot act to seal the slot as the traverser moves in the x-direction.

Each of the three axes are controlled by an individual stepper motor that can be manually moved, or controlled by a PDP-11/55 series computer. Motion in the x and z-directions is powered by Superior Electric SLO-SYN^{TM} Model MO63-FD09 200 step per revolution motors. A spur gear, driven through a 90° worm gear transmission, runs along a test section length gear rack moving the entire traverser in the x-direction. Vertical motion in the test section is controlled by the z-motor, which drives a 1/2-10 Acme lead screw through a 2-to-1 gear ratio. The Acme screw moves the z-traverse, which is guided by two 12.5 mm diameter parallel roundways attached to the front and rear of the vertical portion of the traverser exposed to the flow. All the motors and gearing associated with x and z-traverse axes are mounted on the bottom of the traverse, located below the floor of the wind tunnel, outside of the test section. The y-traverse and all its related mechanicals sits entirely inside the test section. A Velmex Unislide^{TM} machine slide is the basis of the y-traverse, and includes a Clifton Precision Model 15-SHAK-16CZ 192 step per revolution motor driving a 1/4-40 lead screw through a 1.25-to-1 gear ratio. Full length symmetric wood leading and trailing edges are attached to the Unislide^{TM} to reduce blockage effects. Total movement and spatial resolution of each axis, assuming all gear-train backlash has been removed, are summarized in Table 3.1. With a probe is attached to the y-traverse the traverser allows approximately sixty-

two percent of the cross-sectional area in the y-z plane above the ground plane to be mapped without changing the mounting position of the probe.

All Single wire hot-wire probes are mounted to a sting arm attached to the y-traverse slide, locating the probe tip 33 cm forward of the front edge of the y-traverse. X-probes are attached to a probe holder that locates the probe tip 27 cm forward of the y-traverse. The X-probe holder contains a stepper motor at its rear and gearing to rotate a probe for angular calibration.

Table 3.1: Traverser Movement and Positioning Specifications

Axis	Positioning Accuracy	Total Movement
X-Direction	1 motor step = 0.0665 mm	5.28 meters
Y-Direction	1 motor step = 0.002646 mm	0.381 meters
Z-Direction	1 motor step = 0.00635 mm	1.006 meters

3.3 Ground Plane

To simulate a ground surface and to control the boundary layer as it approaches the model a ground plane is installed vertically in the test section (Fig.3.3). Overall dimensions are 3.4 meters in length by 1.22 meters high by 2.79 cm thick, including the trailing edge flap (Fig.3.4). The ground plane is constructed of 1.016 mm aluminum sheet bonded to both sides of an aluminum honeycomb core and is flat to within ±0.254 mm across its surface. Structural aluminum C-channels are located along all the edges for solid attachment of wind tunnel mounting brackets, flap, and leading edge

attachment. A solid aluminum plate embedded in the honeycomb, measuring 152 mm by 152 mm by 25.4 mm thick, and used to support the model and associated hardware, is centered at a location 69 cm downstream of the leading edge, along the ground plane centerline. Distance between the bottom of the ground plane and the side wall is a constant 7.62 cm, and the leading edge is located 20.3 cm back from the start of the test section. The leading edge is constructed of full width (1.22 meters) symmetric, ellipically shaped hard wood (mahogany) 2.79 cm thick and 5.08 cm in length, with the length dimension being included in the previously stated overall dimensions of the ground plane.

A full span flap (1.22 meters) is attached to the trailing edge of the ground plane with a full length piano hinge. The flap's purpose is to control and alleviate any leading edge separation on the upper surface of the ground plane. Flap chord is 0.305 meters. The flap cross-section is of constant angle taper, varying linearly from a thickness of 27.9 mm at the hinge to 2.4 mm at its trailing edge as shown in Figure 3.5. Flap angle is step-wise adjustable to three angles: 0°, −5°, and −10°; negative angles imply the flap trailing edge is above the upper surface of the ground plane, following aircraft convention. At an angle of 0° the upper surface of the flap is parallel with the upper surface of the ground plane, as seen in Figure 3.5.

A 23.8 mm diameter hole for model mounting is located along the centerline, 69.08 cm behind the leading edge of the ground plane. Attached to the back side of the ground plane is the model mount. This device locks the model at any given yaw angle through the incorporation of a rotating and locking slip-ring mechanism in its design. The model strut is located by two ball bearings in the model mount, which provide for a solid mounting and precision yaw angle positioning. A vernier protractor is mounted

to the slip-ring and permits the yaw angle to be set accurately to within 6 minutes of arc.

3.4   Test Model Configurations

The test model is of a modular design that permits the attachment of various fast-back afterbodies. Overall dimensions are 540 mm long, 210 mm wide, and 150 mm tall as seen in Figure 3.6. Forebody dimensions are detailed in Tables 3.2 and 3.3 while side elevation and planform views are seen in Figure 3.7. The afterbodies consist of a series of fastbacks with backlight angles of 20°, 27.5°, 30°, 32.5°, and 35°. Mid-body and afterbody geometries and dimensions are detailed in Figures 3.8–3.13. The mid-body is a hollow aluminum box, while the afterbody consists of a 90° aluminum cradle onto which is attached individual wood modules, each shaped to a specified fastback angle.

The model is attached to the model mount with a 19.05 mm diameter hollow steel strut, giving a ground clearance of 30 mm. In terms of equivalent body diameters, D_{eq}, where D_{eq} is defined by

$$D_{eq} = \sqrt{\frac{4}{\pi}(\text{model cross-section area})}$$

the model ground clearance is $0.15\, D_{eq}$. For the model $D_{eq} = 200.3$ mm. The mounting strut exits the mid-body section of the model exactly at the center of its bottom. A bi-convex airfoil shrouds the mounting strut to reduce interference effects on the underbody and wake flows. The airfoil, detailed in Figure 3.14, is 28 mm in span (height) and has a chord of 159 mm.

A two component force balance to measure lift and drag is built into the model

mid-body. Balance design, calibration, and operation are detailed in Appendix A.

Flow blockage due to the model is about 5 percent of the upper flow path cross-sectional area. Including the ground plane (at 0° flap angle) and the model mount along with the model, blockage of the entire test section area is about 9.5 percent. When the model installed on the ground plane, the forebody starts at a position 45.08 cm downstream of the leading edge.
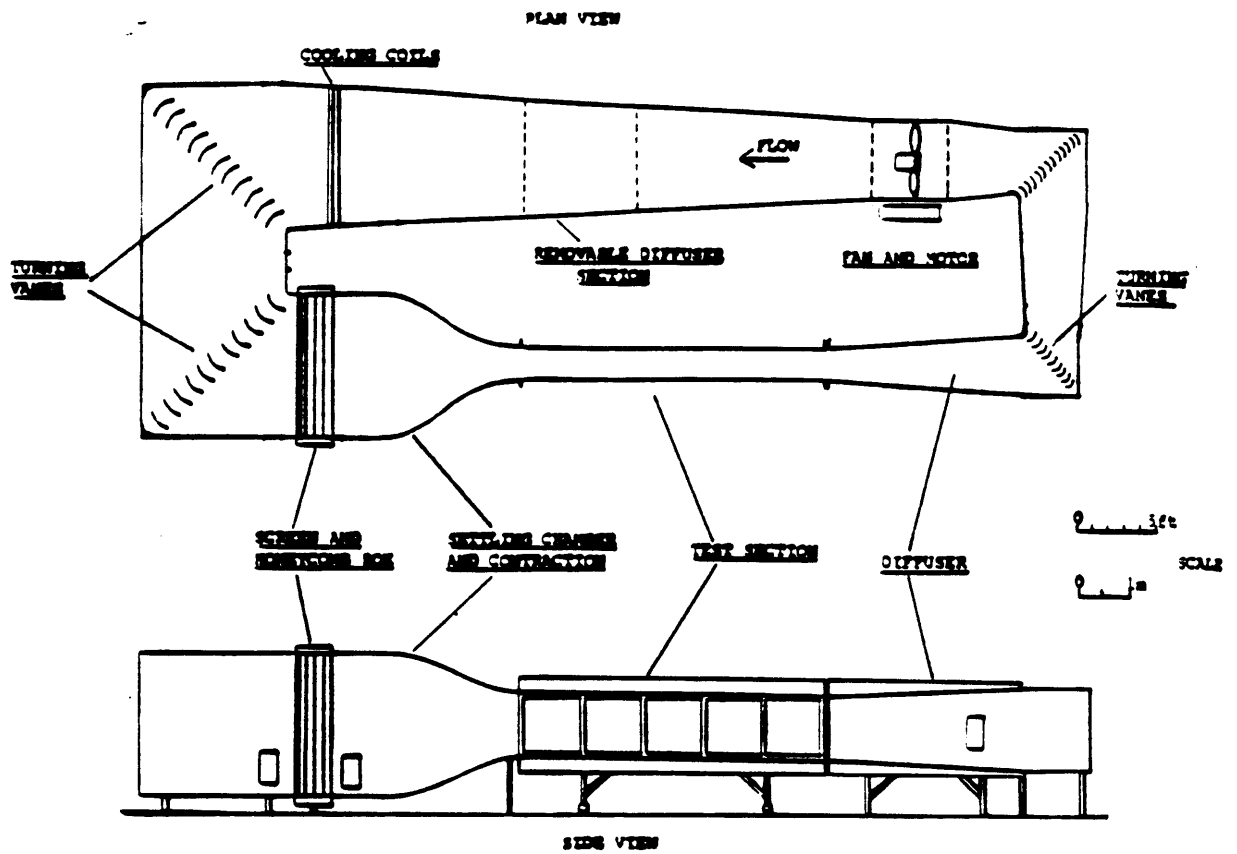
Figure 3.1: MIT Low Turbulence Wind Tunnel

Figure 3.2: Traverser Side View

Figure 3.3: Traverser Cross-Section View

Figure 3.4: Ground Plane Layout and Dimensions
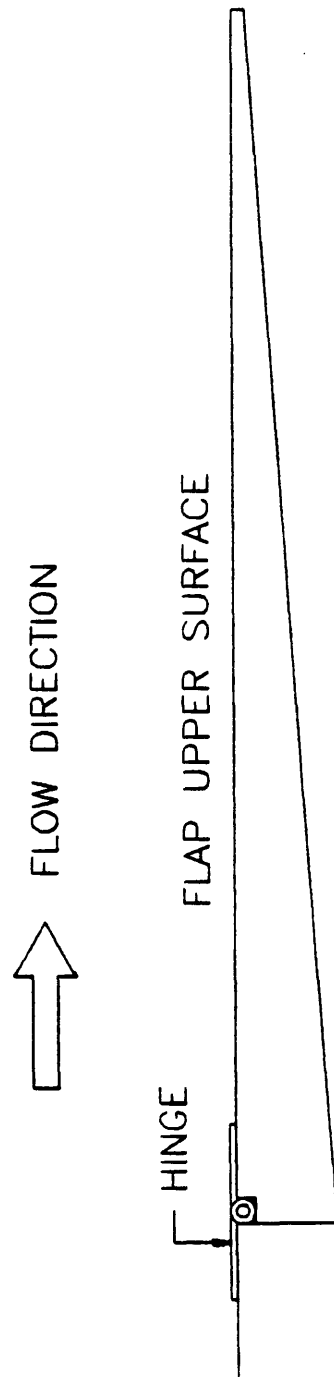
Figure 3.5: Flap End View and Mounting Details

TOP VIEW

210 mm

540 mm

SIDE VIEW

150 mm

STRUT FAIRING

Figure 3.6: Model - Top and Side Views

FOREBODY – PLANVIEW
DIMENSIONS IN MM

FOREBODY – SIDE ELEVATION
DIMENSIONS IN MM

Figure 3.7: Model Forebody - Top and Side View Details

Table 3.2: Model Forebody Module Geometry

SIDE ELEVATION COORDINATES

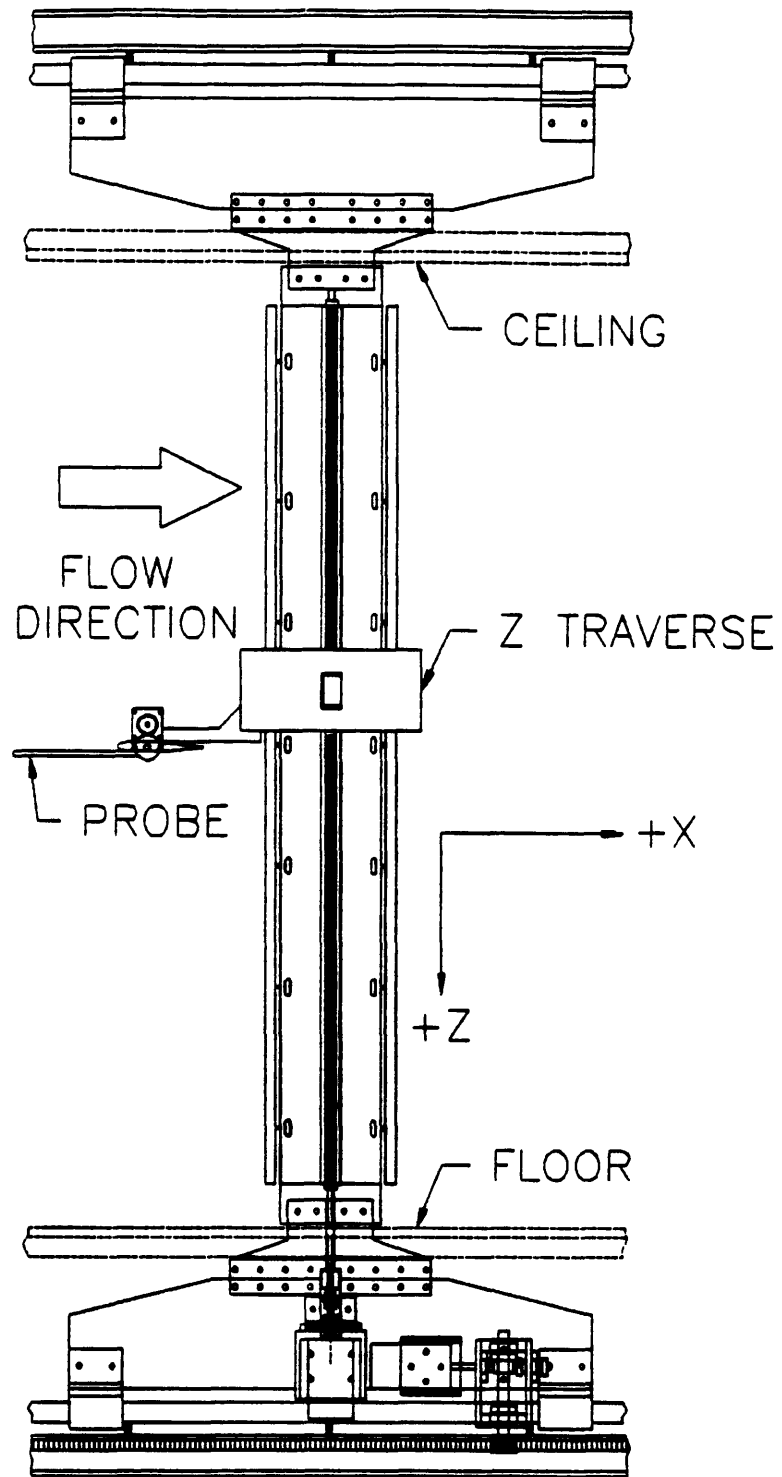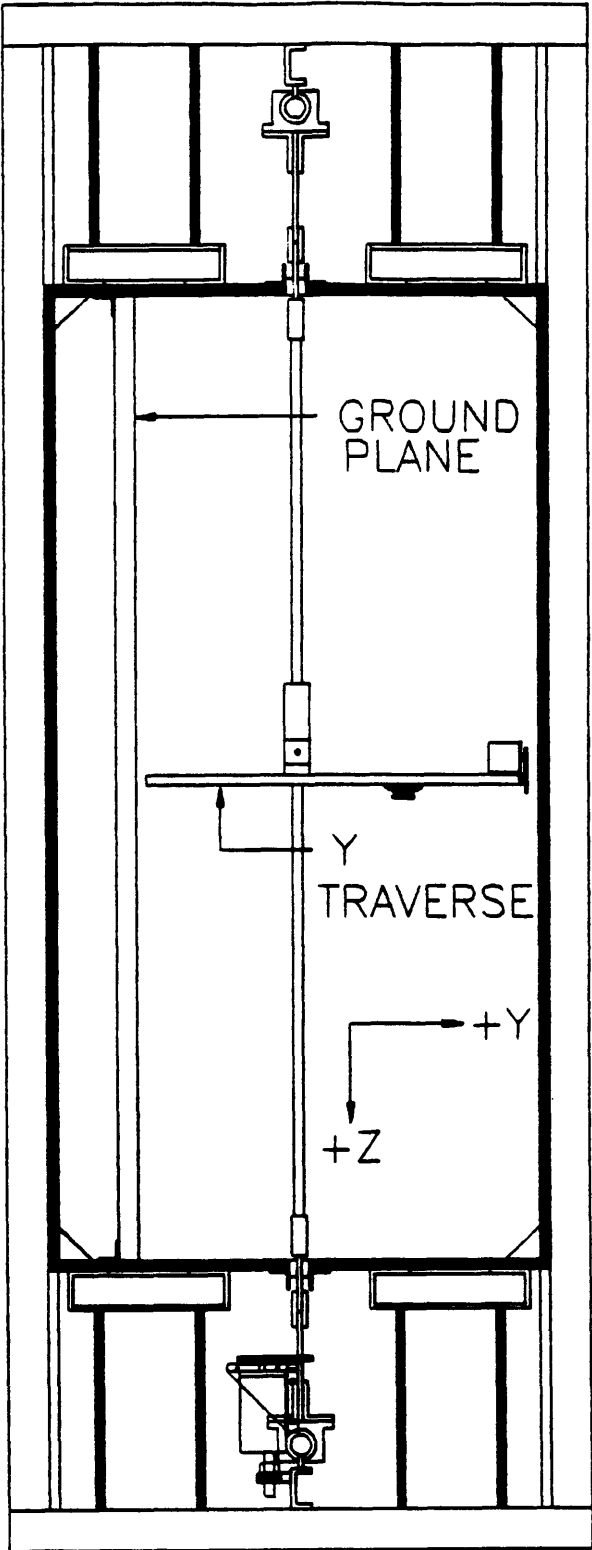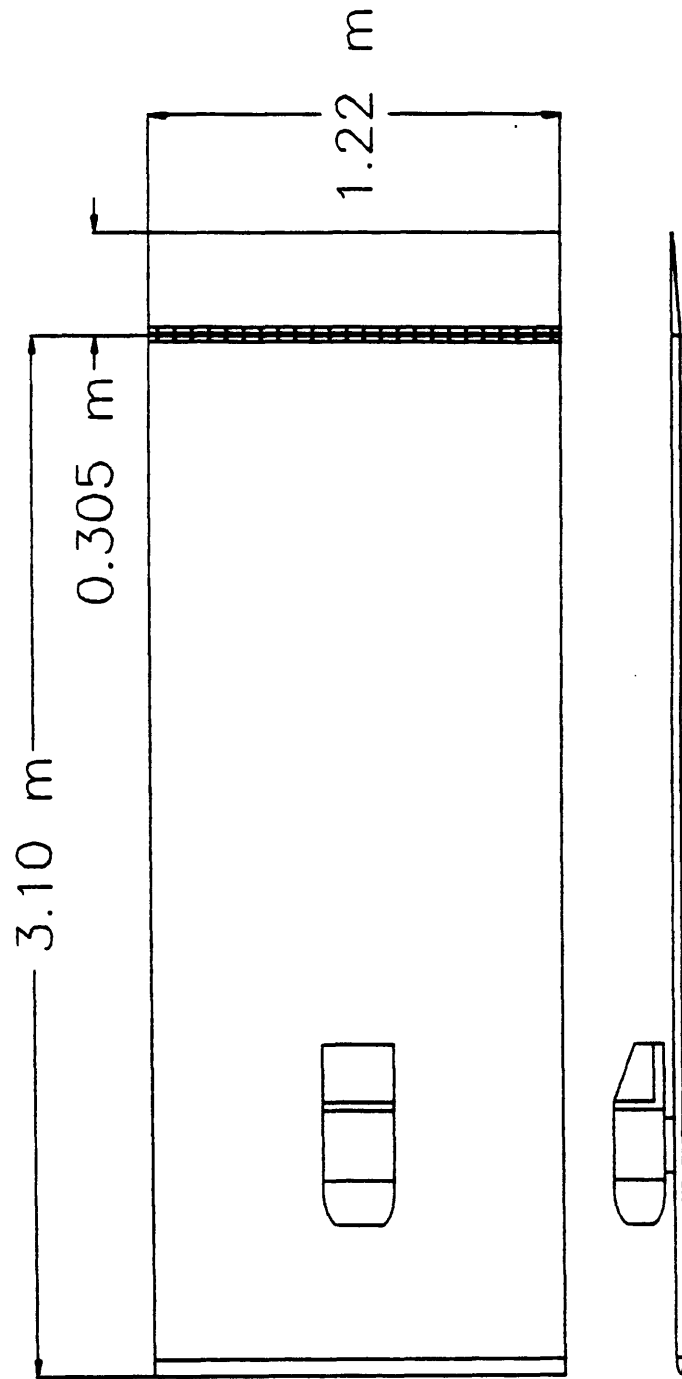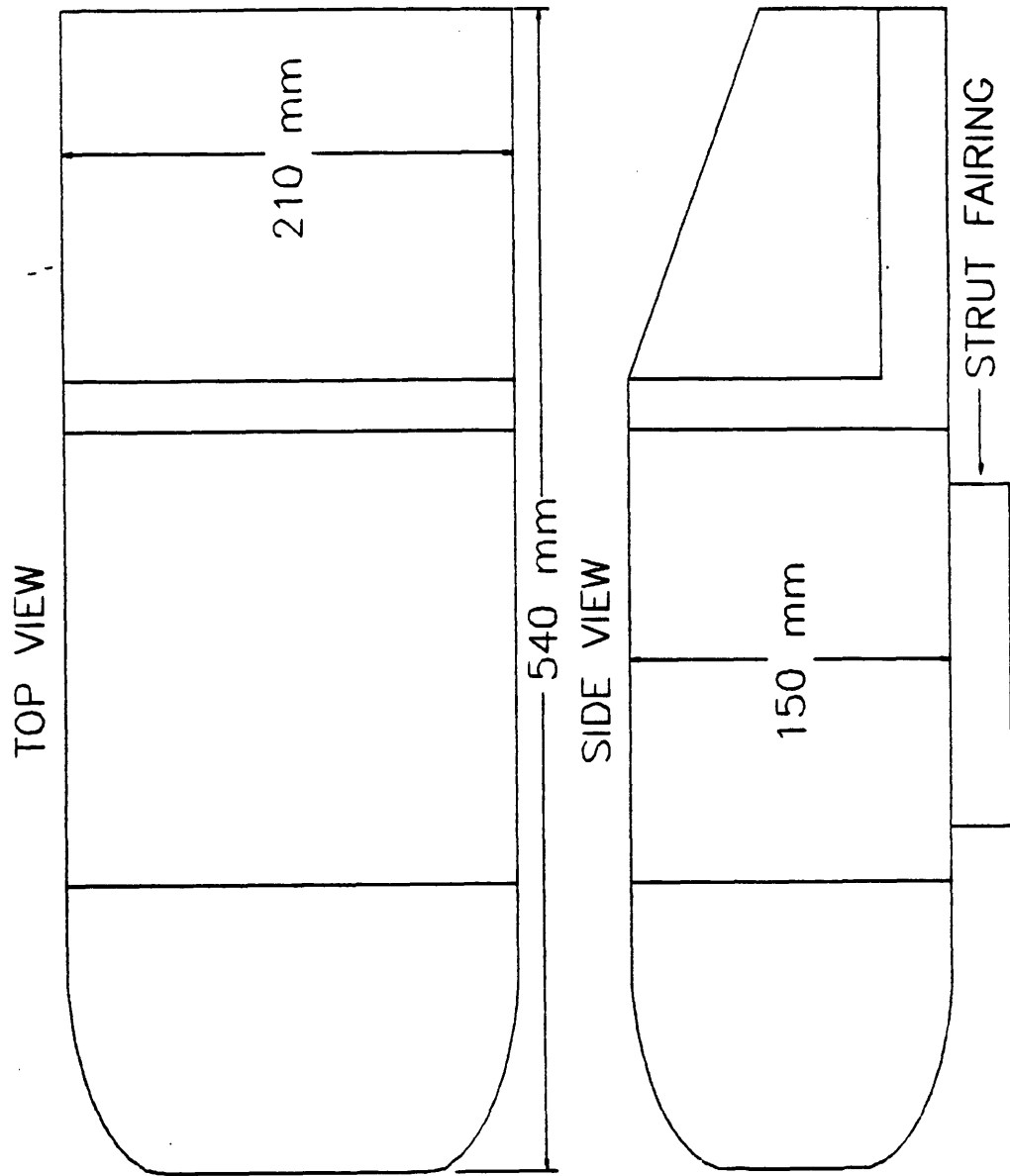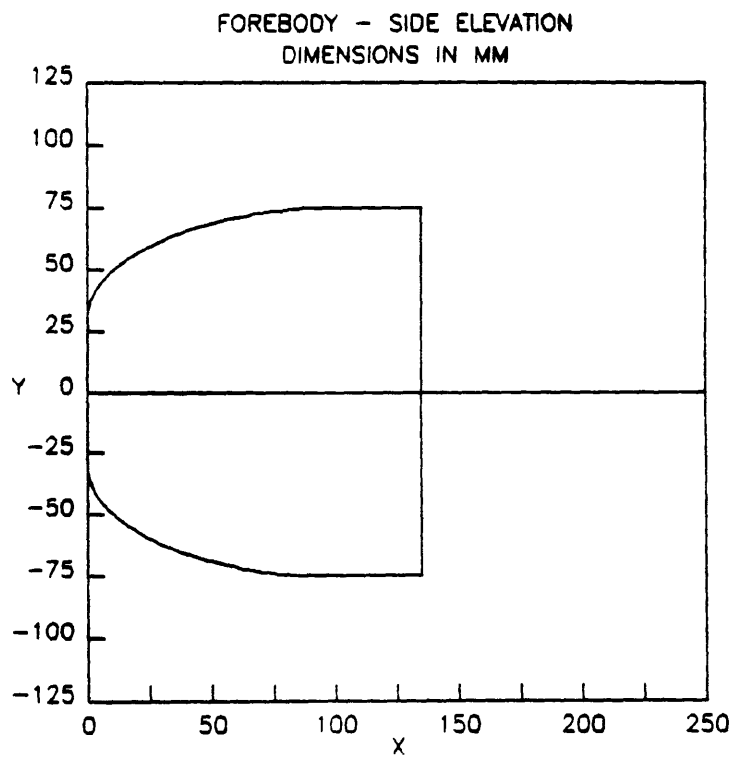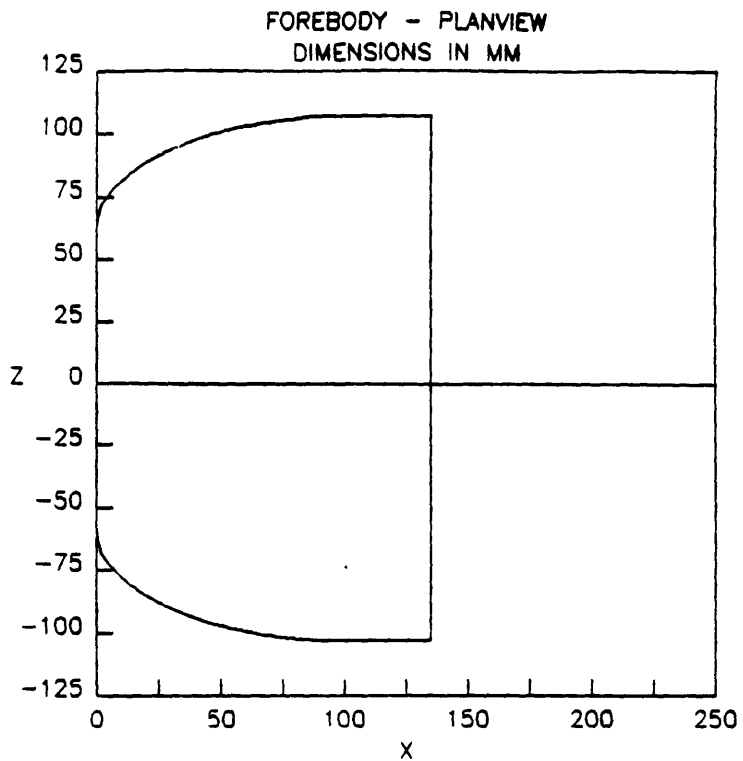| Y(mm)	X(mm)	Y(mm)	X(mm)
0.002	0.002	62.766	31.655
2.705	0.003	63.782	34.136
4.766	0.003	64.865	36.971
7.422	0.003	65.912	39.930
8.852	0.002	66.797	42.608
11.306	0.002	67.628	45.303
12.927	0.002	68.325	47.721
13.671	0.002	69.002	50.210
14.702	0.002	69.866	53.624
16.287	0.002	70.548	56.534
18.341	0.003	71.108	59.119
19.751	0.006	71.594	61.508
21.480	0.009	72.197	64.715
22.758	0.009	72.626	67.236
24.881	0.011	72.945	69.234
26.993	0.012	73.535	73.308
28.599	0.014	73.847	75.706
29.706	0.015	74.198	78.701
32.015	0.075	74.441	81.009
32.856	0.155	74.673	83.511
33.630	0.267	74.829	85.569
34.827	0.515	75.003	88.503
36.294	0.905	75.108	91.793
37.199	1.209	75.146	95.405
37.986	1.509	75.155	97.763
39.195	2.025	75.158	100.322
40.585	2.714	75.164	102.186
41.808	3.416	75.164	104.184
43.100	4.242	75.171	106.673
44.143	4.979	75.173	108.683
45.134	5.736	75.177	111.530
46.812	7.169	75.174	113.142
47.852	8.154	75.176	114.698
48.705	8.997	75.179	115.889
49.815	10.185	75.180	117.492
51.306	11.900	75.177	120.758
52.275	13.106	75.183	123.387
53.150	14.252	75.186	124.763
53.648	14.933	75.185	125.982
54.303	15.873	75.185	128.804
55.173	17.165	75.188	130.230
56.201	18.762	75.189	131.421
57.372	20.703	75.186	132.111
58.195	22.158	75.188	132.347
59.336	24.290	75.188	134.588
60.623	26.874	75.185	135.467
61.470	28.697	75.132	135.881

Table 3.3: Model Forebody Module Geometry

PLANVIEW COORDINATES

| Z(mm)	X(mm)		Z(mm)	X(mm)
0.023	0.002		89.513	24.803
1.770	0.006		90.219	26.222
3.213	0.005		90.762	27.353
5.735	0.003		91.487	28.921
7.817	0.003		91.856	29.745
9.705	0.002		92.496	31.223
11.444	0.000		93.176	32.850
13.101	0.002		93.852	34.544
14.961	0.002		94.358	35.861
17.441	0.003		95.196	38.142
19.287	0.008		95.937	40.395
21.291	0.006		96.777	42.830
23.391	0.006		97.370	44.735
25.488	0.009		97.964	46.740
27.866	0.011		98.569	48.908
30.405	0.012		99.225	51.369
33.002	0.014		99.794	53.640
35.337	0.014		100.488	56.153
37.217	0.015		100.929	58.629
39.099	0.015		101.715	62.512
40.890	0.015		102.337	65.900
43.881	0.014		103.017	70.065
45.968	0.015		103.331	72.183
47.957	0.014		103.839	76.019
49.674	0.012		104.248	79.553
51.776	0.012		104.549	82.521
54.165	0.011		104.793	85.340
55.466	0.011		105.003	88.190
58.700	0.005		105.222	92.280
60.045	0.002		105.333	96.195
61.145	0.050		105.368	98.781
63.252	0.267		105.387	101.369
65.160	0.642		105.404	105.017
67.275	1.278		105.414	107.229
70.103	1.748		105.419	109.227
73.283	4.417		105.423	110.879
75.978	6.497		105.428	113.031
77.484	7.856		105.431	115.706
78.711	9.071		105.437	117.789
79.935	10.380		105.438	120.032
81.225	11.888		105.437	123.728
82.611	13.646		105.440	127.595
83.802	15.270		105.438	129.395
84.494	16.265		105.441	131.735
85.229	17.367		105.443	132.329
86.486	19.359		105.440	134.334
87.524	21.116		105.440	135.002
88.694	23.229		105.438	135.758
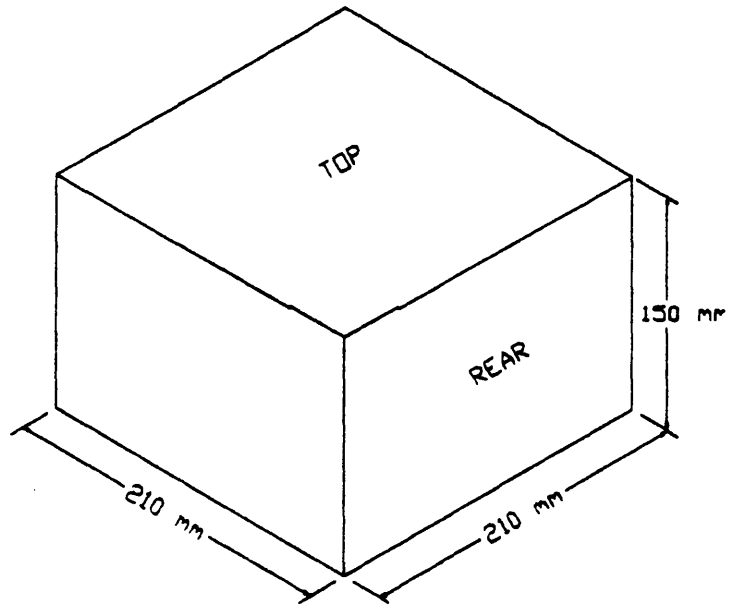
Figure 3.8: Model Mid-Body Schematic
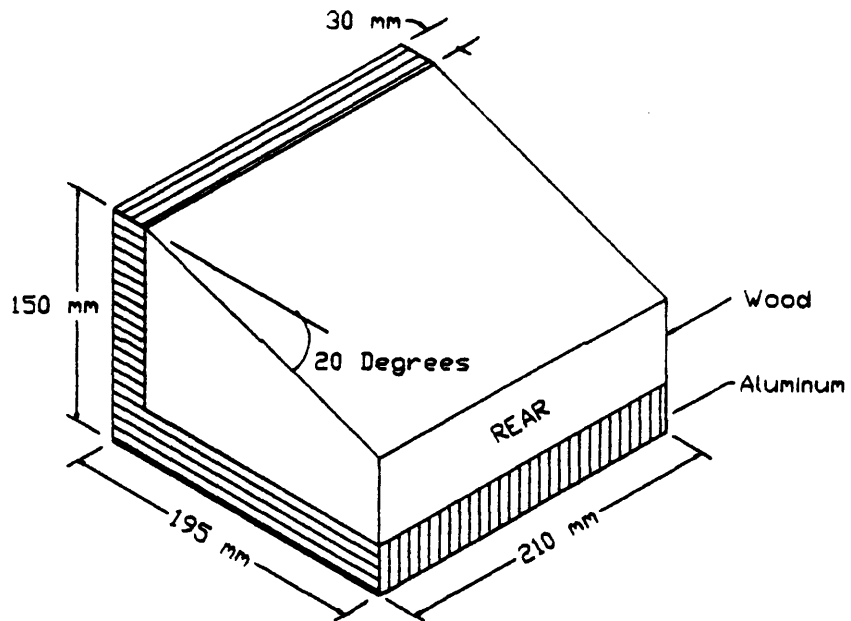
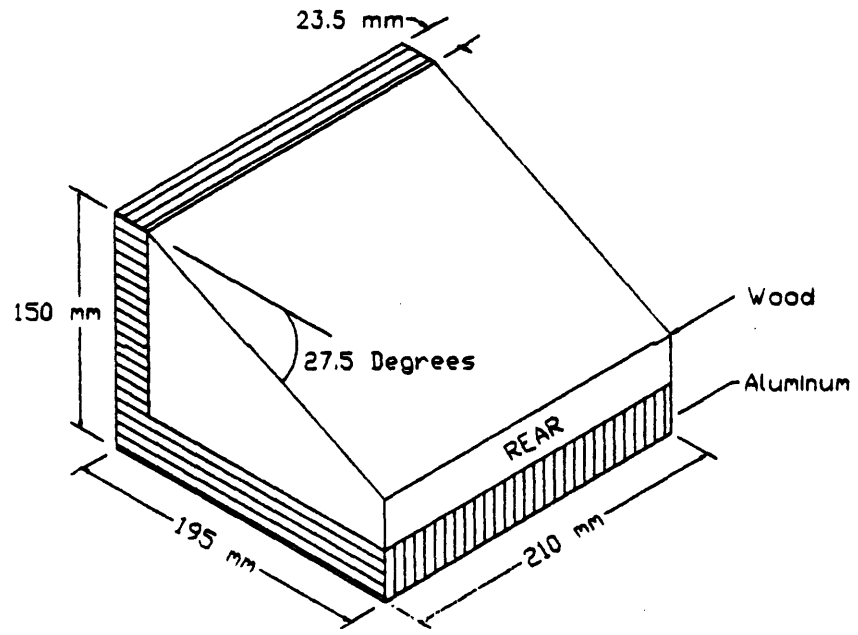

Figure 3.9: 20° Fastback Afterbody Module Schematic

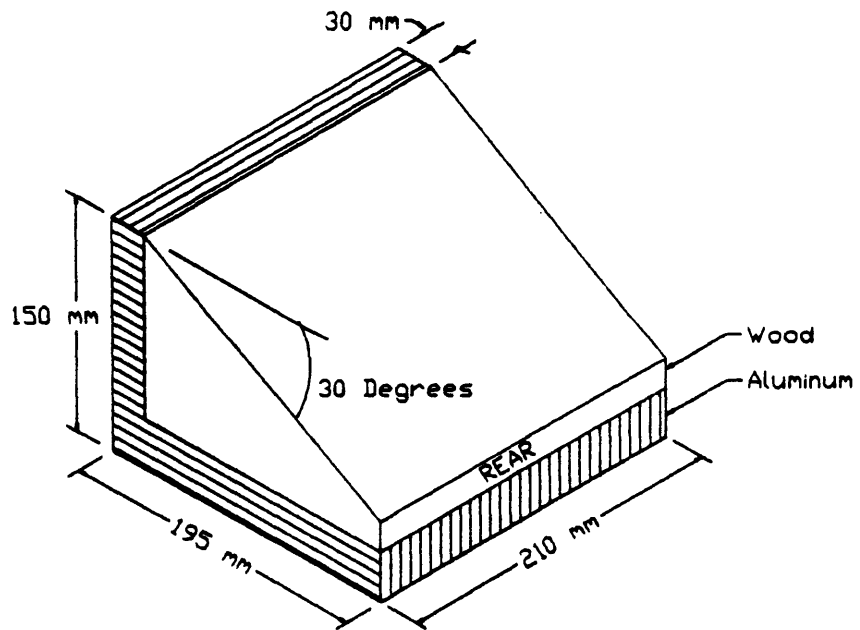Figure 3.10: 27.5° Fastback Afterbody Module Schematic

Figure 3.11: 30° Fastback Afterbody Module Schematic

Figure 3.12: 32.5° Fastback Afterbody Module Schematic

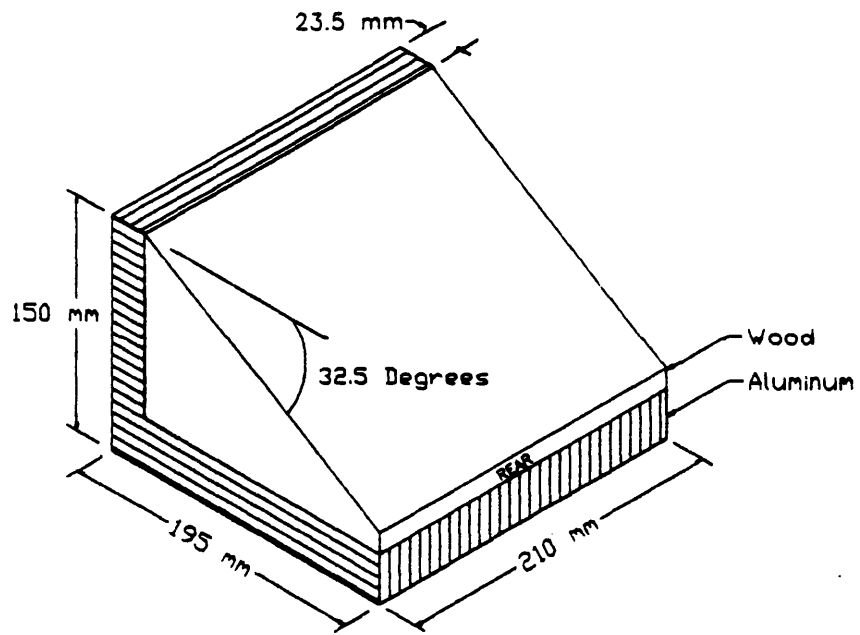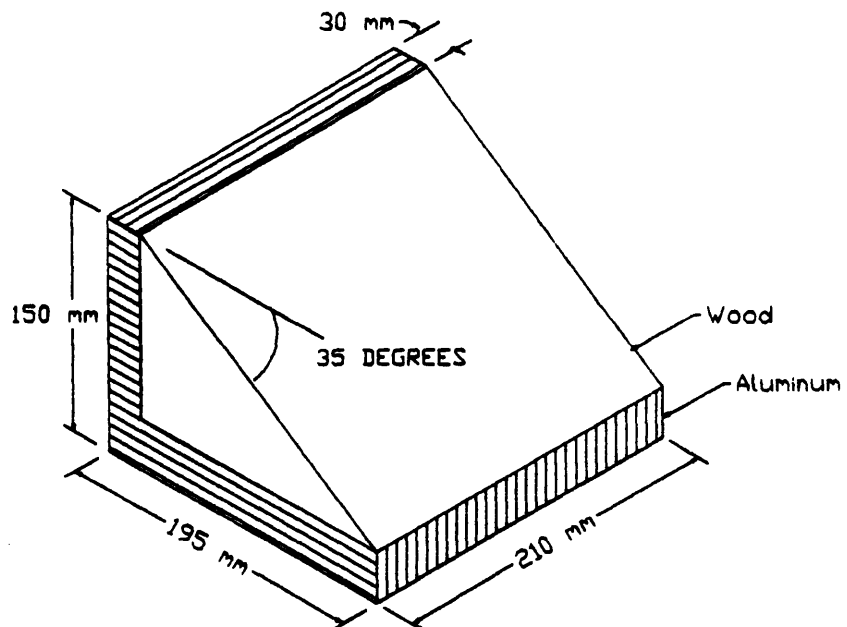Figure 3.13: 35° Fastback Afterbody Module Schematic

REFERENCE LINE

7.594   8.250 RADIUS

0.055 RADIUS

C   B   A   B   C

6.272

FAIRING CROSS SECTION

DIMENSIONS IN INCHES

1.102

SIDE VIEW
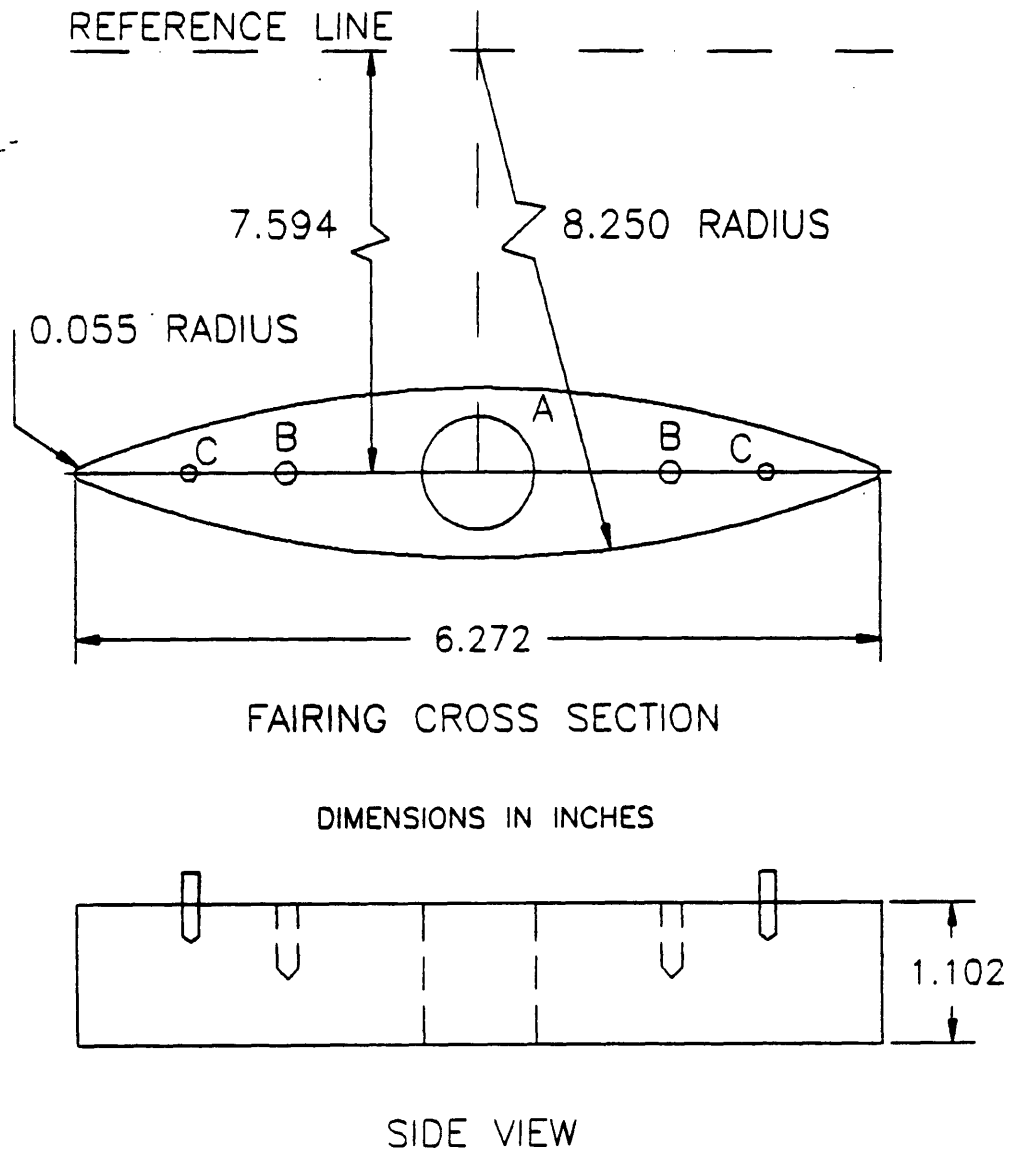
Figure 3.14: Model Mounting Strut Fairing

Chapter 4

Hot-Wire Wake Measurements

Single component hot-wires and two-component x-wires were first used to measure the basic flow properties of the wind tunnel test section and to determine the operating position of the groundplane trailing edge flap. Construction and use of the hot-wire probes is outlined in Appendix B while the empty test section (no model) flow properties are detailed in Appendix C. Wake measurements with the hot-wire probes proved unreliable, as errors in the stream-wise velocity were caused by the large crossflow velocities. A first-order velocity correction to reduce the errors is presented for both single component probes and two component probes.

4.1   Initial Wake Measurements

Velocity measurements were taken in two downstream crossflow planes, one at 0.5 body lengths (X=27 cm) and one at one body length downstream (X=54 cm). Three afterbodies were used, the 20°, 30°, and the 35° fastbacks. Data at X=27 cm was taken on a grid 60 cm by 31 cm with 1 cm spacing for a total of 1952 points (Figure 4.1). Data at X=54 cm was taken on a grid 80 cm by 31 cm with 1 cm spacing for a total of 2592 points (Figure 4.2). Fifteen ensembles of 2048 samples were taken at each point at a sampling frequency of 5 kHz per sensor. The average and RMS velocities were stored

for each point.

As stated in Appendix B, each of these planes had to be repeated twice to acquire all the data, the first pass for u-v data, and the second pass for u-w data. Each of the two passes result in two separate measurements of the u-component of velocity, and should be identical. Figure 4.3 shows the u-mean velocity contours normalized by the free stream velocity for the 30° fastback from a u-v measurement at X=27 cm. For comparison, Figure 4.4 shows the same normalized u-mean contours, this time taken from a u-w measurement. Note the trailing vortices (the circular-like patterns) from the u-v measurement appear to be skewed horizontally in the Z-direction while the vortices in the u-w measurement are skewed vertically, in the Y-direction. The minimum contour level is located at the center of the vortices, as this is the location of the greatest u-velocity deficit. For completeness, the mean u-velocity contours are shown for the same model geometry in the plane one body length downstream in Figures 4.5 and 4.6. Again, note the apparent skewness between the contours, raising concerns over the validity of using X-wire type probes in three-dimensional, highly turbulent flows.

4.2   Single Wire And X-Wire Probes In Highly Three Dimensional Flows

Observe an ideal vortex u-velocity contours in a crossflow plane as shown in Figure 4.7. The rotation is the same sense as the righthand-side vortex mentioned in the previous paragraph. Above the vortex, in the positive Y direction, the crossflow velocities consist of a large w component and a small v component. To the right of the vortex core, in the negative Z direction, the crossflow velocities consist of a large v component

and a small w component. For this discussion, is will initially be assumed that the x-wire is an ideal probe, being perfectly symmetric and having identical sensor length and sensor angles.

If an x-probe probe is placed in this flow field with the sensors lying in X-Y plane (vertical, normal to the groundplane) to measure u-v velocities the following occurs. To the right of the vortex the probe measures the u and v velocities with a good degree of accuracy. Above the vortex, or anywhere there is a large w crossflow component the effects on the sensors are quite dramatic. Single wire probes actually measure the total velocity vector perpendicular to the sensor, so if one were to attempt to measure u and the was a substantial v-velocity perpendicular to the sensor, the measured velocity would be the vector sum of these two velocities. Similarly, for an x-wire probe measuring u and v, anywhere that w is significant results in a larger u velocity being measured. Above the vortex the u velocity will stay larger as one approaches the vortex core, resulting in u-contours that are compressed vertically, giving a horizontally stretched vortex, as shown in Figure 4.8. Similarly, if the probe is rotated to measure u and w, large v velocities will stretch the u-contours in the vertical direction, as in Figure 4.9. This real effect is demonstrated by the velocity contours in Figures 4.3-4.5.

These effects should also be seen in single-wire u-velocity measurements. If the sensor is placed vertically (like measuring u and v with an x-wire), one would expect the u-velocity contours to be skewed horizontally, and similarly for a single sensor oriented horizontally.

The two velocities resulting from an x-wire measurement are essentially the sum and differences of the voltages of the two sensors. The u-velocity is obtained from the sum of the voltages, and the v or w-velocity is obtained from the difference of the voltages.

This being the case, the third component of velocity that affects the x-wire should, theoretically, affect both wires equally, leaving the difference in voltage between the wires the same. Therefore, the v or w component of velocity should not be different from its actual value. This assumption is necessary for the velocity correction analysis that follows.

4.3 Simple Velocity Correction

In order to verify the proposed statements regarding hot-wire measurements a small section of the flow field was surveyed again, in and around the core of the righthand-side vortex, looking upstream. The new surveys were on a grid 9 cm by 10 cm with a spacing of 1 cm at $X=27$ cm, as depicted in Figure 4.10. The survey was repeated four times, once for a u-v measurement, and a second time for a u-w measurement, both with an x-wire probe. The two remaining surveys were done with a single wire probe, one with the sensor horizontal (parallel to the ground plane), amd the other with the sensor vertical (normal to the ground plane). It was hoped that with these measurements the discrepancies between the u-velocity contours would be able to be quantified.

Figures 4.11 and 4.12 show the u-velocity contours for five different measurements of the vortex. The first is from a three- component hot-film measurement, and the next two are from x-wire measurements in both orientations. The last two contours are from single-wire measurements in two orientations. Unfortunately, it was not possible to cover the entire vortex test area with the single-wire vertical due to physical constraints of the traversing mechanism, so the results for the case are only shown for the upper two-thirds of the data grid. Contours from the hot-film are essentially circular, as expected for a

vortex. Comparing the u-v contours to the single-wire vertical, and the u-w contours to the single-wire horizontal contours affirms our concerns stated two paragraphs ago. A single-wire probe measurement in a highly vortical flow will be effected in a similar manner as an x-wire probe with its sensors lying in the same orientation. A vertical wire measurement will be skewed horizontally and a horizontal wire measurement will be skewed vertically.

Single-wire probes, being inherently simpler than x-wires will be analyzed first. Single-wire probes do not actually measure the u-component of velocity, except when they are located in a free stream with no disturbances. What they always do measure is the magnitude of the velocity vector perpendicular to the axis of the sensor, call this $\bar{q}$ in the time- averaged sense. If the sensor is horizontal and the flow is three-dimensional, then the measured $\bar{q}$ is related to the real velocities by,

$$\bar{q}^2 = \bar{u}^2 + \bar{w}^2 \tag{4.1}$$

Since the flow field is unsteady, Equation 4.1 can be expanded to

$$\bar{q}^2 + \overline{q'^2} = \bar{u}^2 + \overline{u'^2} + \bar{w}^2 + \overline{w'^2} \tag{4.2}$$

Solving for $\bar{u}^2$ gives

$$\bar{u}^2 = \bar{q}^2 + \overline{q'^2} - \overline{u'^2} - \bar{w}^2 - \overline{w'^2} \tag{4.3}$$

If we now assume that the flow is essentially isotropic, we can assume that $\overline{u'^2} \approx \overline{w'^2}$ Equation 4.3 is converted into its final form for the velocity correction of a single-wire probe in a three-dimensional flow field:

$$\bar{u}^2 = \bar{q}^2 + \overline{q'^2} - \bar{w}^2 - 2\overline{w'^2} \tag{4.4}$$

Similarly, for a single-wire probe oriented vertically, the velocity correction equation is

$$\bar{u}^2 = \bar{q}^2 + \overline{q'^2} - \bar{v}^2 - 2\overline{v'^2} \tag{4.5}$$

The assumption of isotropic flow is supported by the data obtained with the three-component probes discussed in Chapter 5.

The single-wire data from Figure 4.12 was then corrected using Equations 4.4 and 4.5 along with the v and w-velocities measured with the x-wire probe. The resulting u-velocity contours are shown in Figure 4.13. With the correction, the horizontal wire contour has been stretched out in the horizontal direction, while the vertical wire contour has been stretched out vertically, and, if the two contours are placed on top of each other, the differences between them are very small. It should that emphasized that the contour spacing is rather shallow, only five percent, and differences between the contours are within the limits of error of the measurements.

Based on the success of the single-wire corrections, the same technique was applied to the x-wire measurements. For example, for a u-v measurement, the originally measured u-velocity is assumed to be q, so to determine the actual velocity u, Equation 4.4 was used with the w-velocities from the u-w measurement. A similar procedure is followed to correct the u-w measurement. Results of this simple correction for the x-wire measurements are shown in Figures 4.14 and 4.15, corresponding to the u-v measurement and the u-w measurement, respectively. The top contour in each of these figures corresponds to the u-velocity contours for the uncorrected data and are presentented again for comparison purposes. The middle contour in each figure is from the simple velocity correction discussed above, and the bottom contour in each figure corresponds to a more detailed correction to be discussed shortly. Notice that the effect of the correction for each of the measurements is similar to that for the single-wire cases. Contours from the u-v measurement are stretched vertically after the simple correction, and contours from the u-w measurement are stretched horizontally by the correction. Also note that

the outer contours (away from the vortex core) take on a high degree of similarity after the correction, yet the core region of the vortex was still exhibiting much of the original skewing.

4.4   Geometric Velocity Correction For X-Wires

Encouraged by the simple velocity correction results, a more detailed velocity correction, based on the actual x-wire probe geometry, was pursued. This correction method takes into account the fact that the x-wire sensors are at an angle relative to the streamwise direction, so their sensitivity to the total velocity vector varies geometrically from the simple velocity correction of the previous section. We begin by stating again that the sensors on an x-wire probe essentially measure the component of velocity that is normal to each sensor's longitudinal axis. If we can deduce two expressions for this normal velocity in terms of the known quantities, a new velocity correction expression can be determined. As before, it will be assumed that the v and w measurements are correct, and that only the u velocity must be corrected.

Figure 4.16 shows the physical orientation of one of the sensors of an x-wire in the flow field oriented for u-v measurements. From geometry, it is clear that the normal velocity due to just the u and w components of the velocity field can be expressed in the time average as

$$\overline{U}_n^2 = (\overline{u}\sin\phi)^2 + \overline{w}^2 \qquad (4.6)$$

where ϕ is the angle the sensor makes with the freestream flow. The normal velocity from u and w can also be described in terms of q, the measured velocity. Referring to Figure 4.17, the q- velocity vector lies in the X-Z plane, and therefore has components

along X and Z directions, which will be defined as q_u and q_w, respectively. The q vector makes an angle α with the X axis, so,

$$\bar{q}_u = \bar{q}\cos\alpha$$

$$\bar{q}_w = \bar{q}\sin\alpha \tag{4.7}$$

where α is defined by the equation

$$\alpha = \tan^{-1}\left(\frac{\overline{w}}{\overline{u}}\right) \tag{4.8}$$

We can now write the normal velocity due to q.

$$\overline{U}_n^2 = \bar{q}_w^2 + (\bar{q}_u \sin\phi)^2 \tag{4.9}$$

Substituting Equation 4.7 into 4.9 gives the second equation for the normal velocity due to u and w.

$$\overline{U}_n^2 = (\bar{q}\cos\alpha\sin\phi)^2 + (\bar{q}\sin\alpha)^2 \tag{4.10}$$

Combining Equations 4.6 and 4.10, the two relations for $\overline{U}$, and solving for $\bar{u}$ gives the expression for the steady, time-averaged velocity correction,

$$\bar{u} = \frac{1}{\sin\phi}\left[(\bar{q}\cos\alpha\sin\phi)^2 + (\bar{q}\sin\alpha)^2 - \overline{w}^2\right]^{\frac{1}{2}} \tag{4.11}$$

Next, we add in the unsteady terms, and use the isotropic assumption that $\overline{u'} \approx \overline{w'}$, the correction equation becomes

$$\begin{aligned}\bar{u} = \frac{1}{\sin\phi}\Bigg[&(\bar{q}\cos\alpha\sin\phi)^2 + \left(\overline{\bar{q}'}\cos\alpha\sin\phi\right)^2 + (\bar{q}\sin\alpha)^2 \\ &+ \left(\overline{q'}\sin\alpha\right)^2 - \left(\overline{w'}\sin\phi\right)^2 - \overline{w}^2 - \overline{w'^2}\Bigg]^{\frac{1}{2}}\end{aligned} \tag{4.12}$$

Adding some rearranging to Equation 4.12 gives the final form of the geometric velocity correction equation for x-wires measuring u and v in a highly three-dimensional flow,

$$\bar{u} = \frac{1}{\sin\phi}\left[\bar{q}^2\left(\cos^2\alpha\sin^2\phi + \sin^2\alpha\right)\right.$$

$$+\overline{q'^2}\left[\sin^2\phi\left(\cos^2\alpha-1\right)+\sin^2\alpha\right]$$
$$-\overline{w}^2-\overline{w'^2}\left(1+\sin^2\phi\right)\Big]^{\frac{1}{2}} \tag{4.13}$$

Replacing w with v in Equation 4.13 gives the u-velocity correction equation for a u-w measurement.

$$\overline{u} = \frac{1}{\sin\phi}\bigg[\overline{q}^2\left(\cos^2\alpha\sin^2\phi+\sin^2\alpha\right)$$
$$+\overline{q'^2}\left[\sin^2\phi\left(\cos^2\alpha-1\right)+\sin^2\alpha\right]$$
$$-\overline{v}^2-\overline{v'^2}\left(1+\sin^2\phi\right)\bigg]^{\frac{1}{2}} \tag{4.14}$$

These geometric correction were applied to the x-wire data, with the resulting velocity contours plotted in the bottom pictures of Figures 4.14 and 4.15. Again, the correction has caused the u-v measurement contour to be stretched vertically, fractionally more than with the simple correction, resulting in a better estimation of the actual u velocity. Similarly, the u-contours from the u-w measurement have been stretched out horizontally slightly more that with the simple correction, although comparison of the shape of the vortex core between the two measurements still show signs of their initial stretching.

The correction was applied to the u-v and u-w velocity measurements from the 30° fastback at $x=27$ cm. The resulting corrected u- velocity contours are shown in Figures 4.18 and 4.19. These can be compared with the uncorrected u-velocity contours in Figures 4.3 and 4.4. Overall, the change from uncorrected to corrected contours is rather small.

To determine the effectiveness of the corrections, contours of the percentage difference in the local u-velocities between the u-v and u-w measurements for both the uncorrected and the corrected velocities are shown in Figures 4.20 and 4.21. For the uncorrected velocities, the maximum error is about -45% in the region between the

vortices, just off the center of the vortex cores where the v- velocity is very highly negative. The maximum positive error occurs in the regions where the w-velocity is high, below the vortices, and is 27%. For the corrected velocities, the maximum error in local velocities between the two measurements occurs at the same location as the uncorrected velocities, but is now reduced to -31%, and the maximum positive error has been reduced to 19%. While the trends of the velocity corrections are encouraging, there are indications that there still may be some other important factors missing from the correction analysis.

4.5 Thermal Wake Interference Effects On X-wire Probes

One important factor missing from the previous correction analysis was to allow for the possible interference between the thermal wakes of the two sensors. Both of the two sensors on an x-wire are basically heating devices, and, when submerged in a moving stream, have a wake of heated fluid trailing behind them. If the third velocity component not being measured is very large, or the flow is very turbulent, it is possible for the thermal wake of one sensor to be directed over the other sensor, contaminating its signal. When this happens, the contaminated sensor sees a warmer fluid which reduces its cooling rate, and results in a lower velocity reading for that sensor than what actually exists. Because of this, not only is the u-velocity measurement incorrect (which is the sum of the two wire voltages), the other velocity measurement, be it v or w, is also incorrect as the difference in voltages between the two sensors is not representative of this velocity.

A simple test was run to determine if indeed the x-wire probes were experiencing

89

thermal wake interference. To do this, one of the sensors was run normally as a hot-wire, heating the flow around it. The other sensor was connected to an amplifier and run as a thermometer. Both signals were monitored on an oscilloscope as the probe was manually traversed in the wake region behind the model. Two model geometries were used, the 20° and 30° fastback. The first because it produced the weakest coherent vortices, and the latter for producing very strong vortices. Traverses were done at two X-locations downstream, $X=27$ cm and $X=54$ cm, corresponding to the plane locations of the complete data traverses. The results of these tests proved conclusively that thermal wake interference did exist.

At the $X=27$ cm location, the temperature sensor would experience occasional, but random, large excursions from its mean value, with the frequency of such events becoming more frequent as the probe was moved closer to the vortices. Farther from the vortices, where the turbulence and cross flow velocities are much smaller, no thermal interference was observed. At the $X=54$ cm location, the same excursions were noted near the vortices, but were less frequent. This held true for both model geometries. The tests were then rerun with a modified x-wire with larger spacing between the two sensors, 0.040 inches as opposed to 0.020 inches used in the first thermal tests. It was hoped that the larger distance between the two sensors would suppress the wake interference effects. Results were not much different from the first probe at the closer wake plane, but downstream, at $X=54$ cm, no wake interference was detected. Increasing the sensor spacing did effect the thermal wake interference by reducing it occurrences but did not completely alleviate the problem.

Based on the velocity correction analysis and the existence of thermal wake interference, it was determined that the uncertainties in the results of x-wire measurements in

the wakes of these fastback shapes were too great to permit a useful and correct analysis of the data, therefore, other means of measuring these flow fields were investigated. In particular, the use of three-component hot-film probes.

X-WIRE DATA PLANE   X=27CM
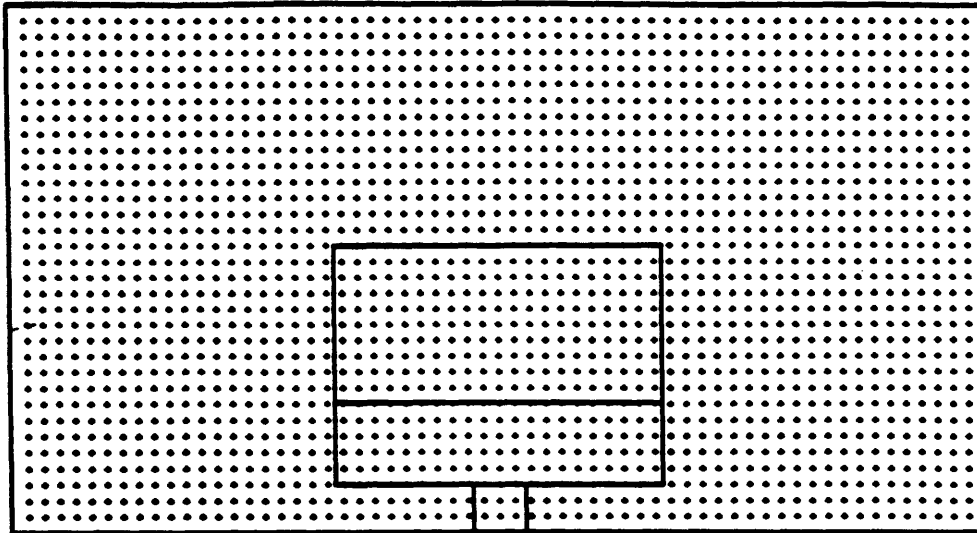
Figure 4.1: Wake data grid, $X=27$ cm.

X-WIRE DATA PLANE   X=54CM
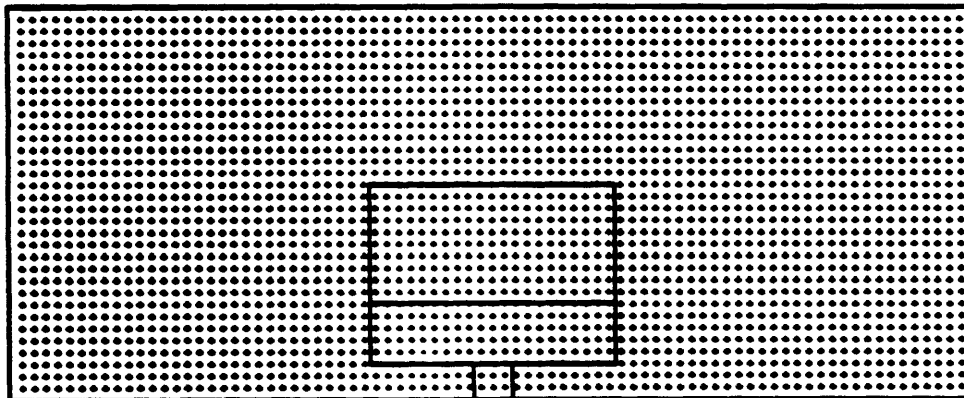
Figure 4.2: Wake data grid, $X=54$ cm.

30 DEGREE FASTBACK   X=27 CM

min= 0.601   max= 1.07   Contour Spacing=   0.05
U mean/Uinf From U-V Measurement
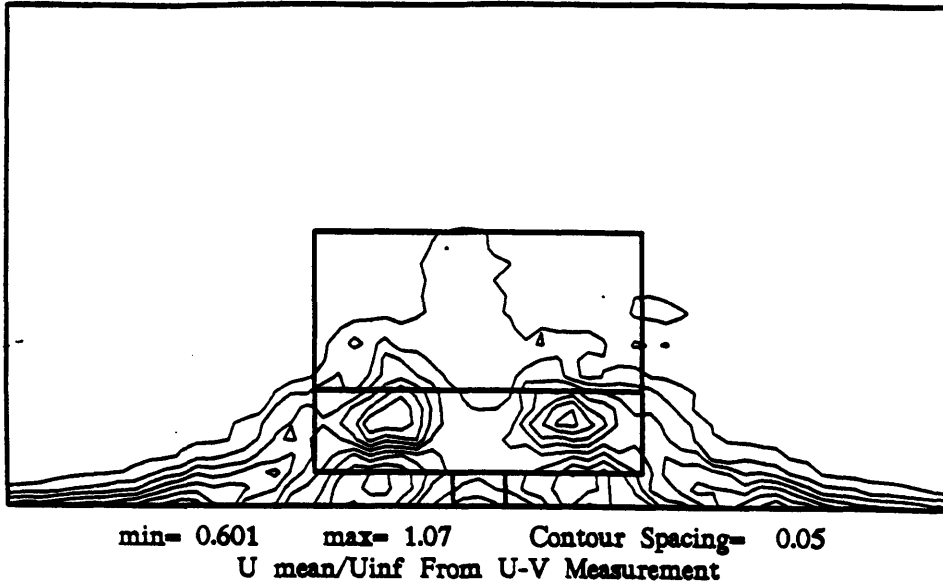
Figure 4.3: Normalized u-velocity contours from u-v measurement, X=27 cm.

30 DEGREE FASTBACK   X=27 CM

min= 0.587   max= 1.18   Contour Spacing=   0.05
U mean/Uinf From U-W Measurement
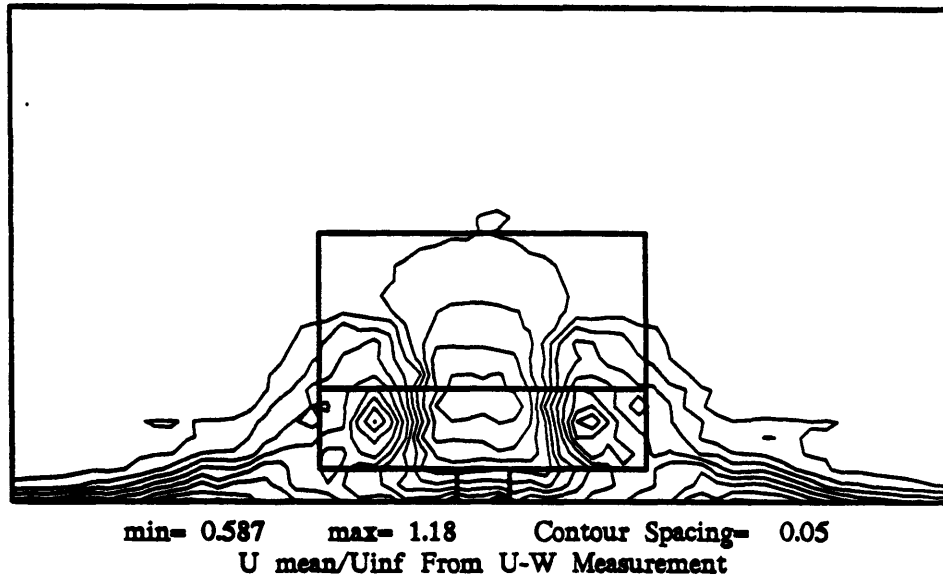
Figure 4.4: Normalized u-velocity contours from u-w measurement, X=27 cm.

30 DEGREE FASTBACK   X=54 CM
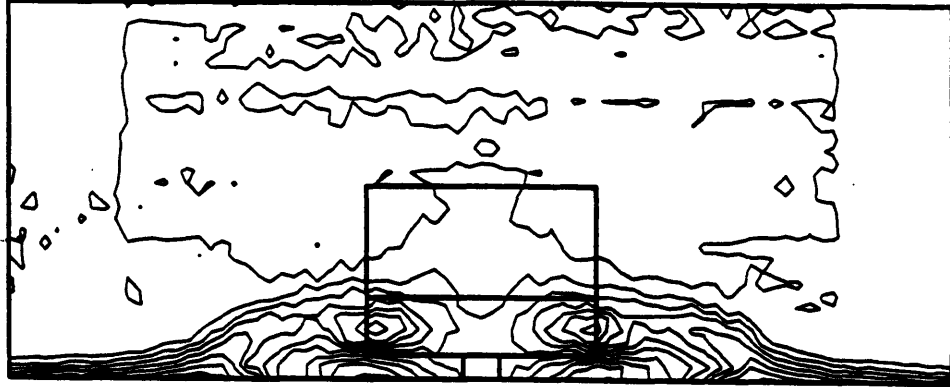
min= 0.622   max= 1.16   Contour Spacing=   0.05
U mean/Uinf From U-V Measurement

Figure 4.5: Normalized u-velocity contours from u-v measurement, X=54 cm.

30 DEGREE FASTBACK   X=54 CM
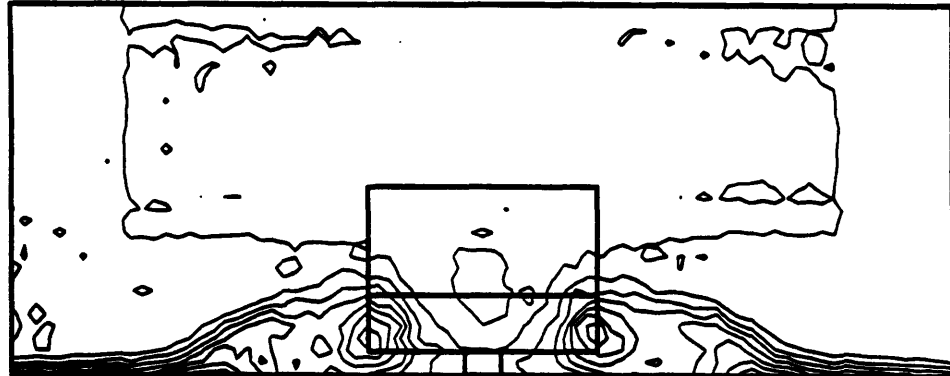
min= 0.62   max= 1.08   Contour Spacing=   0.05
U mean/Uinf From U-W Measurement

Figure 4.6: Normalized u-velocity contours from u-w measurement, X=54 cm.

94

IDEALIZED VORTEX u-VELOCITY CONTOURS
LOWEST u-VELOCITY IN CENTER OF VORTEX
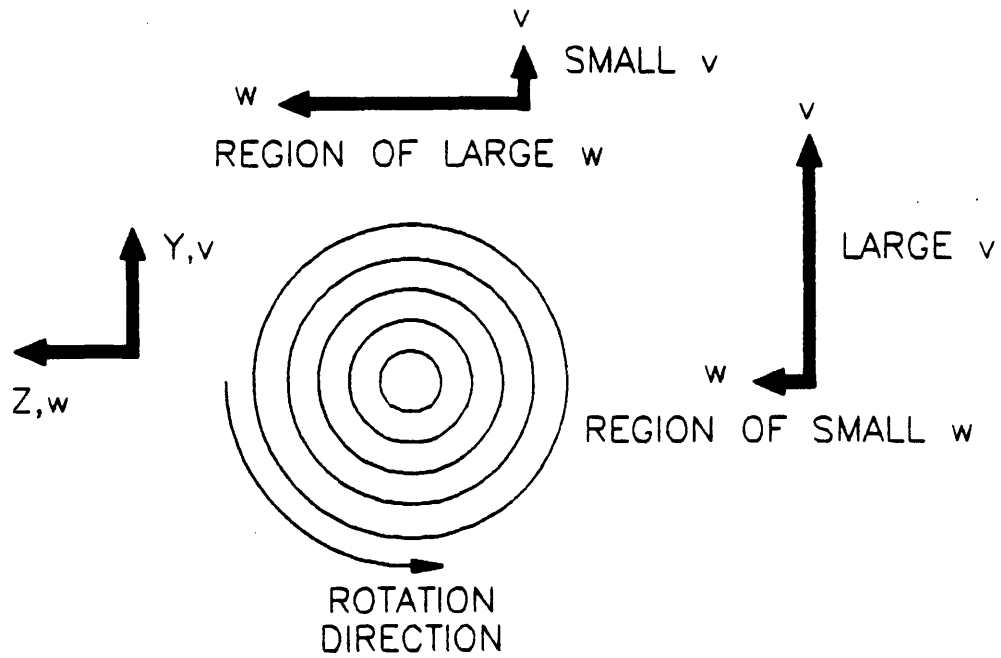
Figure 4.7: Idealized vortex u-velocity contours.

DEFORMED VORTEX CONTOURS
FROM X-PROBE MEASURING
u-v VELOCITIES
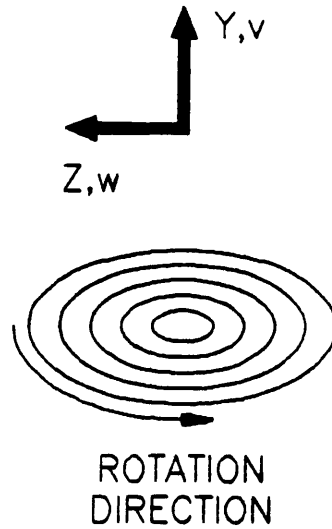
Figure 4.8: Idealized vortex showing horizontal stretching.

DEFORMED VORTEX CONTOURS
FROM X-PROBE MEASURING
u-w VELOCITIES
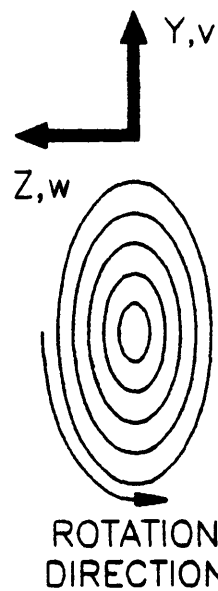
Figure 4.9: Idealized vortex showing vertical stretching.

HOT WIRE CORRECTION DATA GRID
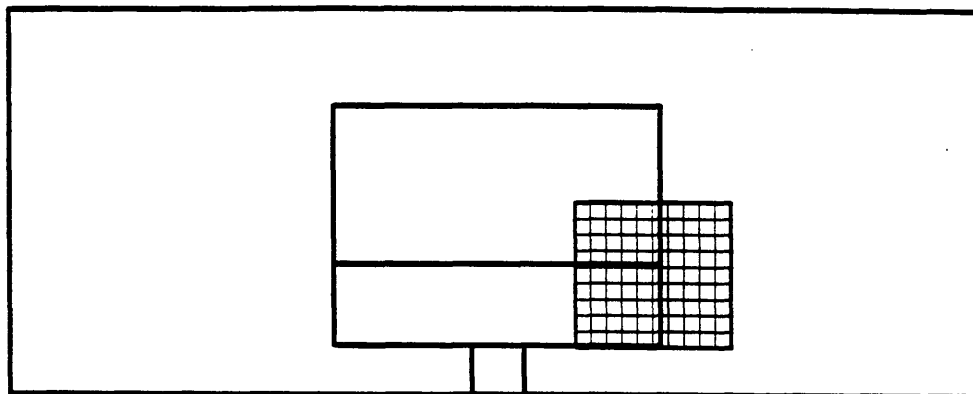
Figure 4.10: Test grid for single-wire and x-wire velocity corrections.

min= 0.626   max= 0.967   Contour Spacing= 0.05
U mean/Uinf 3-Component Measurement

min= 0.628   max= 0.976   Contour Spacing= 0.05
U mean/Uinf   Measured U-V

min= 0.646   max= 0.979   Contour Spacing= 0.05
U mean/Uinf   Measured U-W
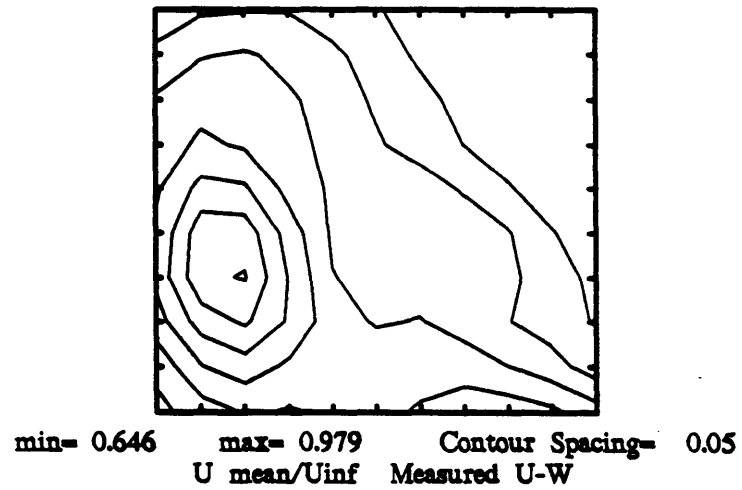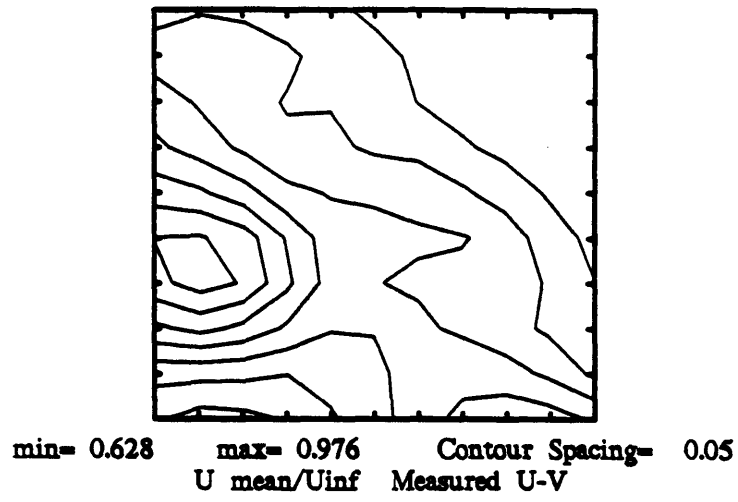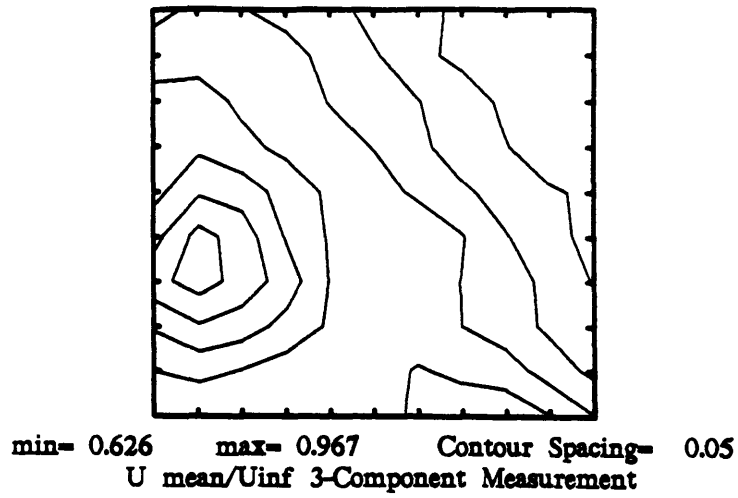
Figure 4.11: u-velocity contours for 3-component hot-film and x-wire measurments.
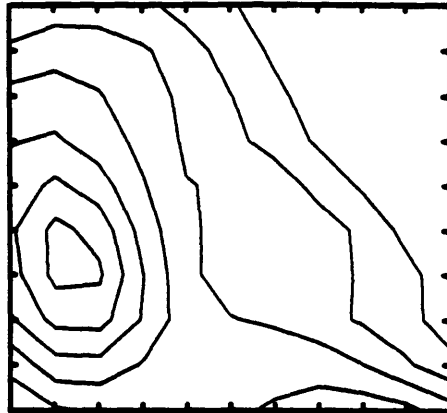
min= 0.635   max= 0.989   Contour Spacing=   0.05
U mean/Uinf   Single Wire Horizontal
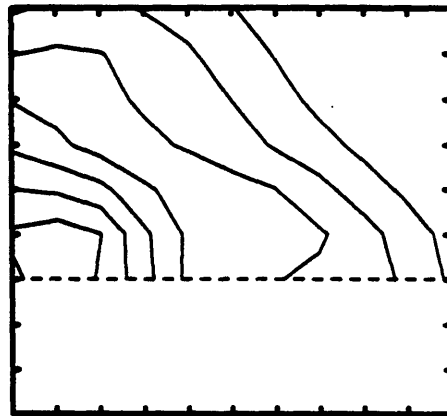
min= 0.62   max= 0.975   Contour Spacing=   0.05
U mean/Uinf   Single Wire Vertical

Figure 4.12: u-velocity contours for single-wire measurements.

min= 0.584   max= 0.985   Contour Spacing= 0.05
U mean/Uinf Corrected Horizontal Wire

min= 0.595   max= 0.973   Contour Spacing= 0.05
U mean/Uinf Corrected   Vertical Wire
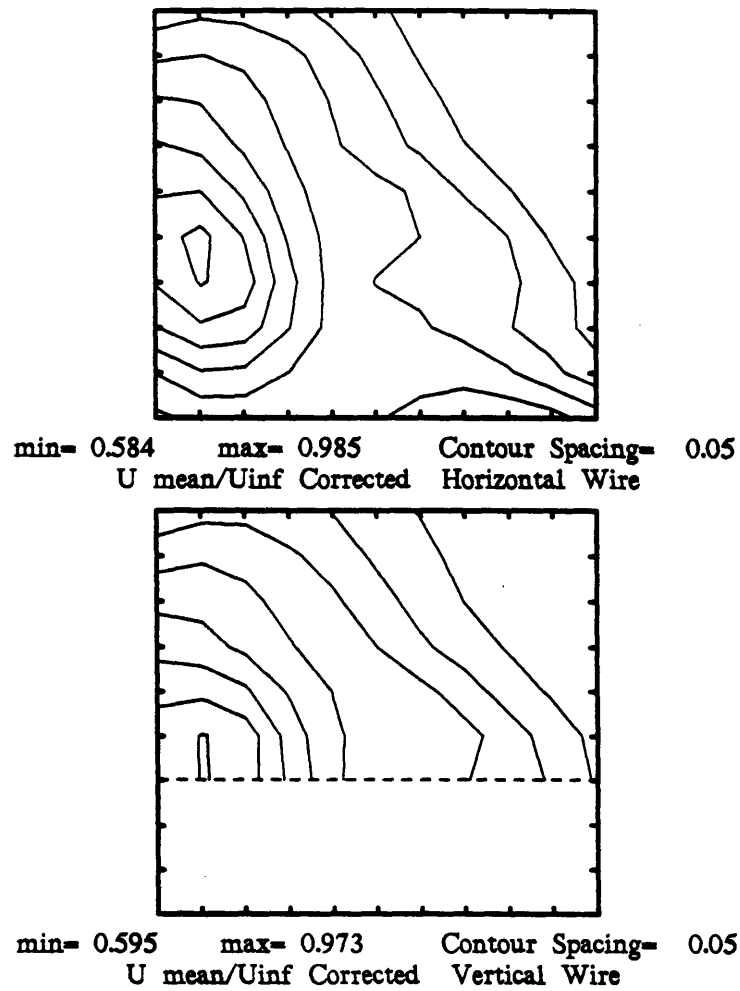
Figure 4.13: Corrected u-velocity contours for single-wire measurements.
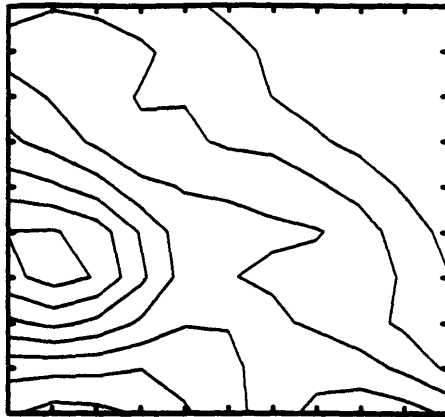
min= 0.628   max= 0.976   Contour Spacing=   0.05
U mean/Uinf   Measured U-V
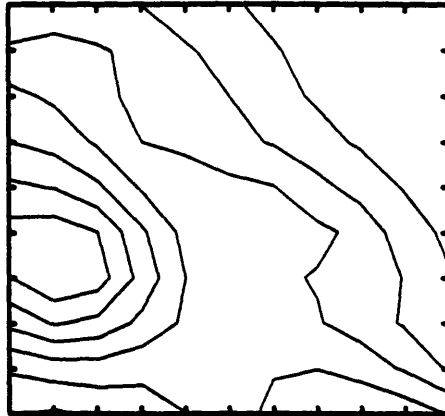
min= 0.602   max= 0.969   Contour Spacing=   0.05
U mean/Uinf   Simple Correction

min= 0.581   max= 0.969   Contour Spacing=   0.05
U mean/Uinf   Geometric Correction

Figure 4.14: Corrected u-velocity contours for u-v x-wire measurments.
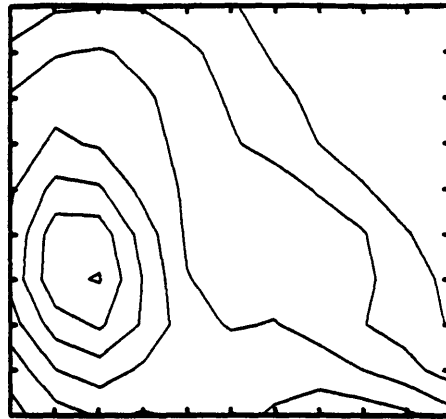
min= 0.646   max= 0.979   Contour Spacing= 0.05
U mean/Uinf   Measured U-W
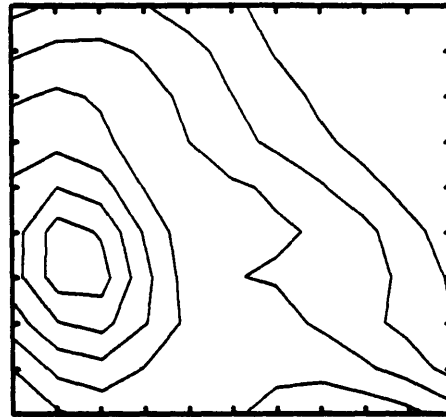
min= 0.623   max= 0.976   Contour Spacing= 0.05
U mean/Uinf   Simple Correction
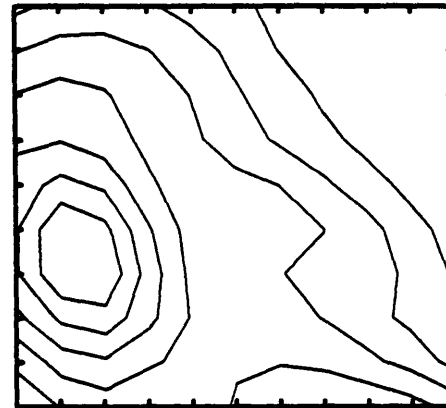
min= 0.601   max= 0.976   Contour Spacing= 0.05
U mean/Uinf   Geometric Correction

Figure 4.15: Corrected u-velocity contours for u-w x-wire measurments.
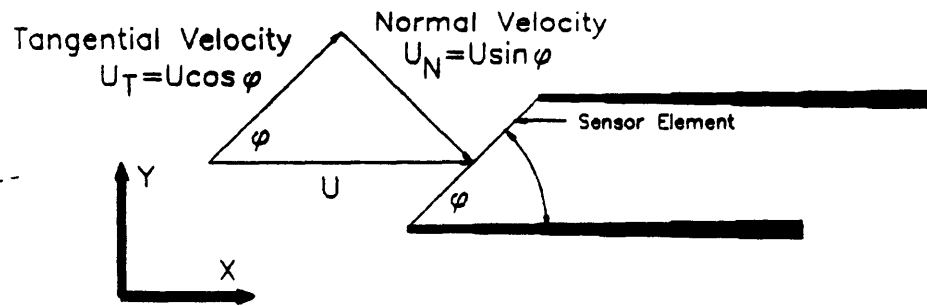
Figure 4.16: X-wire sensor and u velocity geometry.
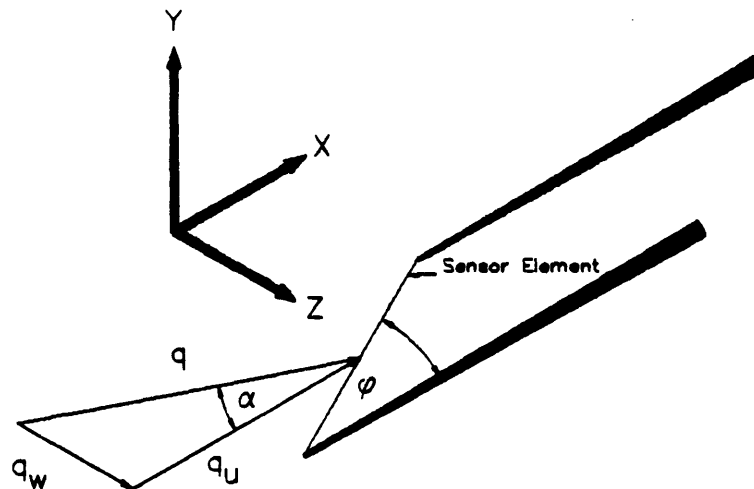
Figure 4.17: X-wire sensor and q velocity geometry.

30 DEGREE FASTBACK   X=27 CM

min= 0.579   max= 0.999   Contour Spacing=   0.05
U mean/Uinf From U-V, Corrected
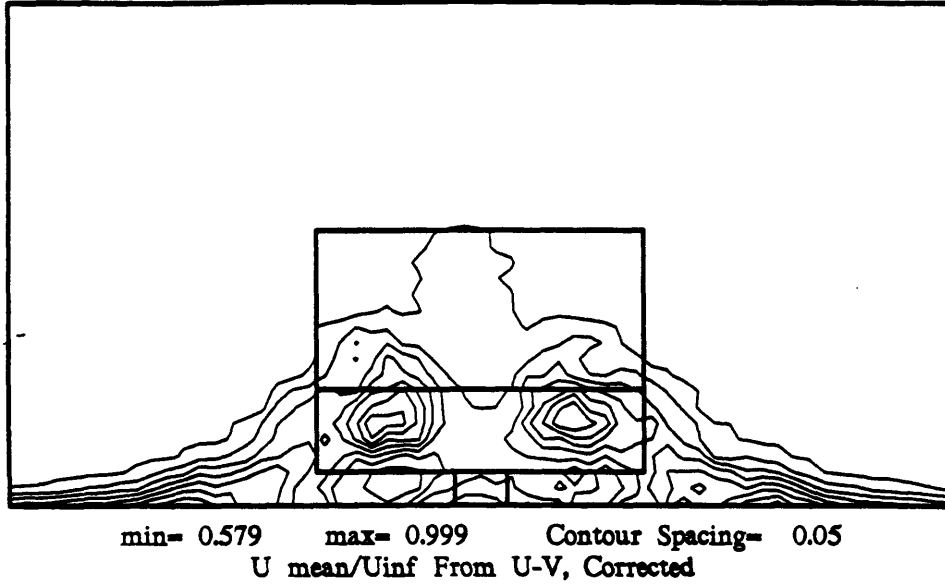
Figure 4.18: Corrected u-velocity contours from u-v measurement, X=27 cm.

30 DEGREE FASTBACK   X=27 CM

min= 0.519   max= 1.1   Contour Spacing=   0.05
U mean/Uinf From U-W, Corrected
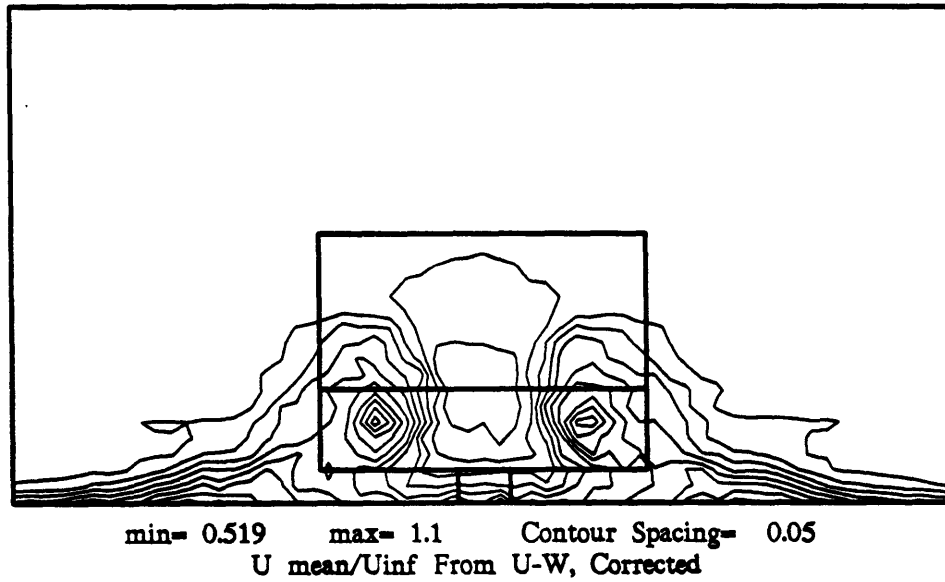
Figure 4.19: Corrected u-velocity contours from u-w measurement, X=27 cm.

30 DEGREE FASTBACK   X=27 CM
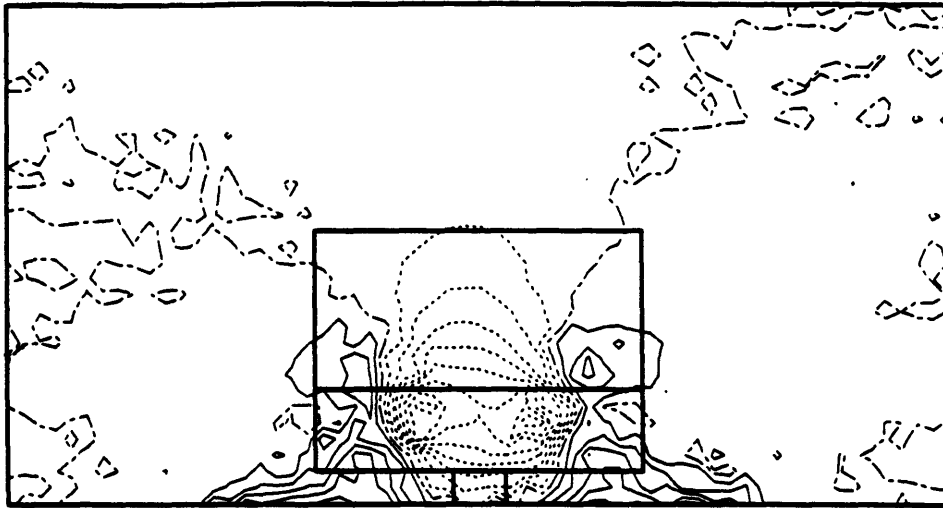
min= -44.9   max= 27.   Contour Spacing= 5.
% Difference Between Mean Velocities

Figure 4.20: Difference contours for uncorrected u-velocities.

30 DEGREE FASTBACK   X=27 CM
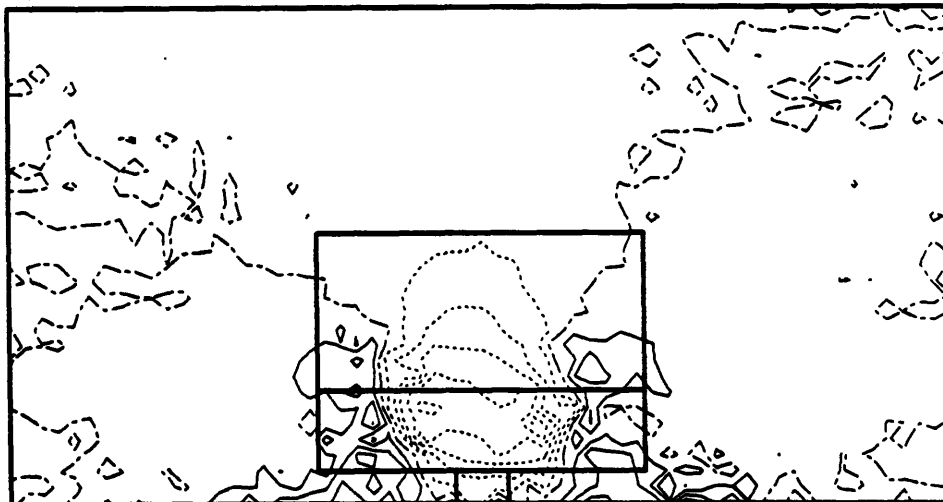
min= -31.4   max= 18.8   Contour Spacing= 5.
% Difference Between Corrected Contours

Figure 4.21: Difference contours for corrected u-velocities.

Chapter 5

Three-Component Hot-Film Wake

Measurements

Results from the three-component hot-film measurements will first be presented graphically as contour plots and crossflow velocity vectors. Next, force balance measurements and drag calculations from the wake surveys will be followed by a discussion of the results. Finally, power spectral density (PSD) characteristics from wake measurements for some of the model geometries will be presented.

5.1   Measurement Locations

Following the problems associated with x-wire measurements in the wake of the bluff body, a three component hot-film probe was then mounted on the traverse to repeat the experiments. Details of the probe's geometry, calibration, performance and use are discussed in Appendix D. Data was then taken at the same two locations as with the x-wire, at $X=27$ cm and $X=54$ cm, corresponding to 0.5 and 1.0 body lengths downstream, respectively. As seen in Figure 5.1, the data grid spanned from $Z = -30$ to $Z = +30$, and from $Y = 3$ to $Y = 21$ cm with equal horizontal and vertical spacing of one centimeter. This resulted in a total of 1159 data locations, and the same data grid was used at both plane locations. With the probe aligned parallel to the freestream

direction, the minimum vertical height of 3 cm above the groundplane was dictated by the geometry of the electrical connectors at the rear of the probe. Any distance closer to the groundplane would have caused the connectors to come in contact with the groundplane and probably destroy the probe. Three centimeters above the groundplane is same height as the bottom edge of the model.

A total of ten wake planes were recorded, two for each of the five afterbody geometries. All test were run at an airspeed of approximately 20 m/s, resulting in a Reynolds' number, based on equivalent body diameter, of 278,000. Data acquired at each gridpoint consisted of a string of 2048 readings for each sensor sampled at 25 kHz total, resulting in a sampling rate of 8.333 kHz per sensor. These real-time strings of data were stored in their entirety for post-acquisition processing. Only one set of data was taken at each gridpoint.

5.2 Graphical Results of Wake Measurements

5.2.1 Velocity Contours

Contours of the three mean and three turbulence or root mean square (RMS) velocities for each of the five model geometries are show in Figures 5.2-5.21. All of the velocity contours were normalized by the freestream velocity, U_∞. Each contour level in the figures represents a line of constant velocity, with positive velocities being solid lines, negative velocities being dotted lines, and a zero velocity contour drawn as a dot-dash line. Indicated below each contour are three values, a minimum, maximum, and the contour spacing. The minimum and maximum specify the lowest and highest

values of the velocity measured of all the data points making up the contour. Contour spacing is the change going from one contour level to the next. Since the data was normalized by the freestream velocity, contour spacing is given as a fraction of U_∞. Mean velocity contours were all plotted with a contour spacing of 0.05, or five percent of the freestream. RMS contours were plotted with a spacing of 0.02, two percent of U_∞. The model outline is shown in each contour, with the horizontal line in the middle of the body located at the height where the backlight meets the vertical base area at the rear of the model.

One note on the mean u-velocity contours and all the RMS contours: As there are no negative contours in these plots, one hase to understand the basic flow characteristics in order to make sense of them. For the mean u-velocity contours, the highest value contour is furthest from the body, being essentially at the freestream velocity, and the velocity decreases towards the center of the vortices directly behind the body. For the RMS contours the opposite is true. Away from the body the RMS contour level is close to zero and increases to its maximum values in the vortex regions directly behind the model.

The primary feature of the model wake is the existence of two large, symmetric, counterrotating vortices that are generated on the backlight along the edge separating the backlight from the vertical side of the body. As the backlight angle is increased from 20° to 32.5° certain trends become apparent from the mean velocity contours. The minimum value in the u-contours decreases and the magnitudes of the maximums and minimums of the v and w-contours increase with an increase in the backlight angle. This trend no longer holds for the v and w-velocities at a backlight angle of 35°, indicating a change in the basic structure of the wake.

As the backlight angle increases, the strength of the vortices increases until an angle is reached where the flow can no longer remain attached to the area of the backlight where the vortices are generated. At this critical angle and greater angles, the flow is separated and no longer supports the strong trailing vortices, although vorticity will still be produced. This phenomenon occurs for the current model somewhere between 32.5° and 35°.

Comparing the contours at X=27 cm (Figures 5.2-5.11) to the contours at X=54 cm (Figures 5.12-5.21) yields information concerning the path of the trailing vortices. From the mean u-velocity contours, it can be seen that as one moves further downstream from the model the cores of the vortices spread out away from each other horizontally (in the Z-direction) and descend towards the groundplane.

The RMS velocity contours are particularly interesting in the similarities between the u, v, and w-contours for each fastback angle. While not identical, the high degree of similarity in the u, v, and w RMS contours indicates that the turbulence is highly isotropic, and would lead one to expect that the terms involving the unsteady quantities in Landahl's drag equation (Eqn.2.15) would be only a small percentage of the total drag. This will be seen shortly.

For the cases up to and including 32.5°, the RMS contours clearly show the distinct vortices and the symmetry between them, at both plane locations. But, at X=27 cm, the vortices are less defined as separate entities in the 35° fastback RMS contours and disappear completely in the X=54 cm RMS contours. This is another indication that the basic structure of the flow field has changed as the fastback angle was increased from 32.5° to 35°.

5.2.2 Crossflow Velocity Vectors

Crossflow velocity vectors are also useful in visualizing the flow field characteristics in the plane of a wake traverse. The crossflow velocity is defined as

$$\overline{V}_{crossflow} = \sqrt{\overline{v}^2 + \overline{w}^2} \tag{5.1}$$

and the crossflow angle is defined as

$$\theta_{crossflow} = \tan^{-1}\frac{\overline{v}}{\overline{w}} \tag{5.2}$$

Figures 5.22-5.25 show the crossflow vectors for all five fastback angles at both data-plane locations. Again, note the symmetry of the vortices in all the cases.

Relative strength of the trailing vortices can be seen from the plots of crossflow velocities be studying the range of influence of the vortices on the flow outside of the vortex core. The 20° fastback shows the smallest effect of the vortices on the outer flow and on the downward flow between the vortices. As the fastback angle increases, so does the effect of the vortices.

While the 27.5° and 30° fastback display great similarity, the velocity vectors between the vortices are greater for the larger angle, indicating stronger vortices. As expected, the 32.5° fastback's vortices appear to be the strongest with more flow curvature near the center of the vortex cores than compared to the lower fastback angles. The 35° fastback also shows signs of trailing vortices, yet much weaker than the 32.5° fastback, indicative of the change in flow structure between the two cases.

The previous discussion concerning the path of the vortices as they move downstream can be reinforced from the crossflow velocity plots. By comparing the X=27 cm and

the X=54 cm crossflow vectors, it is clear once again that the vortex cores move closer to the groundplane and further apart laterally as they move downstream.

5.2.3   Regions of Suspect Data

As mentioned in Appendix D, the performance of the probe, in particular, measuring the v-velocity, is not completely predictable when the pitch angle is less than an angle of $-15°$. Therefore, any data location where this limit was exceeded was considered to be suspect and not taken as a totally accurate measure of the local flow velocities. While not all the wake planes measured contained suspect data, it is necessary to point out the cases where there was some questions in the validity of the data before continuing with further discussions. It should also be noted that some, if not most of the suspect data, could have been more accurate had the probe been offset at an initial pitch angle of $-15°$, as mentioned in Appendix D. This was not learned until after the data was acquired.

Figures 5.26 and 5.27 show the regions of suspect data for the eight planes. Each marker on the grids represents a data location where the pitch angle was less than $-15°$. The suspect areas essentially lie in the central region of the wake between the trailing vortices. Basically what happens is that in the region between the counter- rotating vortices the crossflow velocity vector is dominated by the v-component, and since there is a u-velocity deficit in this area, the pitch angle is large.

All five fastback geometries have regions of suspect data in the close data plane, at X=27 cm. Downstream, at X=54 cm, the 20° and 35° fastback models do not show any regions of high negative pitch angles, and the other geometries show only a few suspect

points. Larger areas of suspect data for the three middle fastback angles, 27.5°, 30°, and 32.5°, were expected due to the stronger vortices developed by these geometries.

The impact of the suspect data on the velocity contours is apparent in the v-velocity contours. For the X=27 cm contours (Figs. 5.2, 5.4, 5.6, 5.8, and 5.10), the v-contours are deformed slightly in the regions of the suspect data, as indicated by the squaring-off of the negative contours between the vortices. From the downstream measurements (Figs.5.12, 5.14, 5.16, 5.18, and 5.20), this squaring off of the contours is not visible at all, indicating that the flow field further downstream has smaller negative pitch angles, and fewer points of concern.

Based on the above information, one must be selective in choosing regions of the flow to analyze in the time domain so as to avoid the locations of suspect data.

5.3   Force Measurements and Drag Calculations From Wake Surveys

5.3.1   Force Balance Results

Lift and drag were measured with the force balance in the model for each of the model configurations. Design and use of the force balance is detailed in Appendix A. Drag and lift coefficients, given by Equations 5.3 and 5.4, were calculated and plotted as a function of backlight angle in Figures 5.28 and 5.29. Five measurements for each model configuration are plotted.

$$C_l = \frac{L_{measured}}{\frac{1}{2}\rho U_\infty^2 S_{body}} \tag{5.3}$$

112

$$C_d = \frac{D_{measured}}{\frac{1}{2}\rho U_\infty^2 S_{body}} \tag{5.4}$$

In the above equations $L_{measured}$ is the measured lift, $D_{measured}$ is the measured drag, and S_{body} is the cross-sectional area of the model. Repeatability of the force measurements was better than $\pm 1\%$ for both lift and drag.

Drag increases with backlight angle up the 32.5°, as seen in Figure 5.28, then decreases dramatically at 35°. The lift curve (Fig.5.29) increases with backlight angle up to 30°, drops off slightly at 32.5°, then falls considerably at 35°. To understand what was happening in the flow field on and around the backlight as the angle was increased, tufts were attached to the backlight and to a stick to probe away from the surface.

At 20°, the flow over the backlight is attached in the region between the vortices. At 27.5° and 30°, small regions of separation on the backlight were detected between the vortices, and at 32.5°, practically the entire backlight area between the vortices had reversed, separated flow. This separation bubble was closed and did not continue downstream, looking identical to Ahmed's high drag configuration discussed in Chapter 1 (Fig.1.5). This large area of separated flow causes an increase in the streamwise force (drag), yet results in a net decrease in the lift force when compared to the 30° fastback, which does not have such a large separated region. Tufts on the 35° fastback showed the entire backlight flow to be separated, except right near the side edges, where very weak vortices were being generated. The flow behind the 35° fastback was then quite different from the other geometries.

5.3.2 Drag Calculations From Wake Surveys

Landahl's equation for total drag from Chapter 2, modified for use with finite wake traverses (Eqn.2.26), was calculated for each model configuration at both wake data locations. Form drag (Eqn.2.29) and vortex drag contributions (Eqn.2.28 to the total were also calculated. All the values have been normalized by $\frac{1}{2}\rho U_\infty^2 S_{body}$. The results are presented as in tabular form in Table 5.1 and graphically in Figures 5.30 and5.31, where the drag coeffecients are plotted as a function of backlight angle. The measured drag coefficients are plotted along with the calculated total drag coefficients in Figure 5.30. Tabular results include the actual drag coefficient, calculated drag coefficient with the percentage error from actual, the form drag and vortex drag contributions to the total drag, and their percentage of the total drag.

Drag predictions range from the largest error, 40%, for the 20° fastback at X=27 cm, to the lowest error of 0% for the 27.5° fastback at X=27 cm, with the estimations at X=27 cm consistently higher than those at X=54 cm. The best average estimations of drag are for the two intermediate backlight angles of 27.5° and 30° with errors of 0% and 1.9% at X=27 cm and -9.8% and -10.6% at X=54 cm. Also, the 35° fastback showed similar agreement, with errors of 11.8% and 0.8% at X=27 and X=54 cm, respectively. The 32.5° fastback showed the most consistent errors, be they somewhat larger than the aforementioned backlights, at -14% and -18.3%.

With regards to the maximum error, the 20° fastback at X=27 cm, the most likely explanation was the inability to measure closer than 3 cm from the groundplane. In the cases of the four fastbacks greater than 20°, the trailing vortices are much closer to the groundplane than for the 20° at $X = 27 cm$, so there is more influence on the underbody

flow and the boundary layer on the groundplane by the trailing vortices. One would expect to find velocities higher than the freestream velocity in this region due to the compressing of the streamlines as the fluid moves under the body, particularly for the 20° fastback, as its vortices have less influence on this flow. If this higher velocity fluid were to be taken into the drag integral, the resulting drag would be lower. Further downstream, the growing boundary layer on the groundplane will cause an additional momentum deficit, that, if it were possible to measure closer to the groundplane, would result in drag estimations higher than measured. This effect was not seen in the current measurements due to the inability to measure close to the ground plane.

Drag is broken down into its form and vortex drag components in Figure 5.31 and in Table 5.1. Form drag, given by Equation 2.29, is the dominant term of the total drag, varying from about 80% to 95% for the various geometries. Vortex drag, given by Equation 2.28, varied from about 5% of the total drag for the 35° fastback to about 21% for the 32.5° fastback. As expected, the vortex drag increased with increasing fastback angle, and then decreased after 32.5°. For the three middle angles, 27.5°, 30°, and 32.5°, the vortex drag stayed between 16% and 21% of the total, indicating that the flow field geometry for these three backlights was similar. The form drag from the X=54 cm measurements increased monotonically with backlight angle, but was not as well behaved for the X=27 cm measurements. Once again, this can be attributed to the inability to measure close to the groundplane, particularly, close to the model where the underbody flow plays an important part in the developing wake.

Form drag (Eqn.2.29) is a combination of mean flow quantities and unsteady (RMS) quantities. As mentioned in Chapter 2, one of the shortcomings of measuring wakes with pressure probes is the lack of turbulence information. With hot-film measurements, this

information is readily available. It then becomes important to determine the effects of the unsteady components of velocity on the calculated drag. The contributions of the total of the mean terms and the total of the RMS terms to the total form drag using Equation 2.29 are compiled in Table 5.2. Also given is the RMS percentage of the total drag. The individual mean velocity terms ($U_\infty \overline{u}$, and $-\overline{u}^2$) are shown graphically in Figure 5.32, while the RMS terms ($-\overline{u'^2}$, $\frac{1}{2}\overline{v'^2}$, and $\frac{1}{2}\overline{w'^2}$) are plotted in Figure 5.33.

The fraction of the form drag related to the RMS terms is quite small, ranging from 0.8% to 4.4%, almost constant for all the model geometries at both measurement locations. This concurs with the earlier observations regarding the similarities between the RMS velocity contours of the three velocity components, meaning that the turbulence in the wake is either very weak or essentially isotropic. If the wake were truly isotropic, the RMS contribution to the drag would be zero. With regards to the total drag, the RMS contribution varies from 0.8% to 3.9%, as seen in the last column of Table 5.2. Therefore, if one were to measure only pressures in the wakes of fastback models between the X-locations used in this study, one would expect that calculations of the drag integral using only mean velocities would vary no more than 4% from the actual drag due to the exclusion of the turbulence information.

Vortex drag contribution to the total drag from the previously reported results discussed in Chapter 2 are shown in Table 5.3. Direct comparison with the current results is not really a fair comparison due to the variety of the model configurations in the comparisons. What can be said is that the current results show vortex drag to vary between 5% and 21% of the total drag, while the previous results in Table 5.3 show variations of vortex drag contribution between 1% and 44% of the total drag.

116

5.3.3 The Effect Of Streamwise Derivatives On Drag Calculations

The development of Landahl's method was based on one crucial assumption, that the flow reaches an approximate equilibrium at some downstream location so that the streamwise derivatives change slowly with streamwise distance. As a result of this assumption, two terms from Equation 2.13 were ignored, $-z\,(\overline{uw})_x$ and $-y\,(\overline{uv})_x$. If indeed these integrals are not small, the calculated drag will be incorrect.

Since data was taken at two downstream locations, an estimation of these streamwise derivatives was possible. The derivatives were calculated and the non-dimensionalized results are shown in Table 5.4, along with the adjusted drag coeffficients and the percent change in drag due to the derivative terms. Of primary importance is that the two geometries with the weakest vorticity, the 20° and 35° fastbacks, showed the largest effect from the streamwise derivatives, ranging from a 16% to 21% decrease in the estimated drag. The middle fastback angles, with the strongest vortices, 27.5°, 30° and 32.5°, showed less effect from the derivative terms, with the maximum change in drag of only 7%. The indication is that there is less change in the streamwise derivatives when there is strong, organized vorticity present in the wake. Also, this exercise again indicates that there important information missing from the data in the region close to the groundplane which would cause the drag estimates to be higher.

5.4 Selected Power Spectra

A secondary consequence of the hot-film wake measurements was the availability of real-time data for limited spectral analysis. Limited in the sense that there was only

one ensemble of data available at each data point, consisting of a string of 2048 events sampled at a rate of 8.333 KHz. The period of sampling lasted for a total of 0.245 seconds, and represents only a snapshot of the flow behavior at a given location for that time period. The minimum resolved frequency was 4.07 Hz, or a wavelength of 4.9m. While it would be necessary to take many ensembles of data to accurately resolve all the frequency components in the flow field, that was beyond the scope of this research. Be that as it may, some useful information can be found from the limited data available.

Power spectral densities of each of the three velocity components were calculated at various locations in the flow field using the following approach. First, the average velocity from the string of 2048 velocities was subtracted from each sample. Then, the data string multiplied by a sine wave type windowing function to reduce leakage from distant frequencies. Windowing data is a standard procedure to remove some of the effects of having a finite length data string. The window function consisted of a rising quarter sine wave for the first 10% of the data string, a value of 1 for the next 80% of the data string, and a falling quarter sine wave for the last 10% of the data string, as depicted in Figure 5.34. After windowing the data, an FFT was performed on the string, and a power spectrum distribution was calculated form the Fourier coefficients. The power spectrum was normalized so that the integral of the power spectrum equaled the square of the RMS of the windowed data.

Two locations in the wake were chosen for investigation, the first near the cores of the trailing vortices, where tie fluctuations are the highest, and on the centerline of the model, between the vortices, to determine if any effects of the separation bubble on the backlight were being carried downstream.

The majority of the energy of the fluctuations for all the data locations investigated

appeared at frequencies below 300 Hz, so the data is presented with this upper frequency limit. Results for the 20° and 27.5° fastbacks were unclear, due to a large number of peaks of low amplitude in the signals at the points of interest.

Power spectra from the 30° fastback vortex cores are shown in Figures 5.35-5.38. Figures 5.35 and 5.36 are from the left and right-hand side vortex cores looking upstream, at X=27 cm. Figures 5.37 and 5.38 are from the left and right-hand side vortex cores at X=54 cm. The top graph is the u-velocity power spectrum, the middle graph is the v-velocity spectrum, and the bottom graph is the w-velocity spectrum. Spectra at the same wake plane location are plotted to the same vertical scale to ease comparisons. At X=27 cm, the largest peak in the u-velocity occurs at 50 Hz in the left vortex (Fig.5.35) while at 100 Hz in the right vortex (Fig.5.36). These frequencies correspond to wavelengths of 0.4 meters and 0.2 meters respectively, and can be compared with one of the two primary physical scales of the flow, the width of the model, 0.21 m. Comparison of the v spectra shows corresponding peaks at about 37 Hz and 74 Hz. 37 Hz corresponds to a wavelength of 0.54 meters, the same as the other physical scale, the 0.54 meter model length. The v spectra also demonstrate the problem of having just a single ensemble of data for the power spectra. The left vortex has a large peak at a frequency of 4.06 Hz, the minimum resolvable frequency, while the right vortex shows little activity at the low frequencies, indicating that each spectrum is not a full representation of the fluctuations. Similarities in the downstream spectra for the 30° fastback abound, with multiple peaks around 50 Hz and 100 Hz (Figs.5.37 and 5.38).

Spectra from the vortex cores of the 32.5° fastback display many of the same peaks as the 30° fastback, as seen in Figures 5.39-5.42. Compared to the X=27 cm spectra for the 30° fastback, there is generally more activity below 50 Hz in the 32.5° spectra

(Figs.5.39 and 5.40). One would expect there to be more low frequency fluctuations for the 32.5° fastback, as there is a substantially larger area of separated flow on the backlight between the forming vortices compared to the 30° fastback.

For the 35° fastback, the power spectra in the region of the vortex cores showed fewer distinct peaks, with those near 50 Hz being the most dominant. Figures 5.43-5.46 are typical of the spectra from this geometry. The existence of fewer primary peaks indicates that the fluctuations are much more coherent than for the other backlight angle. Remember from the velocity contours and the crossflow velocity vectors that the vortices of the 35° fastback were much weaker and that flow field near the backlight had much greater separation the than the other fastbacks. Therefore, one would expect to see more fluctuating activity in the region between the vortices. Figures 5.47 and 5.48 show two typical power spectra on the centerline between the vortices at $X=27$ cm and $X=54$ cm. The peaks are more numerous than for the vortex cores, yet, activity is still high around 37, 50 and 75 Hz. As the 35° fastback has a substantially different flow field near the backlight, it could prove beneficial to make more detailed measurements in this area behind the separated region to help better understand the the mechanisms by which the flow structure has changed going from the 32.5° backlight to the 35° backlight.

3-COMPONENT PROBE DATA PLANE
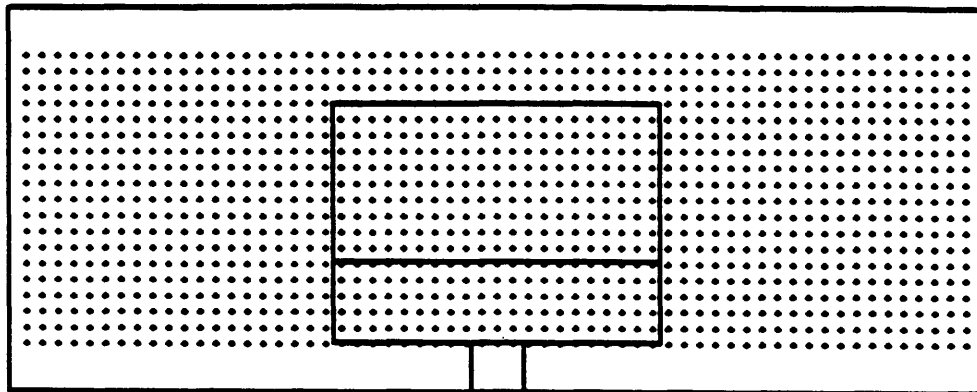
Figure 5.1: Wake plane data locations for three-component hot-film measurements.

20 DEGREE FASTBACK   X=27 CM
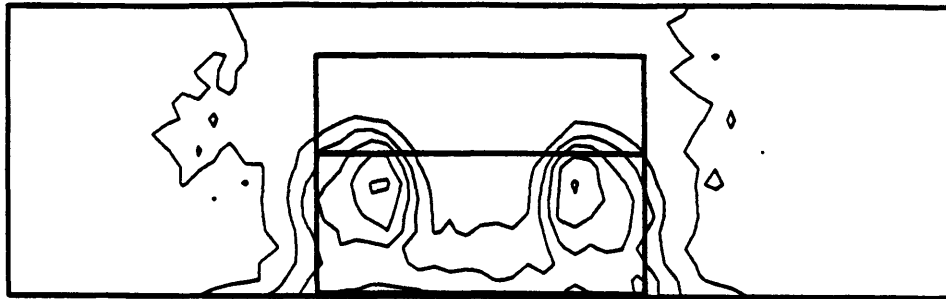
min= 0.691   max= 1.   Contour Spacing=   0.05
U mean/Uinf

20 DEGREE FASTBACK   X=27 CM
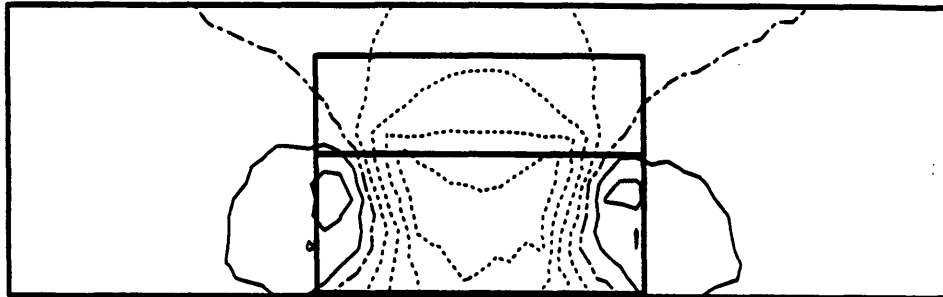
min= -0.243   max= 0.134   Contour Spacing=   0.05
V mean/Uinf

20 DEGREE FASTBACK   X=27 CM
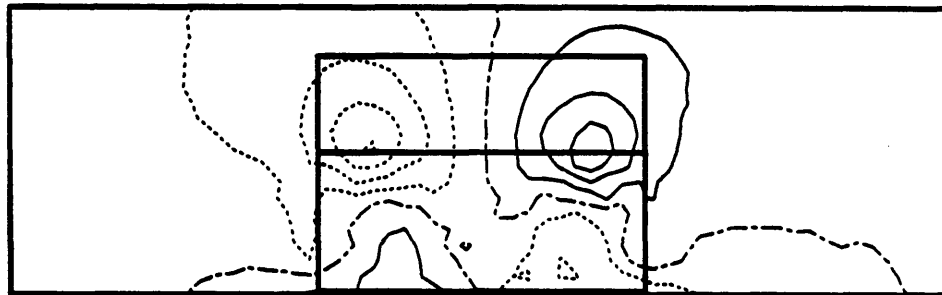
min= -0.202   max= 0.181   Contour Spacing=   0.05
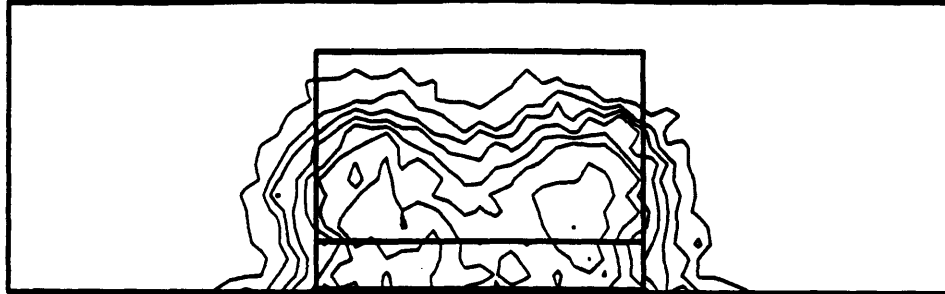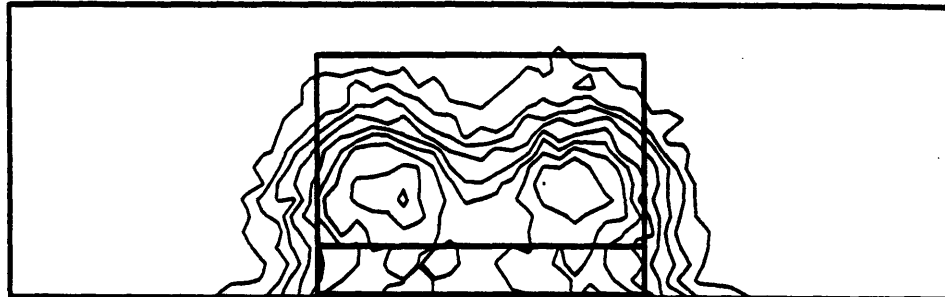W mean/Uinf

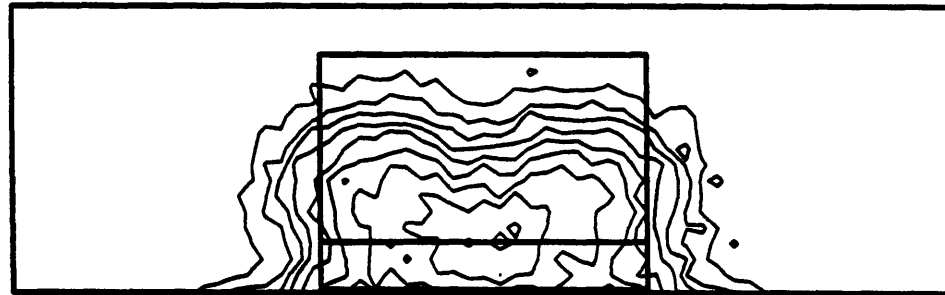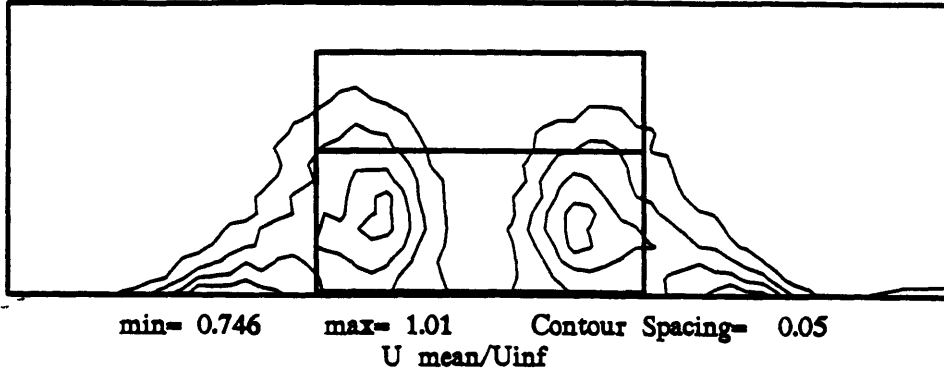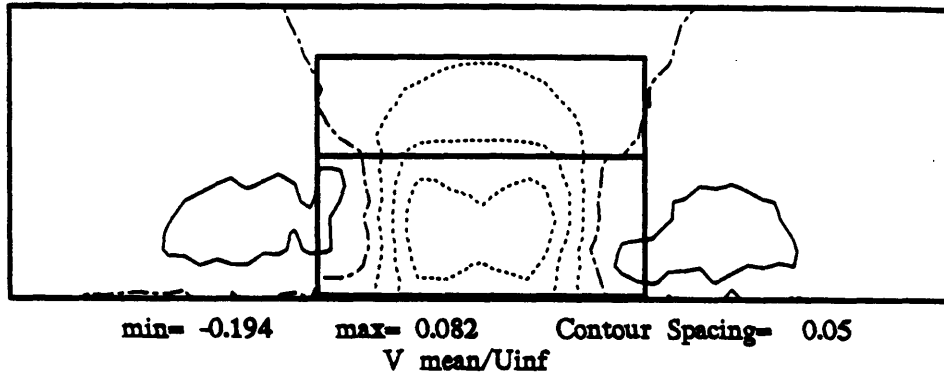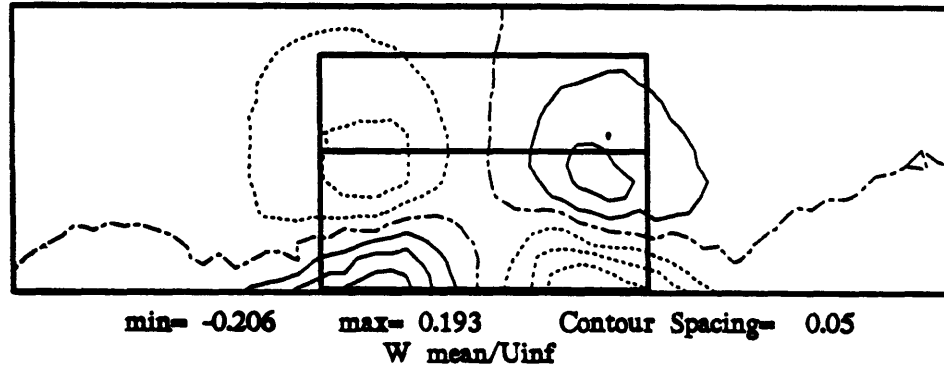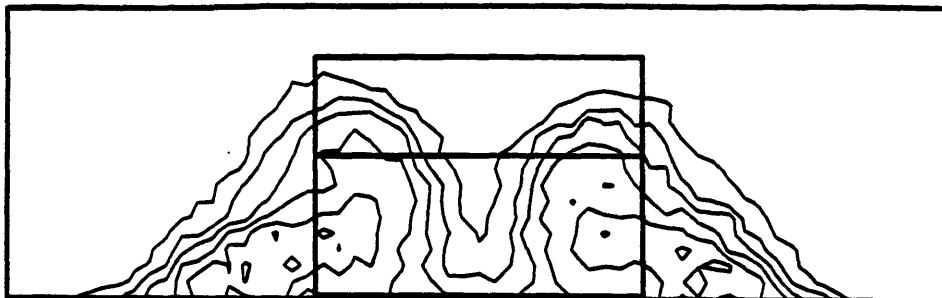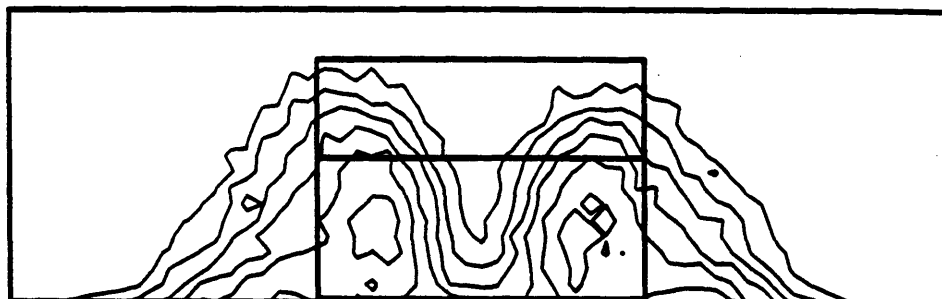Figure 5.2: 20° fastback mean velocity contours, X=27 cm.
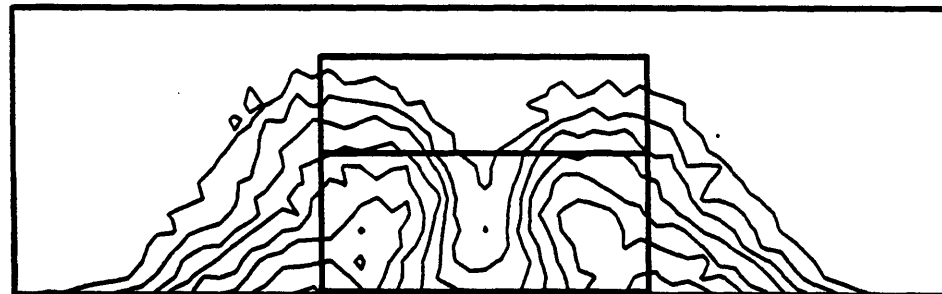
20 DEGREE FASTBACK   X=27 CM
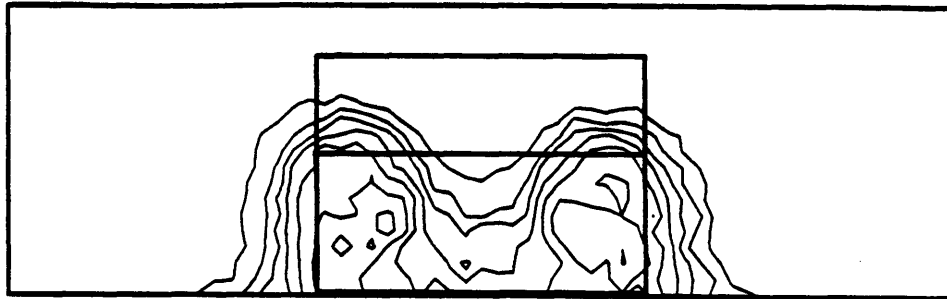
min= 0.002   max= 0.153   Contour Spacing= 0.02
U rms/Uinf

20 DEGREE FASTBACK   X=27 CM
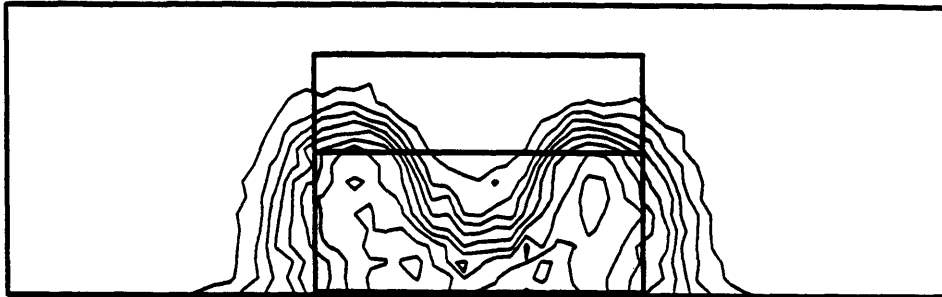
min= 0.003   max= 0.188   Contour Spacing= 0.02
V rms/Uinf
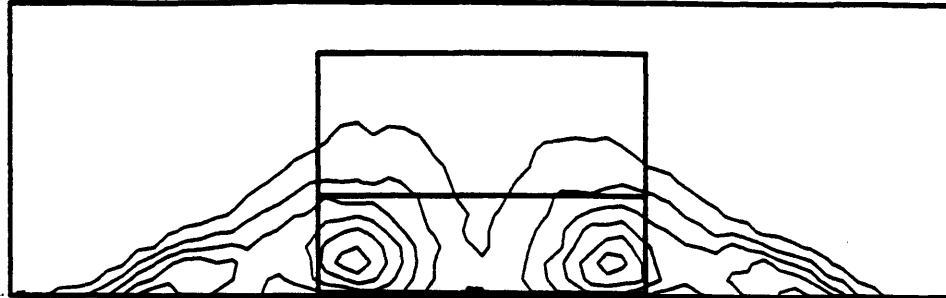
20 DEGREE FASTBACK   X=27 CM
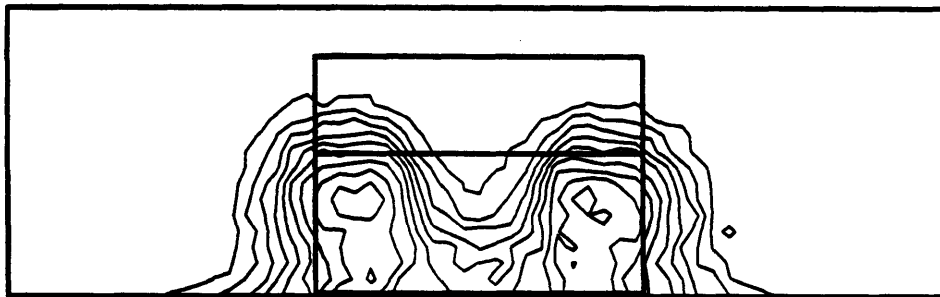
min= 0.003   max= 0.198   Contour Spacing= 0.02
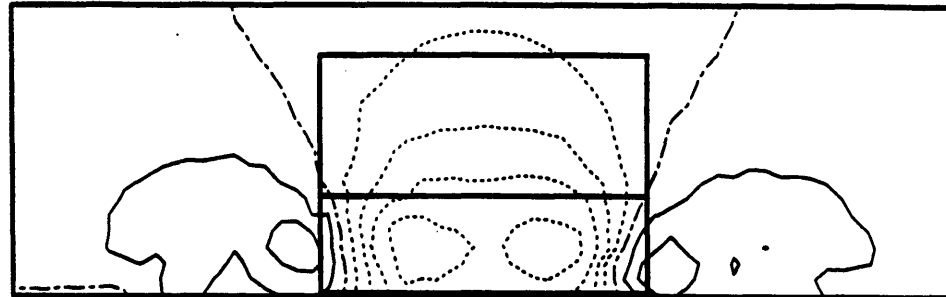W rms/Uinf

Figure 5.3: 20° fastback RMS velocity contours, X=27 cm.

123

27.5 DEGREE FASTBACK   X=27 CM
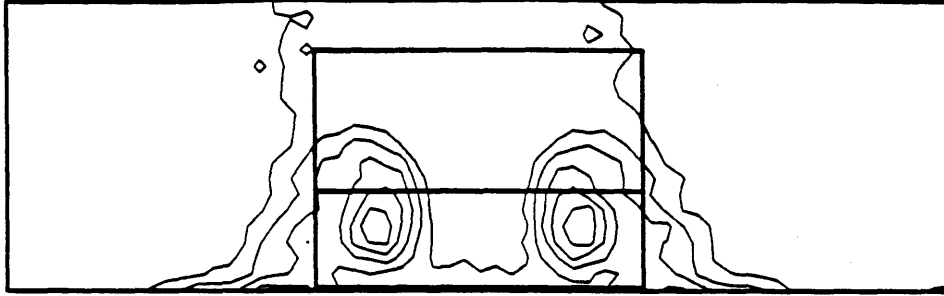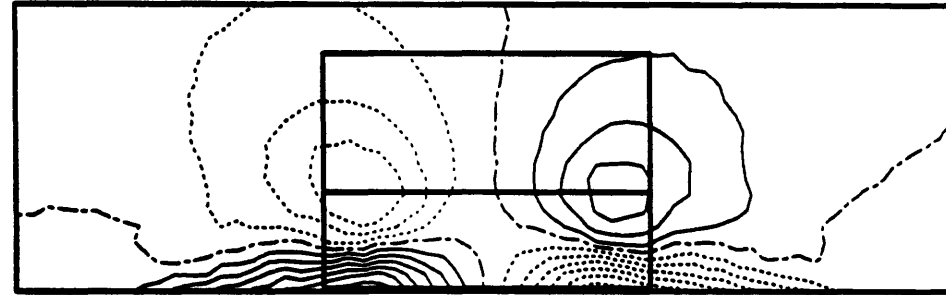

min= 0.651   max= 1.   Contour Spacing= 0.05

U mean/Uinf

27.5 DEGREE FASTBACK   X=27 CM
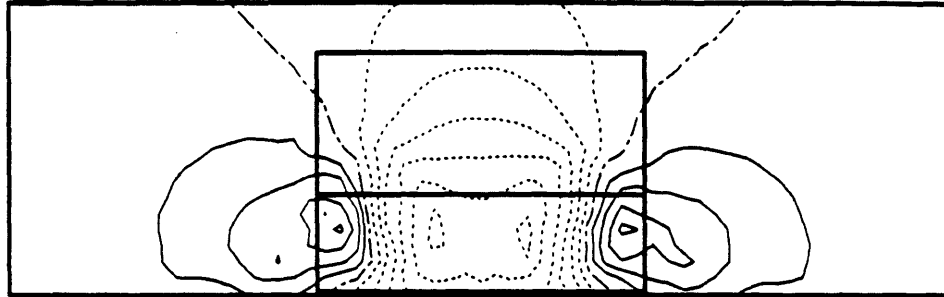
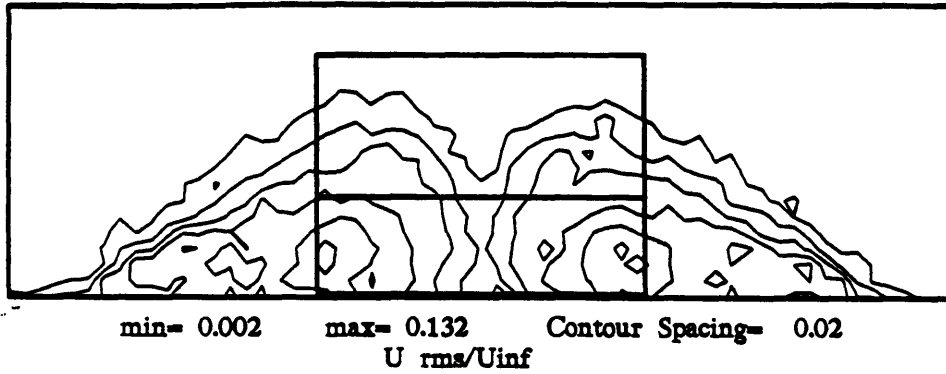min= -0.319   max= 0.215   Contour Spacing= 0.05

V mean/Uinf

27.5 DEGREE FASTBACK   X=27 CM
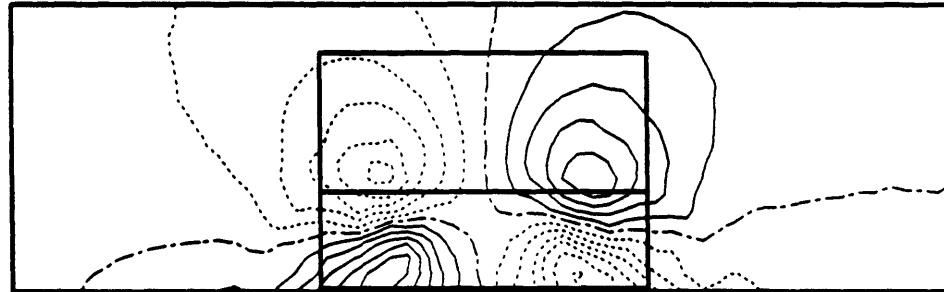
min= -0.308   max= 0.294   Contour Spacing= 0.05

W mean/Uinf

Figure 5.4: 27.5° fastback mean velocity contours, X=27 cm.

124

27.5 DEGREE FASTBACK   X=27 CM
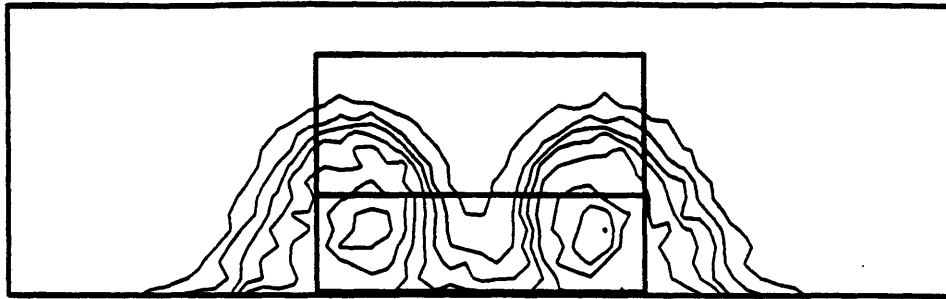
min= 0.002   max= 0.161   Contour Spacing=   0.02

U rms/Uinf

27.5 DEGREE FASTBACK   X=27 CM
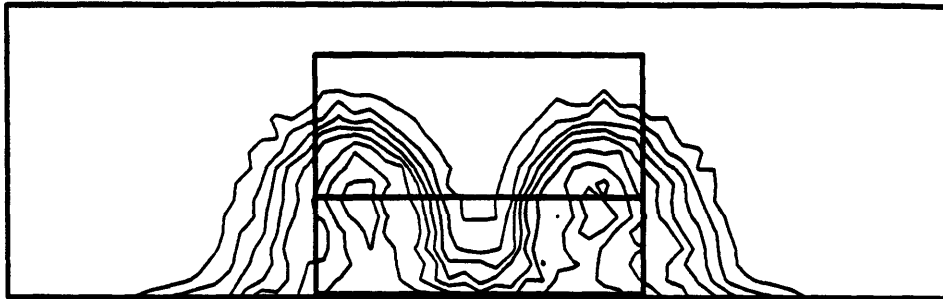
min= 0.003   max= 0.179   Contour Spacing=   0.02

V rms/Uinf

27.5 DEGREE FASTBACK   X=27 CM

min= 0.004   max= 0.196   Contour Spacing=   0.02

W rms/Uinf

Figure 5.5: 27.5° fastback RMS velocity contours, X=27 cm.

30 DEGREE FASTBACK   X=27 CM

min= 0.592   max= 0.993   Contour Spacing= 0.05
U mean/Uinf

30 DEGREE FASTBACK   X=27 CM

min= -0.326   max= 0.208   Contour Spacing= 0.05
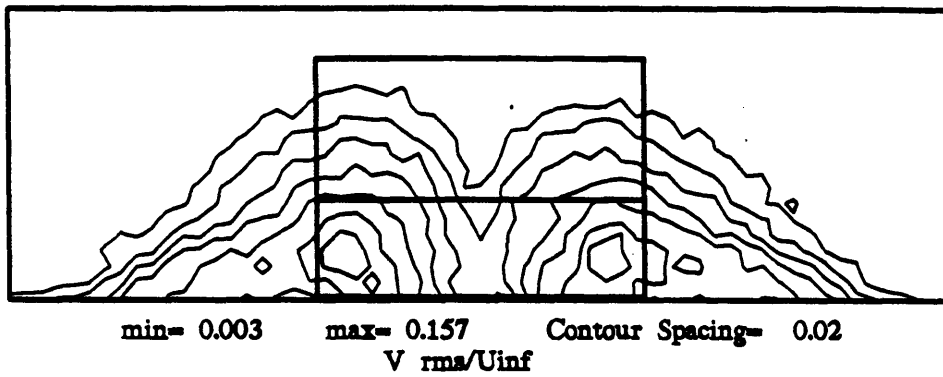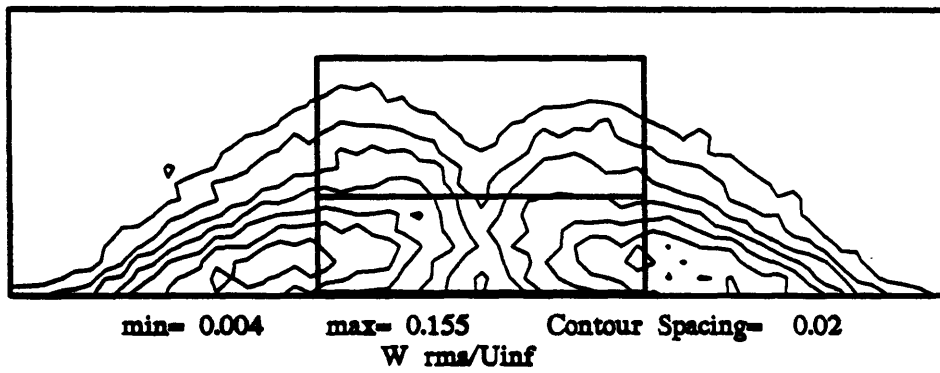V mean/Uinf

30 DEGREE FASTBACK   X=27 CM

min= -0.352   max= 0.319   Contour Spacing= 0.05
W mean/Uinf
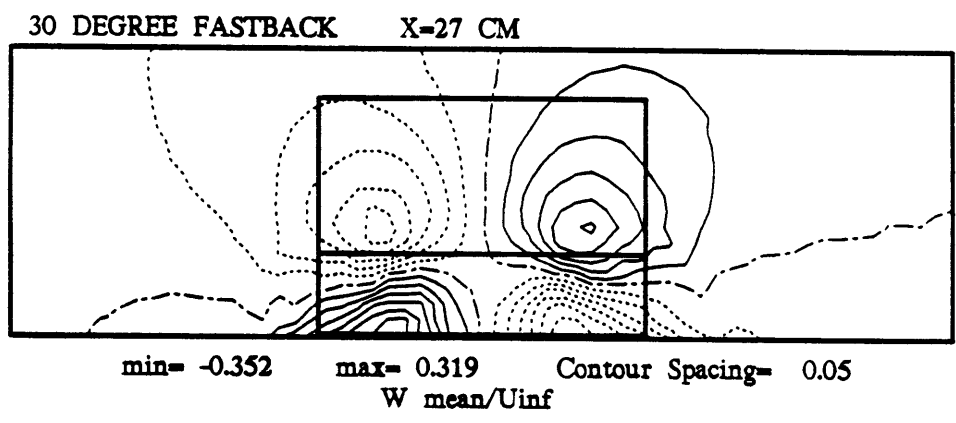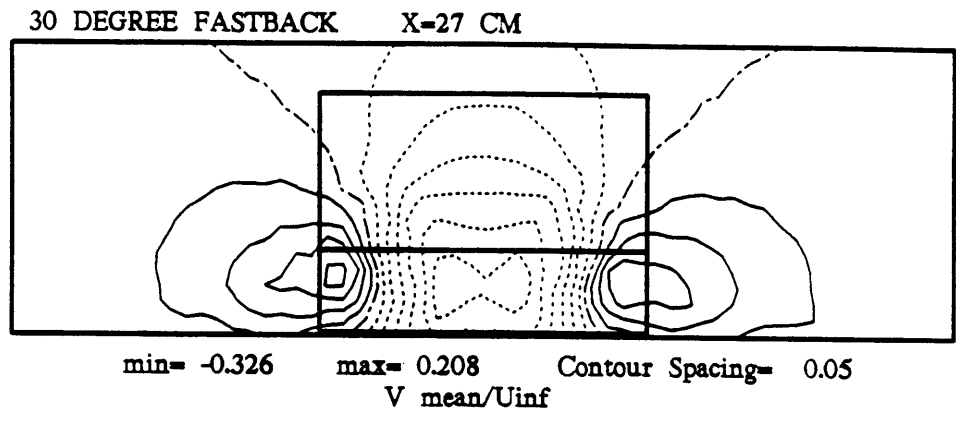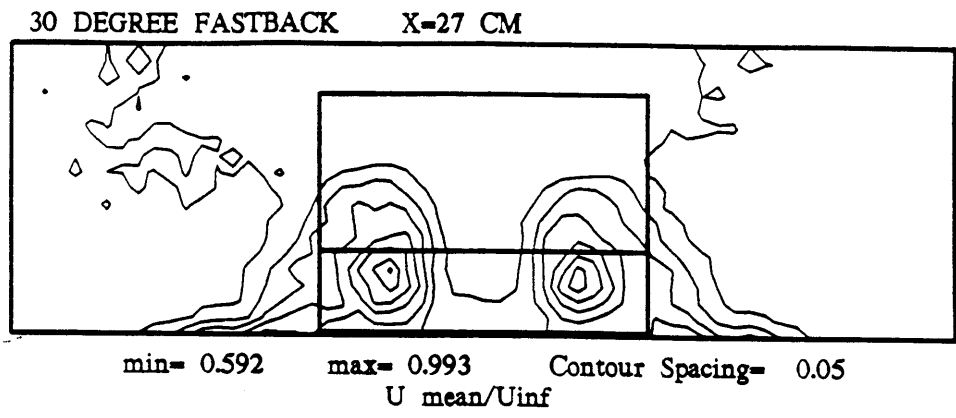
Figure 5.6: 30° fastback mean velocity contours, X=27 cm.

30 DEGREE FASTBACK   X=27 CM
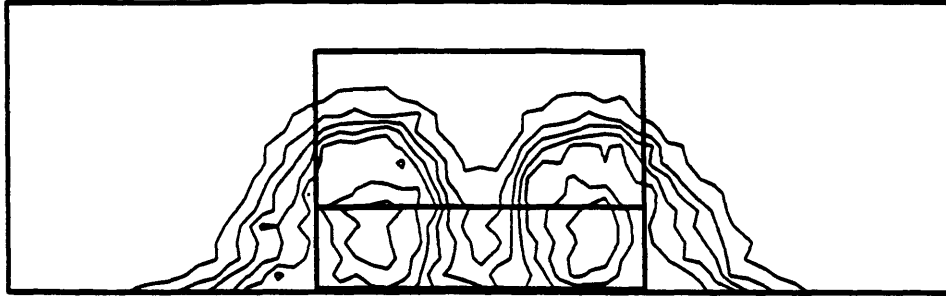
min= 0.002   max= 0.158   Contour Spacing= 0.02
U rms/Uinf

30 DEGREE FASTBACK   X=27 CM
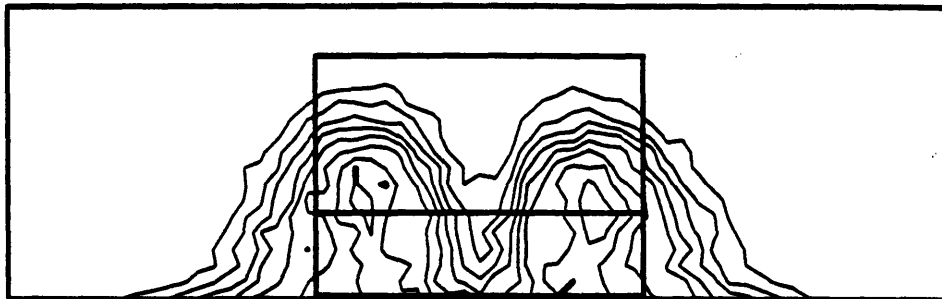
min= 0.004   max= 0.177   Contour Spacing= 0.02
V rms/Uinf

30 DEGREE FASTBACK   X=27 CM
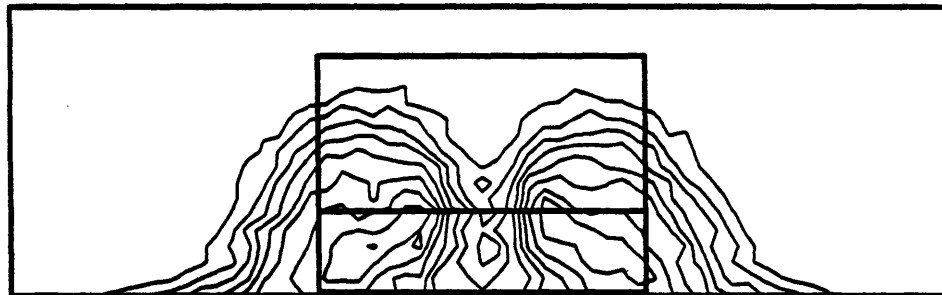
min= 0.005   max= 0.183   Contour Spacing= 0.02
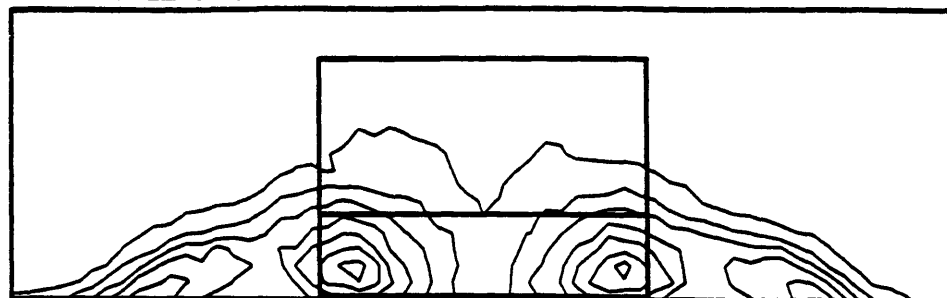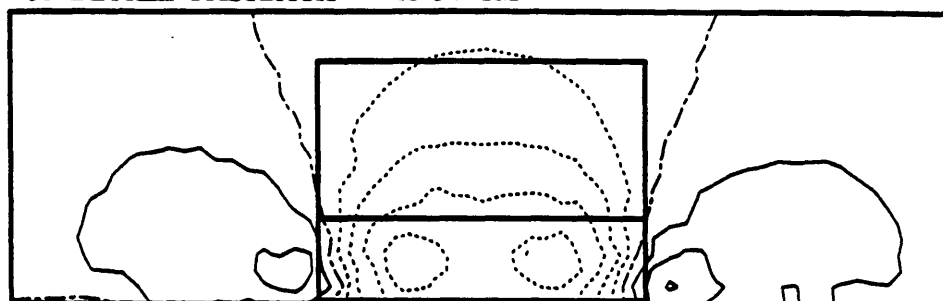W rms/Uinf

Figure 5.7: 30° fastback RMS velocity contours, X=27 cm.

127

32.5 DEGREE FASTBACK   X=27 CM
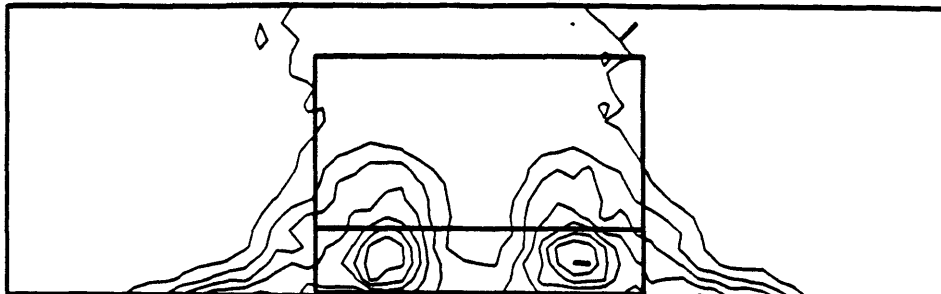
min= 0.597   max= 0.992   Contour Spacing=   0.05

U mean/Uinf

32.5 DEGREE FASTBACK   X=27 CM
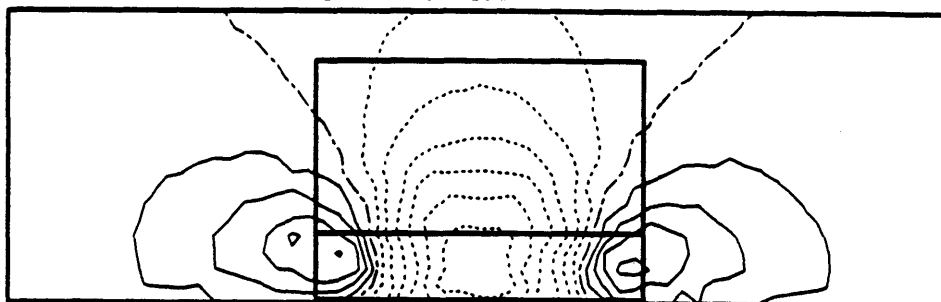
min= -0.345   max= 0.218   Contour Spacing=   0.05

V mean/Uinf

32.5 DEGREE FASTBACK   X=27 CM
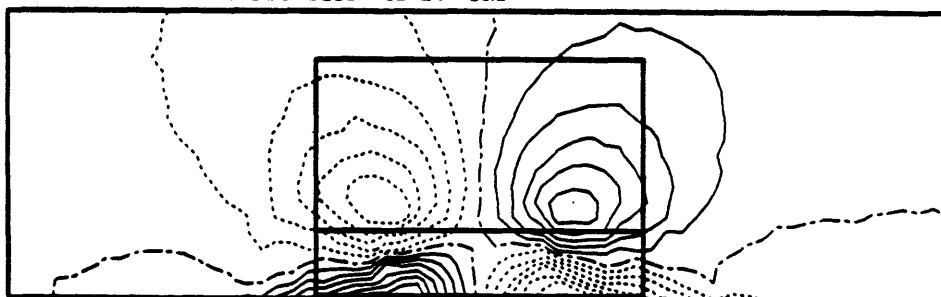
min= -0.379   max= 0.363   Contour Spacing=   0.05

W mean/Uinf

Figure 5.8: 32.5° fastback mean velocity contours, X=27 cm.
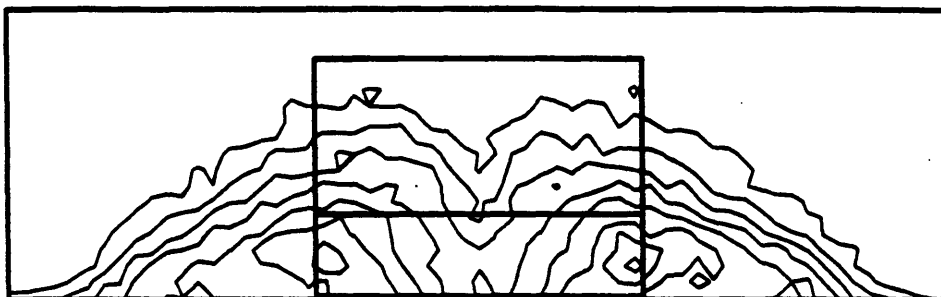
128

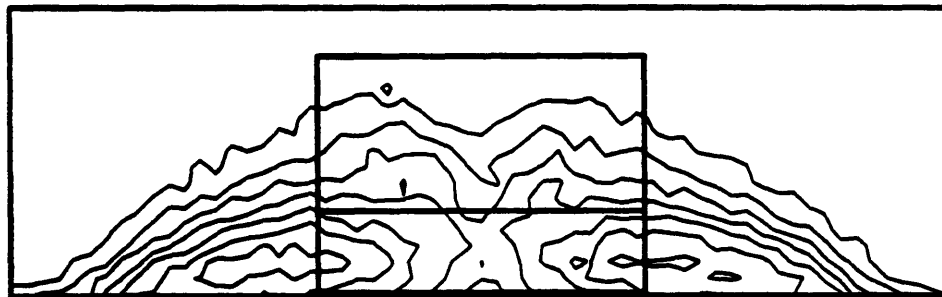32.5 DEGREE FASTBACK   X=27 CM
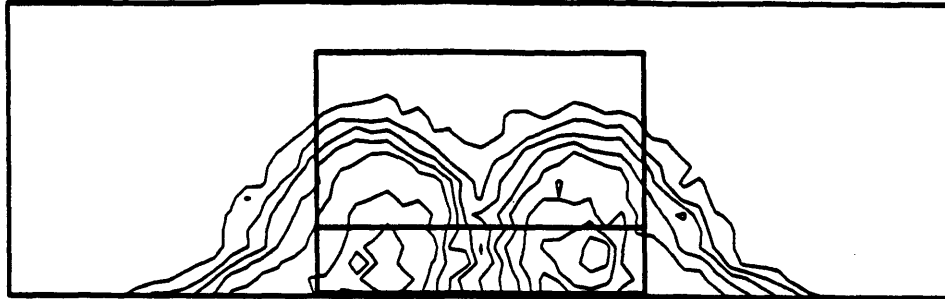
min= 0.002   max= 0.172   Contour Spacing= 0.02

U rms/Uinf

32.5 DEGREE FASTBACK   X=27 CM
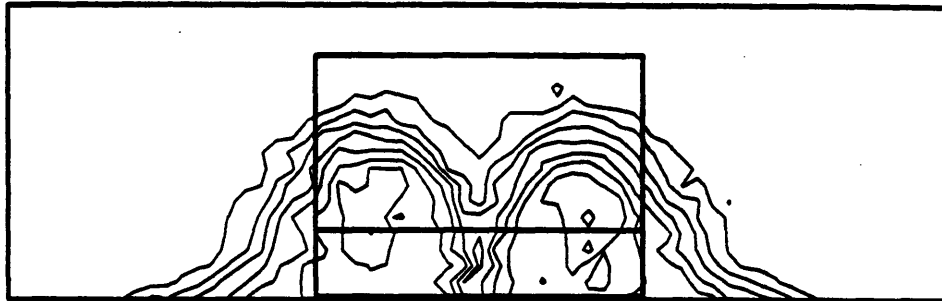
min= 0.003   max= 0.167   Contour Spacing= 0.02

V rms/Uinf

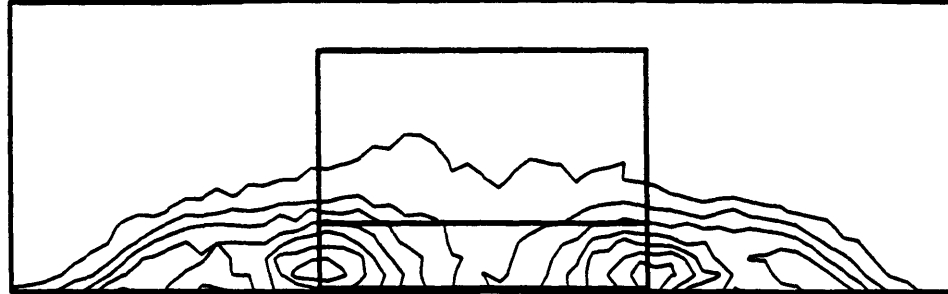32.5 DEGREE FASTBACK   X=27 CM
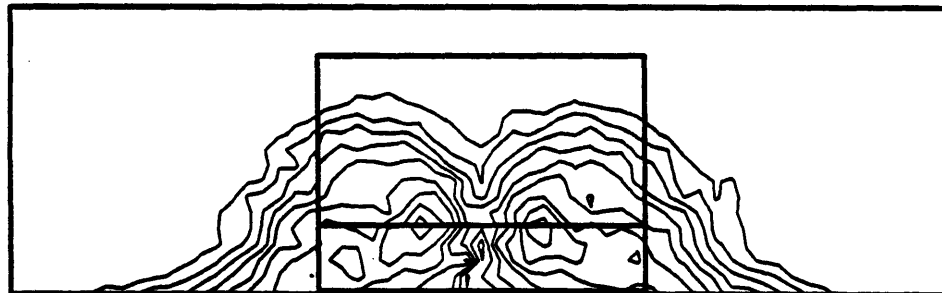
min= 0.004   max= 0.195   Contour Spacing= 0.02

W rms/Uinf

Figure 5.9: 32.5° fastback RMS velocity contours, X=27 cm.

35 DEGREE FASTBACK   X=27 CM

min= 0.57   max= 1.   Contour Spacing= 0.05
U mean/Uinf

35 DEGREE FASTBACK   X=27 CM
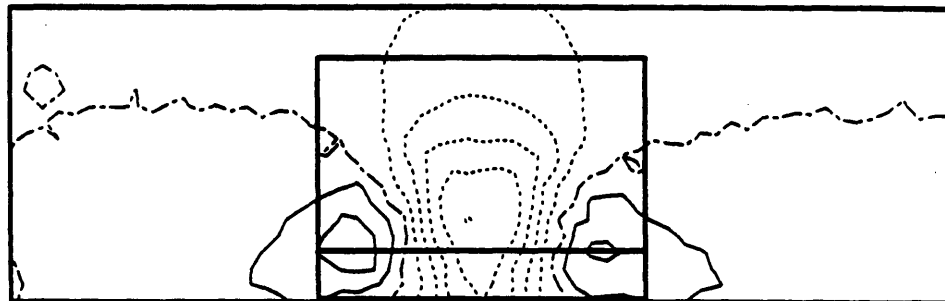
min= -0.254   max= 0.137   Contour Spacing= 0.05
V mean/Uinf

35 DEGREE FASTBACK .   X=27 CM

min= -0.146   max= 0.144   Contour Spacing= 0.05
W mean/Uinf

Figure 5.10: 35° fastback mean velocity contours, X=27 cm.

35 DEGREE FASTBACK   X=27 CM

min= 0.002   max= 0.161   Contour Spacing= 0.02

U rms/Uinf

35 DEGREE FASTBACK   X=27 CM

min= 0.004   max= 0.187   Contour Spacing= 0.02

V rms/Uinf

35 DEGREE FASTBACK   X=27 CM

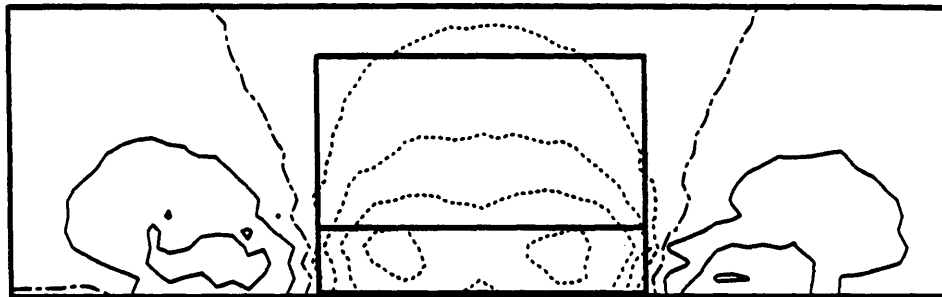min= 0.004   max= 0.192   Contour Spacing= 0.02

W rms/Uinf

Figure 5.11: 35° fastback RMS velocity contours, X=27 cm.

20 DEGREE FASTBACK   X=54 CM
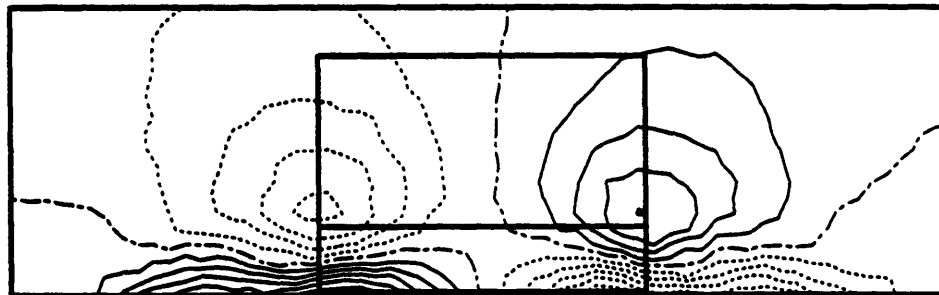
min= 0.746   max= 1.01   Contour Spacing= 0.05
U mean/Uinf

20 DEGREE FASTBACK   X=54 CM

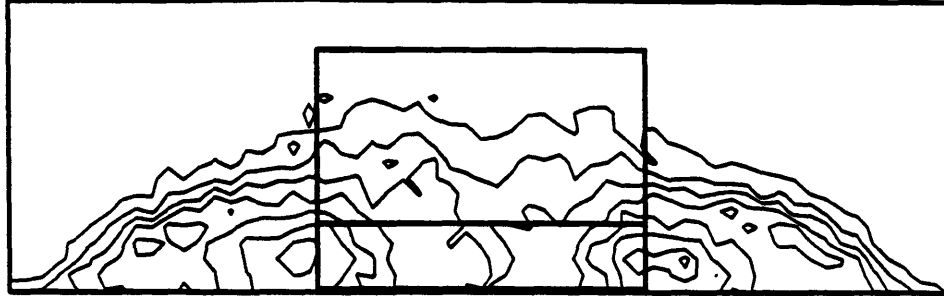min= -0.194   max= 0.082   Contour Spacing= 0.05
V mean/Uinf

20 DEGREE FASTBACK   X=54 CM

min= -0.206   max= 0.193   Contour Spacing= 0.05
W mean/Uinf
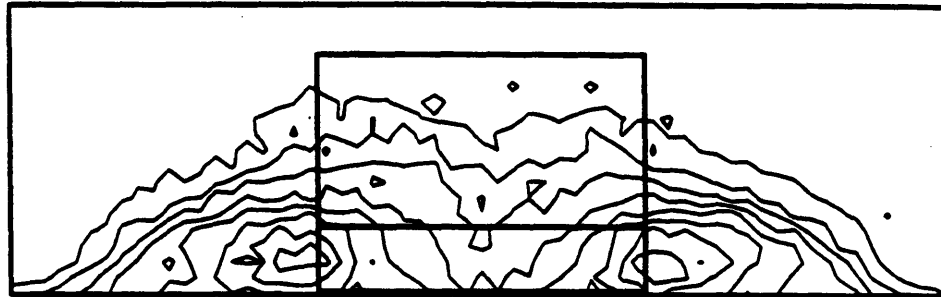
Figure 5.12: 20° fastback mean velocity contours, X=54 cm.
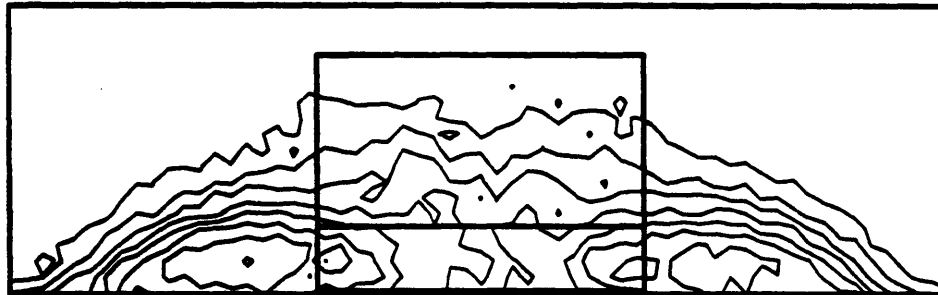
20 DEGREE FASTBACK   X=54 CM

min= 0.002   max= 0.135   Contour Spacing= 0.02
U rms/Uinf

20 DEGREE FASTBACK   X=54 CM

min= 0.003   max= 0.136   Contour Spacing= 0.02
V rms/Uinf

20 DEGREE FASTBACK   X=54 CM

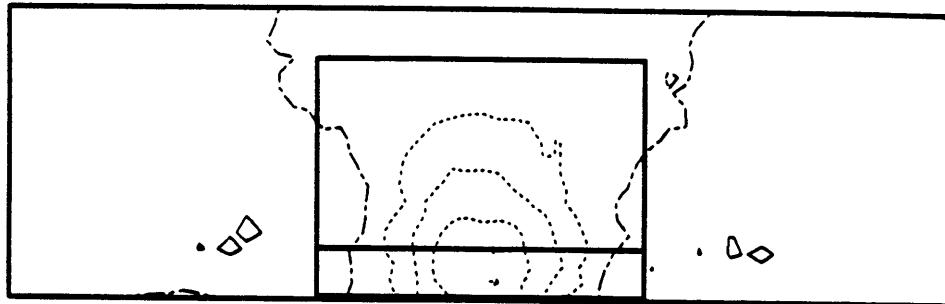min= 0.003   max= 0.163   Contour Spacing= 0.02
W rms/Uinf

Figure 5.13: 20° fastback RMS velocity contours, X=54 cm.

133

27.5 DEGREE FASTBACK   X=54 CM

min= 0.667   max= 1.   Contour Spacing=   0.05

U mean/Uinf

27.5 DEGREE FASTBACK   X=54 CM

min= -0.242   max= 0.138   Contour Spacing=   0.05

V mean/Uinf

27.5 DEGREE FASTBACK   X=54 CM

min= -0.342   max= 0.349   Contour Spacing=   0.05

W mean/Uinf

Figure 5.14: 27.5° fastback mean velocity contours, X=54 cm.

27.5 DEGREE FASTBACK X=54 CM

min= 0.002   max= 0.132   Contour Spacing= 0.02

U rms/Uinf

27.5 DEGREE FASTBACK X=54 CM

min= 0.003   max= 0.157   Contour Spacing= 0.02

V rms/Uinf

27.5 DEGREE FASTBACK X=54 CM

min= 0.004   max= 0.155   Contour Spacing= 0.02

W rms/Uinf

Figure 5.15: 27.5° fastback RMS velocity contours, X=54 cm.
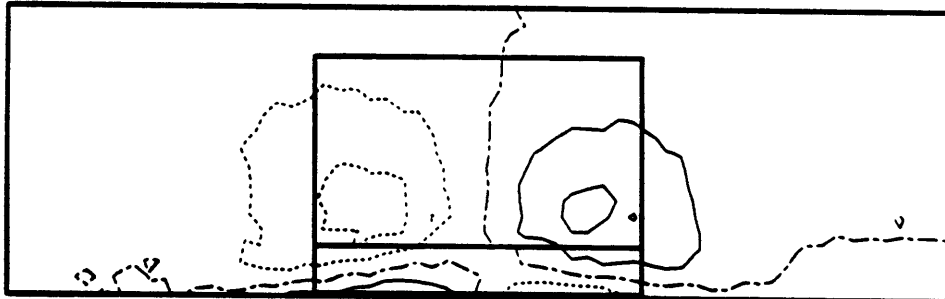
30 DEGREE FASTBACK   X=54 CM

min= 0.629   max= 0.979   Contour Spacing= 0.05
U mean/Uinf

30 DEGREE FASTBACK   X=54 CM

min= -0.225   max= 0.159   Contour Spacing= 0.05
V mean/Uinf

30 DEGREE FASTBACK   X=54 CM

min= -0.336   max= 0.324   Contour Spacing= 0.05
W mean/Uinf

Figure 5.16: 30° fastback mean velocity contours, X=54 cm.

136

30 DEGREE FASTBACK   X=54 CM

min= 0.002   max= 0.15   Contour Spacing= 0.02
U rms/Uinf

30 DEGREE FASTBACK   X=54 CM

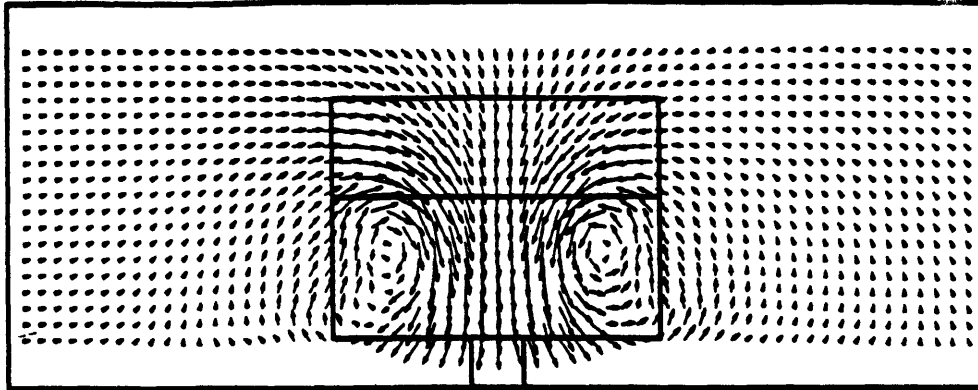min= 0.003   max= 0.17   Contour Spacing= 0.02
V rms/Uinf

30 DEGREE FASTBACK   X=54 CM

min= 0.004   max= 0.152   Contour Spacing= 0.02
W rms/Uinf

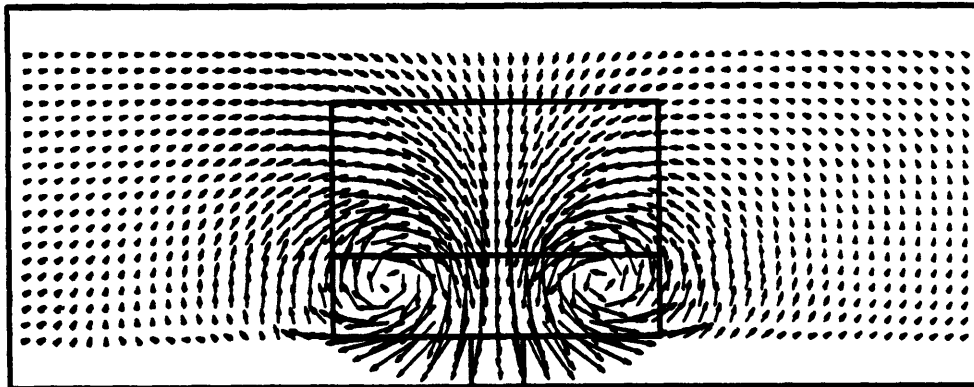Figure 5.17: 30° fastback RMS velocity contours, X=54 cm.

32.5 DEGREE FASTBACK   X=54 CM

min= 0.609   max= 0.986   Contour Spacing= 0.05

U mean/Uinf

32.5 DEGREE FASTBACK   X=54 CM

min= -0.219   max= 0.157   Contour Spacing= 0.05

V mean/Uinf

32.5 DEGREE FASTBACK   X=54 CM

min= -0.295   max= 0.304   Contour Spacing= 0.05

W mean/Uinf

Figure 5.18: 32.5° fastback mean velocity contours, X=54 cm.

138

32.5 DEGREE FASTBACK   X=54 CM

min= 0.002   max= 0.168   Contour Spacing= 0.02
U rms/Uinf

32.5 DEGREE FASTBACK   X=54 CM

min= 0.003   max= 0.172   Contour Spacing= 0.02
V rms/Uinf

32.5 DEGREE FASTBACK   X=54 CM

min= 0.003   max= 0.162   Contour Spacing= 0.02
W rms/Uinf

Figure 5.19: 32.5° fastback RMS velocity contours, X=54 cm.

139

35 DEGREE FASTBACK   X=54 CM

min= 0.602   max= 0.967   Contour Spacing= 0.05
U mean/Uinf

35 DEGREE FASTBACK   X=54 CM

min= -0.205   max= 0.06   Contour Spacing= 0.05
V mean/Uinf

35 DEGREE FASTBACK   X=54 CM

min= -0.124   max= 0.116   Contour Spacing= 0.05
W mean/Uinf

Figure 5.20: 35° fastback mean velocity contours, X=54 cm.

140

35 DEGREE FASTBACK   X=54 CM
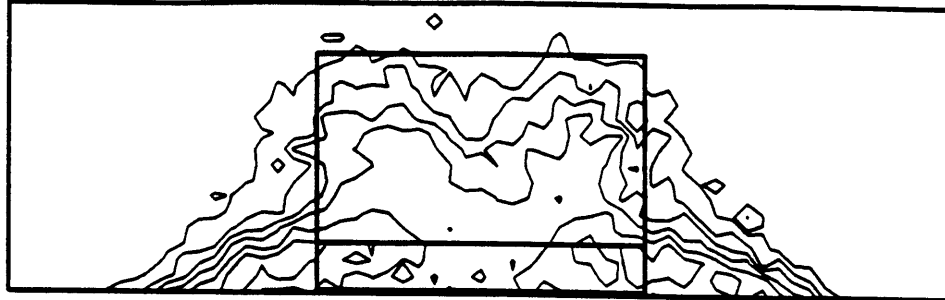
min= 0.002   max= 0.136   Contour Spacing= 0.02
U rms/Uinf

35 DEGREE FASTBACK   X=54 CM
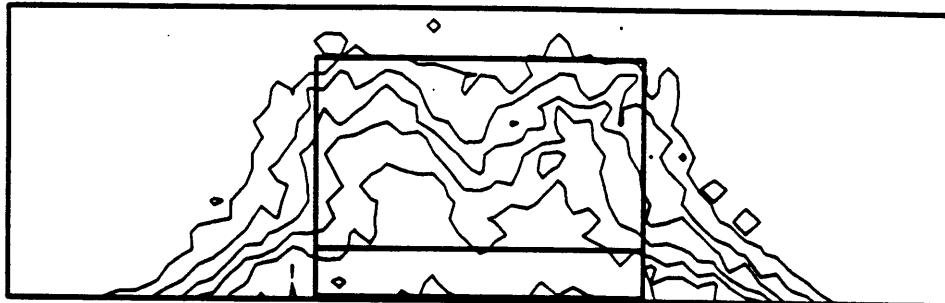
min= 0.003   max= 0.139   Contour Spacing= 0.02
V rms/Uinf

35 DEGREE FASTBACK   X=54 CM
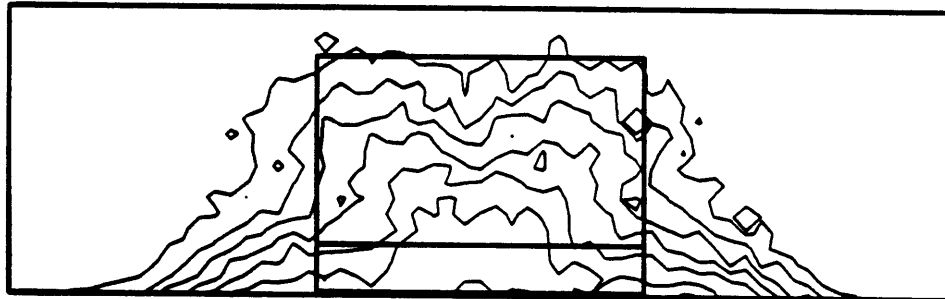
min= 0.003   max= 0.145   Contour Spacing= 0.02
W rms/Uinf

Figure 5.21: 35° fastback RMS velocity contours, X=54 cm.

20 DEGREE FASTBACK   X=27 CM

27.5 DEGREE FASTBACK   X=27 CM

30 DEGREE FASTBACK   X=27 CM

Figure 5.22: Mean crossflow velocity vectors, X=27 cm.

32.5 DEGREE FASTBACK   X=27 CM

— = 5 M/S
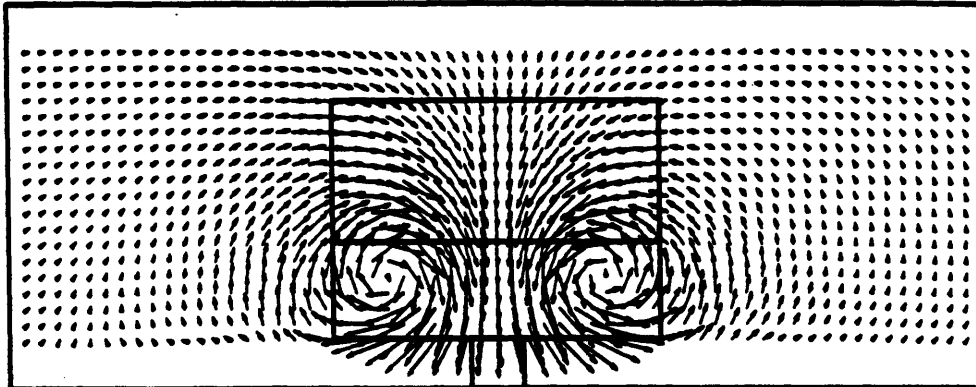
35 DEGREE FASTBACK   X=27 CM

— = 5 M/S
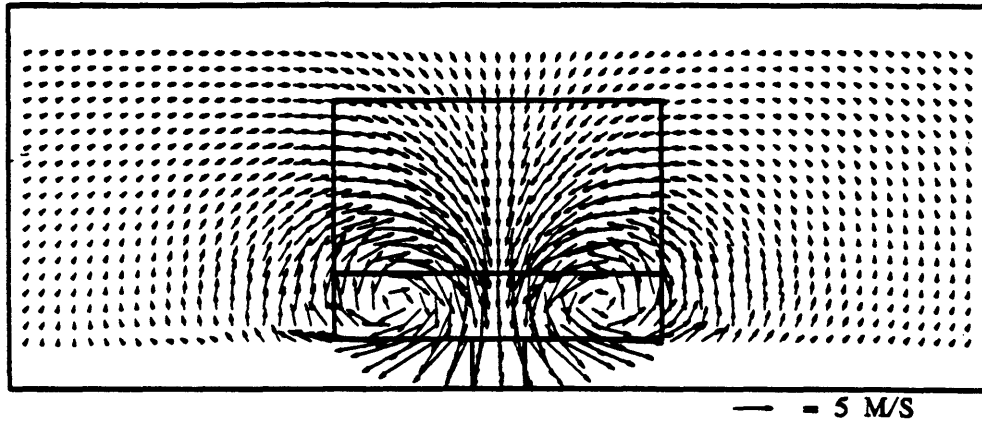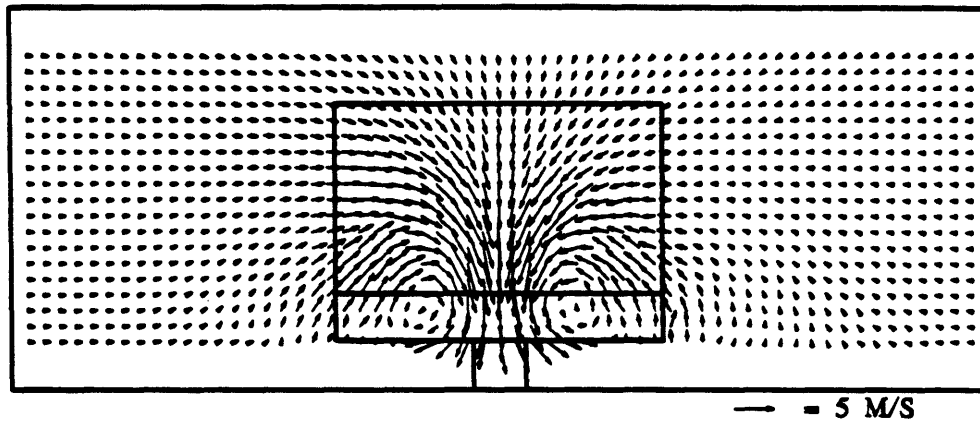
Figure 5.23: Mean crossflow velocity vectors, X=27 cm, continued.

20 DEGREE FASTBACK   X=54 CM
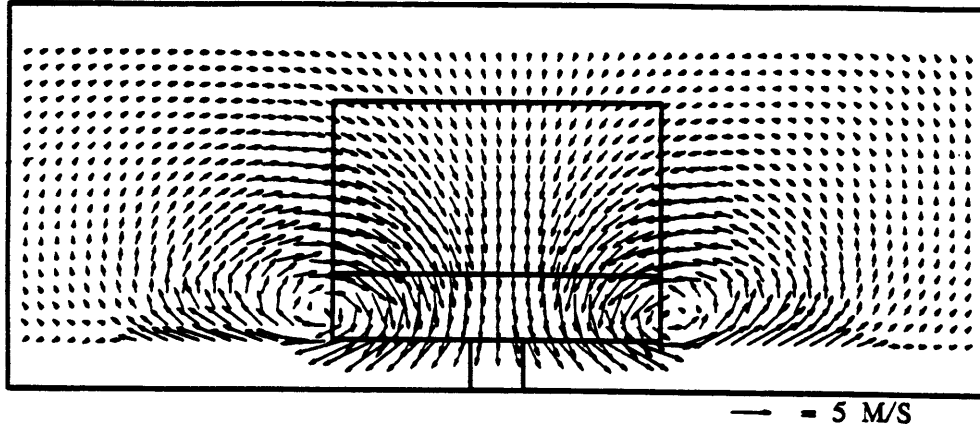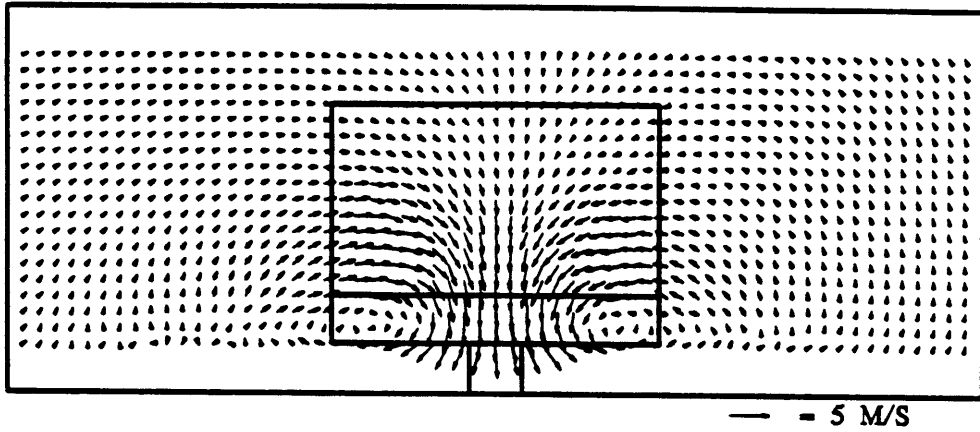
— = 5 M/S

27.5 DEGREE FASTBACK   X=54 CM

— = 5 M/S

30 DEGREE FASTBACK   X=54 CM

— = 5 M/S
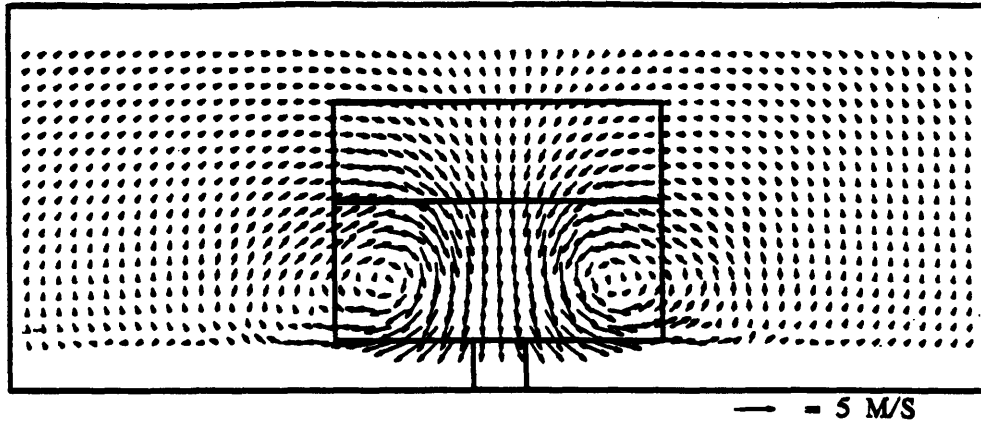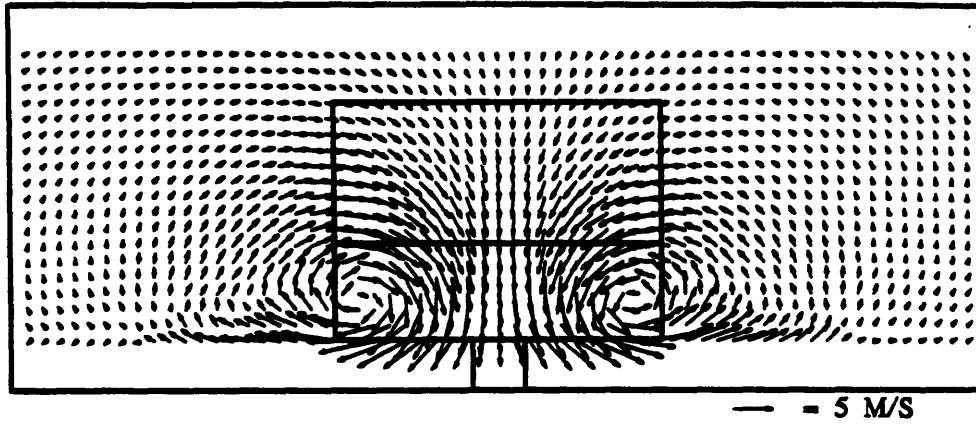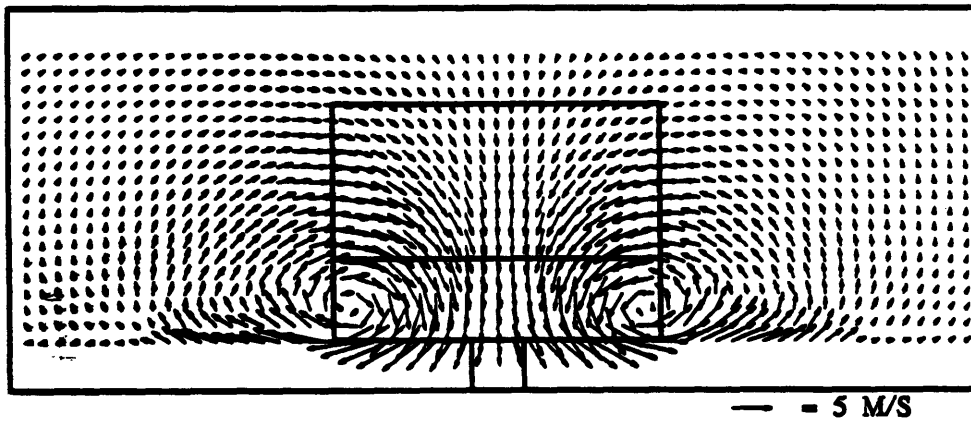
Figure 5.24: Mean crossflow velocity vectors, X=54 cm.

144

32.5 DEGREE FASTBACK   X=54 CM
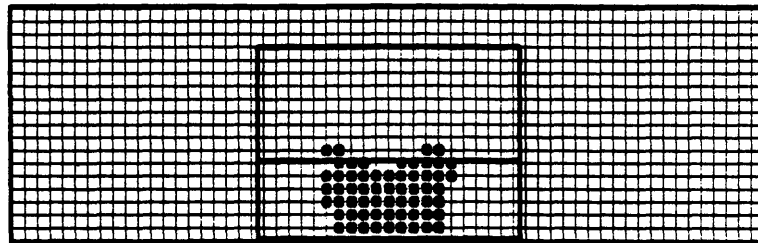

— = 5 M/S

35 DEGREE FASTBACK   X=54 CM

— = 5 M/S

Figure 5.25: Mean crossflow velocity vectors, X=54 cm, continued.

20 DEGREE FASTBACK   X=27 CM
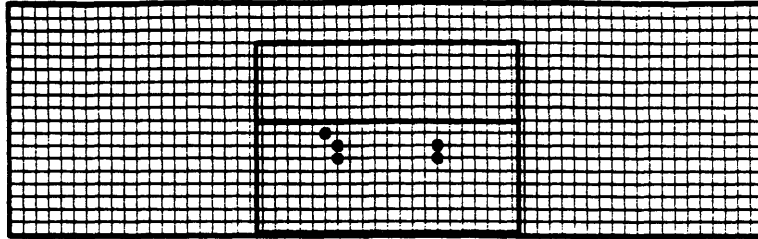
POINTS WITH PITCH ANGLE <-15 DEGREES

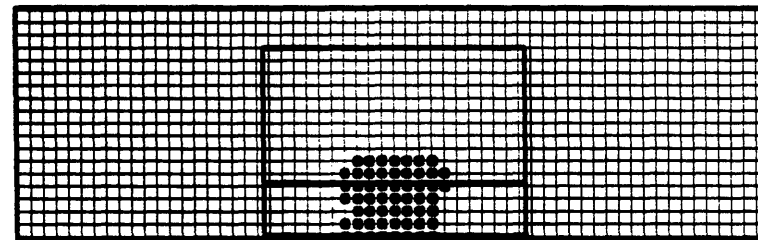**27.5 DEGREE FASTBACK   X=27 CM**

POINTS WITH PITCH ANGLE <-15 DEGREES

30 DEGREE FASTBACK   X=27 CM
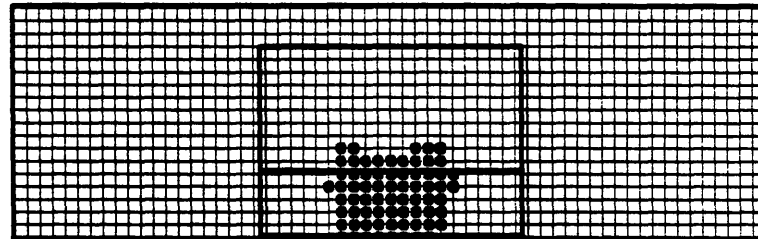
POINTS WITH PITCH ANGLE <-15 DEGREES
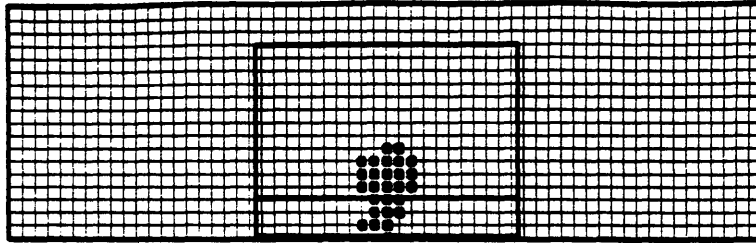
32.5 DEGREE FASTBACK   X=27 CM
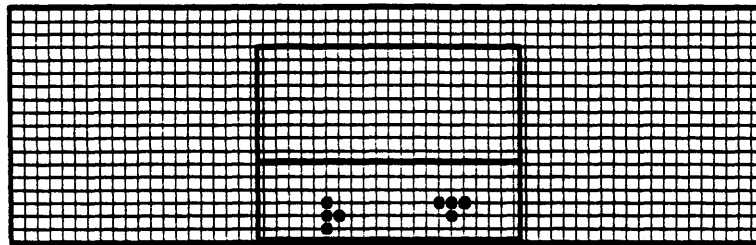

POINTS WITH PITCH ANGLE <-15 DEGREES

Figure 5.26: Locations of suspect data, Part I.

146

35 DEGREE FASTBACK   X=27 CM

POINTS WITH PITCH ANGLE <-15 DEGREES

27.5 DEGREE FASTBACK   X=54 CM
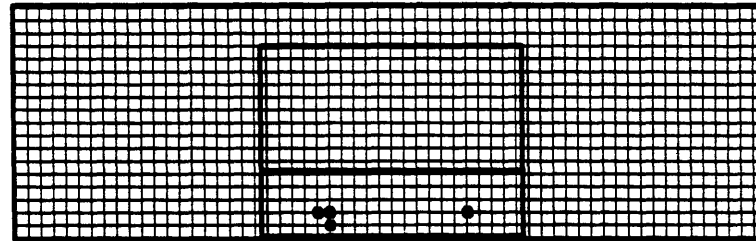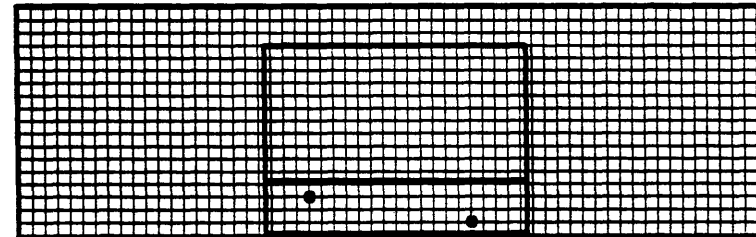
POINTS WITH PITCH ANGLE <-15 DEGREES

30 DEGREE FASTBACK   X=54 CM

POINTS WITH PITCH ANGLE <-15 DEGREES

32.5 DEGREE FASTBACK   X=54 CM

POINTS WITH PITCH ANGLE <-15 DEGREES
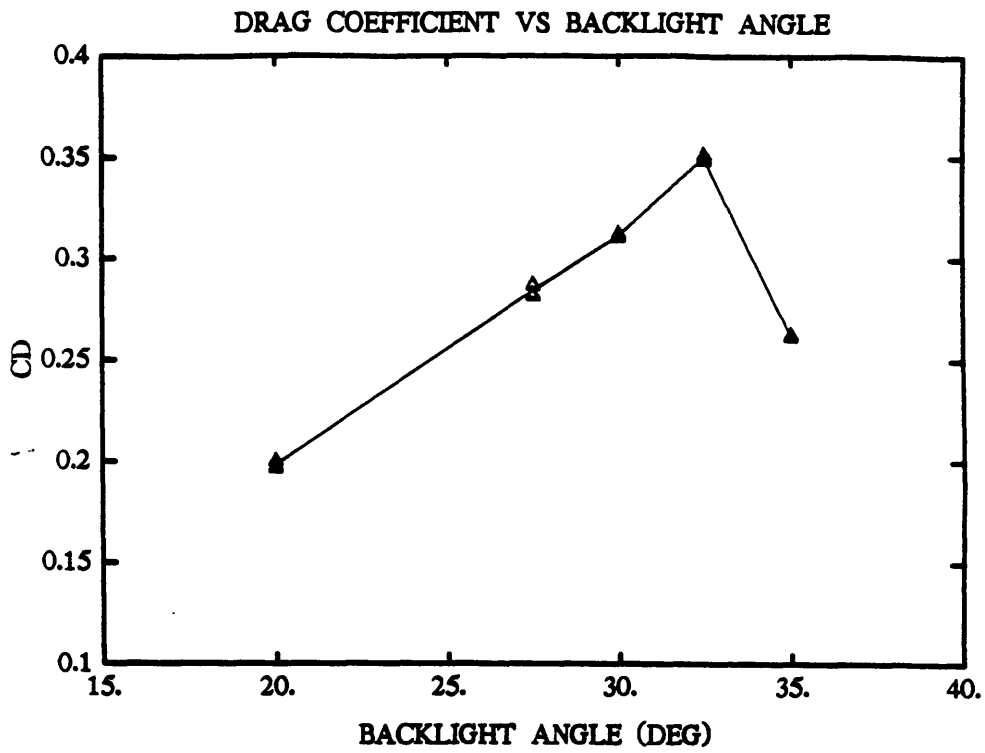
Figure 5.27: Locations of suspect data, Part II.

147

DRAG COEFFICIENT VS BACKLIGHT ANGLE

Figure 5.28: Drag coefficients from force balance.
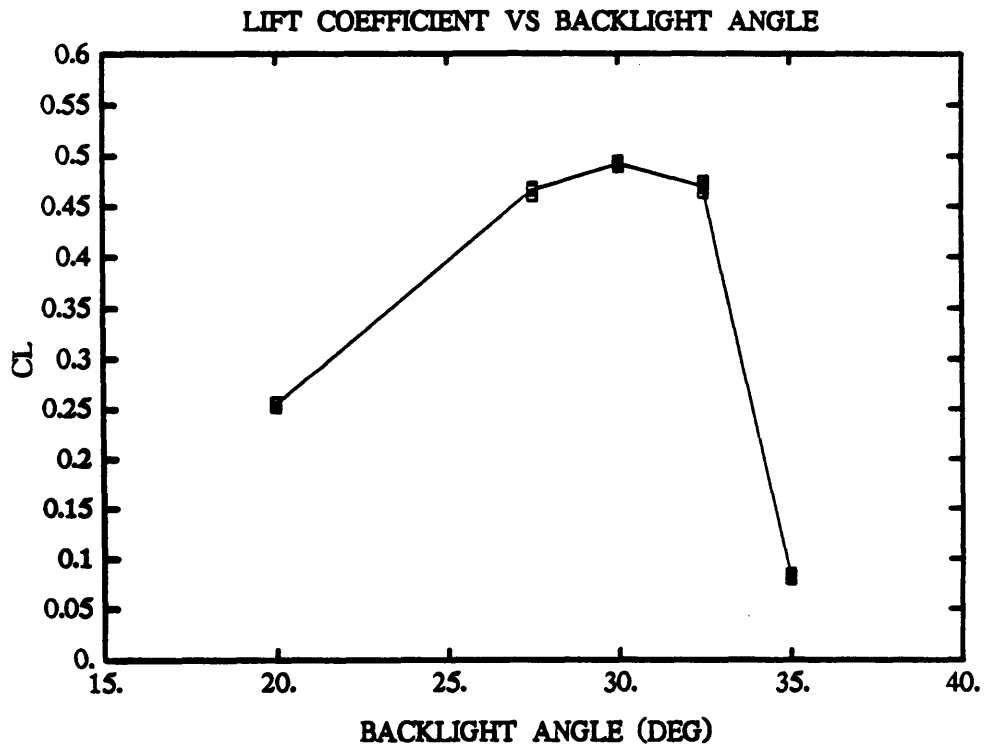
LIFT COEFFICIENT VS BACKLIGHT ANGLE

Figure 5.29: Lift coefficients from force balance.

Table 5.1: Experimental Drag Calculation

Fastback Angle	Plane Location	C_d Actual	C_d Calculated (% error)	C_d Form (% of C_d)	C_d Vortex (% of C_d)
20°	X=27 cm	0.199	0.279 (+40.2)	0.248 (88.9)	0.031 (11.1)
20°	X=54 cm	0.199	0.211 (+6.0)	0.190 (90.0)	0.021 (10.0)
27.5°	X=27 cm	0.285	0.285 (+0.0)	0.227 (79.6)	0.058 (20.4)
27.5°	X=54 cm	0.285	0.257 (-9.8)	0.213 (82.9)	0.044 (17.1)
30°	X=27 cm	0.312	0.318 (+1.9)	0.256 (80.5)	0.062 (19.5)
30°	X=54 cm	0.312	0.279 (-10.6)	0.235 (84.2)	0.044 (15.8)
32.5°	X=27 cm	0.350	0.301 (-14.0)	0.237 (78.7)	0.064 (21.3)
32.5°	X=54 cm	0.350	0.286 (-18.3)	0.237 (82.9)	0.049 (17.1)
35°	X=27 cm	0.262	0.293 (+11.8)	0.268 (91.5)	0.025 (8.5)
35°	X=54 cm	0.262	0.264 (+0.8)	0.251 (95.1)	0.013 (4.9)

TOTAL DRAG VS BACKLIGHT ANGLE
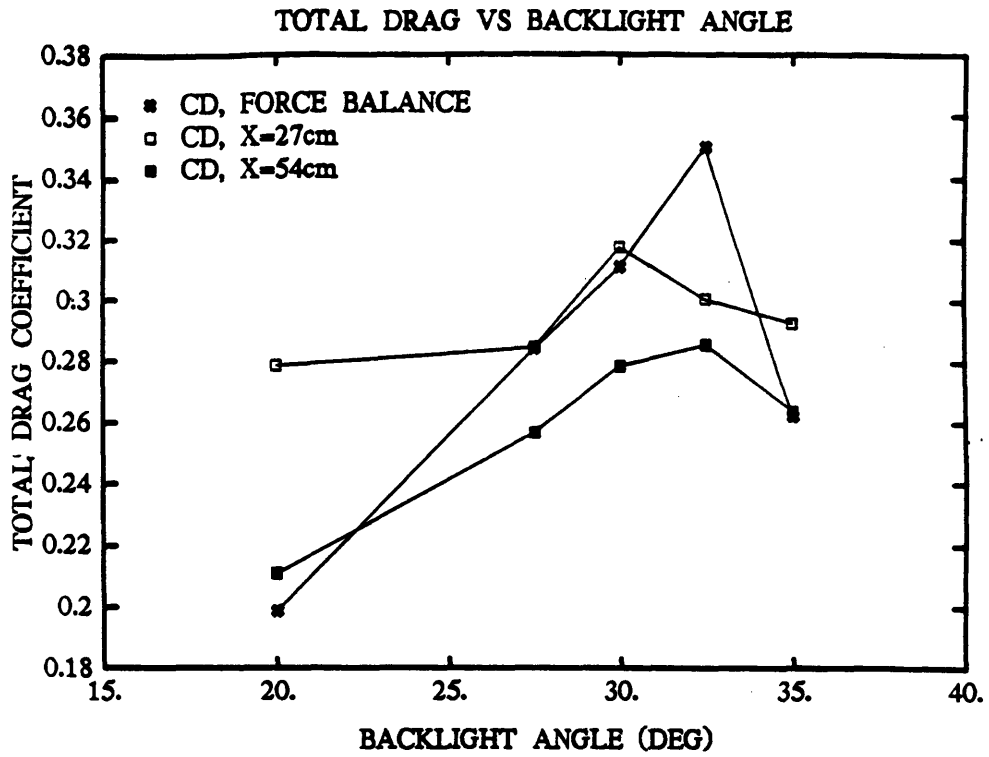
Figure 5.30: Calculated total drag coefficients.

DRAG COMPONENTS VS BACKLIGHT ANGLE
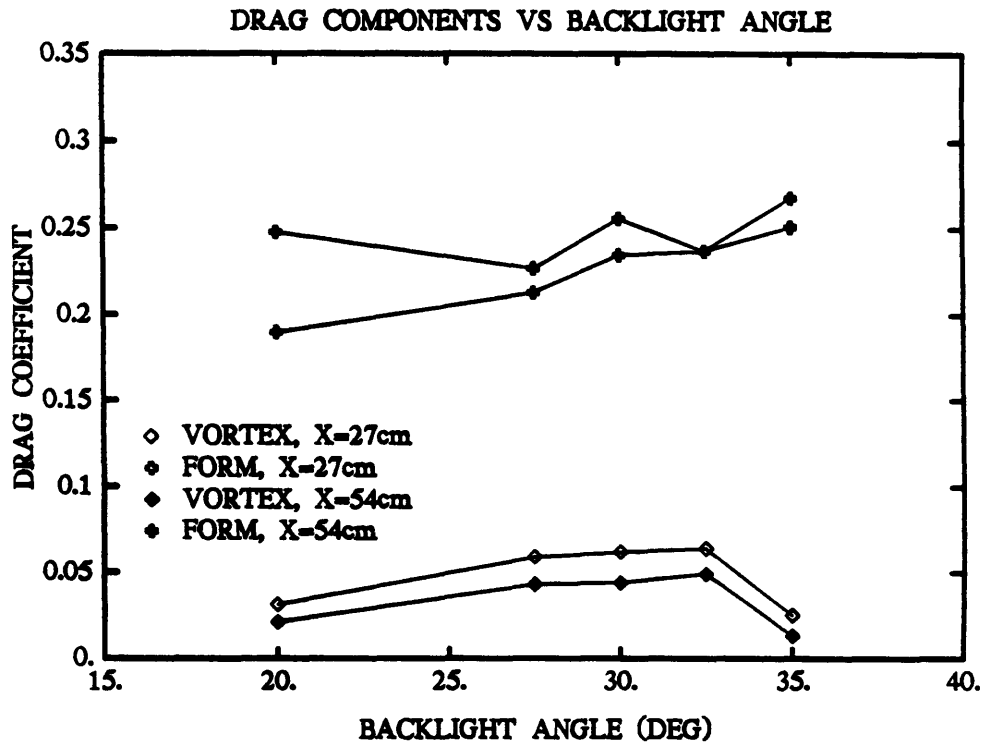

Figure 5.31: Calculated form drag and vortex drag components.

Table 5.2: Form Drag Breakdown

Fastback Angle	Plane Location	C_d Form	C_d Form Mean Term (% of C_d Form)	C_d Form Unsteady Term (% of C_d Form)	C_d Form Unsteady Term (% of C_d)
20°	X=27 cm	0.248	0.237 (95.6)	0.011 (4.4)	0.011 (3.9)
20°	X=54 cm	0.190	0.186 (97.9)	0.004 (2.1)	0.004 (1.9)
27.5°	X=27 cm	0.227	0.219 (96.5)	0.008 (3.5)	0.008 (2.8)
27.5°	X=54 cm	0.213	0.207 (97.2)	0.006 (2.8)	0.006 (2.3)
30°	X=27 cm	0.256	0.249 (97.3)	0.007 (2.7)	0.007 (2.2)
30°	X=54 cm	0.235	0.230 (97.9)	0.005 (2.1)	0.005 (1.8)
32.5°	X=27 cm	0.237	0.232 (97.9)	0.005 (2.1)	0.005 (1.7)
32.5°	X=54 cm	0.237	0.232 (97.9)	0.005 (2.1)	0.005 (1.7)
35°	X=27 cm	0.268	0.264 (98.5)	0.004 (1.5)	0.004 (1.4)
35°	X=54 cm	0.251	0.249 (99.2)	0.002 (0.8)	0.002 (0.8)

FORM DRAG MEAN COMPONENTS VS BACKLIGHT ANGLE
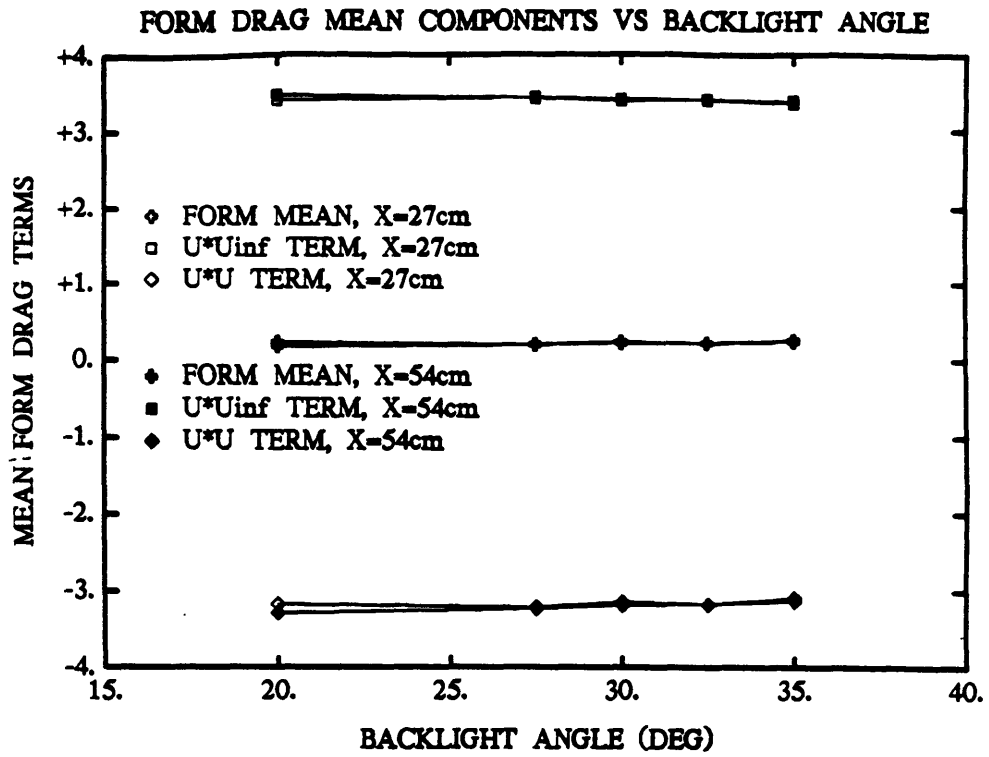
Figure 5.32: Form drag mean velocity components.
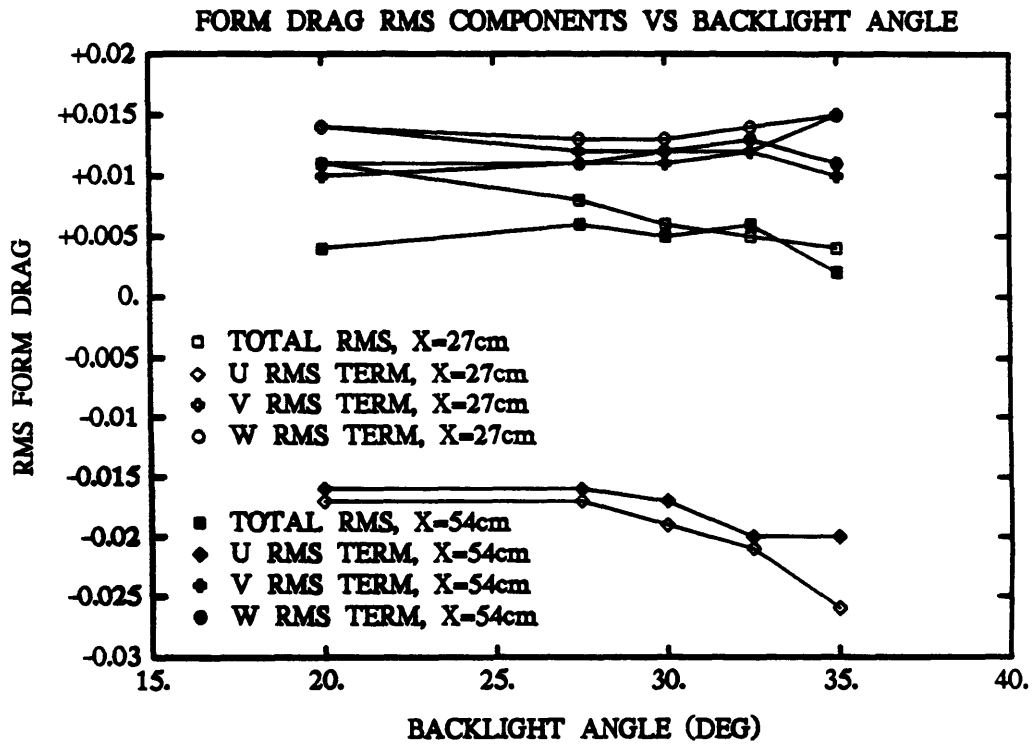
FORM DRAG RMS COMPONENTS VS BACKLIGHT ANGLE

Figure 5.33: Form drag RMS velocity components.

Table 5.3: Previous Vortex Drag Results From Maskell's Method

Author	Probe Type	Wake Plane Location Downstream	Vortex Drag (% of C_d)	Notes
Davis (1982)	Nulling 9–Hole Nulling 9–Hole	0.85 B.L.* 1.33 B.L.	37 31	Moving Ground Plane
Davis (1982)	Nulling 9–Hole Nulling 9–Hole	0.85 B.L. 1.33 B.L.	44 33	Stationary Ground Plane
Hackett & Sugavanam (1985)	Rake of seven 5–Hole probes	0.18 B.L. 0.86 B.L.	6 1	
Onorato, et.al. (1984)	Nulling 9–Hole	0.37 B.L.	19	Boundary Layer Suction
Onorato, et.al. (1984)	Nulling 9–Hole	0.36 B.L. (longer body)	14	Boundary Layer Suction
Hackett, et.al. (1985)	Rake of forty-two Non-nulling 7-Hole	0.40 B.L. 0.52 B.L.	8 8	

* B.L.= Body Lengths

Table 5.4: Effect Of Streamwise Derivatives On Calculated Drag

| Fastback Angle	Plane Location	$-y\,(\overline{uv})_x$ Integral	$-z\,(\overline{uw})_x$ Integral	Adjusted C_d	% Change in C_d
20°	X=27 cm	-0.020	-0.025	0.234	-16.1
20°	X=54 cm	-0.020	-0.025	0.166	-21.3
27.5°	X=27 cm	-0.002	-0.010	0.273	-4.2
27.5°	X=54 cm	-0.002	-0.010	0.245	-4.7
30°	X=27 cm	-0.012	-0.008	0.298	-6.3
30°	X=54 cm	-0.012	-0.008	0.259	-7.2
32.5°	X=27 cm	+0.007	-0.011	0.297	-1.3
32.5°	X=54 cm	+0.007	-0.011	0.282	-1.4
35°	X=27 cm	-0.023	-0.028	0.242	-17.4
35°	X=54 cm	-0.023	-0.028	0.213	-19.3

DATA WINDOWING FUNCTION
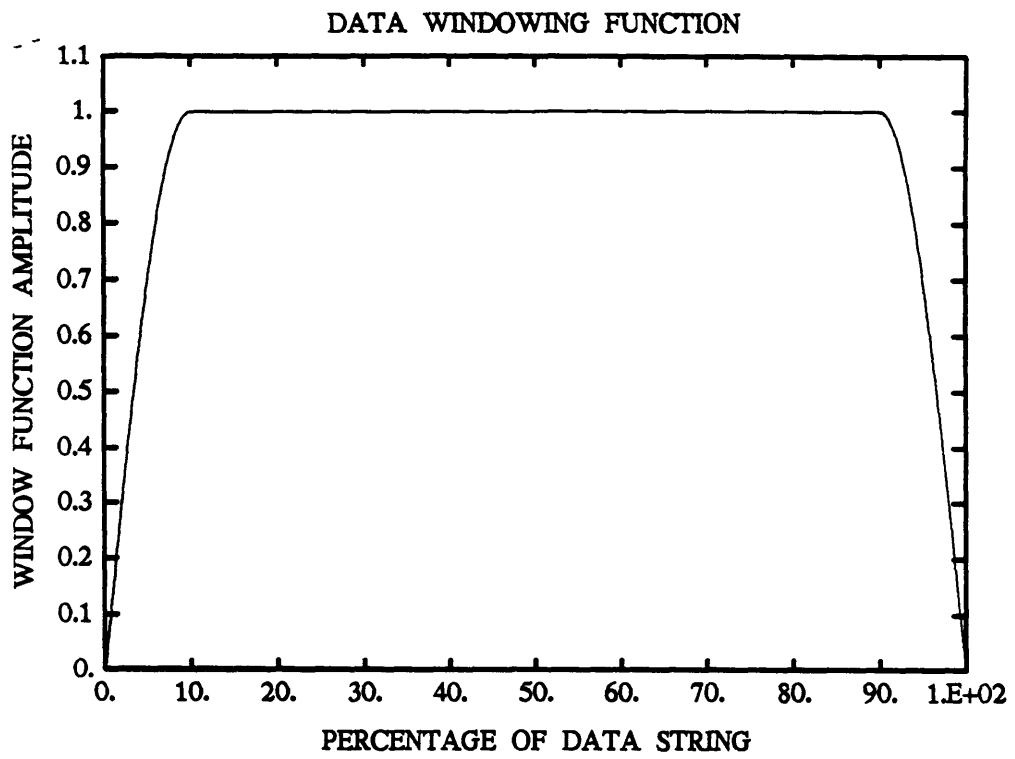
Figure 5.34: Data windowing function for power spectra.

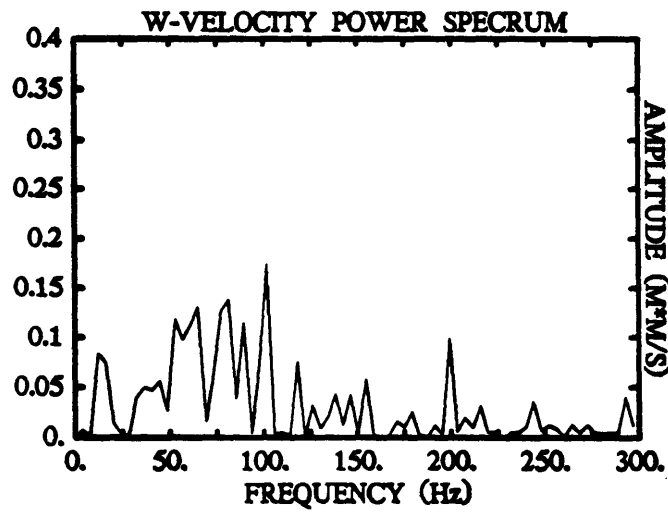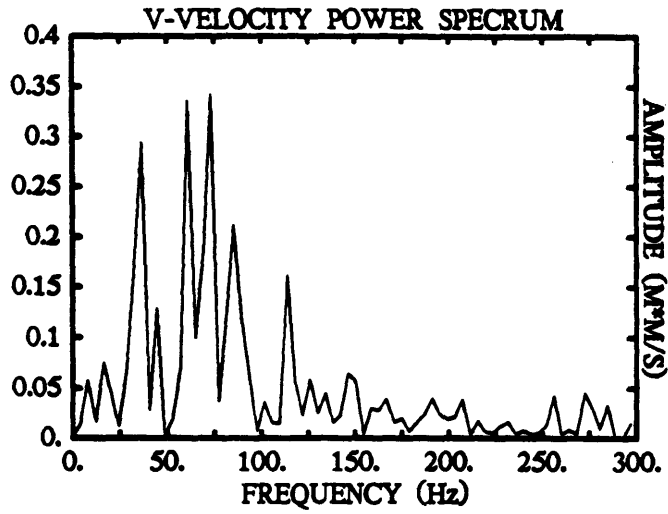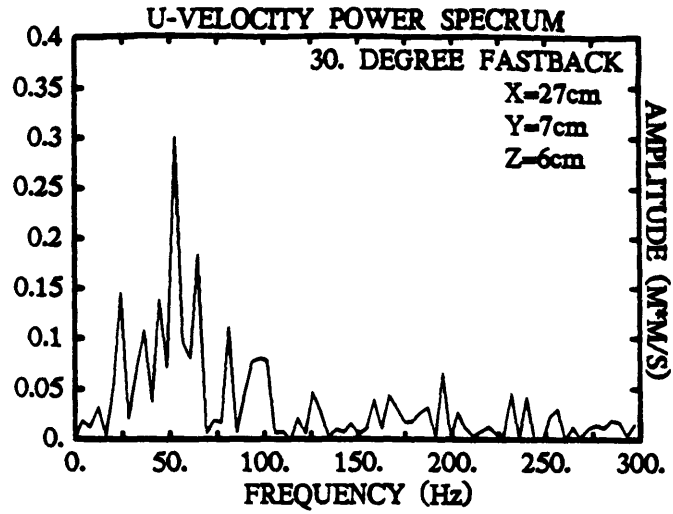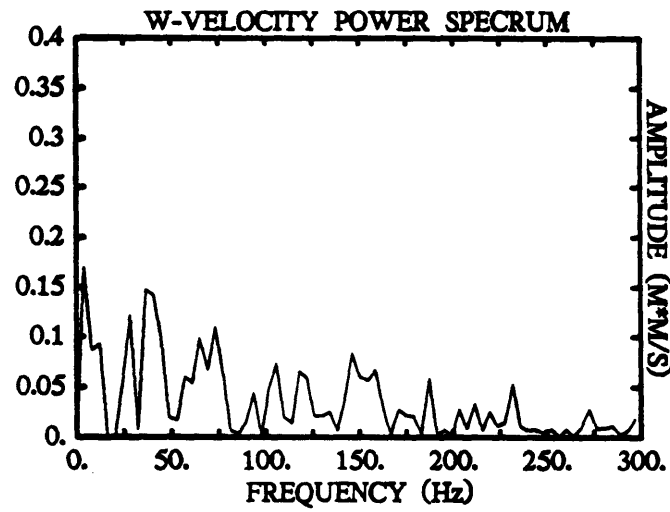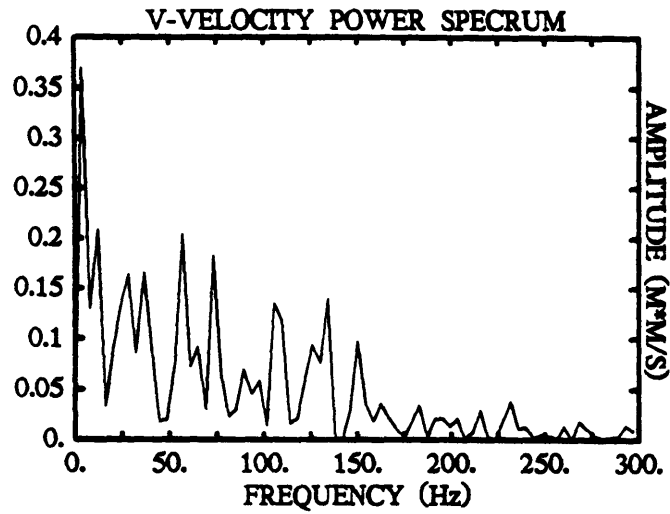Figure 5.35: Power spectra for left-hand side vortex core, 30° fastback, X=27 cm.

Figure 5.36: Power spectra for right-hand side vortex core, 30° fastback, X=27 cm.

Figure 5.37: Power spectra for left-hand side vortex core, 30° fastback, X=54 cm.

Figure 5.38: Power spectra for right-hand side vortex core, 30° fastback, X=54 cm.

Figure 5.39: Power spectra for left-hand side vortex core, 32.5° fastback, $X=27$ cm.

Figure 5.40: Power spectra for right-hand side vortex core, 32.5° fastback, X=27 cm.

Figure 5.41: Power spectra for left-hand side vortex core, 32.5° fastback, X=54 cm.
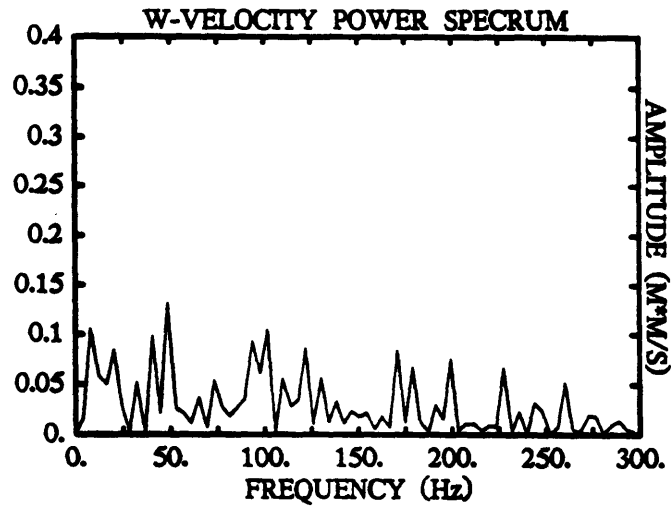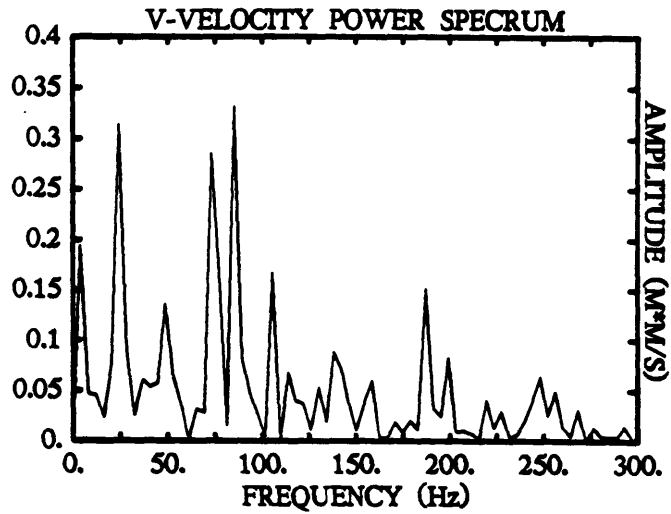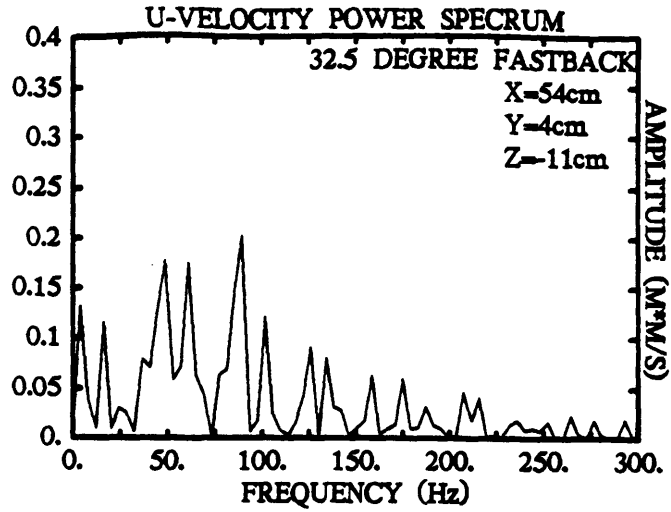
Figure 5.42: Power spectra for right-hand side vortex core, 32.5° fastback, *X*=54 cm.
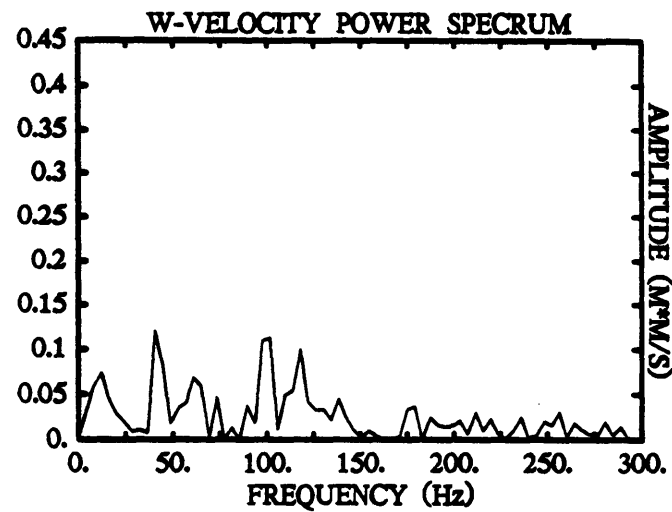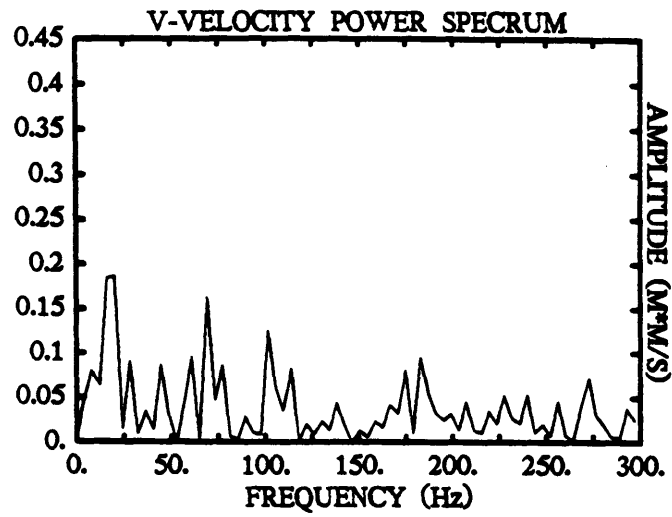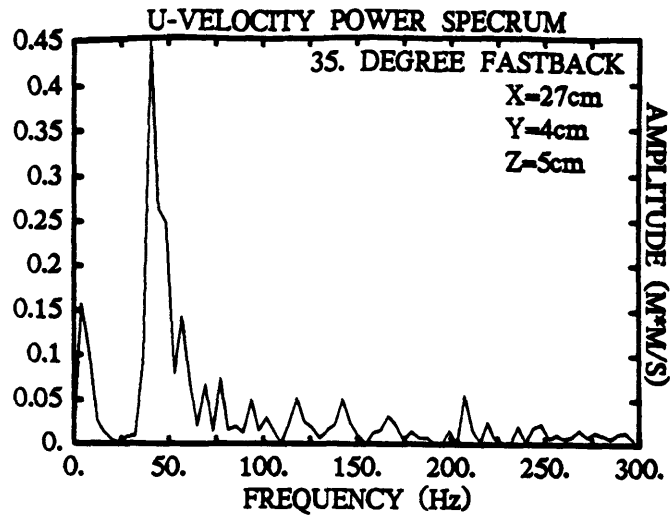
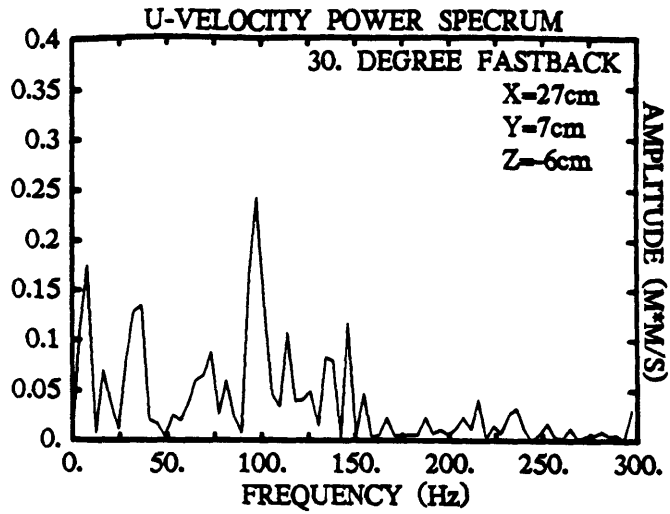Figure 5.43: Power spectra for left-hand side vortex core, 35° fastback, X=27 cm.
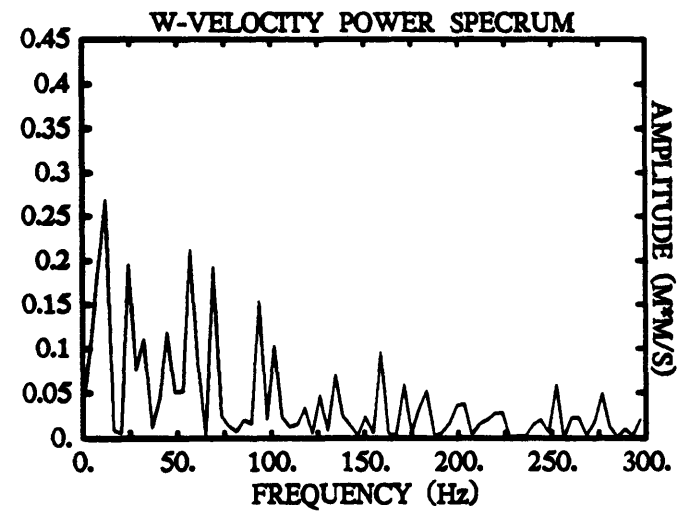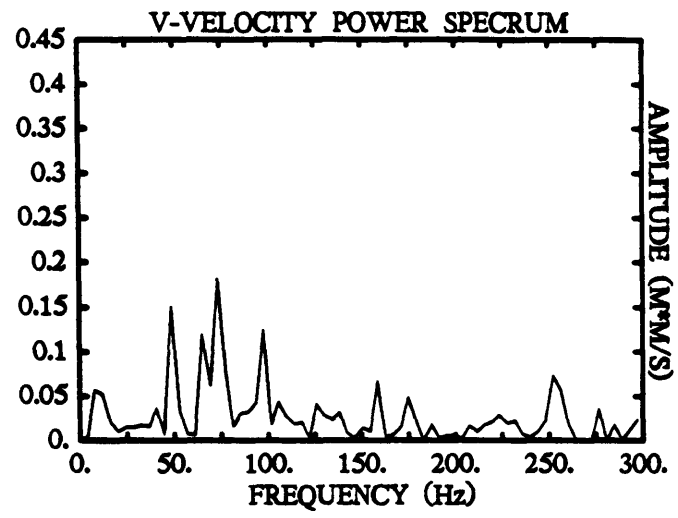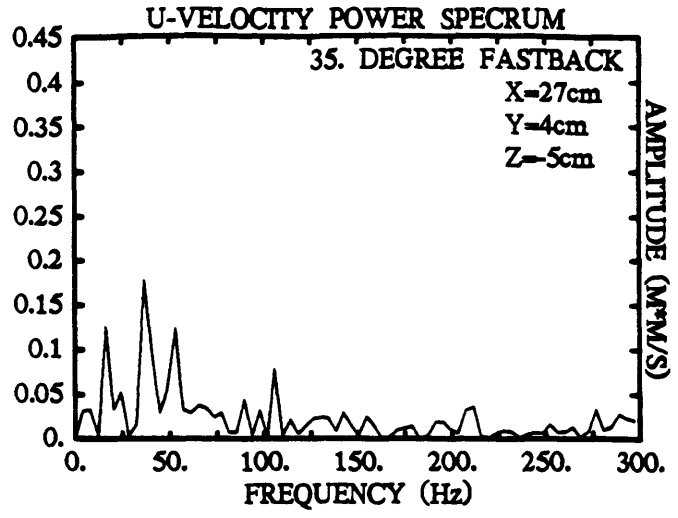
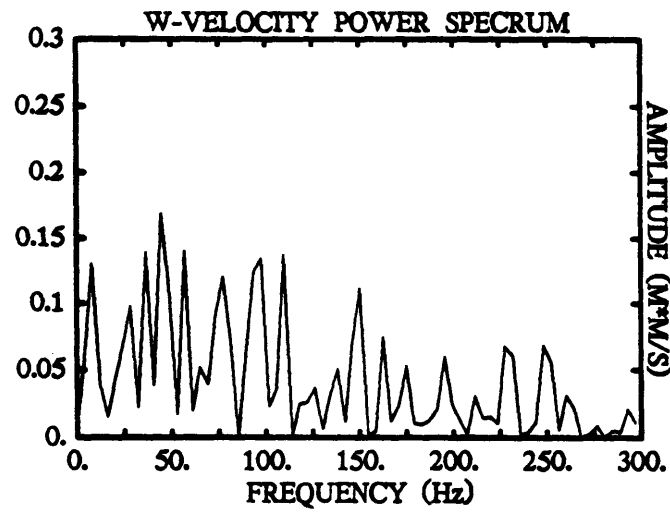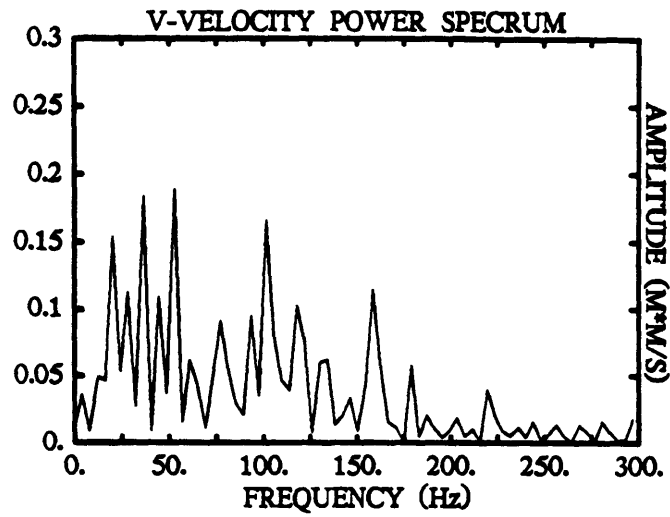Figure 5.44: Power spectra for right-hand side vortex core, 35° fastback, X=27 cm.
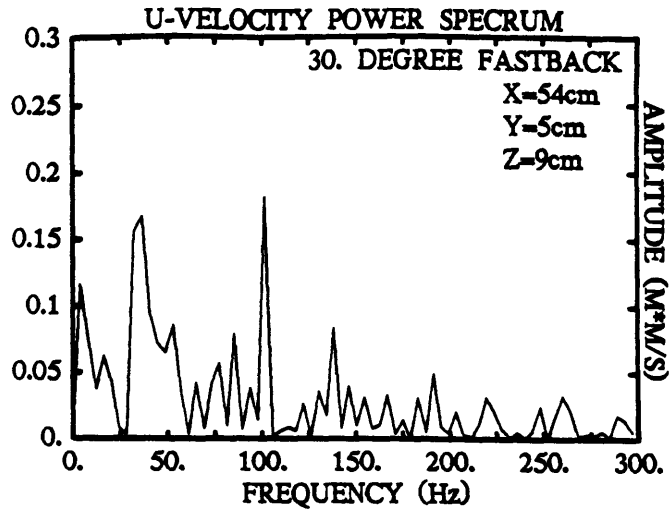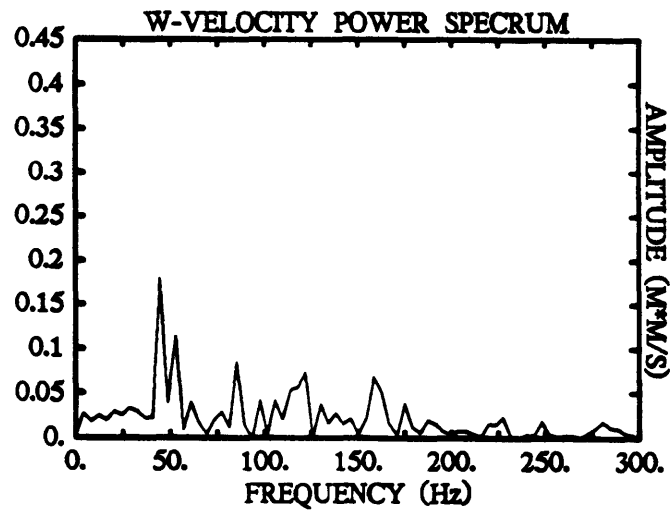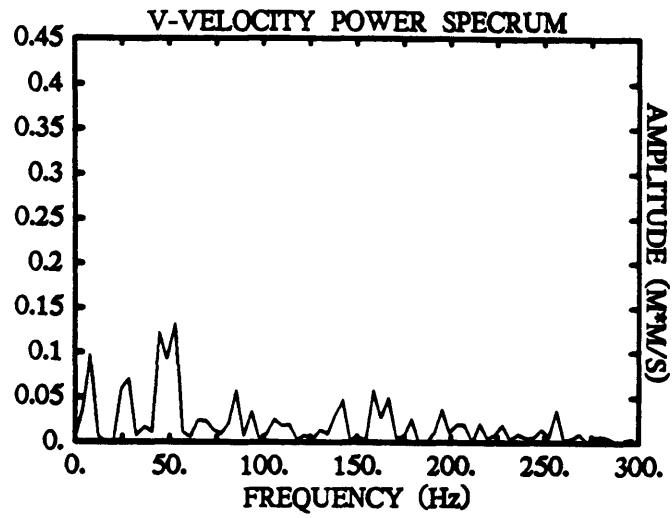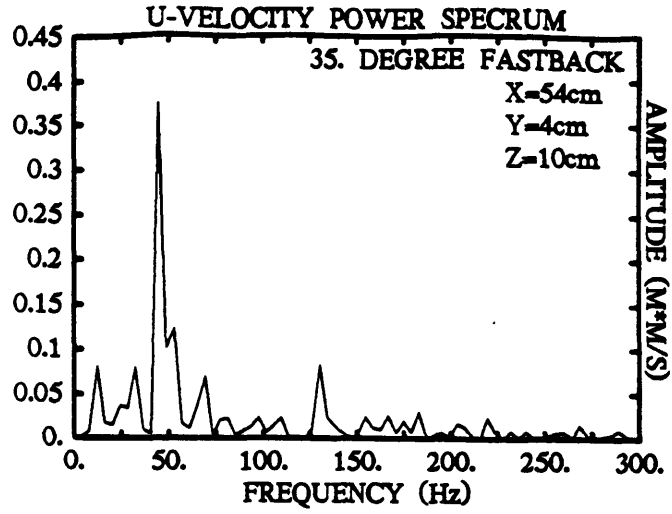
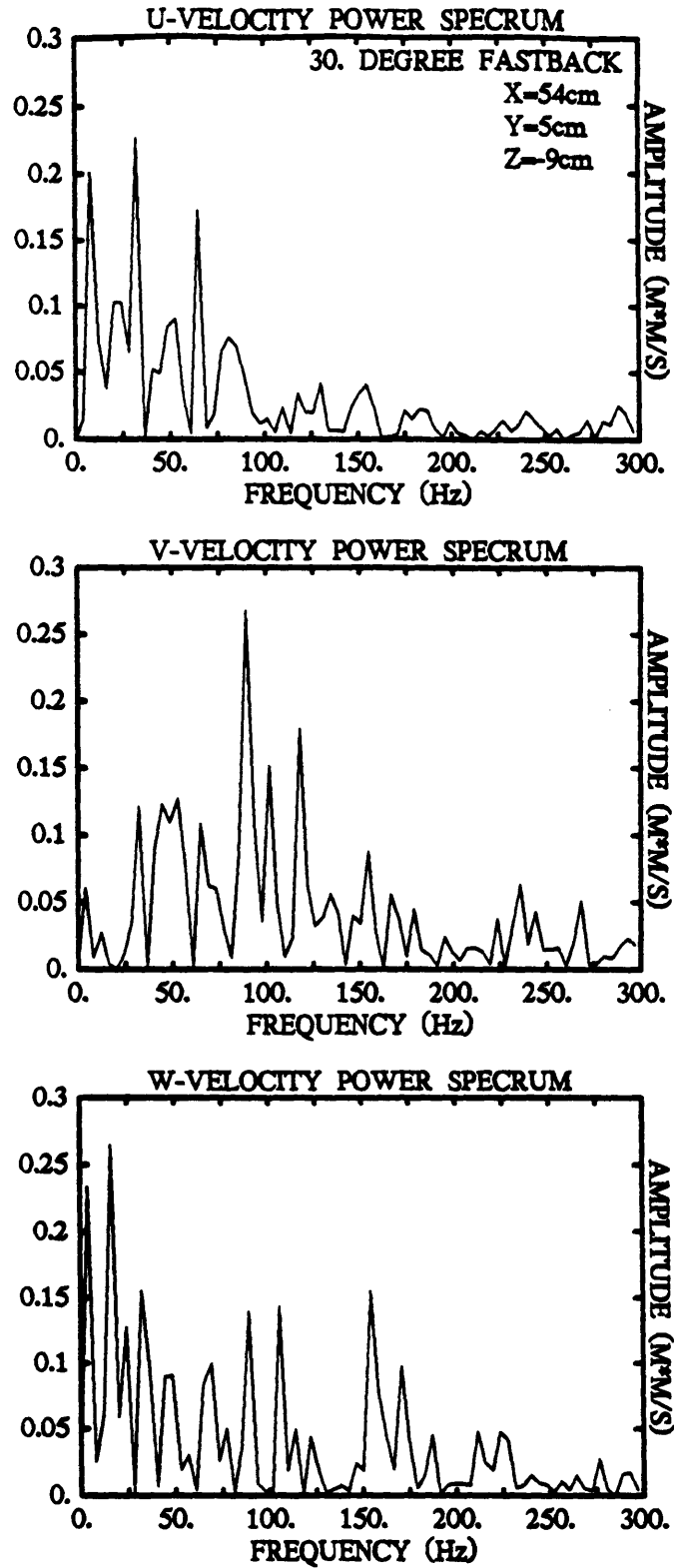Figure 5.45: Power spectra for left-hand side vortex core, 35° fastback, X=54 cm.

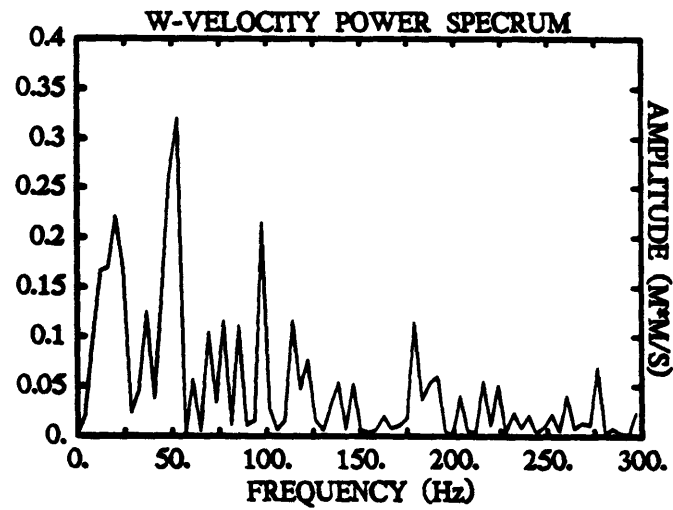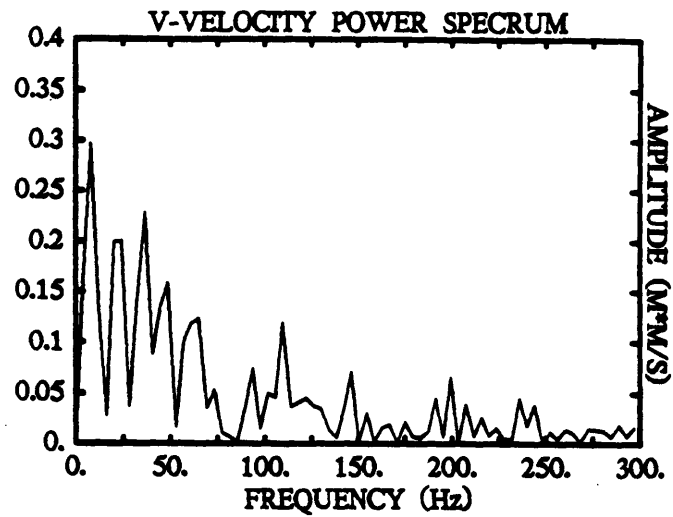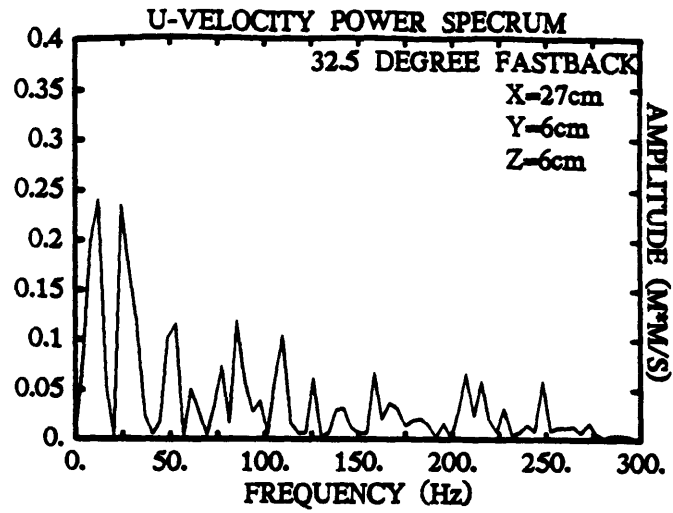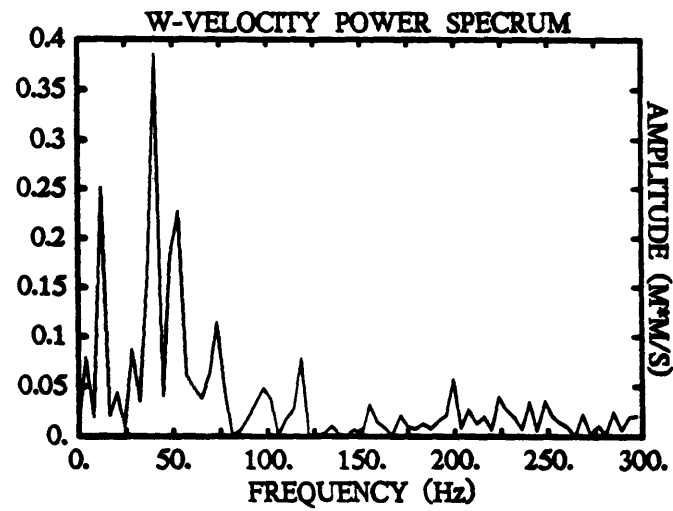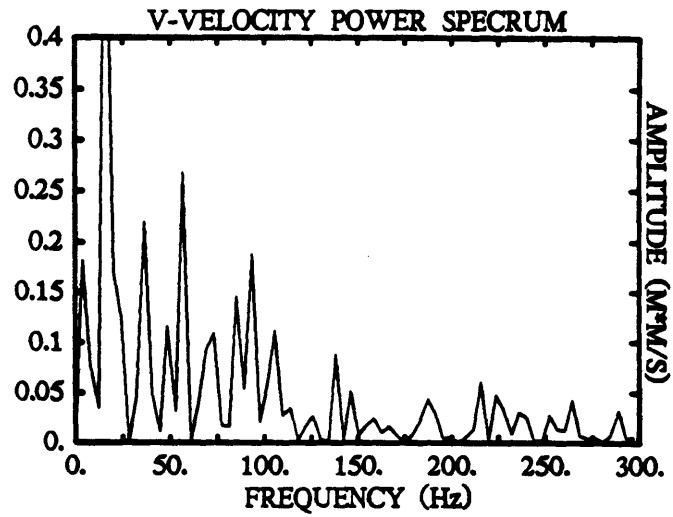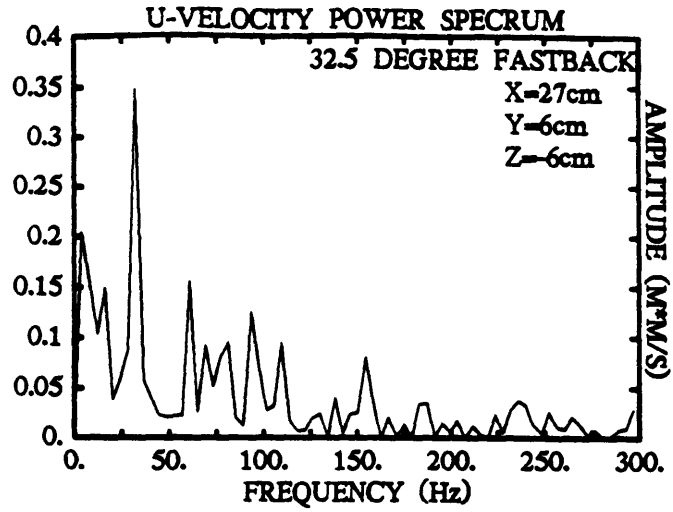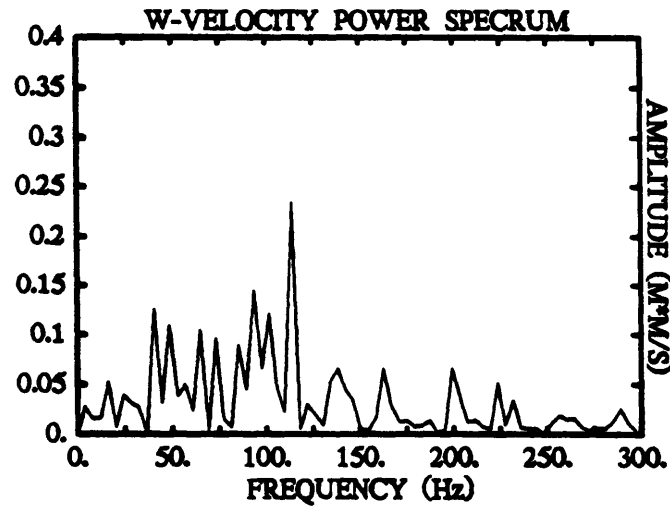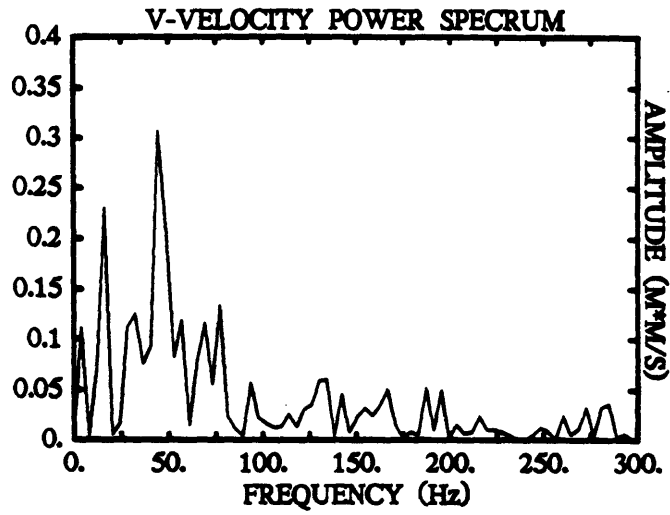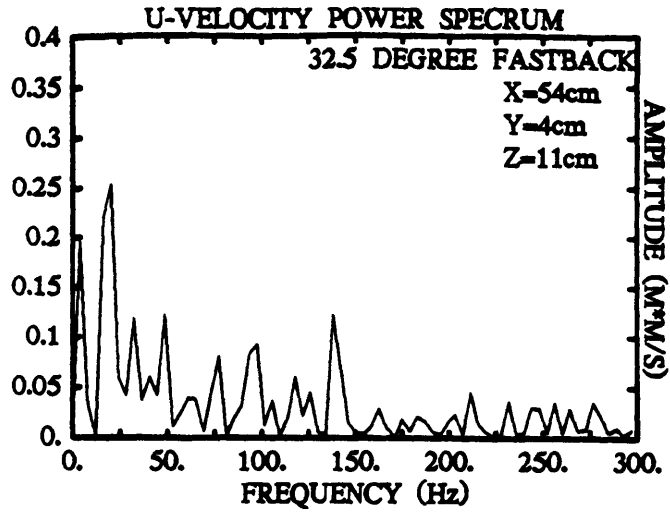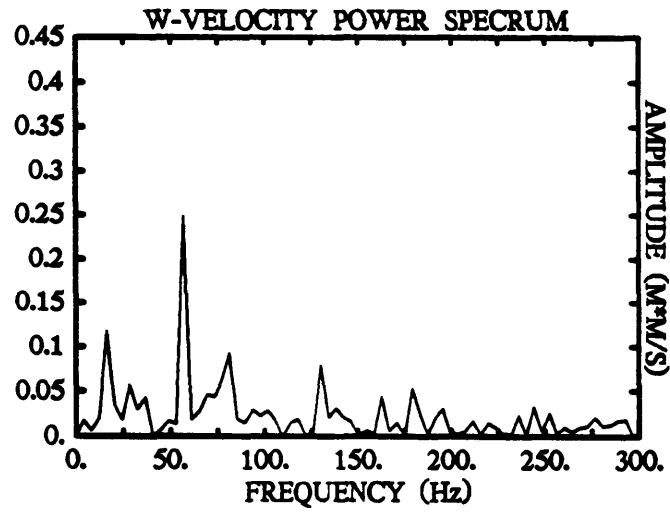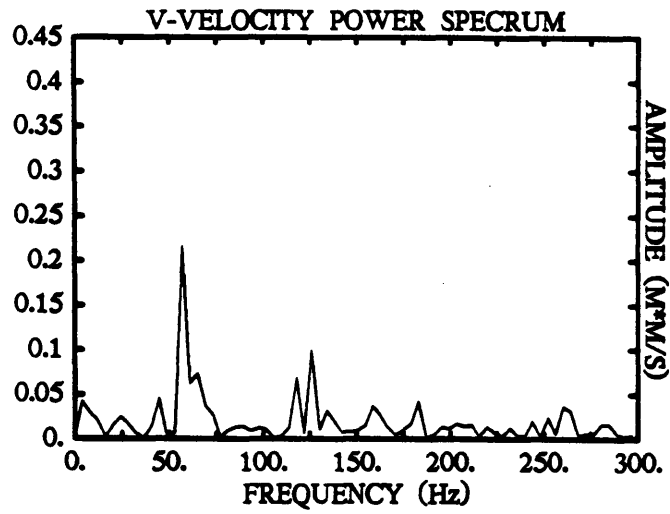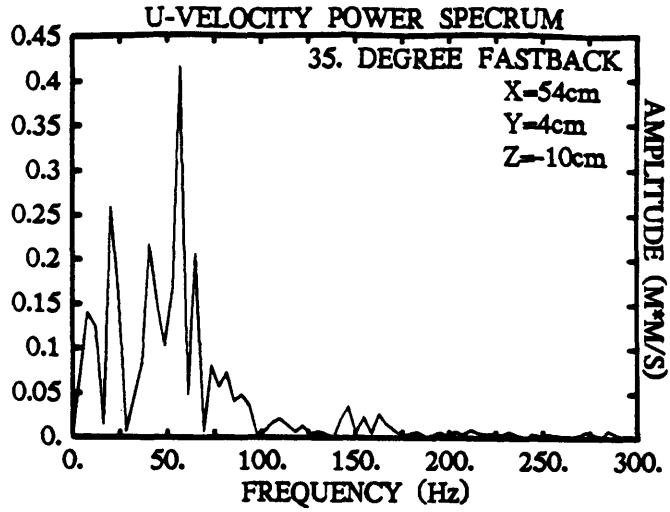Figure 5.46: Power spectra for right-hand side vortex core, 35° fastback, X=54 cm.
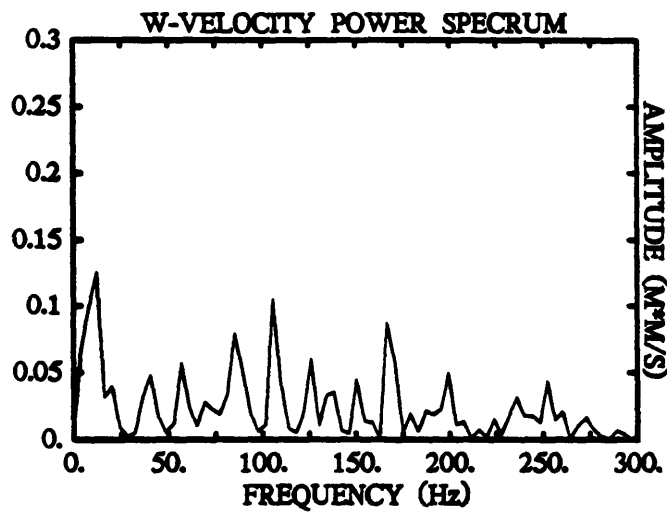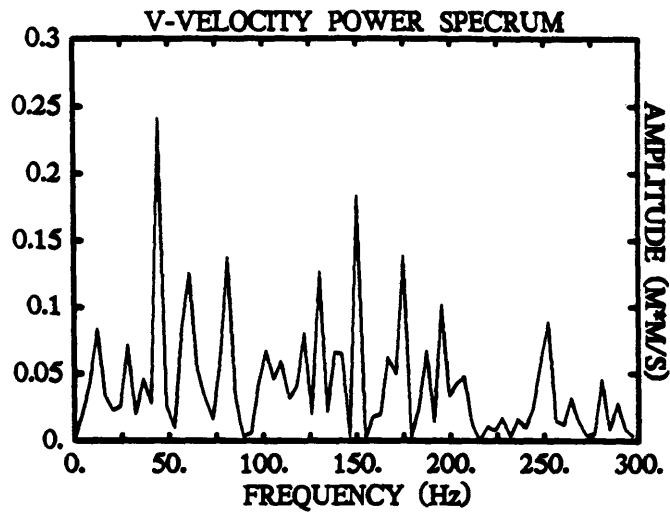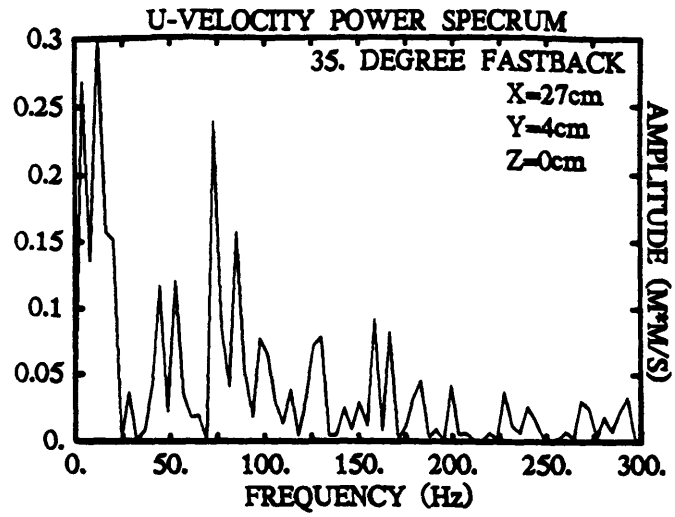
Figure 5.47: Centerline power spectra for the 35° fastback at X=27 cm.
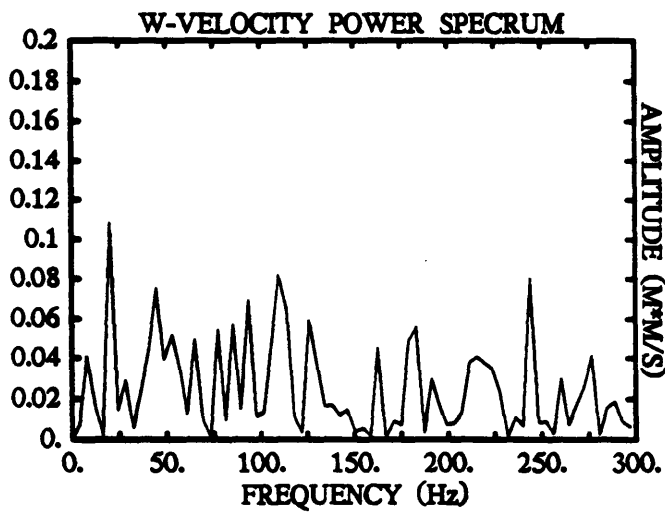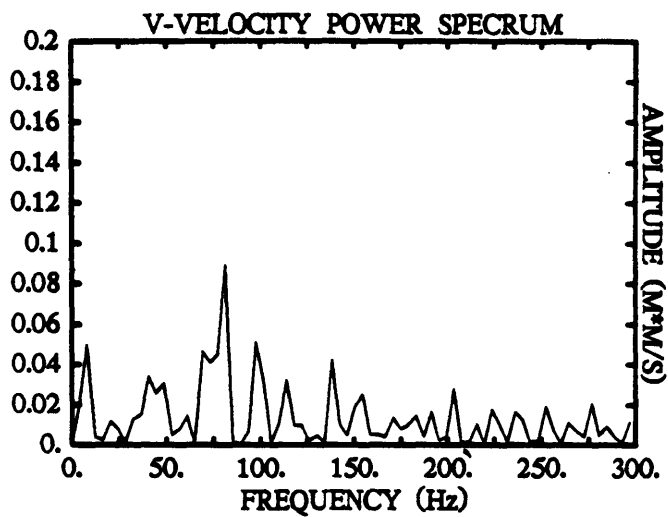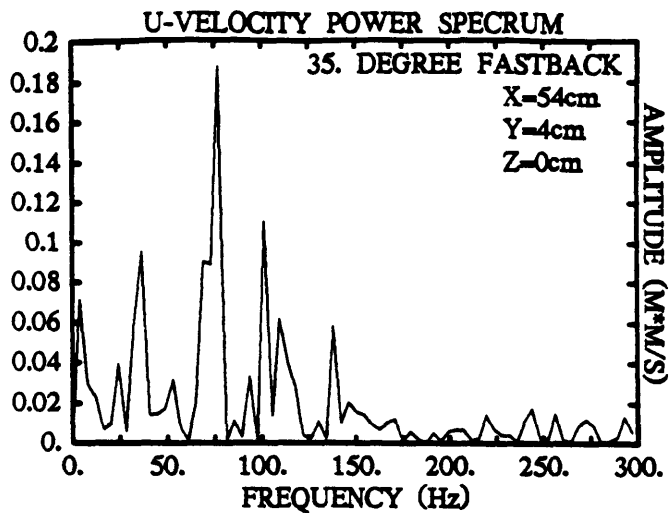
Figure 5.48: Centerline power spectra for the 35° fastback at X=54 cm.

Chapter 6

Conclusions and Recommendations

A new method of vehicle drag estimation based solely on wake mean and RMS velocity measurements was developed and tested. As pressure measurements were not necessary for the new method, wake surveys were conducted with hot-wire and hot-film velocity sensors. Two-dimensional x-wire probe measurements proved to be unreliable in the highly three-dimensional turbulent wakes of an automobile-like bluff body, and should not be considered for use in similar flow fields. Results from a three-component hot-film probe were very encouraging, although there were areas of questionable data due to the probe's inability to measure less than $-15°$ pitch angles when aligned in the flow. A solution for future use of similar probes in highly three-dimensional quasi-steady flows is to incline the probe at some pre-specified pitch angle, thereby shifting the linear region of pitch sensitivity to be centered at a pitch angle of zero. This would also permit the probe to measure closer to the groundplane in the wind tunnel used in this research.

The inability to measure closer than 3 cm to groundplane in this study resulted in some loss of information in the wake surveys, as the calculated drag ranged from 40% over-estimation to 18% under-estimation for various model geometries. Yet, measurements closer to the groundplane would add the effect of the groundplane drag, in terms the boundary layer momentum deficit, to the total drag estimated. This additional drag

would have to be removed in order to get a realistic drag estimation.

Turbulent velocity terms, nonexistent in Maskell's pressure based drag analysis, but measurable with hot-wire probes, add only about 4% to the total drag, compared to only mean velocity drag estimations.

Some power spectra were investigated, but only with a single ensemble of data. More accurate spectra can be obtained from these wakes with three- component probes by taking more ensembles of data.

Wake analysis of automobile-like bodies has been expanded with another method of drag estimation. Measurements of vehicle wakes with two-dimensional hot-wire and hot-film probes have indicated unexpected problems in measuring highly turbulent, three-dimensional flows. It is hoped that this research will act as a guide for future investigations into similar types of flows.

Appendix A

Model Force Balance

A.1 Balance Design

A two-component force balance is mounted inside the aluminum mid-body box structure. Lift and drag forces are measured by Interface Model SM-10 Super-Mini load cells, whose data cables are routed out of the model through the hollow strut. The Interface load cells are of standard resistor-bridge design. The balance is best described as two four-legged "tables" which permit measurement of forces in two perpendicular directions (lift and drag) and is shown in Figures A.1– A.2. Each "table" consists of an aluminum plate "table-top" mounted to four 4140 steel alloy flexures (legs). The "table-top" is displaced through a shearing motion of the flexures, permitting the load cells to directly measure the force in the direction of displacement (The displacement of the "tables" is on the order of micrometers). The lift load cell is mounted the strut mounting block, which is in turn mounted to the lift plate. Lift force is transmitted through the active end of the load cell by way of a loading beam which is attached to the drag plate. The drag load cell is mounted to the drag plate and the active end is connected to the bulkhead at the rear of the model mid-section. This table-on-a-table balance design allows for the sensing of only the required forces as the flexures resist any torques due to mechanical coupling the lift and drag "tables".

Load cell signals were conditioned by Vishay Measurements Group Model 2120 Amplifiers before being output them to the analog-to-digital converters connected to the same PDP-11/55 series computer that controls the traverser. Excitation voltages for the load cells were 14.000 volts for the drag channel and 13.750 volts for the lift channel. Output gain of the Vishay amplifiers was on the order of 1000. The A/D converter was a Phoenix Data Inc. Model No. DAS6000S capable of measuring up to sixteen channels with 12 bit resolution at a maximum multiplexed sampling frequency of 333 kHz. Geometry of the force balance structure inside the model dictated that only time-averaged values of the lift and drag forces could be obtained.

A.2 Balance Calibration

Calibration of the force balance consisted of hanging a series of weights on a wire connected to the lift and the drag axes of the model, not at the same time. Lift and drag channels were both recorded during independent lift and drag calibrations to determine the extent of any mechanical coupling of the balance. Coupling between the channels averaged less than one percent of the output voltage of the force being calibrated. Most of the coupling can be attributed to slight misalignments in the hanging weight calibration system. Results of the calibration yielded a simple linear relationship between the applied force and the load cell output, as seen in Figures A.3 and A.4. A least squares linear fit through the data yielded the following calibration curves for the drag and lift forces,

$$Drag = 1.397 D_{volts} - 0.382 \qquad \text{(A.1)}$$

$$Lift = 0.946L_{volts} - 0.00376 \hspace{3cm} \text{(A.2)}$$

where *Drag* and *Lift* are force in Newtons and D_{volts} and L_{volts} are the drag and lift voltages measured from the balance.

A.3 - Balance Operation

Continual operation of the balance signal amplifiers at high gains ($\sim$ 1000) leads to problems with instrument drift. To alleviate any problems associated with drift the following procedure was used to measure the forces on the model:

- Turn tunnel on to required velocity to settle the balance.

- Turn tunnel off, let flow stop completely and zero the balance amplifiers.

- Take zero velocity balance readings.

- Turn tunnel on to required velocity and take force data.

- Turn tunnel off and take a final zero once flow has stopped.

- Average the two zero readings and subtract from the force data to get the actual change in voltage.

- Use the change in voltage in the calibration equations to determine the model forces.

Using this procedure, repeatability of force balance measurements was less than ±1%.
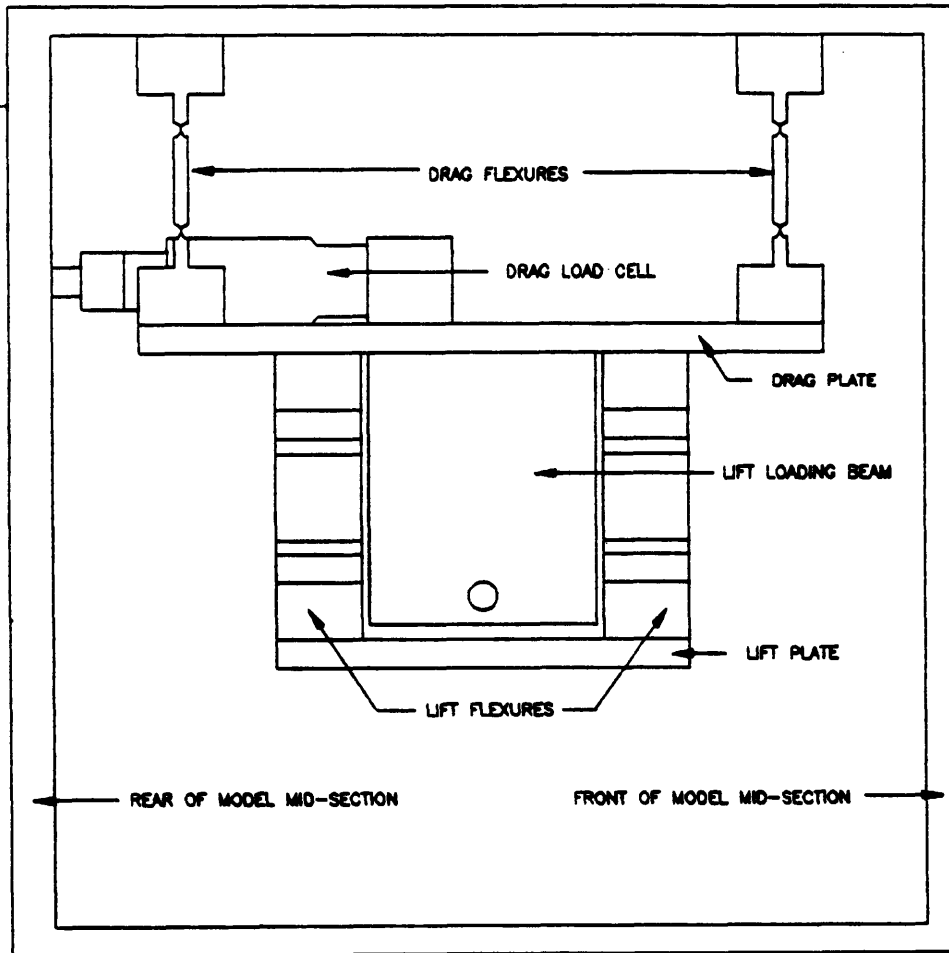
Figure A.1: Model force balance - top view.
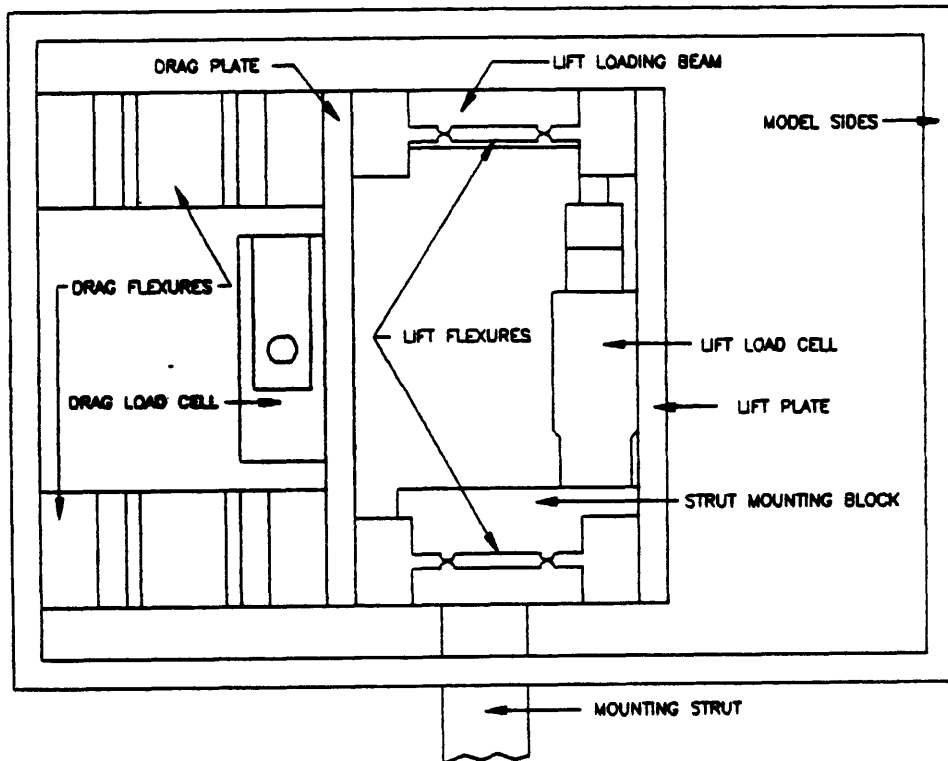
Figure A.2: Model force balance - cross-section view.

DRAG FORCE CALIBRATION
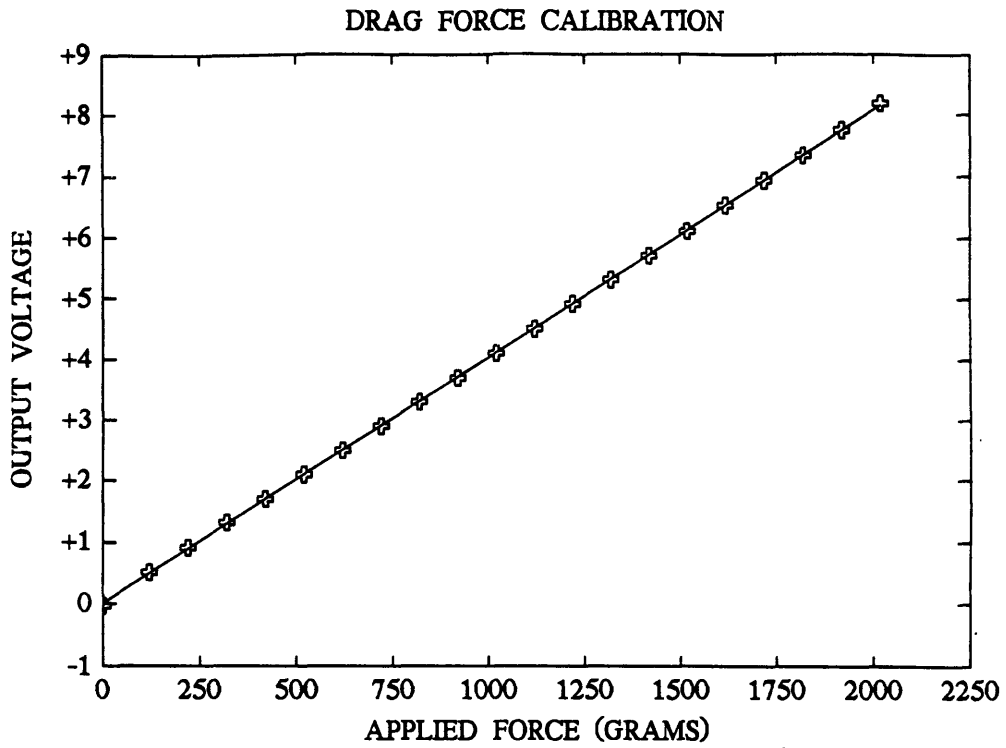
Figure A.3: Model balance drag force calibration.

LIFT FORCE CALIBRATION
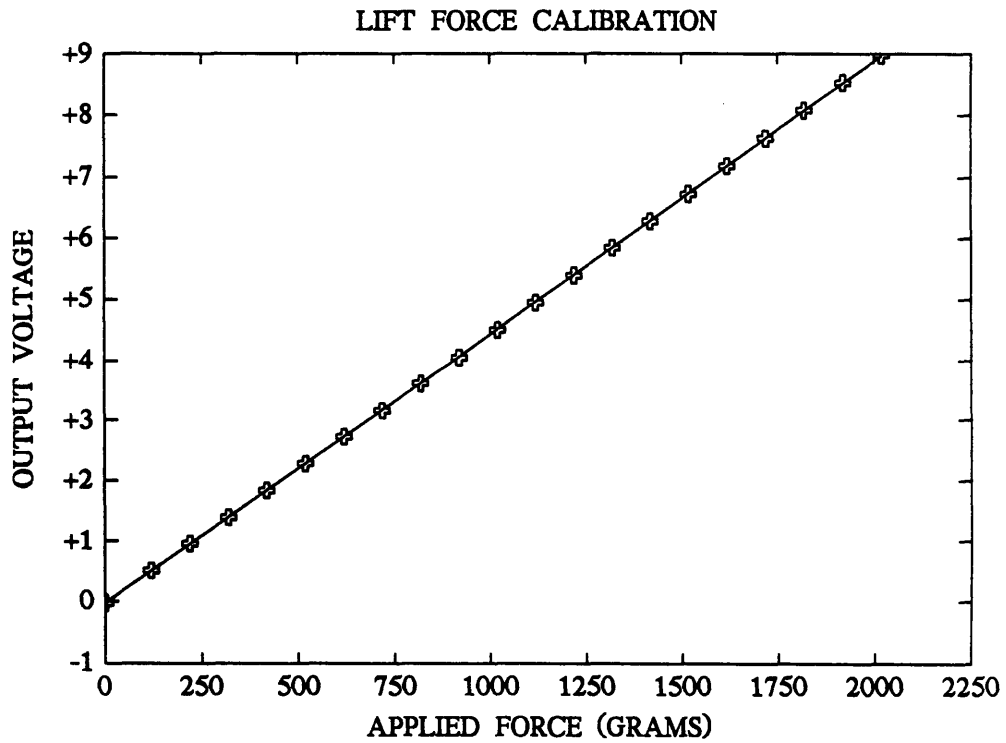
Figure A.4: Model balance lift force calibration.

Appendix B

Hot-Wire Probe Construction and Use

B.1 Hot-Wire Probe Construction

Two types of hot-wire probes were constructed in-house for flow field measurements. Single-wire probes were made to measure a single velocity component, u, and two-wire x-probes were made to measure two components of velocity, u and v or u and w, depending on probe orientation in the flow. Both types were constant temperature hot-wire annemometers and are described by the theory discussed by Blackwelder [9]. The sensing element for the probes was Platinum-10% Rodium wire formed by the Wollaston process. Wire diameter for the u-probes was nominally 2.54 μm while the x-probes utilized wires of diameter 1.27 μm. Figures B.1–B.2 illustrate the design details and dimensions of the probes. The sensing wires were supported by stainless steel jeweler's broaches of tip diameter 127 μm for the u-probes and 76 μm for the x-probes. Probe bodies were made from ceramic thermocouple tubing with holes for the broaches and wiring. Broaches, wiring, and electrical connectors were all epoxied to the ceramic tubes, with the epoxy forming part of the probe's supporting structure.

Hot-wires were constructed under a stereo microscope at 40 X magnification. A ruled eyepiece with scale graduations of 25.4 μm (0.001 in.) facilitated alignment and measurement of the probe tip positions and wire length. The sensing wire for the u-

probes had a length to diameter ratio of 300. The "box" for the x-probes was 508 μm on a side, resulting in a length to diameter ratio of approximately 565 for the sensing wires. Figure B.3 shows the attachment details of the hot-wires to the jeweler's broaches.

Hot-wire balance and amplifier circuitry was built in-house, the schematic of which is shown in Figure B.4. Of importance in the schematic are the two resistors labeled R_2 and R_3, which determine the resistance overheat ratio for the hot-wire, as defined by

$$a_R = \frac{R_2 + R_3}{R_3} - 1.$$
(B.1)

A resistance overheat of 20% was initially used for the u-probes but this was later changed to 33% for the x-probes so as to diminish the effects of wind tunnel temperature changes. Frequency throughput of the system with a single-component wire was 20 kHz, while throughput for both sensors of the x- wires was 25 kHz.

B.2 Hot-Wire Calibration and Use

B.2.1 U–Velocity Probes

U-probes were used for preliminary test section flow field evaluation after the ground plane was installed, as described in Appendix C. To calibrate, a u-probe was positioned in the free stream near a pitot-static tube locate just off the test section centerline and run through a series of seven or eight velocities between 1 and 25 m/sec. The hot-wire output voltages and pitot tube output for each velocity setting was recorded by the analog-to-digital converters controlled by the PDP computer. No filters or signal condi-

tioners were used on the hot-wire signal before being sampled by the a/d converters. A cubic polynomial was then fit to the data with a least squares method and resulted in an equation for U as a function of hot-wire voltage. The error between the calibration data and the polynomial fit was kept below $\pm 0.3\%$. Probe drift was measured after each data run and if it exceded $\pm 0.8\%$ the probe was recalibrated before the next run.

B.2.2 - X-Wire Probes

Calibration of x-probes was by the Polar Look-up Table method developed by Gresko [12], an enhancement of the Cartesian Look-up Table scheme described by Lueptow, Breuer and Haritonidis [20]. The Polar Look-up Table methodology is described below.

The probe is installed in the test section adjacent to the pitot-static tube. The airspeed is set to a series velocities and at each velocity the probe is rotated through a series of angles, θ_j. Velocity, Q_n, from the pitot tube and the two voltages from the two wires are recorded at each probe angle-velocity combination and the look-up table then generated after the measurements are completed. Generation of the look-up table consists of first locating each voltage-velocity pair on cartesian axes, the X-axis being one of the wire voltages, E_1, and the Y-axis being the other voltage, E_2. The cartesian coordinates are replaced with their polar equivalents, r and β after adjusting for a translation of the origin. Origin of the polar grid is found from the maximum angular width of the output voltages E_1 and E_2 at each velocity Q and angle θ. The complete procedure is detailed in Gresko [12], and the remaining steps are diagrammed in Figures B.5 and B.6.

- Using cubic-spline fits determine $\beta = \beta(r)|_{\theta_j}$ and $Q = Q(r)|_{\theta_j}$.

180

- At regular intervals of r, determine β and Q at constant θ.

- Using cubic-spline fits determine $Q = Q(\beta)|_r$ and $\theta = \theta(\beta)|_r$.

- At regular intervals of β, determine Q and θ which gives (Q,θ) at every (r,β) grid point. Finally convert (Q,θ) to (u,v) using

$$u = Q\cos\theta \qquad\qquad (B.2)$$

$$v = Q\sin\theta.$$

A 30×30 polar grid, based on seven velocities in the range $2\text{m/s} \leq Q \leq 25\text{m/s}$, and eleven angles in the range $-40° \leq \theta \leq +40°$ made up the standard calibration. The maximum calibration error in u and v was no more than 0.1% at angles up to $\pm32°$ and ocassionally went as high as 0.3% at angles of $\pm40°$. Drift was measured to to be no more than $\pm2\%$ at the end of a data run.

A data run consisted of a probe calibration followed by data acquisition. Calibrations took approximately 15 minutes to complete, after which the probe was positioned for the data run. For wake plane surveys, a data run consisted of no more than 370 data points, and took no more 37 minutes to complete. Temperature increases in the tunnel during a run were minimized by running the tunnel for a period of two hours prior the first data run each day. After this initial warming of the tunnel, a total temperature increase of less than than 3° Celsius was recorded over a period of 8 hours. Therefore, temperature increases during each individual data run were negligible.

181

B.3 Measurement of u-v and u-w Velocities

X-probes are capable of measuring only two components of velocity, either u and v, or u and w. To measure u-v the wires are aligned parallel to a plane that is perpendicular to the ground plane, as shown in Figure B.7. The probe is calibrated for u-v measurements by rotating it through angles that lie in this perpendicular plane. To measure u-w, the entire probe assembly is rotated 90° so that the wires are now parallel to the ground plane. The probe is rotated in a plane parallel to the ground plane for u-w calibration.

U—Wire Tip Details
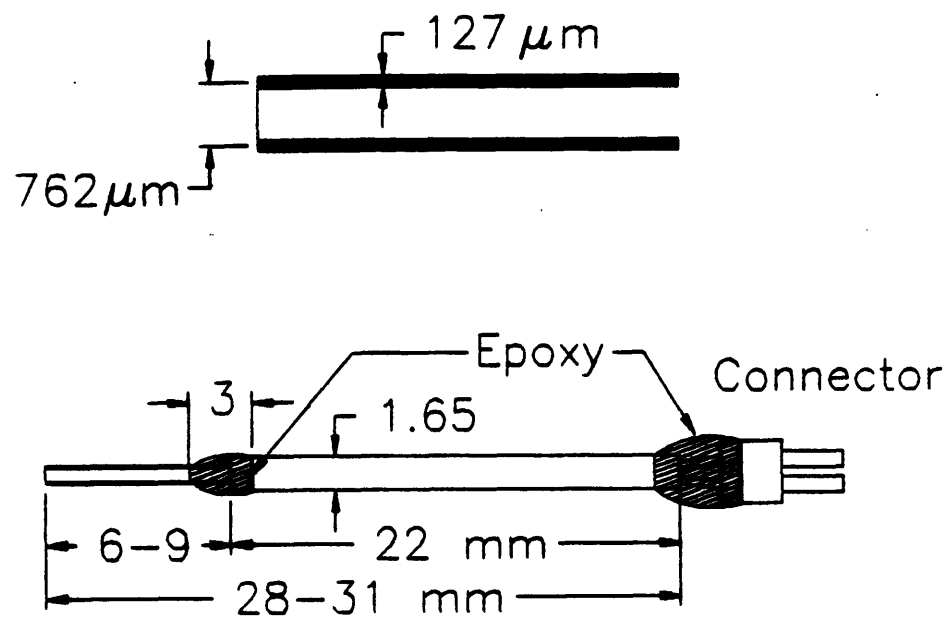
Figure B.1: Schematic of u-probe hot-wire.
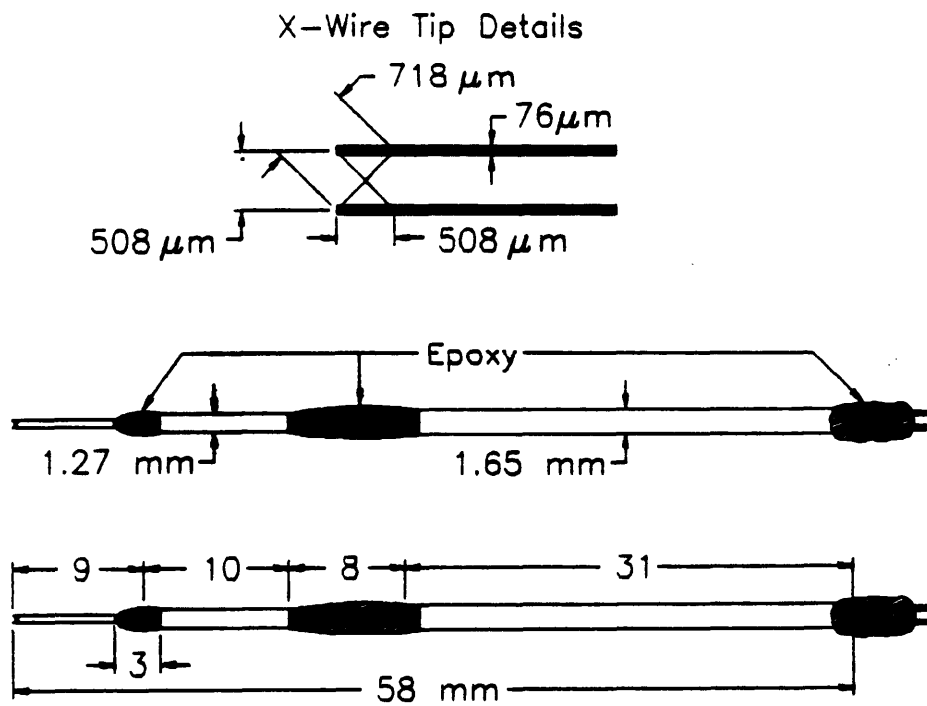
Figure B.2: Schematic of x-probe hot-wire.

STAINLESS STEEL
JEWELER'S BROACH

Pt-10%Rd Wire

SOLDER - SN60 ALLOY

TOP VIEW

SIDE VIEW
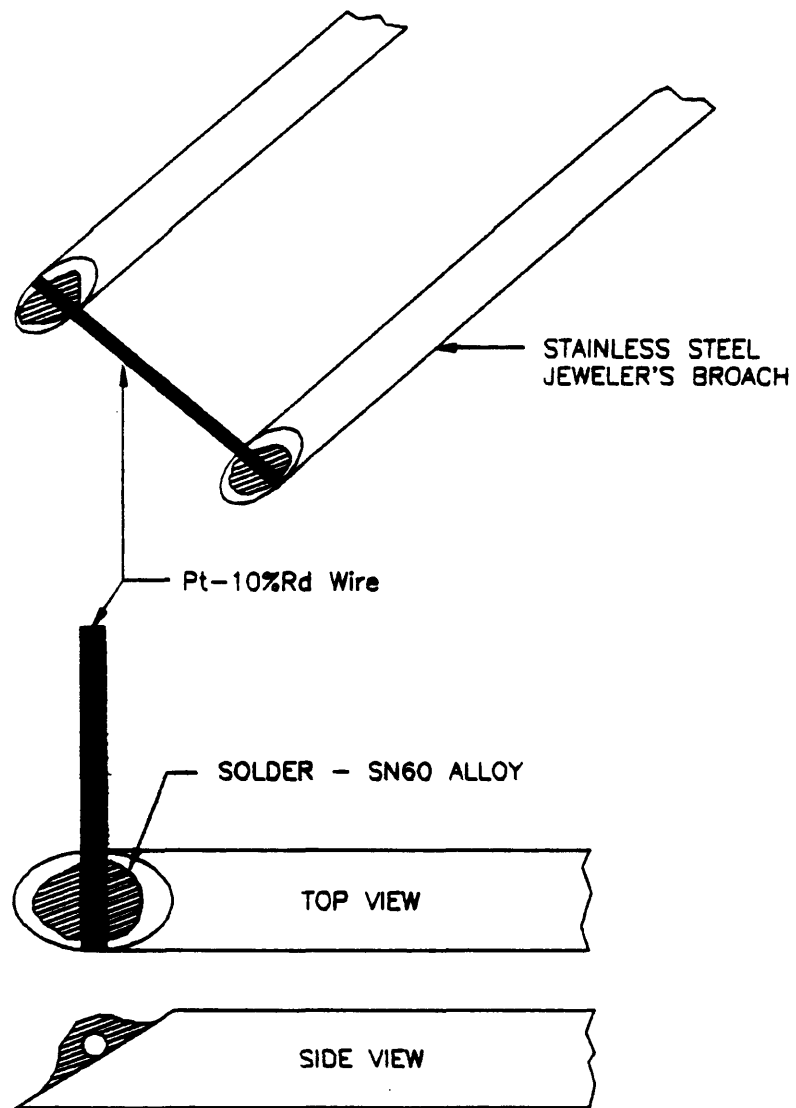
Figure B.3: Details of hot-wire attachment to jeweler's broach supports.
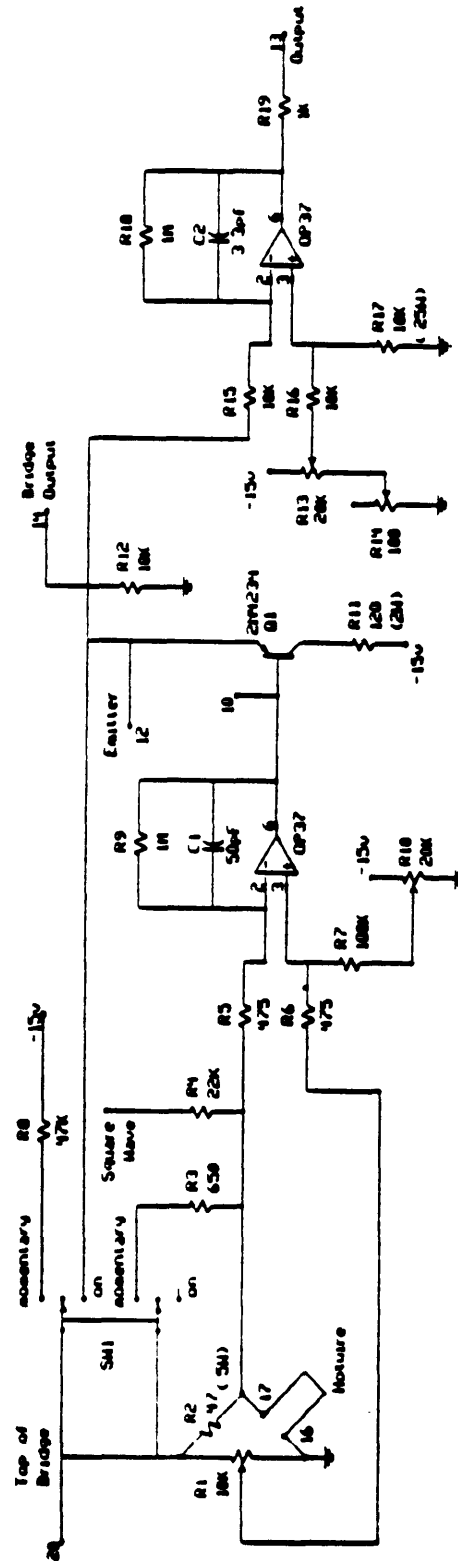
Figure B.4: Hot-wire annemometry circuit schematic.
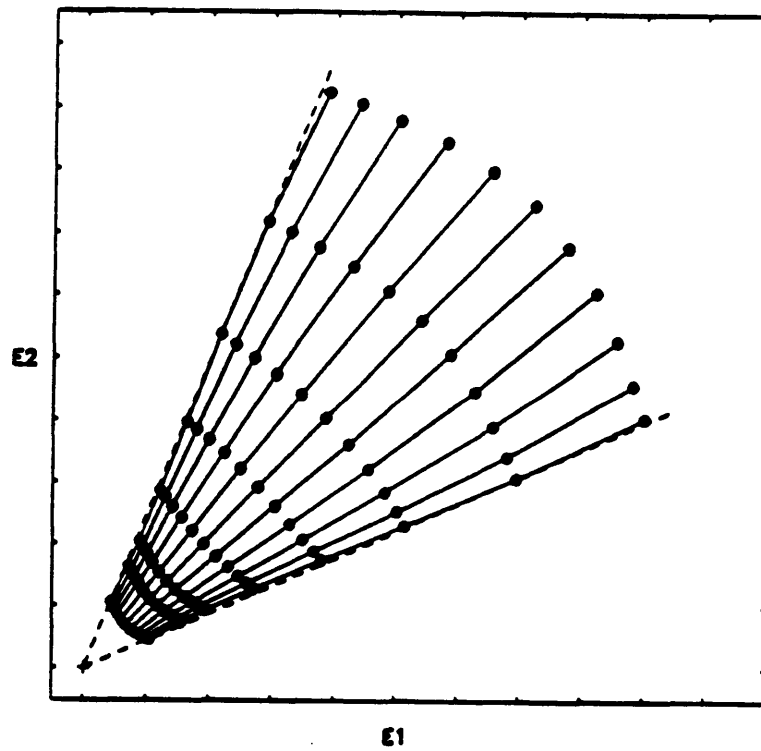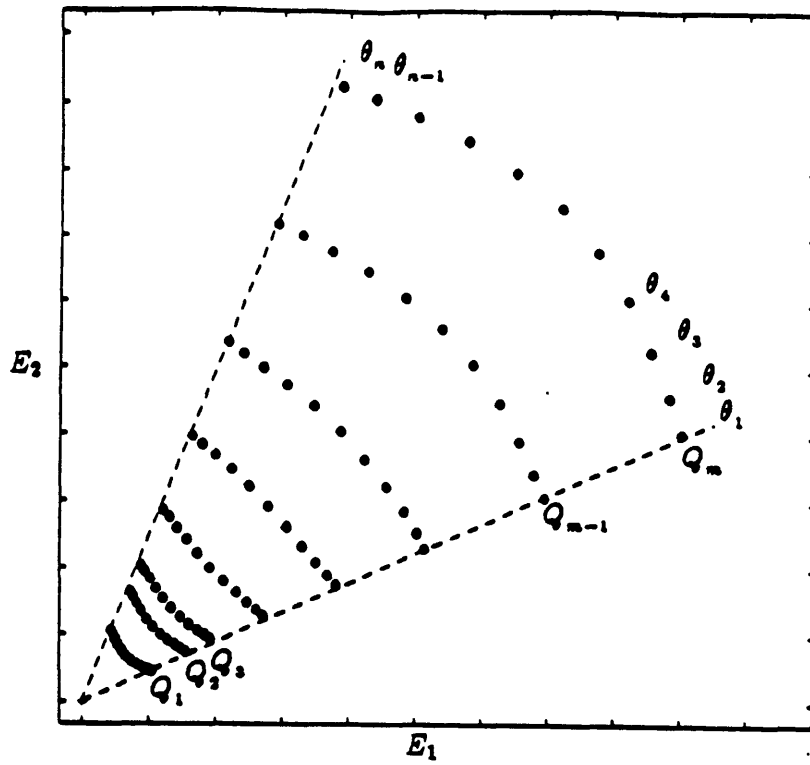
Figure B.5: Development of the polar calibration grid - Part 1: (a) the origin of the polar grid is found; (b) n cubic splines are fit at each angle θ for Q and β as functions of r.
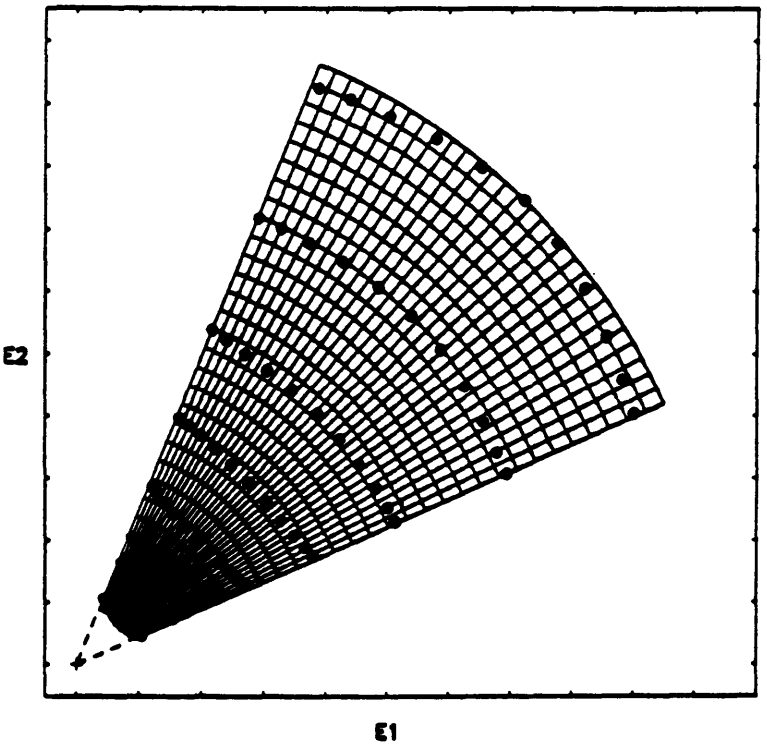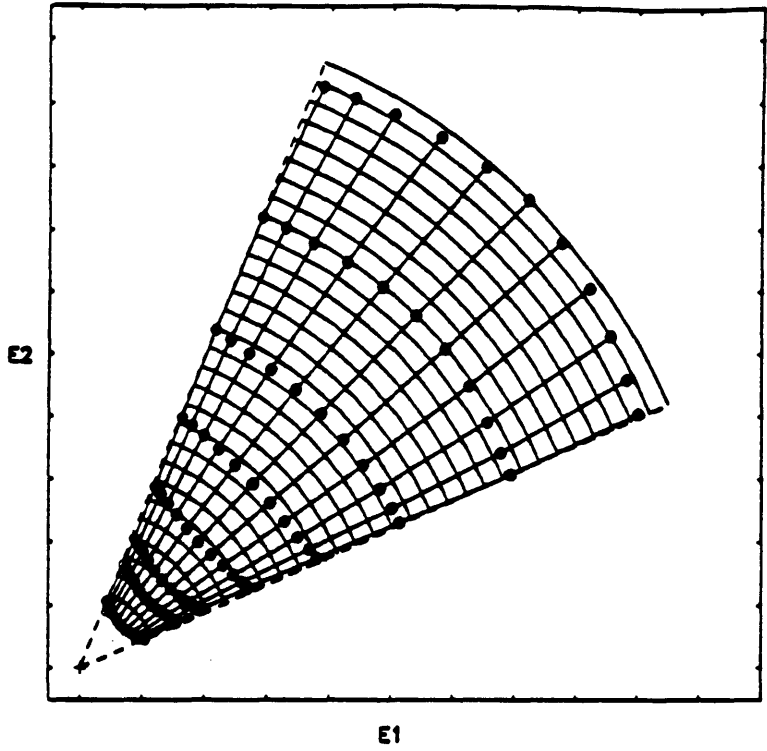
Figure B.6: Development of the polar calibration - Part 2: (c) Q and β are evaluated at regular intervals of r, and (d) Q and θ are evaluated at regular intervals of β.
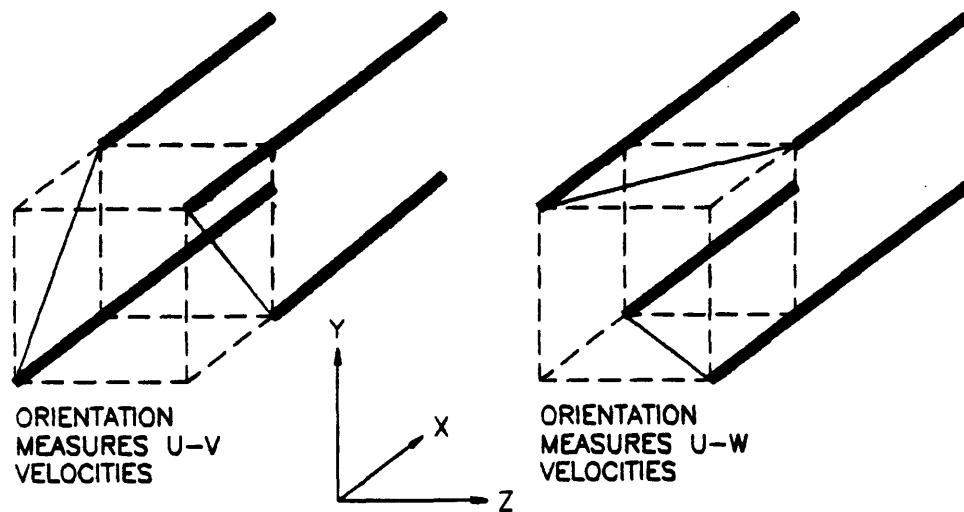
Figure B.7: X-probe orientations for measurement of u-v velocities and u-w velocities.

Appendix C

Empty Test Section Flow Field

Velocity calibration of the test section was conducted to determine the range of Reynolds numbers available. The flow field in the test section with the ground plane installed was surveyed with a single velocity component hot wire probe to observe the quality of the flow and to determine the effect of the flap angle setting on the inlet flow conditions near the leading edge of the ground plane. The model was not installed in the test section for these tests.

C.1 Test Section Velocity Calibration

Calibration of the test section velocity consisted of pressure measurements from a pitot-static tube inserted into the flow through the ceiling just off the centerline of the test section at an X-location which corresponds to the front of the model when it is installed. Speeds available range up to 43 m/sec, but not without problems. At speeds starting around 22 m/sec an acoustic feedback is set up by the interaction of the wake of the traverser and the flow between the traverser and the side walls of the tunnel, resulting in a very loud whistling (greater than 110 db) at frequencies of approximately 340 Hz and 380 Hz. Besides the annoyance factor of the noise itself, the standing waves of the associated pressure field extend far up and downstream thereby modifying the

190

flow fields of interest. Parker studied this type of acoustic mode in the late 1960's [28], [27] and discussed some methods to reduce the strength of the standing waves. There are two simple methods that could be applied to the wind tunnel to diminish the standing wave. The first is to completely streamline the traverser so as to suppress the shedding of vorticity into its wake. As the traverser must be allowed to move freely in the Z-direction, and any streamlining attachments would severely restrict the limits of motion, streamlining was therefore not considered as a viable alternative. The other posibility is to increase the level of turbulence of the flow as it passes over the traverser so as to decrease any organized vortex shedding. This was attempted by attaching a series of one centimeter tall vortex generators on both sides of the front of the traverser, resulting in a significant decrease in the sound level, but not the desired elimination. Unfortunately, any attachments to the surface of the traverser interfere with its motion in the Z-direction, and are therefore unacceptable solutions to the acoustic problem. The solution chosen was to run the tunnel at lower speeds, with 20 m/sec chosen as the top speed so as to avoid any acoustic problems. At 20 m/sec, the Reynolds number, based on equivalent body diameter, is approximately 270,000.

C.2 Flow Field Near The Leading Edge

Two rows of small tufts spanning the width of the ground plane were attached at X-locations of 5 cm and 10 cm downstream of the leading edge to observe if there was any visible flow separation in this critical area of the flow. None was observed at flap settings of $0°$, $-5°$, $-10°$. This was the expected result as the leading edge's elliptic shape was intended to prevent any separation from occurring. Hot wire measurements of the mean velocity and turbulence levels were then carried out in this region to verify

what was observed visually.

The hot wire probe was located at a single X location on the centerline, X=10 cm, and at two Y locations, Y=0.5 and Y=1.0 cm above the ground plane for a series of turbulence measurements with the Reynolds number and the flap angle as the adjustable parameters. The results are seen in Figure C.1, where turbulence level (in percent) is plotted as a function of the Reynolds number per meter, Re_m. Overall effectiveness of the flap is obvious, as the turbulence level decreases in both Y locations with increasing flap angle, particularly at lower values of Re_m. In the inner boundary layer, Y=0.5 cm, the effect is more dramatic, as the the lower velocities there are more sensitive to pressure variations caused by the different flap angles. Towards the outer edge of the boundary layer, at Y=1.0 cm, there is very little difference between the turbulence levels for flap angles of $-5°$ and $-10°$, especially at higher e_m. Between the elliptic leading edge and the trailing edge flap, the pressure field near the leading edge is controlled such that the boundary layer exhibits no separation.

Profiles of the boundary layer turbulence for each flap setting, as a function of Y are seen in Figures C.2–C.4, with the three profiles corresponding to free stream velocities of approximately 10, 15, and 20 m/sec. Once again it can be seen that the 0° flap setting differs slightly from the $-5°$ and $-10°$ settings, but the differences between the $-5°$ and $-10°$ cases are too small to note. After viewing the data it was decided that a flap setting of $-5°$ would be the most effective in reducing leading edge effects without increasing the above ground plane blockage substantially.

C.3 Mean Flow And Turbulence Profiles On And Off The Centerline

Boundary layer and almost full test section height profiles were measured at two X locations, $X=10$ cm and $X=45.1$ cm, the second position corresponding to the flow entry plane at the front of the model when it is installed. Free stream velocity for these and all-the following data was approximately 20 m/sec. Figures C.5 and C.6 show the turbulence and normalized boundary layer profiles for $X=10$ cm at the centerline and at two points one-half body width on either side of the centerline. Within the initial positioning accuracy of ±0.05 cm, the curves are essentially the same. These profiles for $X=45.1$ cm are seen in Figures C.7 and C.8, and again, the similarity of the profiles is noted. The boundary layer is a fully developed, turbulent profile at both X locations.

The velocity field to a height of 34 cm was measured at five Z locations, on the centerline, at $\pm$one-half body width, and at $\pm$one-and-one-half body widths. Normalized velocity profiles are shown in Figures C.9 and C.10 and the corresponding non-normalized profiles are shown in Figures C.11 and C.12. The effect of the leading edge is seen as an acceleration of the flow near the ground plane in the profiles at $X=10$ cm, and result in an increase in velocity of about five percent the mean flow. Once the flow arrives at the model entry plane the leading edge effect has been completely smoothed out by the flow. Normalized velocity profiles show good similarity of the flow at all five profile locations, but there appears to be about a three percent difference in absolute velocities between the individual profiles at both the X locations.

Free-stream turbulence was measured to be below 0.22% at both the inlet plane ($X=10$ cm) and at the model inlet plane ($X=45.1$ cm) independent of the flap setting.

C.4 Data Plane Location Boundary Layers

Boundary layer profiles were also measured at the two locations downstream of the model where the wake surveys were to be performed, at $X = 27$ cm and $X = 54$ cm beyond the end of the model. These profiles were measured without the model in place to determine the undisturbed boundary layer thickness. Profiles were taken at three spanwise locations, the centerline $(Z = 0)$ and at ± 10.5 cm, the spanwise limits of the model width. Figures C.13 and C.14 show the profiles. The boundary layer thickness at $X = 27$ cm is just over 20mm, and the thickness at $X = 54$ cm is almost 30mm. For reference, the height of the model above the groundplane is 30mm.
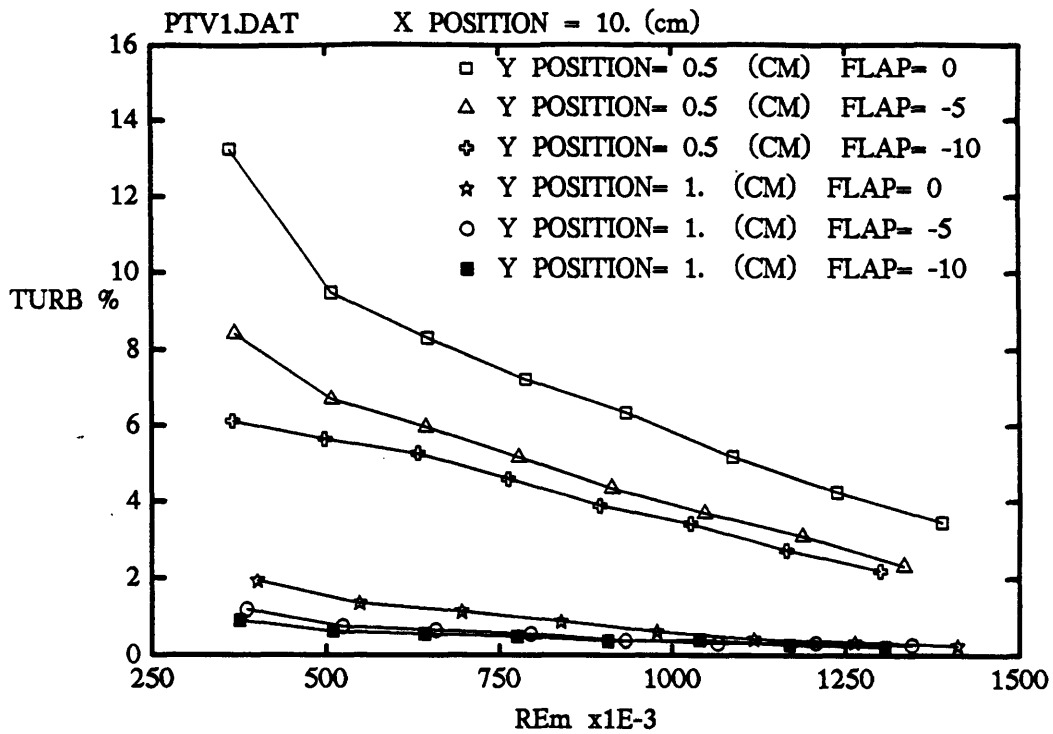
Figure C.1: Variation of turbulence with flap angle and Reynolds number.
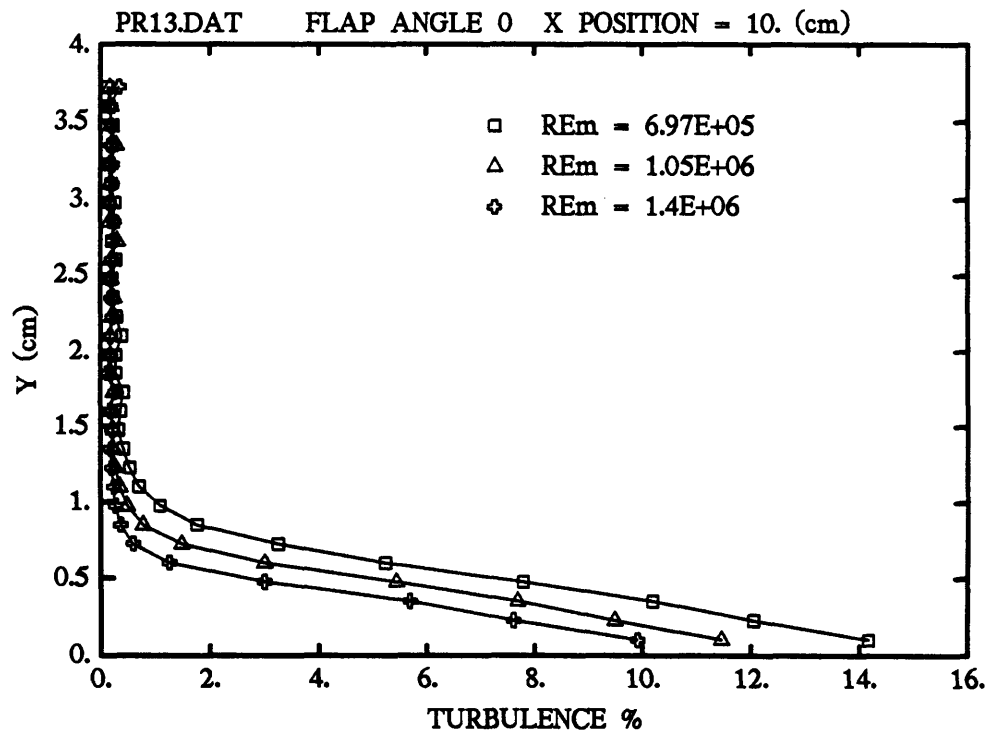
Figure C.2: Turbulence profiles in the inlet boundary layer, flap setting=0°.

195
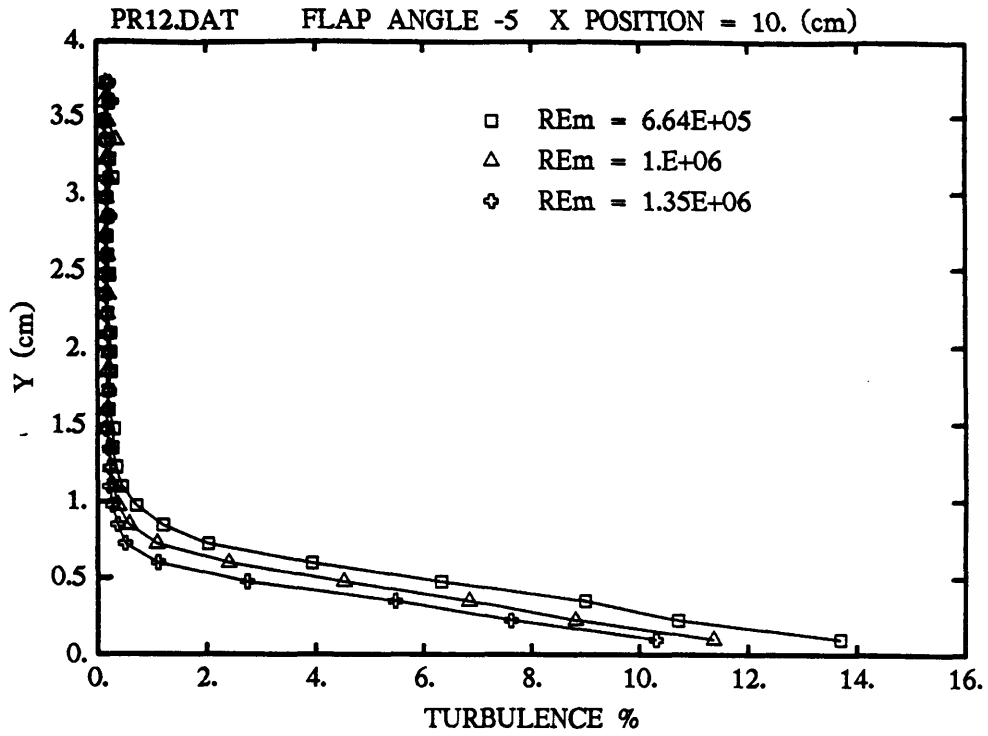
Figure C.3: Turbulence profiles in the inlet boundary layer, flap setting=−5°.
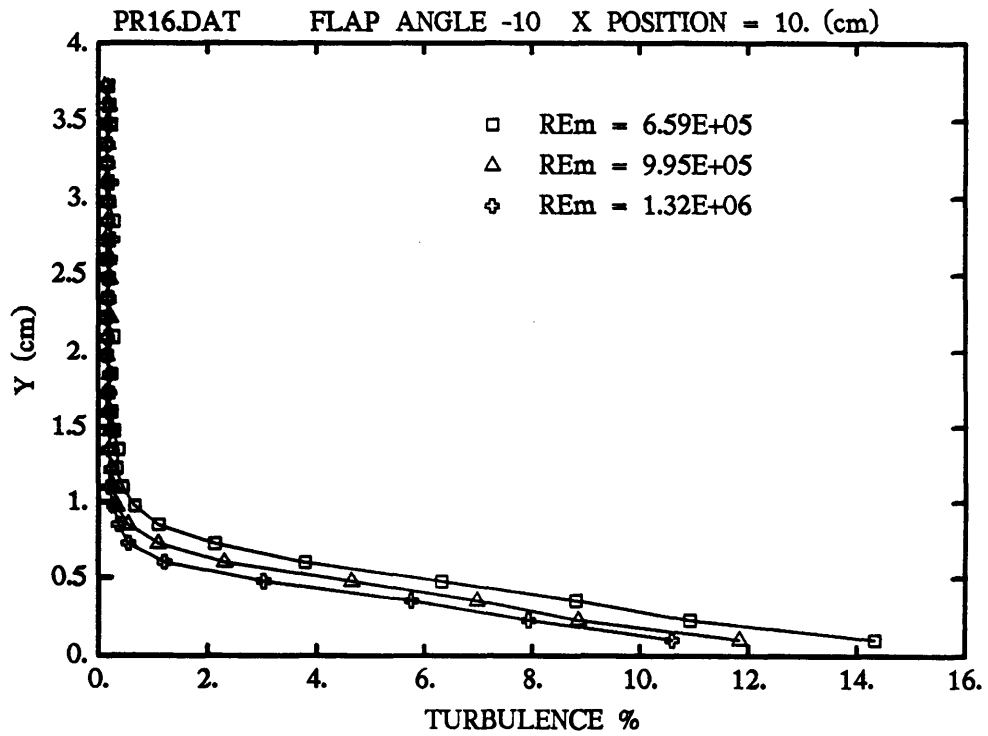
Figure C.4: Turbulence profiles in the inlet boundary layer, flap setting=−10°.
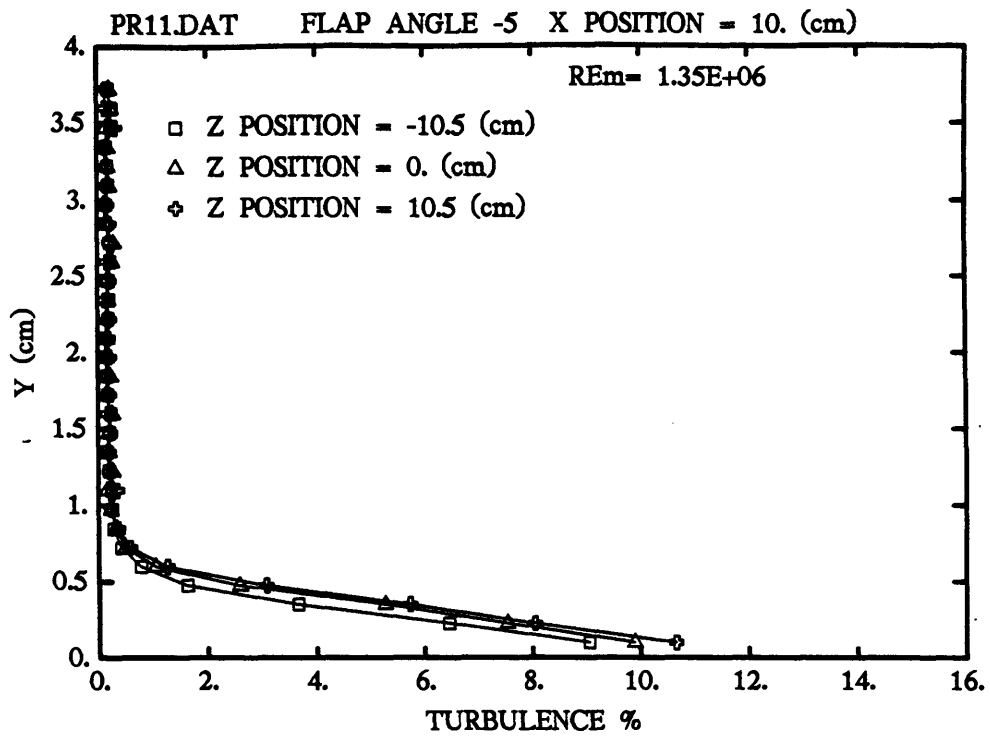
Figure C.5: Turbulence profiles in the inlet boundary layer on and off the centerline.
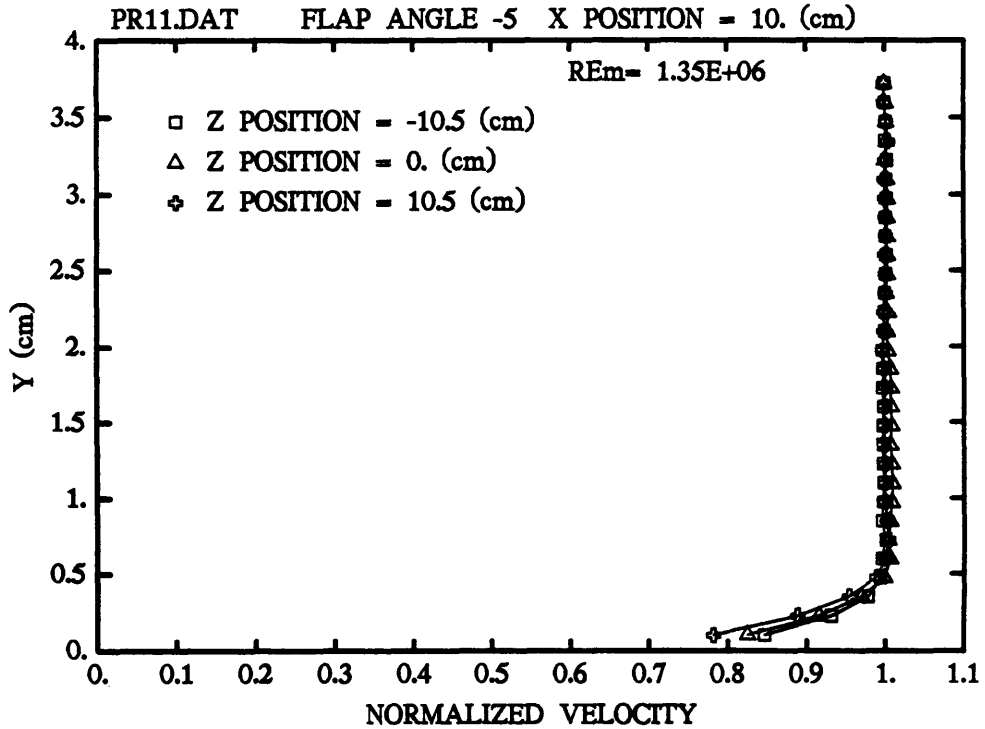
Figure C.6: Velocity profiles in the inlet boundary layer on and off the centerline.

PR11.DAT   FLAP ANGLE -5   X POSITION = 45.1 (cm)

REm= 1.33E+06

□ Z POSITION = -10.5 (cm)
△ Z POSITION = 0. (cm)
✧ Z POSITION = 10.5 (cm)

Y (cm)
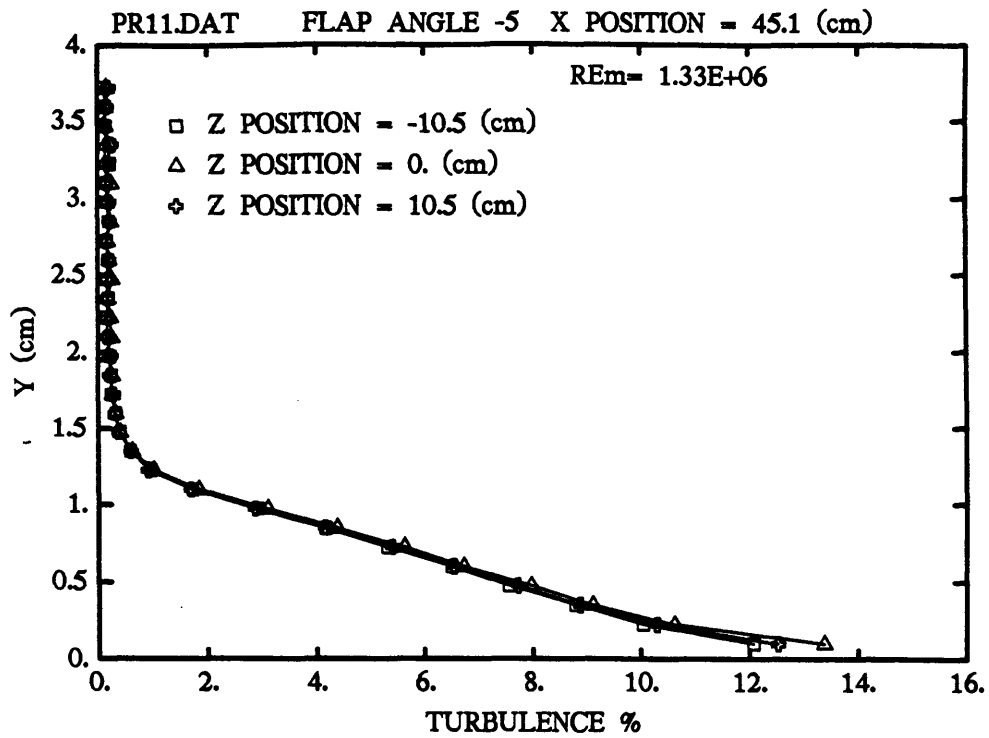
TURBULENCE %

Figure C.7: Turbulence profiles in the model inlet boundary layer on and off the centerline.

PR11.DAT   FLAP ANGLE -5   X POSITION = 45.1 (cm)

REm= 1.33E+06

□ Z POSITION = -10.5 (cm)
△ Z POSITION = 0. (cm)
✧ Z POSITION = 10.5 (cm)

Y (cm)

NORMALIZED VELOCITY
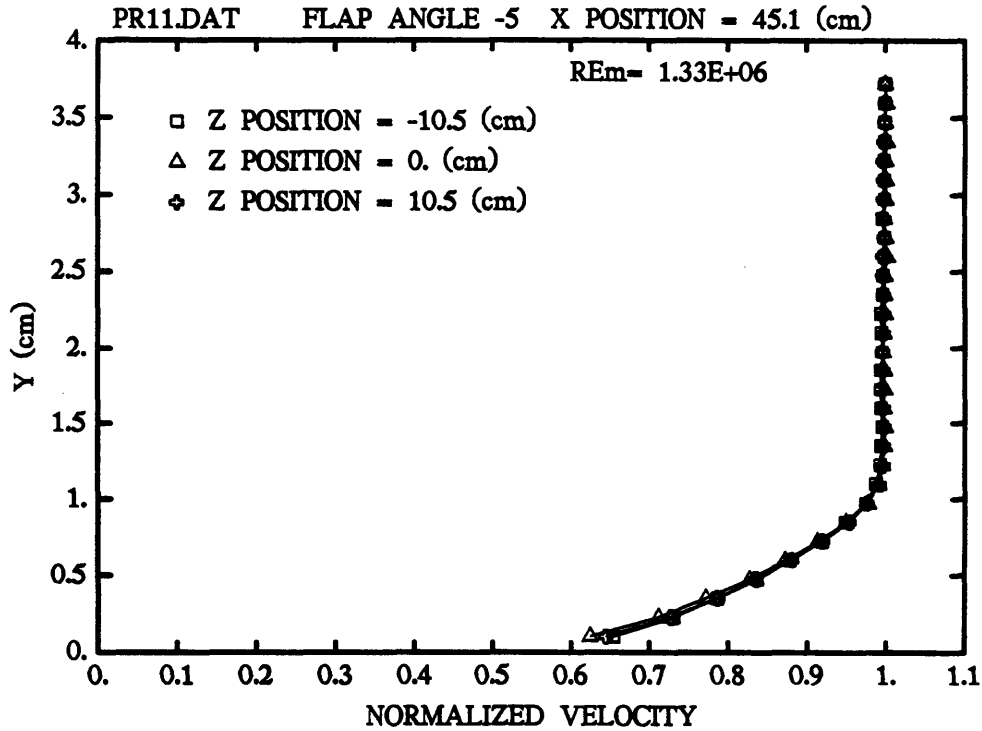
Figure C.8: Velocity profiles in the model inlet boundary layer on and off the centerline.

PR10.DAT   FLAP ANGLE -5   X POSITION = 10. (cm)
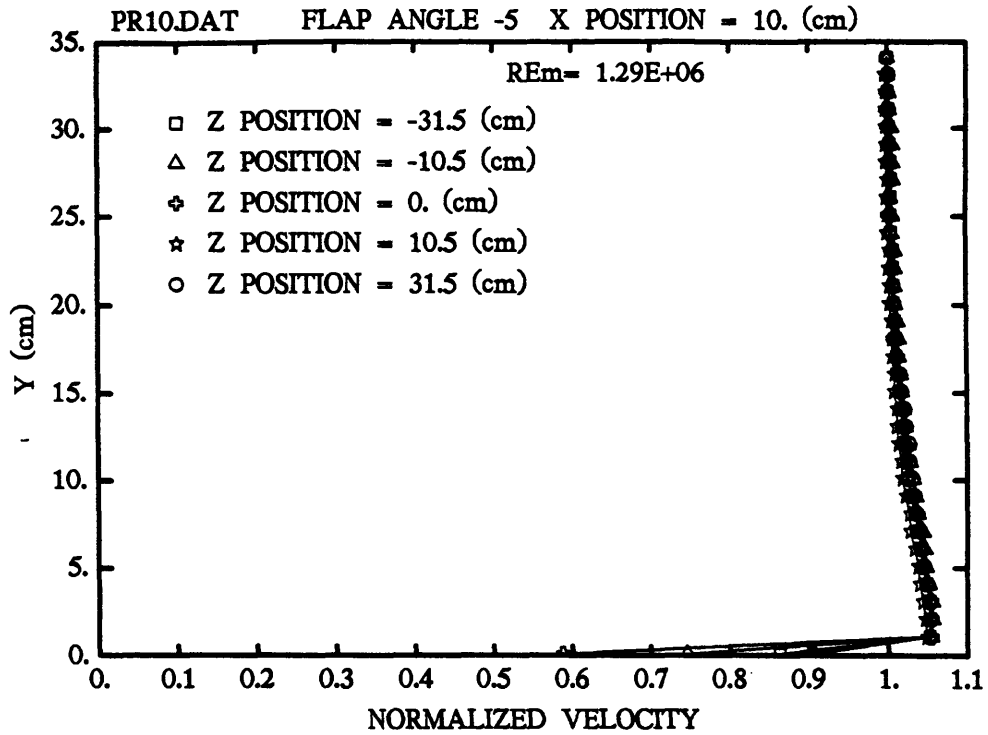
Figure C.9: Normalized velocity profiles across the test section at the inlet plane, on and off the centerline.

PR10.DAT   FLAP ANGLE -5   X POSITION = 45.1 (cm)
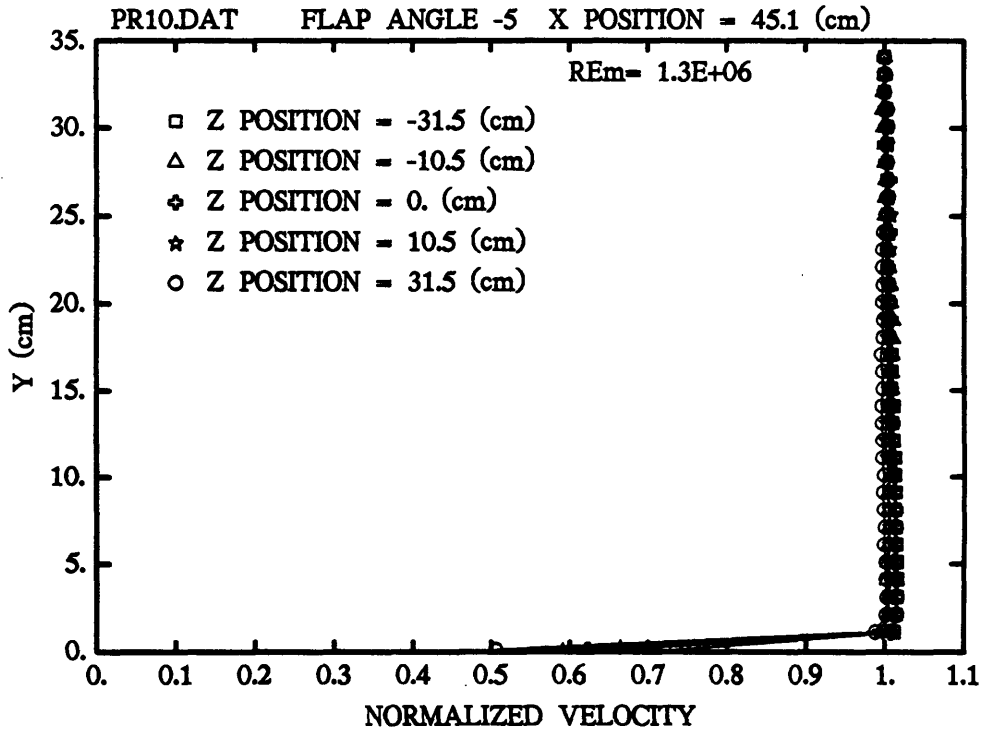
Figure C.10: Normalized velocity profiles across the test section at the model inlet plane, on and off the centerline.

199
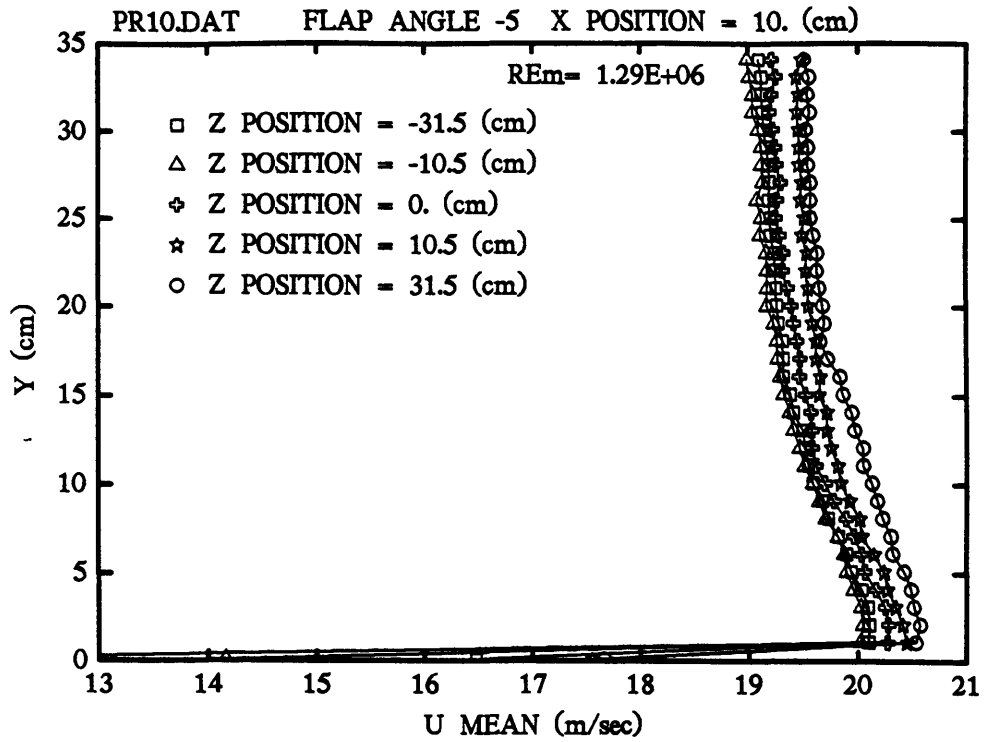
Figure C.11: Velocity profiles across the test section at the inlet plane, on and off the centerline.
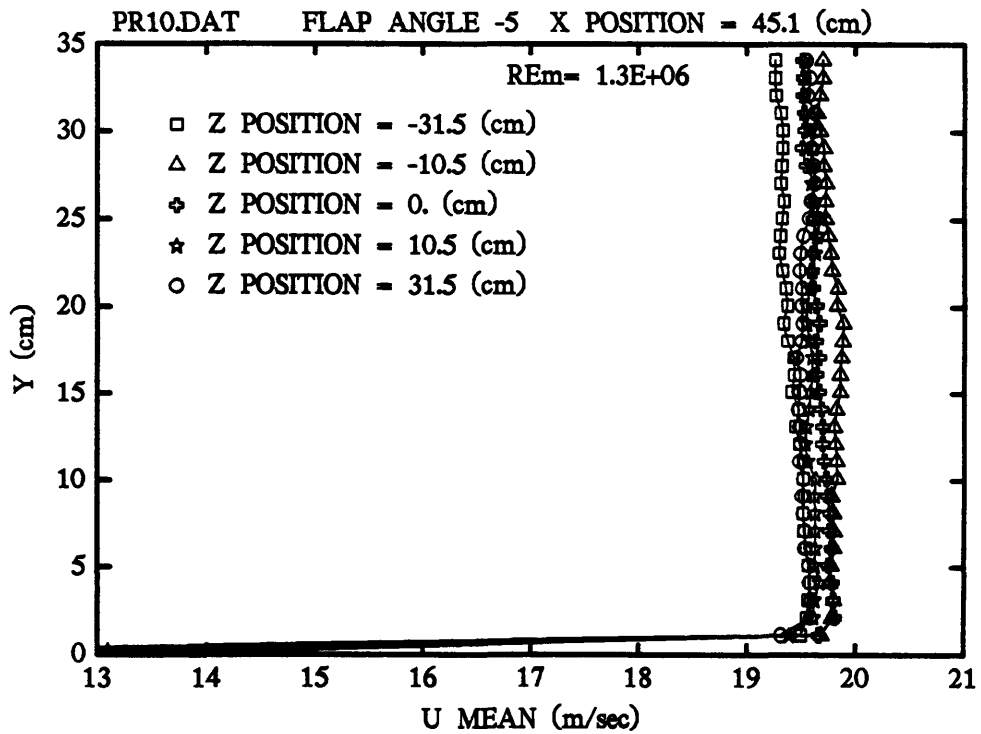
Figure C.12: Velocity profiles across the test section at the model inlet plane, on and off the centerline.

MEAN BOUNDARY LAYER PROFILES   X=27CM
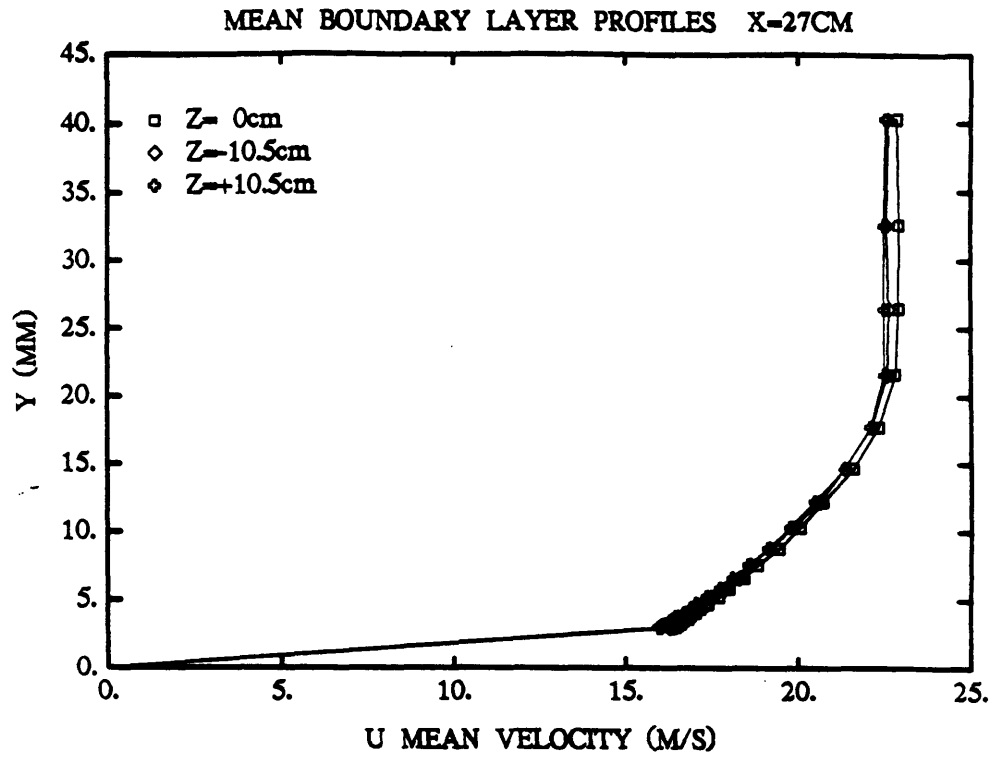
Figure C.13: Boundary layer profiles at $X = 27$ cm wake plane.

MEAN BOUNDARY LAYER PROFILES   X=54CM
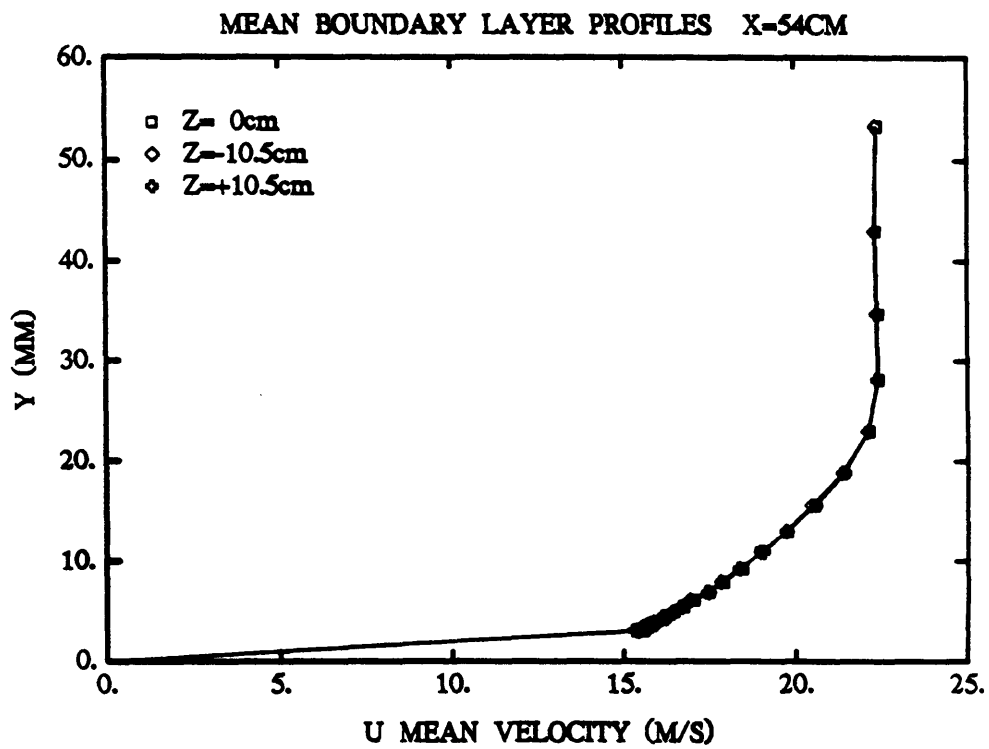
Figure C.14: Boundary layer profiles at $X = 54$ cm wake plane.

Appendix D

Three Component Hot-Film Probes:

Calibration And Use

D.1 Three-Component Probe Geometry And Support Equipment

Due to the measurement constraints inherent in two-dimensional X-wire probes, commercially available three component hot-films were utilized for the wake measurements. The probes used were TSI Model 1294 platinum hot-films consisting of three sensor elements spaced radially at 120° increments around a circle and swept back at an angle of 35.26°, details of which are shown in Figure D.1. Sensor elements consist of high purity platinum bonded to a cylindrical fused quartz substrate 0.05 mm in diameter. The sensors are then coated with alumina to protect the platinum film from abrasive particles. Sensor supports are made of gold for the best possible electrical connection to the platinum film. Sensor supports are connected to a cylindrical strut 4.6 mm in diameter and 457 mm in length.

Hot-films were attached to DISA anemometers Type 55M01. Outputs from the anemometers were routed to a Data Translation DT-2801-A 12 bit analog-to-digital converter installed in an IBM XT Model 286 computer. Maximum sampling frequency

for the Data Translation unit was 25 kHz, resulting in a sampling frequency of 8.333 kHz per sensor when acquiring real-time data. A sampling frequency of 1.0 kHz per sensor was utilized when conducting velocity calibrations.

In order to accommodate the 55+ cm length of the 1294 probe, an long extension was attached between the main traverse body and the Y-traverse, moving the leading edge of the Y-traverse approximately 36 cm forward of the main traverse body. When mounted the tip of the 1294 probe extends 26 cm from the leading edge of the Y-traverse, and cannot be moved closer than 3 cm from the groundplane without fear of interference between the probe's data cables and the groundplane.

Traverse motion was controlled by the IBM computer when using the 3-component probes and pitot-static tube readings were made with the Data Translation A/D converter.

D.2 Angular Calibration Of Sensors

The effective cooling velocity of a single sensor element varies both as a function of pitch angle and yaw angle of the total velocity vector with respect to the longitudinal axis of the sensor. Figure D.2 shows the geometry of the pitch angle, θ, and yaw angle, α, for a single sensor. From Jorgensen [18], the effective cooling velocity for this single sensor can be expressed as follows:

$$U_{eff}^2 = U_N^2 + k^2 U_T^2 + h^2 U_B^2 \qquad \text{(D.1)}$$

where U_N, U_T and U_B are the normal, tangential and binormal components of the velocity vector, and

$$U_{eff}^2(\alpha) = U(0)^2 \left(\cos^2\alpha + k^2\sin^2\alpha\right), \quad \text{for } \theta = 0 \qquad \text{(D.2)}$$

$$U_{eff}^2(\theta) = U(0)^2 \left(\cos^2\theta + h^2\sin^2\theta\right), \quad \text{for } \alpha = 0 \qquad \text{(D.3)}$$

with the angular coefficients

$$k = \text{yaw factor}$$

$$h = \text{pitch factor.}$$

The yaw and pitch factors are found by aligning each individual sensor normal with a known flow and rotating the probe through a series of yaw and pitch angles. U_{eff} is measured directly and the yaw and pitch factors can then be found by solving equations D.2 and D.3 for the respective factors. The values used for the pitch and yaw factors were $k - 0.2$ and $h = 1.0$.

D.3   Velocity Calibration Of Three Component Probes

Velocity calibration of the three components consists of aligning the probe axis with the velocity vector of the wind tunnel. Tunnel speed is varied while an effective voltage, V_{eff}, is measured for each of the three sensors, resulting in a relationship between the effective velocity, U_{eff}, and V_{eff} for each of the individual sensors. The free stream velocity is measured with a pitot-static probe. Due to the incident angle of the sensors relative to the free stream flow, the effective velocity each element sees, U_{eff}, is related to the free stream velocity through geometry and use of the yaw angular coefficient, k.

This relation is given by

$$U_{eff} = U_{freestream}\sqrt{\cos^2 35.26° + k^2 \sin^2 35.26°}. \qquad (D.4)$$

A least squares third order polynomial of the form

$$U_{eff} = A + BV_{eff} + CV_{eff}^2 + DV_{eff}^3 \qquad (D.5)$$

is then fit to the data for each sensor.

D.4 Data Reduction - The Complete System

Combining the previous sections on angular calibration and velocity calibration for the three sensors results in a system of equations that must be solved in order to obtain the three velocity components in wind tunnel coordinates, u, v, and w. This technique presented below is based on works by Yavuzkurt [29] and Andreopolous [5]. First, we start with the three equations relating the effective velocities to the probe coordinate velocities through the angular coefficients,

$$
\begin{aligned}
U_{eff_1}^2 &= k_1^2 X^2 + Y^2 + h_1^2 Z^2 \\
U_{eff_2}^2 &= h_2^2 X^2 + k_2^2 Y^2 + Z^2 \\
U_{eff_3}^2 &= X^2 + h_3^2 Y^2 + k_3^2 Z^2
\end{aligned}
\qquad (D.6)
$$

where X, Y, and Z are the velocity components of the total velocity vector along the probe sensor axes. Next, the relations between U_{eff} and the measured sensor voltages are utilized.

$$
\begin{aligned}
U_{eff_1} &= A_1 + B_1 V_{eff_1} + C_1 V_{eff_1}^2 + D_1 V_{eff_1}^3 \\
U_{eff_2} &= A_2 + B_2 V_{eff_2} + C_2 V_{eff_2}^2 + D_2 V_{eff_2}^3 \\
U_{eff_3} &= A_3 + B_3 V_{eff_3} + C_3 V_{eff_3}^2 + D_3 V_{eff_3}^3
\end{aligned}
\qquad (D.7)
$$

In the above sets of equations V_{eff_i} is measured and gives U_{eff_i} directly. The angular

coefficients k_i and h_i are known from the angular calibration, leaving three unknowns

in equation D.7, X, Y, and Z. Equation D.7 can be rewritten in matrix notation as

follows,

$$
\begin{bmatrix} U^2_{eff_1} \\ U^2_{eff_2} \\ U^2_{eff_3} \end{bmatrix} = \begin{bmatrix} k_1^2 & 1 & h_1^2 \\ h_2^2 & k_2^2 & 1 \\ 1 & h_3^2 & k_3^2 \end{bmatrix} \begin{bmatrix} X^2 \\ Y^2 \\ Z^2 \end{bmatrix}
\tag{D.8}
$$

Solving for X, Y, and Z gives the following equations.

$$
\begin{bmatrix} X^2 \\ Y^2 \\ Z^2 \end{bmatrix} = \begin{bmatrix} k_1^2 & 1 & h_1^2 \\ h_2^2 & k_2^2 & 1 \\ 1 & h_3^2 & k_3^2 \end{bmatrix}^{-1} \begin{bmatrix} U^2_{eff_1} \\ U^2_{eff_2} \\ U^2_{eff_3} \end{bmatrix}
\tag{D.9}
$$

Once equation D.9 is solved the velocity components in wind tunnel coordinates can

then be found through Euler coordinate transformations.

$$
\begin{bmatrix} u \\ v \\ w \end{bmatrix} = N \begin{bmatrix} X \\ Y \\ Z \end{bmatrix}
\tag{D.10}
$$

where N is the transformation matrix between probe coordinates and wind tunnel co-

ordinates.

D.5   3-Component Probe Angular Sensitivity

Testing of the probe's sensitivity and angular accuracy in pitch and yaw angles was

required to determine the useful angular operating range of the probe. To accomplish

this the probe was mounted to a cylindrical strut connected to the rotatable model

mount on the ground plane, enabling the probe to be rotated through 360°. The strut

height was such that the probe was located at $Y = 21$ cm, approximately centering the probe between the ground plane and the test section side wall. The probe tip was located 23 cm forward of the pivot point, the strut center. A small mounting block on the strut with a V-groove allowed the probe to be rotated along its stem axis and to align and lock the sensors in the proper orientation for either pitch or yaw tests.

Yaw and pitch tests consisted of taking measurements at twenty-five separate angles, from $-60°$ to $+60°$ in $5°$ increments. The tests were repeated ten times for both pitch and yaw sweeps to verify repeatability. Note that during a yaw test the pitch angle was set at a constant zero degrees incidence, and similarly the yaw angle was set to zero degrees during a pitch test. Test section velocity was set to 20 m/s for all the angular tests.

Average pitch and yaw angles were calculated for each test and plotted with respect to the actual angle setting. The results of the yaw test are shown in Figure D.3 while the pitch test results are shown in Figure D.4. Both the calculated yaw and pitch angles are plotted in each of these figures.

In the yaw test (Fig.D.3) note the one-to-one linearity between the actual yaw angle and the calculated yaw angle out to about $\pm30°$, where the calculated angle starts to deviate from the desired behavior. This was expected as the sensors make a $35.26°$ geometric angle with the free stream flow when aligned with the flow. Also, the calculated pitch angle stays flat near zero degrees up to the same $\pm30°$ before deviating. The deviation from ideal at $-30°$ yaw was due, primarily, to a calculated w-velocity that was approximately six percent below the actual velocity, while the calculated u-velocity was not quite three percent higher than the actual u-velocity. At the other angular extreme, $+30°$, the calculated w-velocity was 14 percent lower than the actual velocity,

while the calculated u-velocity was about five percent higher that actual. From this test it became obvious that the probe's angular operating range would be limited more by the errors in the estimation of the crossflow velocities v and w than it would be by errors in the streamwise velocity u. The yaw angle operating range for the probe was liberally determined to be between $-30°$ and $+30°$.

Pitch behavior of the probe was somewhat different than yaw behavior. The calculated pitch angle in Figure D.4 maintained a one-to-one relationship to the actual pitch angle between the range of $-15°$ to almost $+50°$. Although the range of angles in the linear region is comparable to the range of yaw angle linearity in the yaw tests, it is shifted towards the positive angles. The physical geometry of the probe sensors causes this shift and the reason is as follows. When pitching the probe, one sensor always lies in a vertical plane and has a greater change sensitivity to the flow angularity than the other two sensors as the pitch angle changes. As the pitch angle increases in the negative sense, the flow becomes more aligned with the longitudinal axis of this sensor, resulting in a lower cooling rate for the sensor. After an angle of about $-15°$ the sensitivity of this sensor has diminished to such a point that the calculated flow angle deviates quite radically from ideal behavior. While pitching in the positive direction, the sensor becomes more and more normal to the flow, until it is actually perfectly normal to the flow at a pitch angle of $+35.16°$. After $+35.16°$ the flow again starts becoming less normal to the vertical sensor. Because of the asymmetry between the sensor and the probe angle, a positive angular bias occurs in the pitch calibration. At an angle of $-15°$ the error in the calculated u-velocity was on the order of one percent, but, the error in the calculated v-velocity was 19 percent, giving an angular pitch error of $3°$. At $-10°$, the error in v was 16 percent, and the pitch angle was underestimated by $1.5°$. Based on these results, the acceptable limits of pitch angles for the probe was set at $-15°$ to

+35° with caution to be taken if the pitch angles approach or exceed these limits. Yaw behavior during the pitch test was good as the calculated yaw angle stayed near zero for all the probe angles.

The solution to the asymmetry of the pitch behavior is to offset the probe about −15° from the mean flow direction so as to get symmetrical performance in pitch. This offset angle is then taken into account during data reduction through the transformation matrix N of Equation D.10. Unfortunately, the angular performance data was not available until after the wake surveys were completed with the probe aligned with the freestream, resulting in some of the data exceeding the limits of pitch angle linearity.

Repeatability and accuracy of velocity measurements observed during the angularity tests was always less than 0.5%.
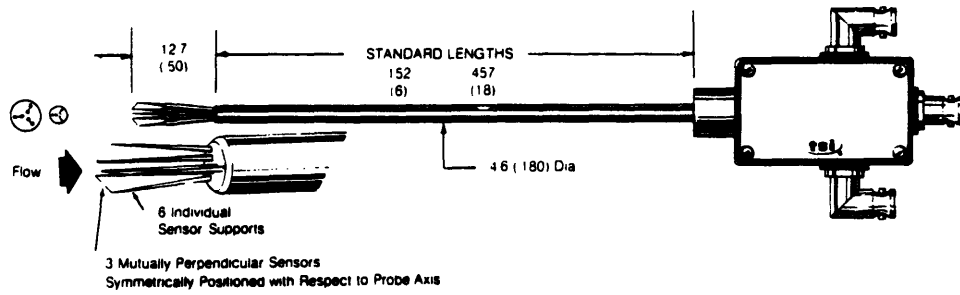
3D Probe - Model 1294

Figure D.1: Schematic of TSI 3-component hot film probe.

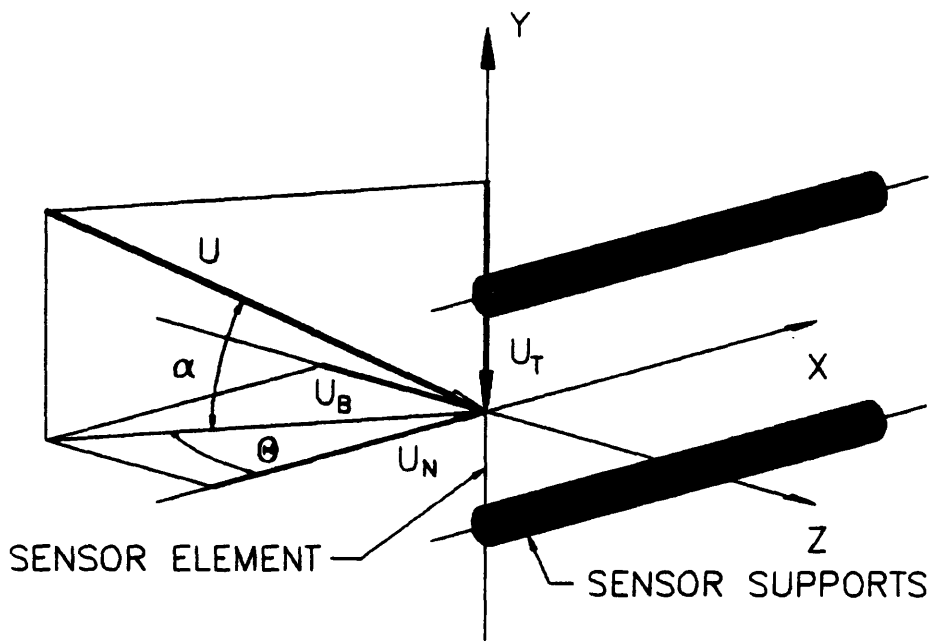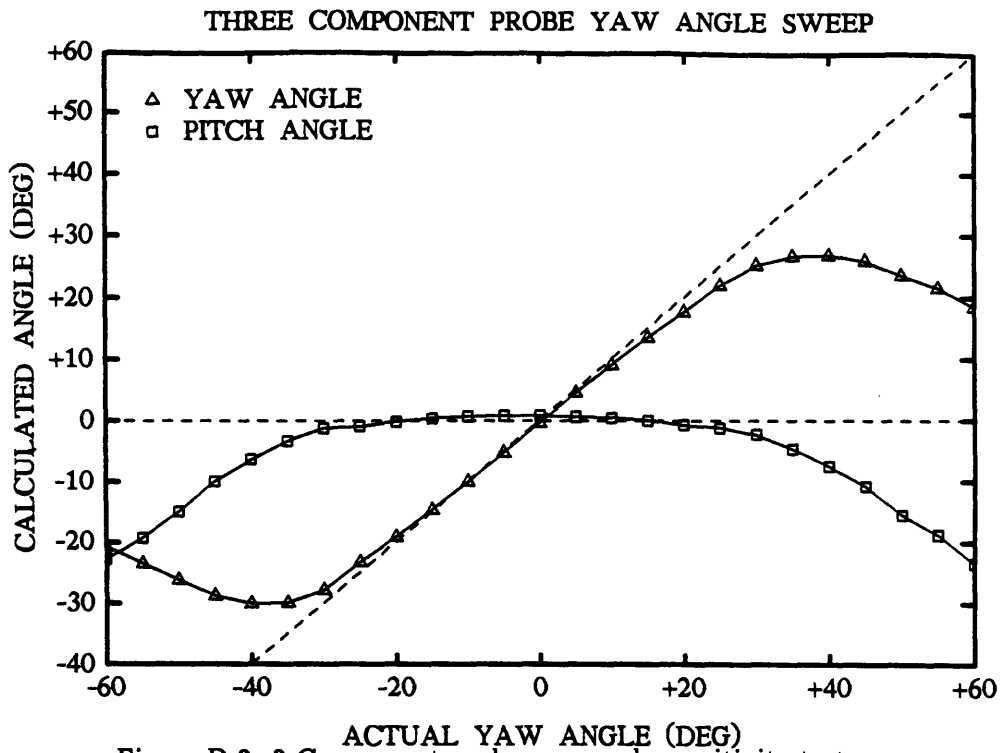Figure D.2: Flow angle definitions for a single sensor.

THREE COMPONENT PROBE YAW ANGLE SWEEP

Figure D.3: 3-Component probe yaw angle sensitivity test.
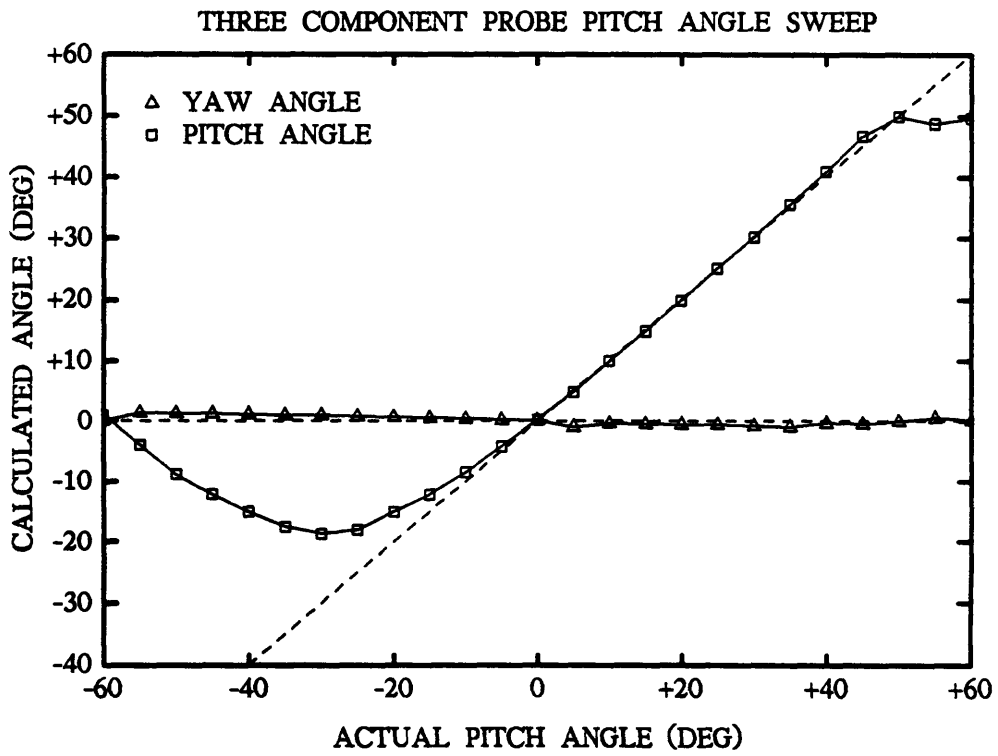
THREE COMPONENT PROBE PITCH ANGLE SWEEP

Figure D.4: 3-Component probe pitch angle sensitivity test.

References

[1] AHMED, S. Dec. 1983. Influence of base slant on the wake structure and drag of road vehicles. *J. of Fluids Eng.* **105**, 429–434.

[2] AHMED, S. March 1981. Wake structure of typical automobile shapes. *J. of Fluids Eng.* **103**, 162–169.

[3] AHMED, S. & BAUMERT, W. June 1979. The structure of wake flow behind road vehicles. In MOTEL, T., editor, *Aerodynamics of Transportation.* pp 93–103 ASME.

[4] AHMED, S., RAMM, G. & FALTIN, G. 1984. Some salient features of the time-averaged ground vehicle wake. *SAE Technical Paper Series* No. 840300.

[5] ANDREOPOULOS, J. 1983. Improvements of the performance of triple hot wire probes. *Rev.Sci.Instrum.* (6) 733–740.

[6] BEARMAN, P. 1984. Some observations on road vehicle wakes. *SAE Technical Paper Series* No. 840301.

[7] BEARMAN, P., DAVIS, J. & HARVEY, J. 1983. Measurement of the structure of road vehicle wakes. *Int. J. of Vehicle Design, Technlogical Advances in Vehicle Design Series, SP3, Impact of Aerodynamics on Vehicle Design* 493–499.

[8] BETZ, A. 1925. A method for direct determination of profile drag (in german). *Z. Flugtechn. Motorluftschiffahrt* (16).

[9] BLACKWELDER, R. 1981. Hot-wire and hot-film anemometers. In *Methods of Experimental Physics.* pp 259–315 ,ed. R.J. Emrich, 18(A).

[10] COGOTTI, A. Feb. 1986. Car-wake imaging using a seven-hole probe. In *Aerodynamics: Recent Developments.* pp 1–25 SAE 860214.

[11] DAVIS, J. Oct. 1982. *Wind Tunnel Investigations of Road Vehicle Wakes.* PhD thesis. Imperial College of Science and Technology. Prince Consort Road, London, S.W.7.

[12] GRESKO JR., L. Nov. 1988. Characteristics of wall pressure and near-wall velocity in a flat plate turbulent boundary layer. *MIT Tech. Rep.* No. FDRLR 88-2 Cambridge, MA.

[13] HACKETT, J. & SUGAVANAM, A. Feb. 1984. Evaluation of a complete wake integral for the drag of a car-like shape. *SAE Tech. Rep.* No. 840577.

[14] HACKETT, J., WILLIAMS, J. & PATRICK JR., J. 1985. Wake traverses behind production cars and their interpretation. *SAE Technical Paper Series* No. 850280.

[15] HARVEY, J. & PERRY, F. 1971. Flowfield produced by trailing vortices in the vicinity of the ground. *AIAA Journal* (61) 1659–1660.

[16] HINZE, J. 1975. *Turbulence.* pp 166–168. McGraw-Hill, Inc.

[17] JANSSEN, L. & HUCHO, W. 1974. Aerodynamische formoptimierung der typen vw-golf und vw-scirocco. *Kolloquium ueber Industrie-aerodynamik* 46–49. Part 3.

[18] JORGENSEN, F. Nov. 1970. Directional sensivity of wire and fiber-film probes. *Danmarks Ingenior Akademi Tech. Rep.* . Published by DISA.

[19] LANDAHL, M. unpublished. Drag on a ground vehicle in separated turbulent flow. *Massachusetts Institute of Technology.*

[20] LUEPTOW, R., BREUER, K. & HARITONIDIS, J. 1988. Computer-aided calibration of x-probes using a look-up table. *Experiments in Fluids* (6) 115–118.

[21] MASKELL, E. Jan. 1973. Progress towards a method for the measurement of the components of the drag of a wing of finite span. *Royal Aircraft Establishment Technical Report* No. 72232.

[22] MAULL, D. 1980. The drag of slant based bodies of revolution. *Cambridge University Engineering Dept.*

[23] MOREL, T. 1978. Aerodynamic drag of bluff body shapes characteristic of hatchback cars. *GMR General Motors Research Internal* No. GMR-2545 General Motors Research Labs, Warren, Michigan.

[24] MOREL, T. 1978. Aerodynamic drag of bluff body shapes characteristic of hatchback cars. *SAE Technical Paper Series* No. 780267.

[25] MOREL, T. 1978. The effect of base slant on the flow pattern and drag of three-dimensional bodies with blunt ends. In SOVRAN, G., MOREL, T. & MASON JR., W., editors, *Aerodynamic Drag Mechanisms of Bluff Bodies and Road Vehicles.* pp 191–217.

[26] ONORATO, M., COSTELLI, A. & GARRONE, A. Feb. 1984. Drag measurement through wake analysis. *SAE Tech. Rep.* No. 840302.

[27] PARKER, R. 1967. Resonance effects in wake shedding from parallel plates: calculation of resonant frequencies. *J.Sound Vibration* (5) 330–343.

[28] PARKER, R. 1966. Resonance effects in wake shedding from parallel plates: some experimental observations. *J.Sound Vibration* (4) 62–72.

[29] YAVUZKURT, S., CRAWFORD, M. & MOFFAT, R. 1978. Real-time hot-wire measurements in three-dimensional flows. *Stanford University Tech. Rep.* .